
Electronic Thesis and Dissertation Repository

7-27-2015 12:00 AM

Production Of Activated Carbons From Pyrolytic Char For Environmental Applications

Anastasia Colomba, *The University of Western Ontario*

Supervisor: Dr. Franco Berruti, *The University of Western Ontario*

Joint Supervisor: Dr. Cedric Briens, *The University of Western Ontario*

A thesis submitted in partial fulfillment of the requirements for the Doctor of Philosophy degree in Chemical and Biochemical Engineering

© Anastasia Colomba 2015

Follow this and additional works at: <https://ir.lib.uwo.ca/etd>

 Part of the [Chemical Engineering Commons](#)

Recommended Citation

Colomba, Anastasia, "Production Of Activated Carbons From Pyrolytic Char For Environmental Applications" (2015). *Electronic Thesis and Dissertation Repository*. 2978.
<https://ir.lib.uwo.ca/etd/2978>

This Dissertation/Thesis is brought to you for free and open access by Scholarship@Western. It has been accepted for inclusion in Electronic Thesis and Dissertation Repository by an authorized administrator of Scholarship@Western. For more information, please contact wlsadmin@uwo.ca.

Production Of Activated Carbons From Pyrolytic Char For Environmental Applications

(Thesis format: Monograph)

by

Anastasia Colomba

Graduate Program in Engineering Science
Department of Chemical and Biochemical Engineering

A thesis submitted in partial fulfillment
of the requirements for the degree of
Doctor of Philosophy

The School of Graduate and Postdoctoral Studies
The University of Western Ontario
London, Ontario, Canada

© Anastasia Colomba 2015

Abstract

Biomass pyrolysis has the potential to become a major component of future biorefineries, since biomass is cracked to produce gases, liquid products (bio-oil) and solid products (bio-char). In order for the process to be economically feasible, it is necessary to obtain the maximum value from each stream, thus no by-product can be regarded as a waste.

Bio-char is normally regarded as a by-product of fast pyrolysis, which is optimized to target bio-oil production. However, there are many potentially attractive applications for it: for example, it can be used for the production of activated carbons, which are the most commonly used adsorbent materials.

In this study, a new reactor technology developed at ICFAR, the Jiggled Bed Reactor (JBR) is employed as a fast and reliable tool for the optimization of the production of activated carbons from biomass. Due to its excellent heating system, both slow and fast pyrolysis conditions can be achieved, and activation can be carried out. The results obtained in the JBR show good comparison with larger scale reactors, thus allowing the screening of new pyrolysis and activation conditions as well as different feedstocks in a fast and reliable way.

The impact of the type of feedstock, activation and pyrolysis conditions (fast/slow) on the final product characteristic and activation kinetics are studied.

Finally, the performance of activated carbons produced in the JBR as adsorbents is evaluated for different environmental applications, such as the removal of ammonia and mercury from wastewater and of naphthenic acids from Oil Sands Process-affected water (OSPW). In particular, activated carbon produced from Kraft lignin is shown to outperform commercial activated carbon for wastewater treatment applications.

Keywords

Activated carbons, biomass, Kraft lignin, pyrolysis, Jiggled Bed Reactor, bio-char, mercury, naphthenic acids

Acknowledgments

First, I would like to acknowledge for my supervisors, Dr. Franco Berruti and Dr. Cedric Briens. Thank you for accepting me into your research group, always believing in me and pushing me to do my best. Thank you for your time and support and for the good times while travelling together.

I would also like to acknowledge the people without whom this work would have not been possible:

Students, Post-Docs and staff at ICFAR and in particular Valentina Lago, Liliana Pardo and Carolina Morales, Dr. Roel Westerhof, Dr. Pietro Palmisano and Dr. Dongbing Li, Caitlin Marshall, Rob Taylor and Karen McDonalds, for your help and for sharing this journey with me. You all are part of the happiest memories of these years.

Ying Zhang from CBE for the help with the BET measurements.

Dr. Ajay Dalai, for inviting me to your lab at the University of Saskatchewan and sharing with me your extensive experience. Thank you for your jokes and your contagious laughter.

Dr. Rambabu Nedunuri, for the time you dedicated to me during my stay at the University of Saskatchewan. Thank you for your immense kindness and for cooking the best biryani for me.

My appreciation also goes to BioFuelNet Canada for the funding and for providing me with two HQP Travel Awards to attend conferences and meetings and the Exchange Award to visit Dr. Dalai's lab in Saskatoon.

Finally, I would like to acknowledge my family and my friends for their unconditioned love and support.

Last, but not least, Mitesh Chaudhari: the most special thanks is for you, for always being by my side in both the tough and happy moments I experienced during the last years. Thank you for pushing me to always see the good in life and never give up. Thank you for loving me. Your presence has been the biggest support in my PhD journey.

Dedication

In loving memory of my Godfather and Uncle Maurizio.

Table of Contents

Abstract	ii
Keywords	ii
Acknowledgments.....	iii
Dedication	iv
Table of Contents	v
List of Tables	x
List of Figures	xii
Abbreviations, Symbols, Nomenclature	xviii
Chapter 1	1
1. Introduction.....	1
1.1 Motivation	1
1.2 What is Pyrolytic Bio-Char?	3
1.3 Possible Bio-Char Applications	3
1.4 Activated Carbons	7
1.4.1 Current and perspective market.....	7
1.4.2 Feedstocks for the production of activated carbons	9
1.4.3 Production processes	9
1.5 Biomass Pyrolysis	12
1.5.1 The pyrolysis process	12
1.5.2 Reactors used for biomass pyrolysis	13
1.6 Context and Scope of this Thesis	15
1.7 Thesis Structure.....	17
Chapter 2.....	19
2. Materials and Methodology	19
2.1 Feedstocks	19

2.2	Experimental Set Up: the Jiggled Bed Reactor (JBR)	22
2.3	Pyrolysis and Activation Procedures.....	27
2.3.1	Batch pyrolysis experiments (with CO ₂ activation)	27
2.3.2	Fast pyrolysis experiments	28
2.3.3	Activation experiments with wet gases	29
2.3.4	Production of HNO ₃ treated activated carbons	29
2.3.5	Reproducibility	29
2.4	Experimental Set Up: the Bubbling Bed Reactor.....	30
2.5	Sample Analyses	32
2.5.1	Proximate analysis.....	32
2.5.2	Elemental Analysis.....	32
2.5.3	Surface area and pore volume	33
2.5.4	SEM.....	37
2.5.5	Thermo Gravimetric Analysis (TGA) of olive residue	37
2.5.6	Temperature programmed desorption (TPD).....	37
2.5.7	Boehm titration.....	37
2.5.8	Particle size distribution	38
2.6	Adsorption Theory and Studies.....	38
2.6.1	Kinetic models.....	38
2.6.2	Adsorption isotherms	40
2.7	Procedure for Adsorption Studies	41
2.8	Preparation of Solutions for Adsorption and Analytical Determination.....	42
2.8.1	Preparation of ammonia solutions and determination of ammonia concentration	42
2.8.2	Preparation of naphthenic acids solutions and determination of naphthenic acids concentration.....	43
2.8.3	Preparation of mercury solutions and determination of mercury concentration	45
	Chapter 3	47

3.	Application of the Jiggled Bed Reactor to the development of Effective Pyrolysis and Activation Processes for the Production of Activated Carbons from Biomass	47
3.1	Introduction	47
3.2	Materials and Methods	48
3.3	Results and Discussion.....	48
3.3.1	Pyrolysis char yield	48
3.3.2	Impact of activation conditions	49
3.3.3	Activation kinetics.....	55
3.3.4	Characterization of the porous structure	61
3.3.5	Possible integration of activation with the pyrolysis process	63
3.3.6	Impact of feedstock characteristics	66
3.4	Conclusions	72
Chapter 4	75
4	Development of a Model for the Prediction of the Yield and Surface Area during Activated Carbons Production in the Jiggled Bed Reactor	75
4.1	Introduction	75
4.2	Model Assumptions.....	77
4.3	Materials and Methods	79
4.4	Model Development and Validation	79
4.5	Using the Model for the Optimization of the Activation Process	87
4.6	Conclusions	89
Chapter 5	95
5.	Influence of Pyrolysis Conditions on the Production of Activated Carbons in a Jiggled Bed Reactor	95
5.1	Introduction	95
5.2	Materials and Methods	96
5.3	Results and Discussion.....	96
5.3.1	Impact of heating rate and pyrolysis temperature on char yield prior to activation.....	96

5.3.2	Impact of heating rate and pyrolysis temperature on activated carbons properties	97
5.3.3	Impact of heating rate and pyrolysis temperature on the activation kinetics: application of the kinetic and physical models.....	103
5.4	Conclusions	110
Chapter 6.....		112
6.	Comparison of the Results Obtained in the JBR with a Pilot Scale Bubbling Bed Reactor and Impact of the Use of a Binder during the Production of Activated Carbons	112
6.1	Introduction	112
6.2	Materials and Methods	112
6.3	Results and Discussion.....	113
6.3.1	Validation of JBR through comparison to bubbling bed with birch bark	113
6.3.2	Application to Kraft lignin and impact of the use of granules.....	114
6.4	Conclusions	122
Chapter 7.....		124
7.	Applications	124
7.1	Structure of the Chapter	124
7.2	Adsorption of Ammonia: Results and Discussion	127
7.3	Adsorption of Naphthenic Acids: Results and Discussion.....	138
7.4	Adsorption of Mercury: Results and Discussion.....	145
7.5	Conclusions	155
Chapter 8.....		161
8.	Conclusions and Recommendations	161
8.1	Conclusions	161
8.2.	Recommendations	162
References		163
Appendix I		177
I.	Production of Bio-Coal from Biomass in a Mechanically Fluidized Reactor (MFR)	177
I.I	Introduction	177

I.II Materials and Methods.....	178
I.III Results and Discussion	179
I.IV Conclusions	187
I.V References.....	188
Appendix II	190
II. Arsenic Removal from Natural Water by Means of Bio-Char: the Case of Bangladesh	190
II.I Abstract	190
Appendix III.....	191
III. Granulation of Bio-Char for Soil Amendment	191
Curriculum Vitae	192

List of Tables

Table 1.1 – Different sources of biomass (adapted from Basu, 2013)	2
Table 1.2- Example of activation type and applications for activated carbons produced from biomass	11
Table 1.3- Example of applications of activated carbons as catalysts	11
Table 1.4- Operating conditions, typical product yield and reactor configurations for different types of pyrolysis (Adapted from Basu (2013), Bridgwater (2000) and Yang (2014)).....	14
Table 2.1- Feedstocks selected in this study, origin and date of harvest	20
Table 2.2- Feedstocks characteristics	21
Table 2.3- Example of reproducibility of replicates for 95 °C/min heating rate, 500 °C pyrolysis temperature	30
Table 2.4- Reproducibility results for elemental analysis, %	32
Table 2.5- Example of reproducibility of results for BET measurements	34
Table 3.1- Summary of experiments and results	51
Table 3.2- Determination of k_y for different temperatures	57
Table 3.3- Determination of k_{yo} and E_{ay}	57
Table 3.4- Determination of k_s for different temperatures.....	58
Table 3.5- Determination of k_{so} and E_{as}	59
Table 3.6- Selection criteria for the comparison of different biomasses	66
Table 3.7- Surface area vs. yield parameters for different feedstocks.....	68
Table 3.8- Composition of pyrolysis gases.....	73
Table 3.9- Combustion reactions for the non-condensable gases stream	73
Table 4.1- Calculated value of $n_p k$	84
Table 4.2- Determination of $n_p k_0$ and E_a	85
Table 4.3- Models parameters.....	93
Table 4.4- Values of SSE and MPE for the different models	94
Table 5.1- Initial surface area for different activation conditions	104
Table 5.2 Particle radius for different pyrolysis conditions.....	106

Table 6.1- Comparison between char and activated char yield and surface area in the JBR and in the bubbling bed during birch bark fast pyrolysis	113
Table 6.2- Elemental analysis of char produced from birch bark at 550 °C.....	113
Table 6.3- Results of activation carried out in the JBR starting from char pyrolyzed in the bubbling bed or in the JBR.....	114
Table 6.4- Comparison of n_{pk} values for slow and fast pyrolysis with granulated and un-granulated lignin	117
Table 6.5- Comparison of n_{pk} values for slow and fast pyrolysis with granulated and un-granulated olive residue	121
Table 7.1- Yield and surface area of the different samples	127
Table 7.2- Elemental analysis of the different activated carbon samples.....	128
Table 7.3- Acidic surface groups obtained from TPD, $\mu\text{mol/g}$	128
Table 7.4- Comparison of the removal efficiencies of the different char samples	133
Table 7.5- Langmuir and Freundlich isotherm parameters.....	133
Table 7.6- Properties of the carbons used (SP=slow pyrolysis, FP= fast pyrolysis)	138
Table 7.7- Model compounds selected for the study	139
Table 7.8- Freundlich and Langmuir parameters for lignin samples.....	144
Table 7.9- Yield and surface area characteristics of the different types of carbons used.....	145
Table 7.10- Elemental analysis of the samples.....	145
Table 7.11- Equilibrium time.....	146
Table 7.12- Parameters calculated from fitting of linearized form of kinetic models (graphs omitted).....	147
Table 7.13- Goodness of fit (SSE) for the different models	149

List of Figures

Figure 1.1- Market segments for each application of activated carbons (adapted from Transparency Market Research, 2013)	8
Figure 1.2- Thesis structure	18
Figure 2.1- Schematic structure of the jigged bed reactor	22
Figure 2.2- Sequence of mixing during a) downward actuator retraction, b) upward actuator extension (Latifi, 2012).....	23
Figure 2.3- Reactor configuration used for batch experiments, full assembly (left) and lid (right)	24
Figure 2.4- Reactor configuration used for fast pyrolysis experiments full assembly (left) and lid (right)	25
Figure 2.5- Schematic of the pneumatic actuator (Latifi, 2012).....	26
Figure 2.6: a) Example of temperature history during pyrolysis (activation carried out at 800 °C for 1h) b) Gas flowrate during activation	28
Figure 2.7- Schematic of the bubbling bed reactor	30
Figure 2.8 Different types of adsorption isotherms (from Lowell, 1984)	35
Figure 2.9- Example of nitrogen adsorption isotherms for three selected samples	36
Figure 2.10- Colorimetric reaction for the determination of ammonia concentration.....	43
Figure 2.11- UV-vis spectra of a) model compounds solution b) real Oil Sands Process Water (OSPW).....	44
Figure 2.12- Calibration curve at 263 nm for a) model compounds solution b) real Oil Sands Process Water (OSPW).....	44
Figure 2.13- Colorimetric reaction of Rhodamine 6G with tetraiodomercurate	45
Figure 2.14- Calibration curve with Rhodamine 6G	46
Figure 3.1- a) Thermogravimetric profile and b) weight loss derivative of olive residue obtained with TGA obtained in the same conditions used for slow pyrolysis in the JBR	49
Figure 3.2: Effect of activation gas flowrate on a) the activated char yield and b) the activated char surface area	52

Figure 3.3: Effect of activation temperature on a) the activated char yield and b) the activated char surface area	53
Figure 3.4: Effect of activation time on a) the activated char yield and b) the activated char surface area.....	54
Figure 3.5: Relation between yield and surface area during olive residue activation (points with the same symbol were obtained at the same temperature and flowrate but different times)	55
Figure 3.6- Linearized Arrhenius plot for yield.....	57
Figure 3.7- Comparison between the yield calculated with the kinetic parameters and the yield obtained experimentally.....	58
Figure 3.8- Linearized Arrhenius plot for surface area.....	59
Figure 3.9- Comparison between the surface area calculated with the kinetic parameters and the one obtained experimentally	60
Figure 3.10- Comparison between the surface area vs. yield plot obtained experimentally (closed symbols) or calculated (open symbols) using the kinetic parameters.....	60
Figure 3.11: Relationship between micropore surface area and total surface area for different activated olive residue samples.....	61
Figure 3.12- SEM image of non activated char sample from olive residue	62
Figure 3.13- SEM image of activated char sample from olive residue	62
Figure 3.14- Integration of activation with the pyrolysis process	63
Figure 3.15- a) Yield b) Surface area variation with activation temperature using simulated combustion gases (open symbols) or pure CO ₂ (closed symbols) as activating agent	64
Figure 3.16- Trade-off between surface area and yield for char samples activated with pure CO ₂ (closed symbols) and CO ₂ /steam mixture (open symbols).....	65
Figure 3.17- Relationship between micropore surface area and total surface area for char samples activated with pure CO ₂ (closed symbols) and CO ₂ /steam mixture (open symbols).....	65
Figure 3.18- Surface area vs. yield trade-off for different feedstocks	67
Figure 3.19- Comparison between calculated and experimental values for a) intercept b) slope of the surface area vs. yield trade-off for different feedstocks.....	69
Figure 3.20- Surface area vs. yield trade-off comparison for olive residue and lignin	70
Figure 3.21- Comparison between mesopore surface areas for olive and lignin activated carbons	71

Figure 3.22- SEM images of lignin activated carbon samples	71
Figure 3.23- Methylene blued adsorption capacity as a function of mesopore volume for selected samples of olive residue and lignin activated carbons.....	72
Figure 3.24- Surface area vs yield trade-off for individual feedstocks	74
Figure 4.1- Reactions occurring within a char particle during activation.....	77
Figure 4.2- Particle size distribution for activated and non-activated samples of olive residue ..	79
Figure 4.3- Evolution of micropore and total surface area during activation of olive residue activated carbon	80
Figure 4.4- Evolution of average pore diameter with activation time for an activation temperature of 850 °C and 200 ml/min CO ₂ flowrate.....	81
Figure 4.5- Comparison between experimental values of surface area and a) a calculated with Equation 4.25 b) a calculated with Equation 4.27	86
Figure 4.6- Variation of the optimum activation time with the activation temperature	88
Figure 4.7- Selection of experimental conditions to maximize Yield*Surface area	89
Figure 4.8- Comparison of the predicted vs. experimental yields for the different models	93
Figure 5.1- Effect of pyrolysis temperature and heating time on the char yield (no activation) in the JBR.....	97
Figure 5.2- Effect of pyrolysis temperature on a) the activated char yield and b) surface area ...	98
Figure 5.3- Effect of heating rate on a) the activated char yield and b) surface area	99
Figure 5.4- Yield vs. surface area trade-off for activated carbon produced from char obtained with different heating rates during the pyrolysis step	100
Figure 5.5- Surface area vs. yield for different activation (black symbols) and pyrolysis conditions (open symbols) for a) all the experimental conditions from Chapter 3 and 5 b) for samples produced with a heating rate of 95 °C/min	101
Figure 5.6- Micropore surface area as a function of total surface area.....	102
Figure 5.7- Variation of the relationship between micropore surface area and total surface area for different activation conditions and different pyrolysis conditions	102
Figure 5.8- Variation of the initial surface area a_0 with the reciprocal of the heating rate during pyrolysis.....	104
Figure 5.9- Average pore diameter as a function of pyrolysis temperature and heating rate	105
Figure 5.10- a) k_s and b) k_y as functions of temperature for different heating rates	106

Figure 5.11- Values of n_{pk} as a function of the pyrolysis heating rate	107
Figure 5.12- Predicted vs. experimental a) yield b) surface area for activated carbon produced from char obtained with different heating rates during the pyrolysis step	109
Figure 5.13- Yield*surface area as a function of a) heating time and b) pyrolysis temperature	110
Figure 5.14- Detail of the surface of the char produced by a) slow pyrolysis and b) fast pyrolysis	111
Figure 6.1- Comparison between results obtained with bubbling bed and JBR with lignin fast pyrolysis and activation conditions of 1h 900 °C and 1h 850 °C, 200 ml/min CO ₂ flowrate.....	116
Figure 6.2- Comparison between results obtained with granulated and ungranulated lignin for slow and fast pyrolysis (activation conditions: 850 °C, 1h, 200 ml/min CO ₂ flow).....	117
Figure 6.3- Influence of the use of granules on lignin pyrolysis on the char yield as a function of the reciprocal of the heating rate.....	119
Figure 6.4- Influence of the use of granules on olive residue pyrolysis in the JBR	120
Figure 6.5- Comparison between results obtained with granulated and ungranulated olive residue for slow and fast pyrolysis (activation conditions: 850 °C, 1h, 200 ml/min CO ₂ flow)	121
Figure 7.1- Determination of equilibrium time.....	129
Figure 7.2- Effect of surface area on adsorption capacity for the different char samples.	130
Figure 7.3- Outer surface of a) Raw Olive Char (ROC), b) CO ₂ Activated Char (CAC), c) Acid-treated Activated Char (AAC).	131
Figure 7.4- Internal surface of CO ₂ activated (CAC) and HNO ₃ treated char samples (AAC)..	132
Figure 7.5- Equilibrium adsorption capacity as a function of acid surface groups content.....	132
Figure 7.6- Adsorption isotherms	134
Figure 7.7- Separation factor for different types of activated carbons	135
Figure 7.8 - Effect of adsorbent dose on equilibrium adsorption capacity for AAC.....	136
Figure 7.9- Effect of temperature on the equilibrium adsorption capacity for AAC.....	137
Figure 7.10- Example of equilibrium time determination (for lignin fast pyrolysis non activated) a) with NAs solution b) with OSPW.....	140
Figure 7.11- Relationship between a) surface area b) mesopore surface area and adsorption capacity for the adsorption of model compounds onto different types of activated carbons. Symbols legend: ■ Non activated petroleum coke ● Non activated slow pyrolysis lignin char ▲ Non	

activated fast pyrolysis lignin char ♦ Commercial coconut activated carbon □ Activated petroleum coke ○ Activated lignin slow pyrolysis char Activated lignin fast pyrolysis char	141
Figure 7.12- Relationship between a) surface area b) mesopore surface area and adsorption capacity for the adsorption of NAs from OSPW onto different types of activated carbons. Symbols legend: ■ Non activated petroleum coke ● Non activated slow pyrolysis lignin char ▲ Non activated fast pyrolysis lignin char ♦ Commercial coconut activated carbon □ Activated petroleum coke ○ Activated lignin slow pyrolysis char Activated lignin fast pyrolysis char	142
Figure 7.13- Relationship between total basic group concentration and adsorption capacity for the adsorption of a NAs from a) model compounds solution b) OSPW onto different types of activated carbons. Symbols legend: ■ Non activated petroleum coke ● Non activated slow pyrolysis lignin char ▲ Non activated fast pyrolysis lignin char ♦ Commercial coconut activated carbon □ Activated petroleum coke ○ Activated lignin slow pyrolysis char Activated lignin fast pyrolysis char.....	143
Figure 7.14- Adsorption isotherm results for a) slow pyrolysis lignin b) fast pyrolysis lignin and OSPW	144
Figure 7.15- Determination of equilibrium time.....	146
Figure 7.16- Comparison between experimental kinetic profile and predicted using kinetic parameters for commercial activated carbon	148
Figure 7.17- Comparison between experimental kinetic profile and predicted using kinetic parameters for lignin activated char.....	148
Figure 7.18- Comparison between experimental kinetic profile and predicted using kinetic parameters for olive residue activated char	149
Figure 7.19- Relationship between adsorption capacity and mesopore surface area for activated carbons with different ash contents. Symbols legend: ● Olive residue activated chars ▲ Commercial coconut activated char Lignin activated char.....	150
Figure 7.20- Adsorption capacity calculated through the correlation in Equation 7.1 vs. experimental adsorption capacity. Symbols legend: ● Olive residue activated chars ▲ Commercial coconut activated char Lignin activated char.....	151
Figure 7.21- Langmuir and Freundlich adsorption isotherms for lignin	152
Figure 7.22- Langmuir and Freundlich adsorption isotherms for olive residue	153
Figure 7.23- Separation factor for olive and lignin activated chars.....	154

Figure 7.24- Determination of a) Langmuir b) Freundlich adsorption parameters (Section 7.2)	156
Figure 7.25- Determination of a) Langmuir b) Freundlich adsorption parameters (Section 7.3)	156
Figure 7.26- Determination of a) Langmuir b) Freundlich adsorption parameters for lignin activated carbon (Section 7.4)	157
Figure 7.27 -Determination of a) Langmuir b) Freundlich adsorption parameters for olive residue activated carbon (Section 7.4)	157
Figure 7.28- Determination of kinetic parameters for commercial coconut activated carbon a) First order b) Pseudo second order c) Particle diffusion (Section 7.4)	158
Figure 7.29- Determination of kinetic parameters for lignin activated carbon a) First order b) Pseudo second order c) Particle diffusion (Section 7.4)	159
Figure 7.30- Determination of kinetic parameters for olive residue activated carbon a) First order b) Pseudo second order c) Particle diffusion (Section 7.4)	160
Figure I.1- Torrefaction yield of different biomasses at 260 and 300 °C	179
Figure I.2- HHV for different torrefied biomasses	180
Figure I.3- Energy recovery as a function of torrefaction temperature for different feedstocks	181
Figure I.4- Morphology of sorghum particles a. untreated b. torrefied at 260 °C c. popping of the seeds at 300 °C, d. stirrer after torrefaction at 300 °C	182
Figure I.5- Van Krevel diagram for the different biomasses. Black symbols: untreated biomass, grey symbols: torrefaction at 260 °C, white symbols: torrefaction at 300 °C	183
Figure I.6- Variation of the moisture content in willow over a period of 21 days in saturated water atmosphere	184
Figure I.7- Reduction in moisture content after 21 days as compared to virgin biomass	185
Figure I.8- Example of biological activity on the virgin biomass samples of sunflower husk and sorghum after 21 days	185
Figure I.9- Reduction in the energy required for grinding for torrefied samples	187
Figure I.10- Example of particle size reduction in the MFR as the torrefaction temperature is increased to 300 °C	187

Abbreviations, Symbols, Nomenclature

AAC: acid-treated activated carbon

BET: Brunauer-Emmett-Teller (surface area)

CAC: CO₂ activated carbon

FP: fast pyrolysis

GAC: granular activated carbon

JBR: Jiggled Bed Reactor

MPE: mean % error = $\frac{1}{n} \sum_{i=0}^n \frac{|y_{predicted} - y_{experimental}|}{y_{experimental}}$

NAs: naphthenic acids

OSPW: oil sands process affected water

PLC: programmable logic controller

PID: proportional integral derivative (controller)

ROC: raw olive char

RPM: random pore model

SCM: shrinking core model

SEM: scanning electron microscope

SP: slow pyrolysis

SSE: sum of squared errors = $\sum_{i=1}^n (q_{e,calculated} - q_{e,measured})^2$

STP: standard temperature and pressure

VRM: volume reaction model

a =surface area, m^2/g

a_0 = initial surface area, m^2/g

A = area of pores in one particle of activated carbon, m^2

A_0 = area of pores in one particle of non-activated carbon, m^2

b = Langmuir isotherm characteristic constant, L/g

c = Weber-Morris constant, $\text{mg/g} \cdot \text{min}^{0.5}$

c_e = equilibrium concentration, mg/L

c_0 = initial concentration, mg/L

d = pore diameter, m

d_0 = initial pore diameter, m

$D_p (R_p)$ = particle diameter (or radius), m

$D_{p0} (R_{p0})$ = initial particle diameter (or radius), m

E_a = activation energy, J/mol

E_{ay} = activation energy for yield reaction, J/mol

E_{as} = activation energy for surface area reaction, J/mol

k = kinetic constant, m/min

k_f = Freundlich isotherm adsorption capacity, L/g

k_{int} = kinetic constant for intraparticle diffusion model, $\text{mg}/(\text{g} \cdot \text{min}^{0.5})$

k_y = apparent kinetic constant for yield, min^{-1}

k_{y0} = reaction rate coefficient for yield, min^{-1}

k_s =apparent kinetic constant for surface area formation, $\text{m}^2/(\text{g}\cdot\text{min})$

k_{s0} = reaction rate coefficient for surface area formation, $\text{m}^2/(\text{g}\cdot\text{min})$

k_1^{st} = kinetic constant for first order adsorption model, min^{-1}

k_2^{nd} = kinetic constant for pseudo-second order adsorption model, $\text{mg}/(\text{g}\cdot\text{min})$

L_0 = pore length, m

m_c = mass of activated char, g

m_{c0} = mass of non-activated char, g

n = number of carbon atoms in NAs

n = Freundlich isotherm exponent

n_p = number of pores in one particle of char

p = partial vapour pressure of adsorbate gas in equilibrium with the surface at 77.4 K (liquid nitrogen)

p_a = partial pressure of activating agent

p_0 = saturated pressure of adsorbate gas

q_t = adsorption capacity at time t, mg/g

q_e = adsorption capacity at equilibrium, mg/g

Q^0 = Langmuir isotherm maximum adsorption capacity (monolayer)= Q_{max} , mg/g

R_L = ripartition coefficient

r_v = reaction rate for particle volume reduction, m^3/min

r_1 =reaction rate for pore enlargement, m/min

r_2 = reaction rate for pore deepening, m/min

t =time, minutes

V_a = volume of gas adsorbed at standard temperature and pressure

V_c = volume of one particle of activated char, m^3

V_{c0} = volume of one particle of non- activated char, m^3

V_m = volume of gas adsorbed at STP

V_{pores} = volume of pores in one particle of activated char, m^3

y = pore depth, m

Y =yield of activated char, %

Y_0 = yield of non-activated char, %

x = conversion, %

x : number of oxygen atoms in NAs

z : hydrogen deficiency due to rings formation in NAs

ε_0 = solid porosity

ρ_c = density of activated char, m^3/g

ρ_{c0} = density of non-activated char, m^3/g

ψ =surface function parameter for random pore model

Chapter 1

1. Introduction

1.1 Motivation

Renewable energy from biomass has received increasing interest due to the growing concerns over declining fossil oil reserves and increases in energy demand and cost. Biomass can come from a variety of sources as shown in Table 1.1 (from Basu, 2013).

The International Renewable Energy Agency (IRENA) estimates that total biomass supply world-wide could range from 97-147 EJ/yr by 2030 (IRENA, 2014). About 38-45% of the total supply is estimated to originate from agricultural residues and waste (37-66 EJ/yr). The remaining supply potential (60-81 EJ/yr) is shared between energy crops (33-39 EJ/yr) and forest products, including forestry residues (27-43 EJ/yr). (To provide a reference, USA energy consumption is estimated to be 100 EJ/yr (Capareda, 2013)).

Besides its use as fuel, the emerging green bio-economy targets biomass as a source for the production of value-added chemicals. This philosophy led to the development of the concept of biorefineries, where the combination and integration of different biomass conversion processes generates both fuels and chemicals, very much as in traditional petrochemical refineries. This approach has two advantages: on one side, it maximizes the feed utilization and the product values, while, on the other side, both feedstocks and products slates can be adapted to the continuously fluctuating markets.

Biomass pyrolysis has the potential to become a major component of future biorefineries, since biomass is cracked to produce gases, liquid products (bio-oil) and solid products (bio-char). In order for the process to be economically feasible, it is necessary to obtain the maximum value from each stream, thus no by-product can be regarded as a waste.

Bio-char is normally regarded as a by-product of fast pyrolysis, which is optimized to target bio-oil production. However, there are many potentially attractive applications for it: for example, it can be used for the production of activated carbons, which are the most commonly used adsorbent materials.

In this study, a new reactor technology developed at ICFAR, the Jiggled Bed Reactor (JBR) is employed as a fast and reliable tool for the screening of different types of biomasses for the production of activated carbons. The JBR allows operating in conditions that are representative of large scale reactors and, due to its excellent heating system, both slow and fast pyrolysis conditions can be achieved, and activation can be carried out.

The first objective of this study was to investigate the suitability of the JBR for slow and fast pyrolysis and for activation of the produced pyrolytic bio-char into activated carbons. The second objective was to study the impact of the type of feedstock, activation and pyrolysis conditions on the final product characteristics. Finally, the performance of the produced activated carbons for adsorption applications was undertaken, and the results compared with commercial products.

Table 1.1 – Different sources of biomass (adapted from Basu, 2013)

A. Virgin biomass	A1. Terrestrial	i.	Forest biomass
		ii.	Grasses
		iii.	Energy Crops
		iv.	Cultivated Crops
	A2. Aquatic biomass	i.	Algae
		ii.	Water Plant
B. Waste biomass	B1. Municipal waste	i.	Municipal solid waste
		ii.	Biosolids, sewage
		iii.	Landfill gas
	B2. Agricultural solid waste	i.	Livestock and manure
		ii.	Agricultural crop residues
	B3. Forestry residues	i.	Bark, leaves
	B4. Industrial wastes	i.	Demolition wood
		ii.	Sawdust

1.2 What is Pyrolytic Bio-Char?

For the context of this thesis, the terms “pyrolytic bio-char”, or, simply “bio-char”, are used to refer to the solid co-product of biomass pyrolysis. Pyrolysis is a thermochemical process involving the thermolysis or chemical decomposition of organic (carbon-based) materials that takes place in the absence of an oxidizing agent. During pyrolysis, the large complex hydrocarbon molecules that constitute biomass (hemicellulose, cellulose and lignin) break down into smaller and simpler molecules of gas, liquid and solid. Generally, the product of interest in pyrolysis is the bio-oil, which can be used as a fuel or be refined for chemicals production. Bio-oil production can be maximized by using fast pyrolysis, while the gaseous stream (containing mainly CO, CO₂, CH₄ and H₂) is usually combusted to provide process heat. The third co-product of pyrolysis is pyrolytic bio-char, a solid residue containing mainly carbon and the biomass minerals (ashes).

The production of bio-char traces back to ancient times, and is one of the oldest industrial technologies developed (Antal, 1996). It was originally intended for the production of charcoal that was used to smelt tin for the manufacturing of bronze tools, or as a high-grade cooking fuel. Due to the decrease of petroleum resources, the environmental impact of the increased amounts of atmospheric greenhouse gases, the desire for sustainability of resources and, consequently, the increased interest in alternative feedstocks for the production of fuels and chemicals, the pyrolysis process tends to be oriented to the maximization of the bio-oil production, leaving bio-char as a by-product. Nonetheless, bio-char has several attractive applications such as a carbon-neutral fuel with properties similar to coal, reductant in the metallurgical industry as a coke substitute, adsorbent material, soil amendment and others (Antal et al., 2003).

1.3 Possible Bio-Char Applications

Despite its great popularity and promising potential, the use of bio-oil as a fuel or for chemical production requires expensive upgrading processes. Thus, the economics of the pyrolysis process needs to be improved by finding suitable applications for bio-char. The main challenge related to the development of commercial bio-char projects is the lack of information on how to produce an engineered product with the desired properties required for each application from suitable biomass sources. Brown (2009) pointed out that the increase in understanding bio-char characteristics for a specific application and how to acquire them will eventually encourage the use of different names

for different products; for example, bio-char when intended for soil amendment, bio-coke when used in the metallurgical industry, and bio-coal when used as coal substitute. Lehmann and Joseph (2009), and Kwapinski (2010) reported that the main causes of the poor use of bio-char for high value applications are: 1) the lack of systematic methods to characterize bio-char, 2) the lack of standard specifications for each application 3) a knowledge gap on the relationship between product characteristics, feedstock and operating conditions. Part of the challenge in making a process successful is the selection of the proper application. Producers would need to sell their product for approximately two to three times the cost of the original biomass to be profitable, because during pyrolysis only approximately a half to a third of the original biomass is transformable into saleable bio-char (although getting additional value from the bio-oil improves the economics).

Thus, two aspects are crucial: the selection of a proper application, with a well-established or, at least, a very promising market and price, and the selection of production conditions that would be relevant both for bio-oil and bio-char production, to maximize the process benefits.

In the case of bio-char, the following applications can be considered:

-FUEL: The use of biomass as a fuel has already been extensively investigated; nevertheless, biomass suffers of problems like high moisture content and low energy density, which leads to high transportation costs. Moreover, the grindability of biomass is poor, due to its fibrous nature; it has hydrophilic behavior, heterogeneous properties and relatively low calorific value (Tumuluru, 2011). As a result of pyrolysis, biomass can be converted into biomass-derived fuels such as bio-coal (charcoal) and bio-oil (Cruz, 2012).

Charcoal has always been used as a cooking fuel, and is the main fuel in developing countries. Due to its good calorific value, some fast pyrolysis processes use the bio-char, produced as a by-product, as a fuel to provide the process heat required for bio-oil production. In fact, bio-char has a good calorific value (19-25 MJ/kg), is basically S and N free, and thus a potential good fuel in term of emission and soot formation (Mullen et al., 2010).

For example, Boateng et al. (2007) asserted that burning the 15-20 % of bio-char with a calorific value of 20000-25000 kJ/kg produced as a by-product of the bio oil production (assuming a bio oil yield of 60-70%), would make the pyrolysis process for bio-oil production economically sustainable. A recent report on the potential use of bio-char as a fuel in British Columbia (de Ruiter,

2014) outlines how incentives such as carbon taxes and regulations on the production, transportation and use can also help the development of bio-carbon based bioenergy systems.

However, when the primary objective of biomass conversion is the production of a solid fuel, the process selection tends to be oriented to torrefaction. Torrefaction is a milder type of pyrolysis process which takes place at moderate temperatures (200-300 °C), which are sufficient to modify the structure of biomass, make it less hygroscopic and improve its grindability while still achieving a very high energy recovery in the solid product. Bio-char produced from pyrolysis contains a high quantity of carbon content i.e. between 20-50% of the carbon originally contained in the biomass in the case of pyrolysis, compared to around 70% in the case of torrefaction, with 90% of the energy content (Van der Stelt, 2011; Cruz, 2012).

-SOIL APPLICATION: The interest in soil application of bio-char arose since the discovery of “*Terra Preta*”. As reported by Lehmann (2003), Terra Preta is the local name given to certain dark earths of the Amazonian region, which have been proven to be highly fertile. This particular feature is related to the high carbon content detected (150 g C/kg soil), which is highly recalcitrant and, thus, can be stored in the soil for very long periods. Structural analysis, which demonstrated the similarity between Terra Preta and bio-char, lead researchers to focus on the potential application of bio-char to soil to improve its fertility. Thus, it is believed that the use of bio-char in soil can improve the productivity and, at the same time, due to its recalcitrant nature, is an efficient method to promote carbon sequestration, helping to mitigate global climate change.

Despite the fact that this is a very attractive application, it is still at an early stage and more research is needed to identify how parameters like soil type, plant type, and climate affect the performance of bio-char for soil application. Also, this is a multidisciplinary application that requires joint efforts involving engineers, soil and plant scientists. This contributed to the creation of a great number of organizations, such as the International Biochar Initiative, that have the aim of promoting the creation of standards and policies to guide public and regulatory confidence. The philosophy of the Lehmann group at Cornell University is that, instead of thinking of bio-char as a “one-size-fits-all” soil enhancer, tailor-made bio-char systems have to be created for individual applications, taking into account factors like soil type, climate and social setting (Abiven, 2014). The aim of their research program spans from increasing basic understanding of nutrient and organic matter dynamics in different soils to nutrient pathways and effects of bio-char on

microbial, faunal and root abundance once applied to soil (Lehmann, 2011). Brewer (2009, 2011, 2012) carried out a combination of soil application and analytical studies at Iowa State University, to understand the implication of the physical and chemical properties of different types of bio-char to soil responses (such as, for example, pH and cation exchange capacity) and CO₂ emissions, identifying potentially favorable scenarios for bio-char engineering. From the engineering point of view, significant amount of work is being carried out at the U.K. biochar institute, where the focus is to understand how the production conditions and the feedstock characteristics influence the stability of bio-char and the availability of nutrients in soil (Mašek, 2013; Crombie, 2013).

-CARBON FIBERS: Carbon fibers can be defined as fibers containing at least 92 wt % carbon. They are mainly used as a filler in composites, due to their excellent tensile properties, low densities, high thermal and chemical stabilities in the absence of oxidizing agents, good thermal and electrical conductivities, and excellent creep resistance (Huang, 2009). The current carbon fiber market is dominated by polyacrylonitrile (PAN) feedstock, but a significant research effort is being devoted towards its production from renewable sources with low cost without sacrificing the high carbon content. Feedstocks such as lignin have already been investigated for this purpose starting from the 70's (Otani, 1969). More recently, this has been the focus of research networks such as Lignoworks, which have proved the feasibility of producing carbon fibers from Kraft lignin (Lin, 2013). The electrical conductivity and magnetic properties of lignin-based nanofibers were found to be comparable or superior to that of PAN based magnetic carbon nanofibers, and the addition of single wall nanotubes (SWNT) allowed achieving higher values of tensile and Young's modules. In 2013, precursor fibers from lignin were converted into carbon fibers in the first commercial-scale trial, a partnership between Weyerhaeuser and Zoltek (Weyerhaeuser, 2013). Since the production process involves a carbonization step, to remove volatiles, oxygen and nitrogen, it is believed that bio-char resulting from pyrolysis of biomass with high carbon content and low ash content could be successfully used for this application.

-OTHER CARBON-BASED MATERIALS: There is also the potential for bio-char to be converted into high-value carbon products. Applications could include manufacturing of synthetic graphite, which can be used in some types of batteries and fuel cells, and carbon electrodes (de Ruiter, 2014). Other high value applications can be the substitution of carbon black as filler in composite materials (Abdul Khail, 2007 and 2010; Peterson, 2011), thermoplastics (Lou, 2007) as

well as the production of catalysts for tar cracking, esterification and hydrolysis (Kastner, 2012; Ormsby, 2012). These products can surely represent the future of high value applications for bio-char, but are currently limited to smaller scales and laboratory research.

-ACTIVATED CARBONS: Pyrolytic bio-char can be used as a precursor for the production of activated carbons. Activated carbons are the most used adsorbent material, with a price ranging from hundreds to several thousand dollars per metric ton, depending on formulation, specificity, and performance. Their applications range from wastewater treatment, air purification, removal of contaminants and many others. More insight into this application will be discussed later (Paragraph 1.4).

The main application selected for this thesis is the production of activated carbons. Insight into the activated carbons market that can justify this choice will be given in the following paragraphs.

1.4 Activated Carbons

1.4.1 Current and perspective market

According to the global activated carbons market forecast and opportunities (The Freedonia Group, 2014), the demand for activated carbons is expected to increase more than 10% per year for the next 5 years to reach a \$3 billion market by 2017. The main applications are water treatment and air purification.

Figure 1.1 shows the demand for each application as of 2012 (adapted from Transparency Market Research, 2013). The water treatment application segment held the largest market share in 2012, and its consumption is expected to grow at a rate of 10.2% per year from 2013 to 2019.

On the other hand, the air purification segment is tagged as the fastest growing application segment for the activated carbon market. With respect to revenue generated, it is expected to grow at a rate of 13% from 2012 to 2019.

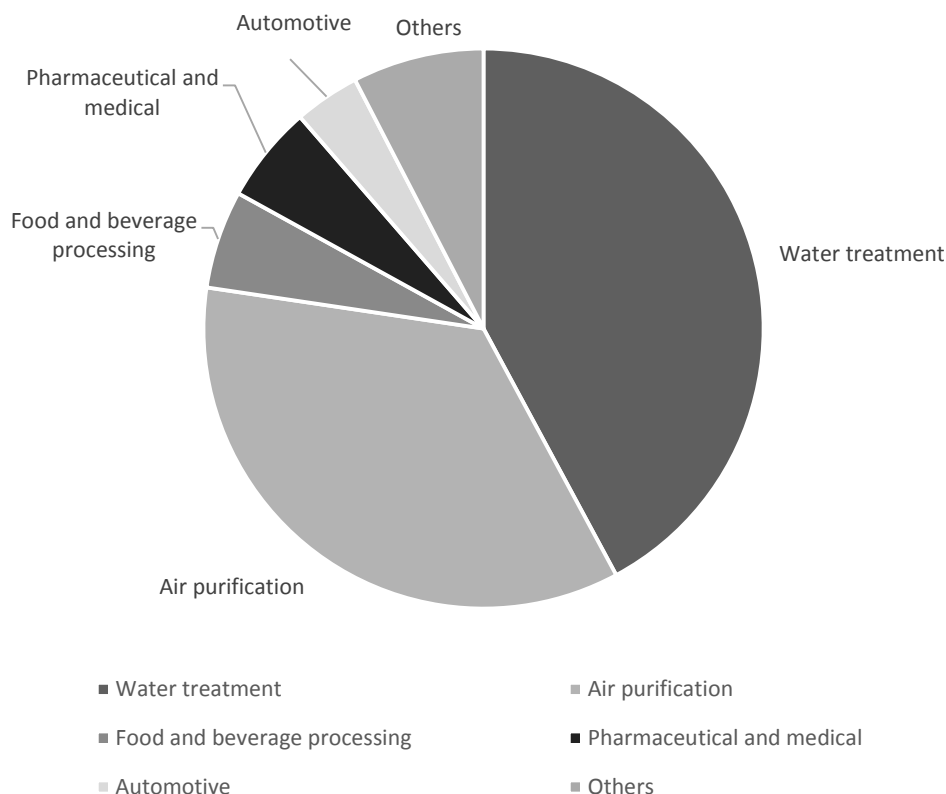


Figure 1.1- Market segments for each application of activated carbons (adapted from Transparency Market Research, 2013)

Regulatory changes, particularly in the two largest markets - the US and China - will be the main drivers for growth.

In the US and other industrialized countries, the demand for activated carbons will be influenced by stricter standards, for example, for mercury removal: the market for this application is expected to more than double by 2018 in response to the full implementation of the US Environmental Protection Agency’s Mercury and Air Toxic Standards (The Freedonia Group, 2014).

In contrast, in China and other developing countries, the main drive will be the introduction and enforcement of standards as efforts to battle air and water pollution caused by rapid industrialization. Increasing manufacturing activity in many developing countries will also contribute to the increased demand for activated carbons.

A new market segment that is being explored in the literature is the use of bio-based activated carbons as catalyst support. This is particularly attractive for some feedstocks with high ash content that are usually not considered suitable for applications such as wastewater treatment because of

their mineral content that could instead make it suitable as a catalyst. Tables 1.2 and 1.3 show different applications of biomass-based activated carbons for adsorption and catalysis.

1.4.2 Feedstocks for the production of activated carbons

While activated carbons are mostly produced from non-renewable carbonaceous materials such as peat, lignite, and coal, their production from renewable feedstocks such as coconut husks is also used at the industrial scale. Nonetheless, one of the key challenges in the market is the shortage of raw materials such as coconut-based charcoal that is used for making activated carbons. In Sri Lanka, there has been an increment of around 50% in the prices of coconut shell charcoal between 2010 and 2011 (Markets and Markets, 2012). The shortage of traditional raw materials is identified as a potential threat to market growth also by Infiniti Research Limited (2014).

There are a large number of globally available agricultural and forestry wastes that do not yet have high-value applications. Recent research has been focused on those feedstocks. Examples that can be found in the literature include wheat, corn straw, olive stones, bagasse, birch wood, miscanthus, sunflower shells, pinecones, rapeseed, cotton residues, olive residues, pine rye, eucalyptus maculata, sugar cane bagasse, almond shells, peach stones, grape seeds, straw, oat hulls, corn stover, apricot stones, cotton stalk, cherry stones, peanut hull, nut shells, rice hulls, corn cob, corn hulls, hazelnut shells, pecan shells, rice husks and rice straw (Ioannidou, 2007).

1.4.3 Production processes

Activated carbons are most commonly produced via two types of industrial processes: physical activation or chemical activation. Physical activation involves the carbonization (pyrolysis) and reaction of the solid pyrolytic bio-char material using hot oxidizing agents, such as steam or CO₂. Chemical activation is achieved through the use of an impregnating agent, such as a strong acid or base. The resulting carbon structure has a surface area of between 500-2500 m²/g, which explains activated carbons' large adsorptive capacity

1.4.3.1 Chemical activation

Prior to thermal treatment, the raw material is doped with chemicals: usually an acid, strong base, or salt. The most popular activating agents are phosphoric acid, zinc chloride and potassium hydroxide. The chemical addition allows the bio-material to be activated at a temperature between

450 and 700 °C, which is lower than the required activation temperature range for physical activation, and can be carried out in a one-step process. The activated carbon product is then washed with water and dried. Activated carbons produced by chemical activation generally result in a larger pore size than with physical activation, which is ideal for the adsorption of large molecules. Despite the possibility to obtain higher surface areas using chemical activation, this method presents three main drawbacks:

- Use of chemicals that are potentially toxic, such as zinc chloride (Rambabu, 2014);
- Intensive washing required after activation, which also generates a great amount of wastewater;
- Risk of leaching chemicals that have not completely been washed (especially when used for wastewater treatment).

For these reasons, this method will no further be discussed in this thesis.

1.4.3.2 Physical activation

Physical activation is carried out in two steps:

Initially, carbonization of the feedstock takes place through pyrolysis. Sustained temperatures remove moisture and volatiles and leave a fixed carbon mass with an initial porous structure within which ashes are dispersed. Then, the bio-char is activated in the presence of CO₂, air, or steam at temperatures between 800 and 1100 °C. The following reactions take place:



Activation burns off remaining tars and further oxidizes the carbon structure from the skeleton of pores that were formed during carbonization. CO₂ is normally preferred for this application, since it is clean, easy to handle and facilitates the control of the process.

Examples of activated carbons production and applications are reported in Tables 1.2 and 1.3.

Table 1.2- Example of activation type and applications for activated carbons produced from biomass

Reference	Type of activation	Application
Hameed (2009)	CO ₂ activation	Removal of 2,4,6-trichlorophenol
Foo (2011)	Impregnation with KOH and microwave heating	Methylene blue adsorption
Klasson (2011)	H ₃ PO ₄ impregnation, steam activation	Furfural and hydroxymethylfurfural (HMF) adsorption during hemicellulose fermentation
Uchimiya (2011)	H ₃ PO ₄ impregnation	Heavy metals adsorption
Gupta (2012)	Steam activation	Removal of Chromium (III) from aqueous solutions
Rambabu (2013)	CO ₂ , steam and KOH activation	Removal of hydrogen sulphide from gaseous streams
De (2013)	Steam activation + impregnation with KCl, KBr, KI, NH ₄ I, and NH ₄ Br	Mercury removal from gas stream

Table 1.3- Example of applications of activated carbons as catalysts

Reference	Type of activation	Application
Muradov (2012)	CO ₂ activation	Biogas reforming
Wang (2014)	KOH activation	Methanation
Zhu (2015)	KOH activation	Methanation
Kastner (2015)	H ₂ SO ₄ , KOH activation	Tar decomposition

1.4.3.3 Reactors used for the activation process

A number of different types of kilns and furnaces can be used for carbonization/activation and include rotary kilns (fired directly or indirectly), vertical multi-hearth furnaces, fluidized bed reactors and vertical single throat retorts (Cameron Carbon, 2006)

1.5 Biomass Pyrolysis

1.5.1 The pyrolysis process

The pyrolysis process influences not only the products distribution (yield of each stream), but also has a great influence on the products properties. Through the selection of an appropriate feedstock and the control of process parameters such as heating rates, reaction temperature and vapor residence times, it is possible to maximize the formation of one product over the other, and control their quality.

Traditionally, the different pyrolysis processes are classified as:

- Slow pyrolysis: slow pyrolysis is characterized by slow heating rates of the biomass and long gas and solid residence times. Since the rate of devolatilization is slow, the main product is bio-char. Operating temperatures are higher than 400 °C (Basu, 2013), and can reach 800 °C, depending on the final product requirements (Brewer, 2012);
- Fast pyrolysis: fast pyrolysis is characterized by extremely high heating rates (100-1000 °C/s) and, very short residence times of vapors (<2 s). Operating temperatures are usually in the range 450- 550 °C;
- Intermediate pyrolysis: intermediate pyrolysis is characterized by moderate temperatures (400-600°C) and moderate heating rates (of the order of minutes). Vapor and solid residence times are longer than the ones required for fast pyrolysis (10-30 s for the vapors, in the order of minutes for the solid). This allows for a more even distribution of pyrolysis products and, potentially, better product quality (Yang, 2014).

1.5.2 Reactors used for biomass pyrolysis

Charcoal production is a technology that has been known for thousands of years, most likely since humans learned how to control fire. In the first stages of production, wood logs were stacked into a pyramidal pile, leaving room at each end for an air inlet and outlet, causing the combustion region to gradually move across it (Brewer, 2012). The first reactors built to produce charcoal were simple kilns, which were operated for long periods of time with low heating rates to maximize the solid product (Basu, 2013). Nowadays, the reactors configuration has changed according to the increasing interest in the liquid and gas products.

One of the main points of research is the reactor technology in which the process is carried out: the critical points for fast pyrolysis reactors, according to Bridgwater, (2000), are the control of temperature, heating rates, rapid cooling of the gas to separate the oil and char separation. A comprehensive review of fast pyrolysis reactors has been done by Bridgwater in several papers (1999, 2000, 2001), and Briens (2008). The main distinction between pyrolysis reactors depends on the gas-solid contact mode, which divides the reactors into fixed bed, fluidized bed, and entrained bed. From the design point of view, the main types of reactors are: fixed beds, rotary drums, auger reactors, bubbling fluidized beds, circulating fluidized beds, rotative cone pyrolyzers, ablative pyrolyzers, and vacuum pyrolyzers.

Table 1.4 briefly summarizes the main reactor types used for different pyrolysis conditions.

Table 1.4- Operating conditions, typical product yield and reactor configurations for different types of pyrolysis (Adapted from Basu (2013), Bridgwater (2000) and Yang (2014))

	Slow pyrolysis	Intermediate pyrolysis	Fast pyrolysis
<u>Operating conditions</u>			
-Heating rate	<10°C/min	Up to 100 °C/min	100-1000 °C/s
-Temperature range	400-800 °C	400- 600 °C.	450- 550 °C.
-Vapor residence time	Minutes	10-30 s	<2s
-Solid residence time	Hours	Minutes	Seconds
<u>Typical product yields</u>			
-Liquid	~30%	~50%	~60-75%
-Solid	~30%	~30%	~15-25%
-Gas	~35%	~20%	~15%
<u>Typical reactor configurations</u>	Fixed bed, kilns, augers	Augers	Fluidized and circulating fluidized bed reactors, ablative pyrolyzers,

1.6 Context and Scope of this Thesis

In general, current processes for the production of activated carbons from renewable resources do not provide valuable co-products. This is mainly due to the fact that the carbonization step is carried out at excessively high temperatures (up to 800 °C, where the production of vapors is not favorable) or extremely low heating rates, which do not allow the integration of the production of activated carbons with bio-oil. Since, as previously discussed, bio-oil is a source of attractive chemicals and fuels, using bio-char produced from controlled pyrolysis conditions that are also relevant to the production of bio-oil can greatly improve the economics of the pyrolysis process and contribute the development of bio-refineries.

Despite the great amount of work that has already been done on the production of activated carbons from biomass, it is still difficult to determine whether a feedstock will be attractive or not, and for which application it might be suitable. In fact, the extremely large variety of biomass types available and the variability within the same biomass material depending on the origin, harvesting, etc., make it very difficult to generalize.

The properties of activated carbons are strongly related to the activation process conditions (gas flowrate, temperature, residence time) but also to the type of carbon precursor. While extensive study has been carried out on the influence of these activation parameters (Jung, 2014; Lua, 2000; Valente Nabais, 2011; Yang, 2003; Yang, 2010), very little attention has been paid in the literature to carbon precursors produced from the same feedstock under different pyrolysis conditions, and how this affects the activation process. Also, the studies that are presented in the literature are often limited by the very small scale (Pottmaier, 2013) or the type of reactors with which experiments are carried out, which are irrelevant at the large scale (Onay, 2007), or that the range of heating rates considered is too narrow (Lua, 2004).

It has previously been shown that gas-solid fluidized bed reactors offer some advantages when used for pyrolysis and activation reactions, due to higher rates of mass and heat transfer when compared to fixed bed reactors. Bench scale and pilot plant scale fluidized bed reactors would thus be the most appropriate options to investigate the effect of some operating conditions while ensuring that both the mixing pattern and the heat transfer are realistic and, thus, the results offer a reliable source of information for the scale-up.

However, due to the high cost and time constraint, besides significant technological challenges in the development of large-scale reactors, the use of laboratory scale reactors is more common in

both academia and industry for the screening phase of new technologies, or for the optimization of reaction conditions and screening of new feedstocks.

Most of the studies reported in the literature about the influence of pyrolysis conditions on the production of activated carbons at the laboratory scale are carried out in fixed beds (Onai, 2007; Şensöz, 2008; Angin, 2013; Jung, 2014). Fixed bed reactors are characterized by relatively poor heat and mass transfer between the gas and the particles, and pronounced radial temperature profiles; these reactor characteristics have been proved to have a detrimental impact on the production and quality of activated carbons from biomass (Minkova, 2000). Moreover, with these types of reactor, it is impossible to achieve both fast and slow pyrolysis conditions in the same reactor, thus limiting the studies mostly to slow pyrolysis conditions.

Thermo-gravimetric analysis (TGA) is another tool that is often used to study the thermal decomposition of biomass and others materials. Its use for the determination of the weight loss characteristics and its associated reaction kinetics is well established (Moilanen, 2006). In spite of a wide range of applications in academia and the industry, the TGA technique shows some limitations, which may reduce the reliability of the obtained results.

Some of the drawbacks have been highlighted by Samih (2015):

- Non-uniformity of the temperature throughout the sample
- Poor mixing
- Low heating rate
- Small amount of solid sample, which is not enough to be representative.

Some improvements have been made by Samih (2015), who developed a fluidized bed TGA (FB-TGA), in which proper mixing and uniform distribution of gas-solid and solid-solid are ensured by fluidization, while also allowing for a sufficient amount of sample to be processed with heating rates that are more representative of conditions encountered in large scale reactors.

Latifi (2012) developed the Jiggled Bed Reactor (JBR), an excellent tool to study gas-solid reactions. While mixing is achieved through mechanical agitation, thus producing a mixing pattern equivalent to that of a fluidized bed without the need of fluidization gas, fast heating is provided by induction. The JBR has successfully been used for the study of bio-oil gasification and for catalysts screening.

This thesis has the following objectives:

- 1) Use a lab-scale reactor that allows to perform both pyrolysis and activation in the same equipment;
- 2) Use of a lab-scale reactor (JBR) that enables fast screening of operating conditions but is representative of conditions that are obtained in larger scale reactors for both pyrolysis and activation;
- 3) Carry out trials under operating conditions that are relevant for the production of by-products, as well as bio-char (fast pyrolysis, short solid residence times) and develop tools to predict the properties of the activated carbons produced based on the carbon precursor;
- 4) Perform a screening of different types of biomass and identify the most attractive ones based on simple correlations; and
- 5) Identify potential applications for the most attractive materials.

1.7 Thesis Structure

- Chapter 2 presents the materials and methodology that are used throughout the thesis: the feedstock selection and characterization, experimental set up and analytical techniques;
- Chapter 3 validates the use of the Jiggled Bed Reactor (JBR) for the activation process of olive residue, identifies optimal activation parameters and studies the kinetic of the process. It also provides a screening of the performance of different feedstocks and characterizes the most attractive;
- Chapter 4 presents a simple physical model for activation that allows predicting the yield or surface area of activated carbons based on the char precursor properties. This model is applied to the results obtained in Chapter 3 and 5 and is used as a reference for the discussion of the results obtained in Chapter 6;
- In Chapter 5 the JBR set-up is modified to allow the pyrolysis conditions to be varied from slow to fast in the same reactor. The impact of the heating rate and temperature during the pyrolysis step on the properties of activated carbons produced from olive residue is studied;
- In Chapter 6 the results obtained with the JBR are compared with those obtained in a pilot scale bubbling bed for the pyrolysis and activation of birch bark. The first objective is to prove that the JBR is an excellent tool for the simulation of reaction conditions encountered in larger scale reactors. The JBR is then used as a tool to study the influence of the initial biomass form

(e.g. granulated and un-granulated) on the processability of feedstocks that are difficult to handle, such as Kraft Lignin;

- Chapter 7 covers the application of the activated carbons produced in the previous chapters for the adsorption of selected contaminants:
 - i. Mercury
 - ii. Naphthenic acids from oil sands tailing pond water
 - iii. Ammonia
- Chapter 8 includes the final conclusions and recommendations.

Additional work is reported in Appendixes I and II. Appendix I presents a study about biomass torrefaction in a Mechanically Fluidized Reactor (MFR), while Appendix II investigates the application of low technology adsorbent materials (i.e. non activated bio-char) to the removal of arsenic from groundwater, since water contamination by arsenic is a major concern in countries like Bangladesh.

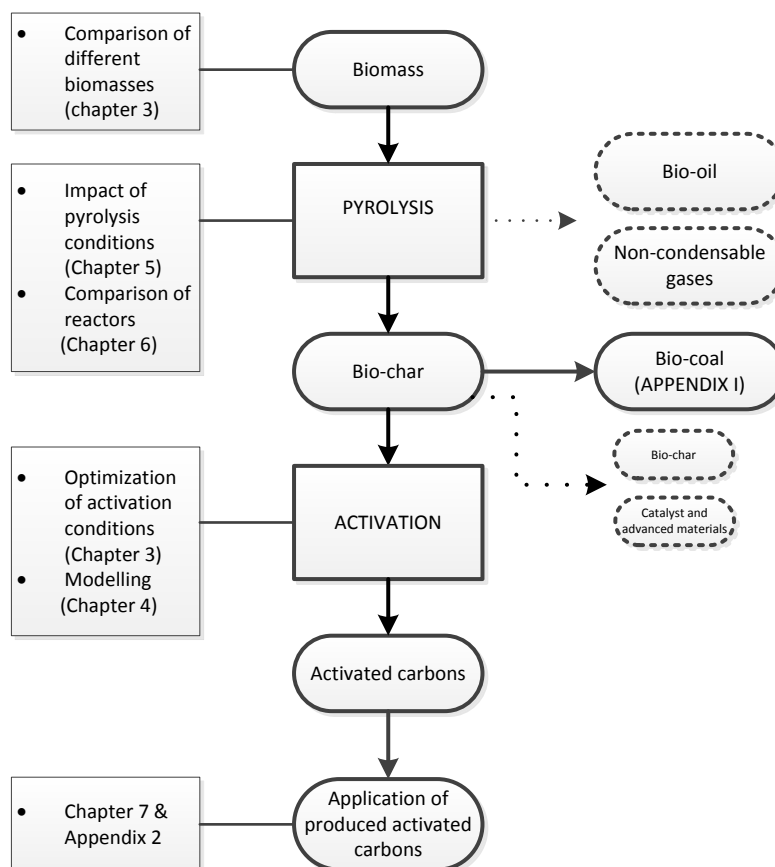


Figure 1.2- Thesis structure

Chapter 2

2. Materials and Methodology

This chapter describes all the common materials, methodologies and analytical techniques used in this thesis.

2.1 Feedstocks

A number of different feedstocks were considered in this study. These biomasses were selected based on different criteria:

- A wide range of properties such as fibre length, lignin content and ash content
- Availability, especially in Canada
- The need of the forestry sector to find markets for Kraft lignin.

The materials selected represent crop residue (Canola), milling residue (Olive residue, Sunflower husk) and purpose grown energy crops (Willow, Miscanthus, Switchgrass, Sorghum), examples of energy seed crops (Sunflower seeds), some with long stringy fibres and some with very short fibres and a different chemical composition, moving from biomasses that contain a low amount of lignin to Kraft lignin, biomasses with low or high content of ashes. These biomasses were selected based on their availability in Canada (apart from the olive residue which comes from California, but is widely available in other regions such as the Mediterranean area). Kraft lignin has also been considered in the study, in the attempt to investigate technologies to increase its value and, consequently, provide added benefits to the pulp and paper industry in Canada. In pulping and bleaching processes, lignin is degraded and separated from the other wood components; the Kraft pulping process is the most used extraction method for paper production, accounting for up to 90% of the total production capacity (Azadi, 2013) generating a carbon source estimated to 50 million tons per year worldwide (Sixta, 2006). The Kraft, or sulfate, process uses sulfide and hydrogen sulfide ions generated from sulfate under alkaline conditions to cleave ether bonds in lignin (Fellows, 2012). The alkaline liquid remaining after pulp extraction, the black liquor, contains 29-

45% lignin that can be recovered through weak acid precipitation. The so obtained lignin, commonly referred to as Kraft lignin, has a sulfur content of about 1-2% (Evans, 1986).

Table 2.1- Feedstocks selected in this study, origin and date of harvest

	Origin	Date of harvest
Canola	Alberta	Summer 2012
Miscanthus	Drumbo, Ontario	Spring 2012
Switchgrass	Clinton, Ontario	Spring 2012
Willow	Alberta	Summer 2011
Sunflower Residue	Manitoba	Spring 2012
Sorghum	Manitoba	Spring 2012
Olive residue	California	Summer 2012
Kraft lignin	Weyerhaeuser Canada	n.a.
Birch bark	n.a.	n.a.

The physical and chemical properties of the feedstocks are shown in Table 2.2.

Biomass components analysis was obtained from suppliers, while proximate and elemental analyses were carried out using the methodology described in Paragraphs 2.5.1 and 2.5.2.

Table 2.2- Feedstocks characteristics

	Biomass components (% dry basis)				Proximate analysis (% dry basis)			Elemental Analysis (% dry basis)				
	Extractives	Hemicellulose	Cellulose	Lignin	Ash	Volatiles	Fixed carbon	N	C	H	S	O
Canola (plant residue)	13.6	24.1	38.5	20.9	6.8	79.3	13.9	1.7	42.0	5.5	3.4	43.2
Miscanthus	6.1	24.9	42.3	24.7	2.7	82.9	17.1	1.2	46.3	5.8	0.0	41.9
Switchgrass	7.4	27.1	35.1	27.7	2.3	84.0	13.1	1.3	46.9	6.0	0.0	42.3
Willow	6.5	18.4	38.1	35.7	0.7	87.1	12.2	1.41	48.23	5.85	0.0	42.42
Sunflower Residue	31.2	15.0	26.9	23.8	3.6	79.6	16.8	2.5	51.4	7.1	1.5	38.3
Sorghum	12.9	3.5	78.4	4.7	0.9	86.5	12.6	1.8	44.9	6.8	0.0	44.2
Olive residue	11.8	19.6	25.8	40.1	2.7	68.8	22.0	1.57	49.88	6.11	0.0	20.20
Kraft lignin	n.a.	n.a.	n.a.	93	1.0	68.0	31.0	0.2	62.4	6.1	2.0	29.1
Birch bark	n.a.	n.a.	n.a.	n.a.	2.1	76.8	21.1	0.3	55.9	5.8	0.0	36.0

2.2 Experimental Set Up: the Jiggled Bed Reactor (JBR)

The pyrolysis and activation screening experiments were carried out in the Jiggled Bed Reactor (JBR). The JBR is a micro-reactor in which fluidization is achieved through jiggling by mean of a pneumatic piston instead of using a gas, while heat is provided through an induction coil.

The reactor includes three sections: the linear pneumatic actuator, the reaction zone, and the induction heating system, which comprises the power supply and the induction coil. The main structure of the JBR is shown in Figure 2.1

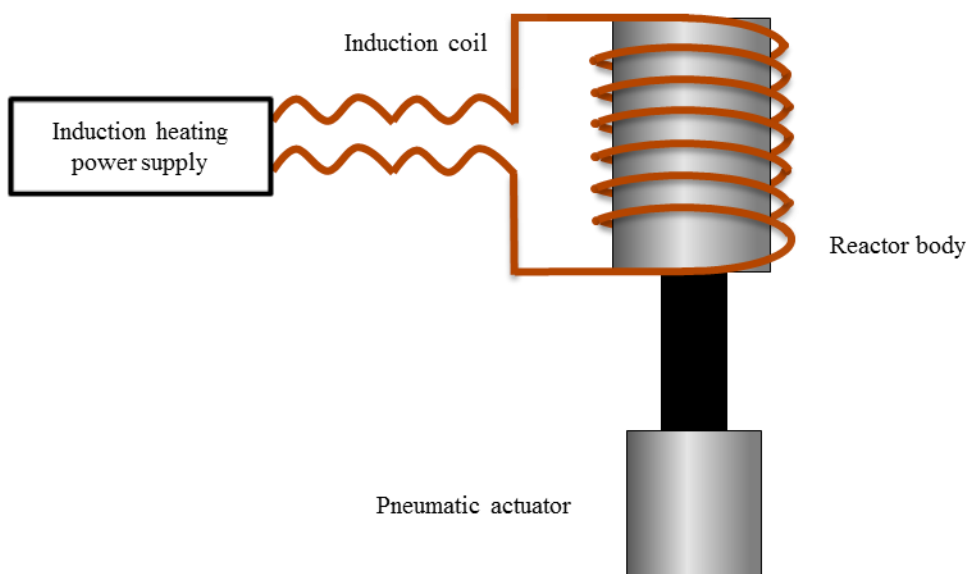


Figure 2.1- Schematic structure of the jiggled bed reactor

As a result of the linear motion of the pneumatic actuator, the bed of particles alternately expands and contracts, inducing intense radial and axial mixing, as clearly shown by the photographs in Figure 2.2 (Latifi, 2012). Studies by Latifi (2012) also showed that the heat transfer inside the JBR is excellent, with negligible differences ($< 6\text{ }^{\circ}\text{C}$) between the temperature inside the bed and the temperature of the heating element (in this case, the reactor wall).

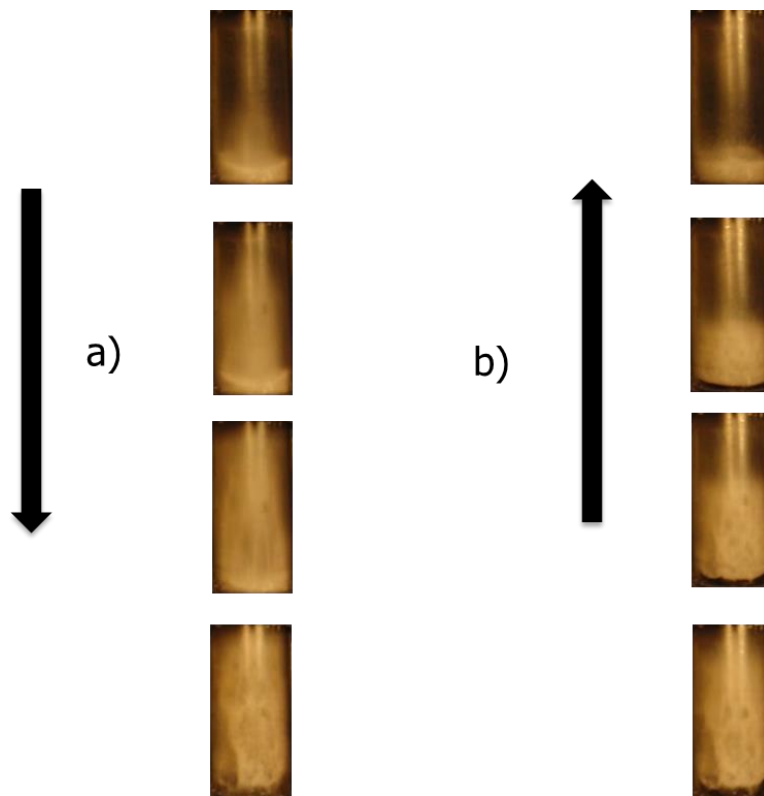


Figure 2.2- Sequence of mixing during a) downward actuator retraction, b) upward actuator extension (Latifi, 2012)

The reactor body is made of 316 Stainless Steel and has a height of 85 mm, 39 mm I.D. and 45 mm O.D.. The top flange and the lid have a diameter of 82 mm and are closed together by 8 bolts (#10-24, 3.8 mm diameter, 32 mm long). A metal and graphite gasket is placed in between the two to prevent leaking. In order to introduce the inert gas for the pyrolysis process and the activating agent during activation, two 6.35 mm inlet ports are placed on the lid: one for the gas inlet and the other one for the gas outlet. A hot filter (steel wire cloth, 0.4 mm opening) placed before the gas outlet is used to prevent particles elutriation from the bed. A third port is placed on the lid (3.17 mm) to house a thermocouple (type K) to control the temperature inside the bed.

The reactor configuration used for batch studies is shown in Figure 2.3.

For the fast pyrolysis experiments, the reactor configuration is modified, and in particular the inlet hole is enlarged to 14 mm to allow for direct feeding of biomass as shown in Figure 2.4.

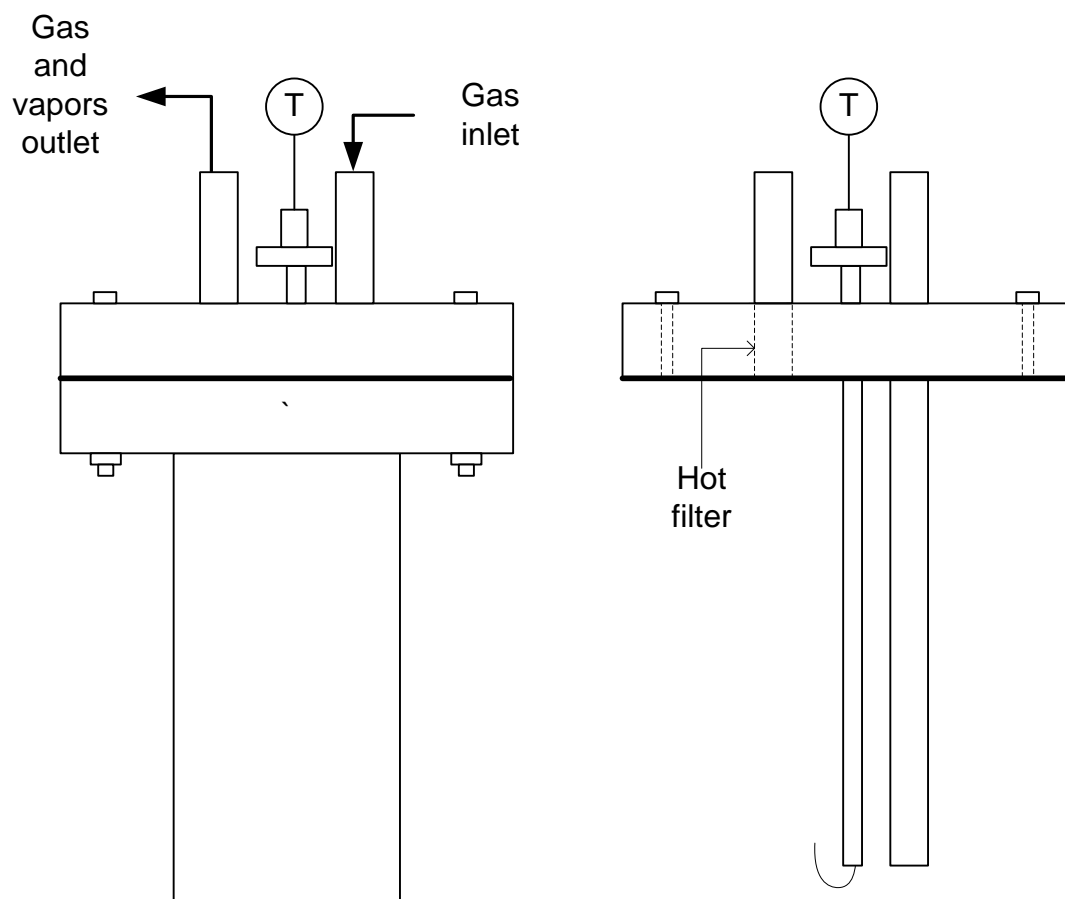


Figure 2.3- Reactor configuration used for batch experiments, full assembly (left) and lid (right)

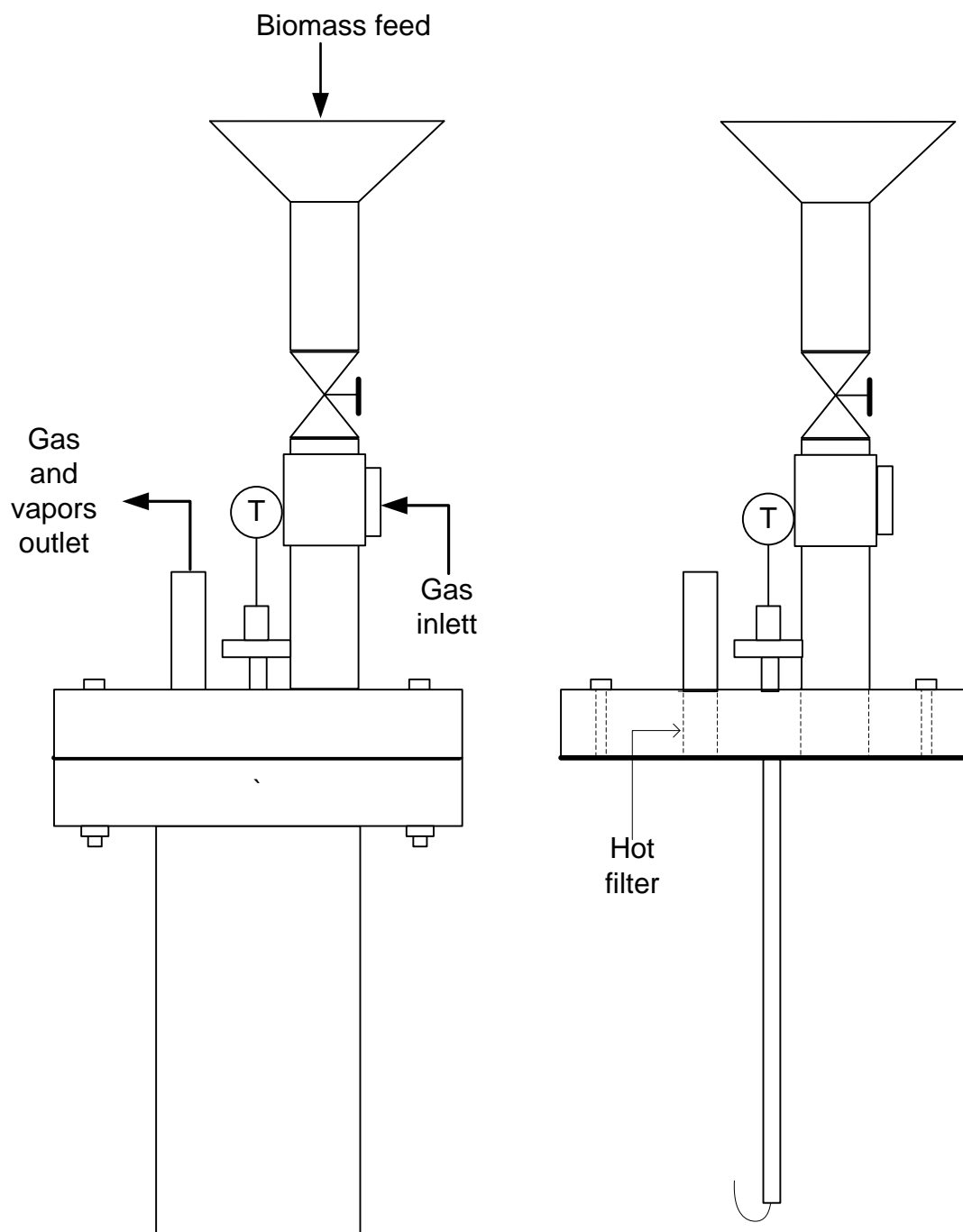


Figure 2.4- Reactor configuration used for fast pyrolysis experiments full assembly (left) and lid (right)

The linear pneumatic actuator, originally developed by Latifi (2012), consists of the following parts:

- Compressed air line

- A double acting BIMBA FLAT-II air cylinder with dual piston rods and a rod end block to ensure that the rods work in tandem;
- Two BIMBA reed switches (RS) attached on the external surface of the air cylinder to control the motion of the piston;
- A 2 position, 3-way solenoid valve to alternate the direction of the compressed air flow between extension and retraction modes;
- Two air flow controllers to adjust the flow rate of the compressed air;
- Tubing between the solenoid valve and the air cylinder;
- A programmed logic controller (PLC) to start up and shut down the actuator and to actuate the solenoid valve to alternate the direction of the compressed air flow between extension and retraction modes.

A schematic of the pneumatic actuator is reported in Figure 2.5.

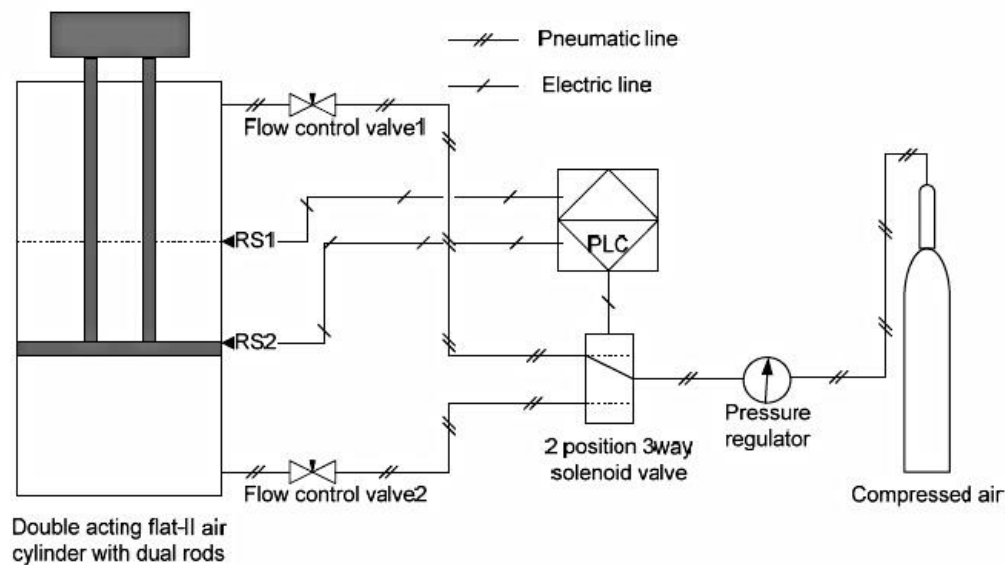


Figure 2.5- Schematic of the pneumatic actuator (Latifi, 2012)

Based on the optimization study previously performed by Latifi (2012), the frequency of the actuator for this study was selected to be 3 Hz and its amplitude 100 mm.

The induction system is an EASYHEAT LI 7590 system by Ambrell, with a maximum power output of 9 kW and a frequency range of 150-400 kHz. A UP550 YOKOGAWA controller is used to adjust the output power of the power supply to maintain the desired temperature set-point within

the reactor, which is measured with a type K thermocouple. The metallic wall of the reactor acts as a shield, thus preventing heating of the thermocouple.

The copper coil of the induction system is made of 6 turns of a tube with 6.4 mm O.D. Both coil diameter and height are 76 mm. The external surface of the coil is covered with an insulation sleeve for safety reasons. A high temperature sleeve is used for the lower turn of the coil where it is in contact with very hot surfaces.

2.3 Pyrolysis and Activation Procedures

Prior to pyrolysis, 15 grams of the samples were bone dried at 105°C and placed in the reactor. The reactor was then purged with a constant flow of nitrogen of 33.3 ml/min for 5 minutes to remove the air.

2.3.1 Batch pyrolysis experiments (with CO₂ activation)

The JBR agitation was started and maintained during the whole experiment, to ensure good mixing, excellent heat transfer and a uniform sample temperature. Samples were heated to the pyrolysis temperature (475 to 550°C) at a rate set between 47.5 to 158 °C/min, under a flow of nitrogen of 33.3 ml/min. The temperature during the pyrolysis step was maintained constant for 5 minutes and then ramped to the final activation temperature (ranging from 800 to 900 °C) at a rate of 60 °C/min under the same flow of inert gas (nitrogen, 33.3 ml/min). Once the final temperature was reached, the gas was switched to CO₂ with a varying flow (20 to 400 ml/min) and then maintained for the desired activation time (10 minutes to 2 hours).

At the end of the designated time, the heating system was turned off and the samples allowed cooling to 100 °C under nitrogen while maintaining agitation. An example of reactor temperature and gas flow profile for an experiment carried out 500 °C with 95 °C/min heating time with 800 °C activation temperature for 1h with 200 ml/min CO₂ flowrate is shown in Figure 2.6 (a and b respectively).

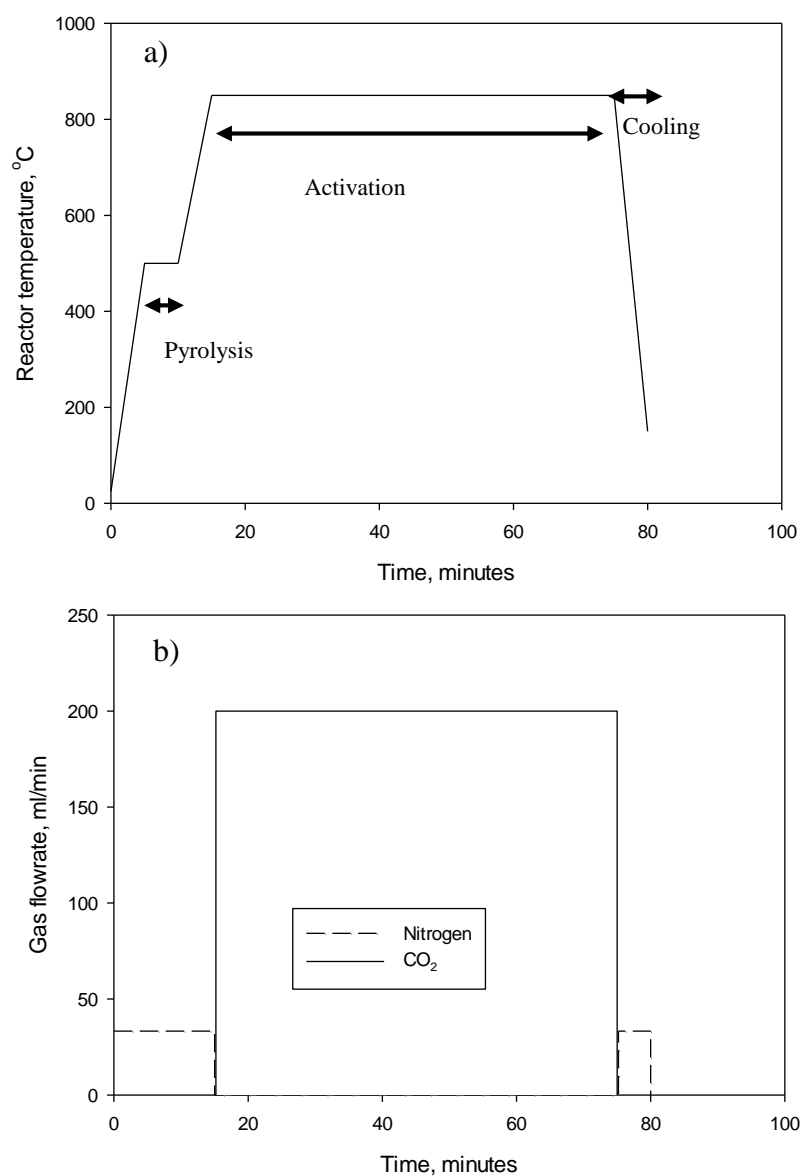


Figure 2.6: a) Example of temperature history during pyrolysis (activation carried out at 800 °C for 1h) b) Gas flowrate during activation

2.3.2 Fast pyrolysis experiments

The reactor was heated up to the final pyrolysis temperature (475 to 550°C) under a flow of nitrogen (100 ml/min) while jiggling. Once the final temperature was reached, the biomass was injected into the reactor. No significant temperature drop was registered (< 10 °C, which was recovered within 20 seconds of injection). The pyrolysis reaction was allowed to proceed for 5 minutes, and the activation procedure was the same as reported in 2.3.1 for batch pyrolysis. It is

important to notice that in the JBR, due to the very fast response of the temperature controller, fast pyrolysis conditions were achieved without any bed material, thus giving the possibility to study a char produced from fast pyrolysis without any contamination from sand through the formation of agglomerates, which would have made it almost impossible to obtain pure activated carbon, as shown by Burton (2012).

2.3.3 Activation experiments with wet gases

In order to be able to simulate the composition of combustion gases, the set up was modified to allow for injection of steam into the system. The CO₂ flow was bubbled through water at 90 °C to obtain a mixture of 25 mol % steam and 75 mol% CO₂.

2.3.4 Production of HNO₃ treated activated carbons

5.0 g of CO₂ activated sample (produced from pyrolysis at 500 °C with 95 °C/min heating rate, activated at 850 °C for 1h with a CO₂ flowrate of 200 ml/min) were added to 32 ml of 70wt% HNO₃. This mixture was refluxed at 90 °C for 2.5 h using a reflux column to recover the oxidizing agent evaporated during the process. A magnetic stirrer was used for mixing during the reflux. The sample was washed with water to remove remaining acid until it reached neutral pH to prevent leaching. The product was dried overnight at 120 °C.

2.3.5 Reproducibility

Given the number of experiments carried out in this thesis, the repetition of each single experiment would have been impossible due to time constraint. The very accurate monitoring of the temperature was such that anomalies in the experiment caused by experimental errors or equipment malfunctions could be easily detected and, thus, the results discarded. However, in order to ensure that the results were reproducible and significant for the purpose of the study, three replicates of randomly selected experiments were carried out, including the full characterization. The same was done every time a new parameter (pyrolysis or activation temperature, flowrate) was investigated. The results were always found to be reproducible. An example is shown in Table 2.3. For the batch pyrolysis conditions, we can thus say that our results have an error of +/-4% (based on the yield). The fast pyrolysis experiments have a slightly larger error, estimated to be +/-5%.

Table 2.3- Example of reproducibility of replicates for 95 °C/min heating rate, 500 °C pyrolysis temperature

	Initial biomass mass, g	Final char mass, g	Char yield, %	Time to reach pyrolysis temperature of 500 °C	Elemental composition, %			
					C	H	N	O
	15	4.4	29.3%	4m 48s	85.9	1.7	0.3	2.3
	15	4.2	28.3%	4m 58s	86.7	1.6	0.3	2.1
	15	4.4	29.5%	5m 01s	86.4	1.8	0.8	2.2
Standard deviation		0.08	0.005		0.33	0.09	0.22	0.06

2.4 Experimental Set Up: the Bubbling Bed Reactor

In Chapter 6, the results obtained in the JBR are compared with the results obtained in a bubbling bed reactor. The experimental set up mainly consists of the biomass feeder, the pyrolysis reactor and the fractional condensation train. A schematic of the set-up is shown in Figure 2.7 (Tumbalam-Gooty, 2014).

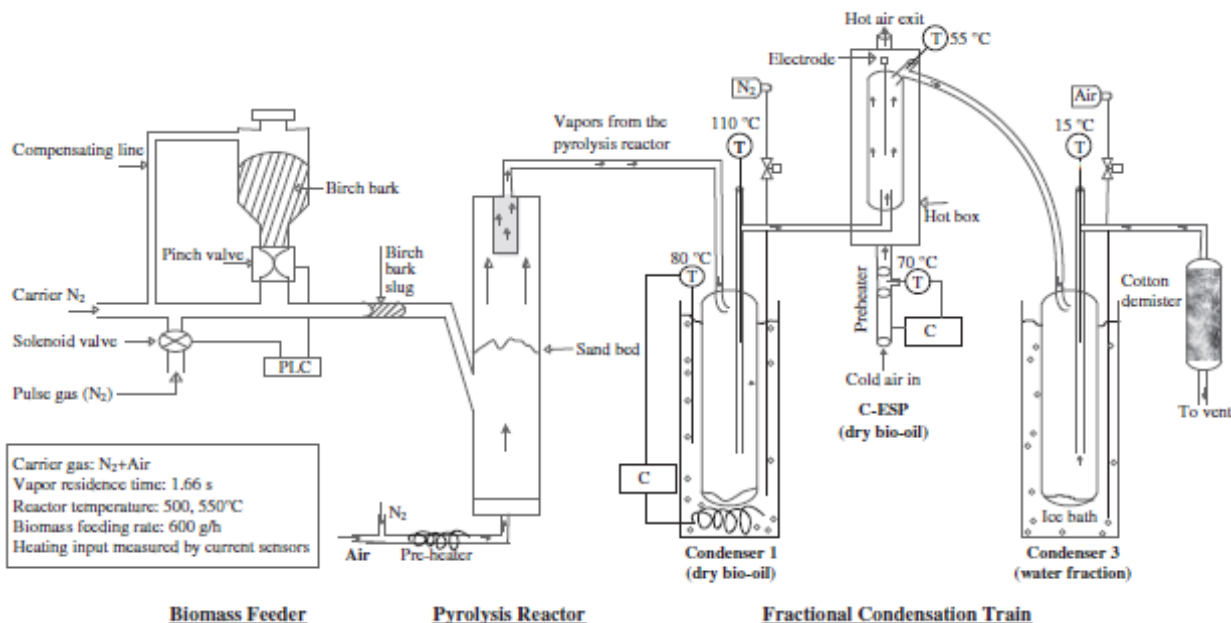


Figure 2.7- Schematic of the bubbling bed reactor

The ICFAR biomass “slug injector” feeder (Berruti, 2013) was used to feed the biomass into the bed at 150 mm above the gas distributor through a 45° inclined line. The biomass was discharged

from the hopper through a pneumatically activated pinch valve. The pinch valve opened periodically (every 5 s) for short periods of time (0.7 s), allowing small amounts of biomass particles to fall into a horizontal injector tube. During each cycle, the biomass formed a slug, which was propelled into the reactor by intermittent pulses of nitrogen and a continuous stream of nitrogen carrier gas. The continuous carrier gas and the intermittent pulses prevented any solids from settling inside the injector tube. The pinch valve used to discharge biomass and the solenoid valves used to generate the pulse flow were synchronized and controlled with a programmable logic controller (PLC). The flow rate of the carrier nitrogen gas was metered and controlled with an Omega mass flow meter, while the amount of pulse gas was calculated from the pressure and volume of a buffer tank and the pulse frequency. The 78 mm I.D., 580 mm high reactor was made of Inconel[®] 600. The reactor was heated by three radiant electric heaters, covering both the dense fluidized sand bed and the freeboard sections. The heaters were independently controlled using Watlow PID controllers so that a constant temperature was maintained everywhere along the axis of the reactor during the pyrolysis process. Temperature feedback for the PID controllers was provided through type-K thermocouples placed within the reactor at the same height as the heaters. The condensation system consisted of two cyclonic condensers (Condenser 1 and 3), an electrostatic precipitator-cum-condenser (referred to in the figure as C-ESP), and a cotton wool demister. A detailed description of the condensation system can be found in Tumbalam-Gooty (2014).

For the experiments carried out with birch bark, the bed material used in the reactor was silica sand with a Sauter mean diameter of 70 μm , with a bed mass of 1500 g, while in the case of lignin, the bed material was composed by 150 g of lignin char. In the case of lignin, in order to prevent agglomeration, the bed was equipped with an additional mechanical mixer. The mechanical stirrer intensified the mixing between the hot bed material and the lignin foam and prevented the formation of large agglomerates, consequently ensuring better conditions for fast pyrolysis. During all the experiments, the mechanical stirrer was operated with a rotation speed of 60 rpm. The additional mechanical mixing together with the shearing forces between the fluidized bed particles and the lignin foam helped produce fine char particles. The use of a mechanical mixer ensures good mass and heat transfer with any bed material (Li, 2015).

The combined flow rate of nitrogen (fluidization and carrier/pulse gases) was adjusted to keep the nominal vapor residence time constant, at 1.7 s. Before each experiment, the reactor temperature and the gas flow rates were set to the desired values, between 500 and 550 °C. After the system had reached steady state, biomass was fed. The amount of biomass used for each run was 200 g, with a feeding rate of 600 g/h (i.e., each run was of 20 min duration).

2.5 Sample Analyses

2.5.1 Proximate analysis

Proximate analysis is used to indicate the quantity of volatile matter, fixed carbon and ash contained in a sample. Proximate analysis was carried out following standard ASTM D1762 – 84. Prior to analysis, the samples were dried overnight at 105 °C. 1 gram of sample was placed in a porcelain crucible and weighted to the closest decimal. The muffle furnace was heated up to 950 °C and the crucibles, covered with a lid, were inserted and maintained at 950 °C for 11 minutes. The samples were then dried in a desiccator for 1 hour and ashed at 575 °C (ASTM E1755 – 01) for a minimum of 6 hours. The fixed carbon content was then calculated on a weight percent basis by subtracting moisture, volatile matter and ash values from the original starting mass.

2.5.2 Elemental Analysis

The C,H,N,S and O content were determined separately using an AN634 Flash 2000 CHN Analyzer. 1 mg of vanadium pentoxide was added to the silver crucibles in order to allow the detection of sulfur. Measurements were always conducted in triplicates to ensure the reproducibility of results. Table 2.4 shows an example of results reproducibility. The maximum error observed was +/- 5%.

Table 2.4- Reproducibility results for elemental analysis, %

	N	C	H	O	S
	0.7	79.8	2.0	15.3	0.0
	0.7	79.8	1.9	15.5	0.0
	0.7	79.6	1.9	15.7	0.0
Standard deviation	0.02	0.09	0.04	0.16	0.0

2.5.3 Surface area and pore volume

The BET surface area of the samples was determined using a TriStar II 3020 BET Surface Area and Pore Analyzer from Micromeritics. Prior to analysis, the samples were degassed at 105 °C for 1 hour and then at 300 °C for 5 hours.

The surface area was calculated from 7 points analysis using the Brunauer, Emmett and Teller (BET) equation:

$$\frac{1}{\left[V_a \left(\frac{p_0}{p} - 1\right)\right]} = \frac{C - 1}{V_m C} \frac{p}{p_0} + \frac{1}{V_m C} \quad (2.1)$$

Where p is the partial vapour pressure of adsorbate gas in equilibrium with the surface at 77.4 K (liquid nitrogen), p_0 is the saturated pressure of adsorbate gas, V_a is the volume of gas adsorbed at STP (standard temperature and pressure), V_m is the volume of gas adsorbed at STP to produce an apparent monolayer on the sample surface, and C is a dimensionless constant that is related to the enthalpy of adsorption of the adsorbate gas on the sample.

From the value of V_m so determined, the specific surface area, S , in m²/g, is calculated using Equation 2.2

$$S = \frac{V_m \cdot N \cdot a}{m \cdot 22400} \quad (2.2)$$

where N is Avogadro's number, a the effective cross-sectional area of one adsorbate molecule (0.162 nm² for nitrogen), m is the mass of solid used for the test, and 22400 is the volume (in milliliters) occupied by one mole of the adsorbate gas at STP. Replicates of the same sample showed very good reproducibility of the results obtained, as shown in Table 2.5: the error was always in the range +/-5%.

Table 2.5- Example of reproducibility of results for BET measurements

Surface area, m ² /g	
732.9	
734.6	
735.2	
Standard deviation	0.9

According to the IUPAC classification, pores are classified as macropores when their width is larger than 500 Å, mesopores in the 20-500 Å range and micropores for pores that are smaller than 20 Å. While mesoporous materials show type IV and V isotherms, microporous materials exhibit, in the ideal case, type I isotherms. The characteristic feature of the Type I isotherm is a long horizontal plateau that extends to relatively high p/p_0 , as shown in Figure 2.8.

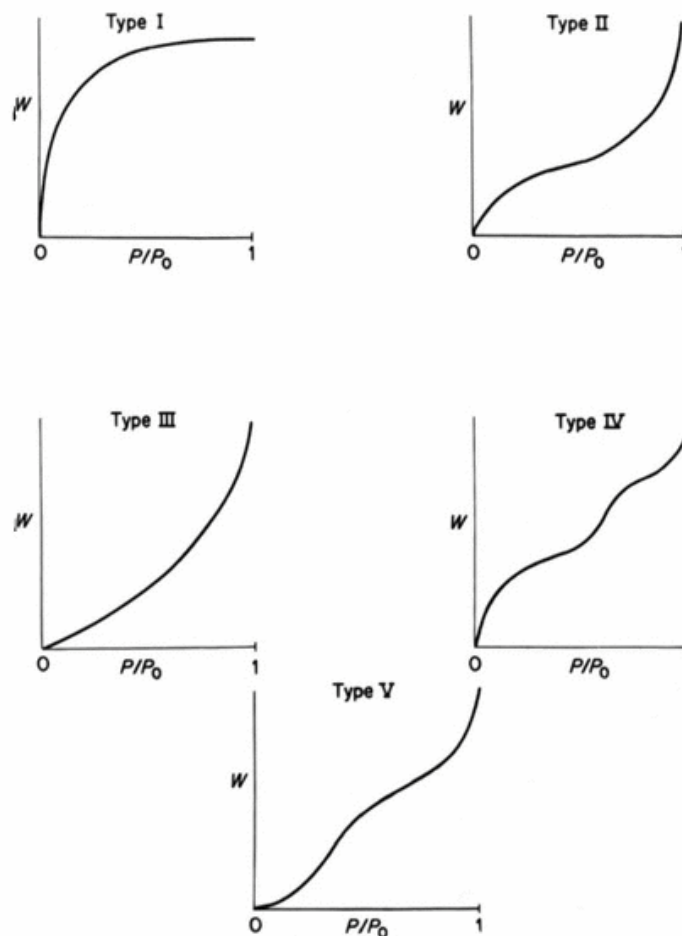


Figure 2.8 Different types of adsorption isotherms (from Lowell, 1984)

Differences in micro and mesopores contribution to the total surface area can be observed qualitatively through the comparison of nitrogen adsorption isotherms shape. For example, Figure 2.9 shows three adsorption isotherms for olive residue chars produced with a heating rate of 95 °C/min at a temperature of 500 °C for:

- Mildly activated char (20% yield, 618 m²/g surface area);
- Aggressively activated char (9.4% yield, 1262 m²/g surface area);
- Non-activated char (29% yield, 6.5 m²/g surface area).

A rapid increase in the volume adsorbed at relatively low partial pressure ($p/p_0 < 0.2$) denotes the predominant microporous structure of both the activated samples; it can be observed how, while the mildly activated sample shows very little or no adsorption at higher partial pressures, with a plateau typical of microporous materials (type I isotherm), for the aggressively activated carbon

the plateau commences at higher relative pressures (p/p_0) and a steeper gradients exists for values of p/p_0 higher than 0.8 (shape similar to type IV and V isotherms).

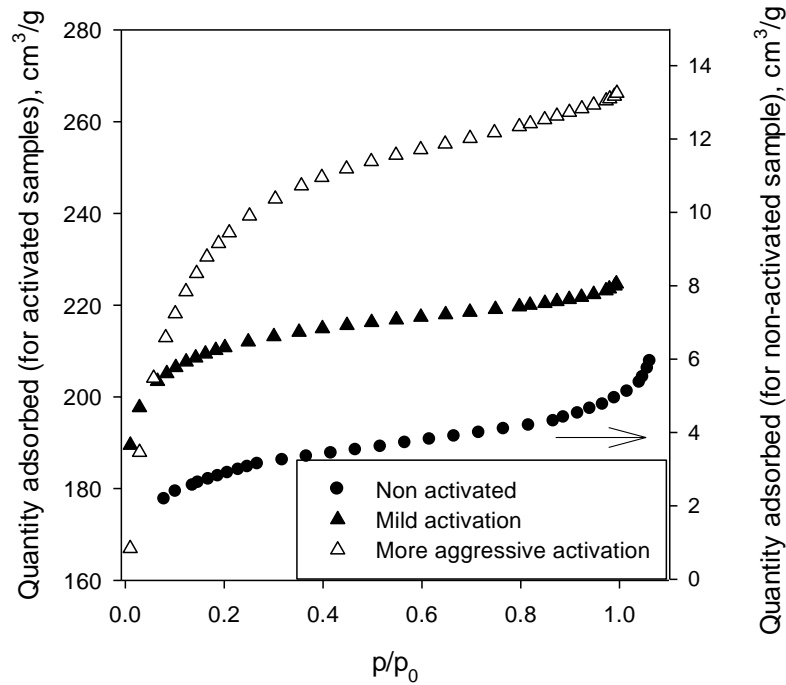


Figure 2.9- Example of nitrogen adsorption isotherms for three selected samples

This is attributable to the presence of mesopores, leading to gradual increase in adsorption after the initial filling of the micropores, followed by more rapid enhancement near saturation (Chandra, 2009; Gonzales, 2009). Nitrogen adsorption isotherms of these activated carbons can be properly classified as a mixture of type I and type IV isotherms. Type IV isotherm are characterized by the mixture of microporous and mesoporous material (Sutcu and Demiral, 2009).

The non-activated sample, on the contrary, shows little or no adsorption in the microporous range, with a steep increase near saturation levels, similar to a type II isotherm, typical of non-porous or macroporous materials. This clearly shows that the material is non porous, and the adsorption observed at high partial pressure is attributable to macropores, most likely, located on the external surface of the sample. In order to numerically determine the micro and mesopores contributions for a given material, the t-plot method is usually employed. This technique, based on the principles originally proposed by Lippens and de Boer (1965), is based on the comparison of the sample isotherm with a reference type II isotherm (non-porous material). Deviations of the real sample

from this isotherm are then used to calculate the micropore volume, the average pore diameter and the micropore surface area.

2.5.4 SEM

SEM images were obtained, without coating, using a Variable Pressure SEM: Hitachi S-3400N Microscope located at the Biotron Center in London, Ontario.

2.5.5 Thermo Gravimetric Analysis (TGA) of olive residue

Thermo Gravimetric Analysis was carried out in a PerkinElmer Pyris 1 TGA Thermogravimetric Analyzer. A sample of 20 mg was placed onto the plate and heated up from 50 to 500 °C at a rate of 95 °C/min under a nitrogen flowrate was 20 ml/min. The sample was held at the final temperature for 5 minutes and then cooled down to 50 °C.

2.5.6 Temperature programmed desorption (TPD)

Temperature programmed desorption was used for the determination of acidic surface groups onto the activated carbon surface. Ammonia-TPD of the samples was carried out in a TPD/TPR Quantachrome (USA) instrument. A total of 100 mg of sample was taken in a quartz tube and purged with helium at 500 °C for 1 hour. The sample was then cooled down to room temperature under flowing helium. A mixture of 3% NH₃/He (v/v) was passed through the sample at a flow rate of 30 ml/min. After that, physisorbed ammonia was removed from the sample by circulating helium at 100 °C for 1 hour. NH₃-TPD analysis was then carried out by heating the sample at 10 °C/min from 100 to 800 °C. The TPD profiles were recorded with a thermal conductivity detector. The results of temperature programmed desorption were used to quantify the surface acidic groups content on the different carbon samples with the in-built software. The peaks attributable to weak, medium and strong Brønsted acids were detected in the temperature ranges of ~190 °C, 250-350 °C and 350-450 °C, respectively.

2.5.7 Boehm titration

Boehm's titration was performed to determine the amount of basic surface groups on activated carbons. 1.5 g of activated carbon were mixed with 50 ml of a 0.05 M NaOH solution and soaked for 24 hours. After filtration, a 10 ml aliquot was taken and mixed with few drops of

phenolphthalein indicator. The sample was then titrated with a 0.05 M HCl solution. The concentration of basic surface groups was calculated from the volume of HCl necessary for the titration.

2.5.8 Particle size distribution

The particle size was obtained using a Sympatec Helos/BF Particle Size Analyzer.

2.6 Adsorption Theory and Studies

Adsorption is one of the most widely applied techniques for removal of pollutants from contaminated media (Qiu, 2009). Like many other processes, adsorption occurs into two stages. The first is a dynamic state, during which concentrations are changing with time until steady state is reached, and the second stage is an equilibrium state and concentrations remain constant over time. At equilibrium, a material has adsorbed the maximum amount possible under those conditions. The equilibrium adsorption capacity is a function of solution parameters such as initial contaminant concentration in the solution, solution pH, temperature, adsorbent loading as well as adsorbent properties such as surface chemistry and functional groups, pore volume, total surface area as well as micro or mesoporous surface area. The dynamic state is normally described through adsorption kinetics, while the relationship between the quantity adsorbed at equilibrium and the initial solution concentration or the solid load can be studied through adsorption isotherms. The study of the adsorption isotherms can provide further insight onto the type of adsorption process and help in the design of the adsorption equipment.

2.6.1 Kinetic models

The different models can be described as:

- 1st order

The model developed by Lagergren (1898) describes the adsorption process as a first order reaction:

$$\frac{dq_t}{dt} = k_{1st}(q_e - q_t)$$

(2.3)

where q_e is the adsorption capacity at equilibrium and q_t is the adsorption capacity at a given time t . The equation is normally applied in its linearized form:

$$\ln(q_{eq} - q_t) = \ln q_{eq} - k_{1st}t \quad (2.4)$$

- Pseudo 2nd order

In this model, the rate-limiting step is the surface adsorption that involves the formation of complexes, thus the removal from a solution is due to physicochemical interactions between the two phases (Ho, 1995) and can be described as:

$$\frac{dq}{dt} = k_{2nd} (q_{eq} - q_t)^2 \quad (2.5)$$

which can be solved into

$$\frac{t}{q_t} = \frac{1}{k_{2nd}q_{eq}^2} + \frac{1}{q_{eq}t} \quad (2.6)$$

- Particle diffusion

While the previous two models neglect the effect of transport phenomena, and are thus commonly referred to as adsorption reaction models, it is well known that adsorption can also be limited by diffusion. The diffusion limitation can occur during the transport of the adsorbate to the external surface of the adsorbent (film or surface diffusion) or can be due to the speed at which adsorbate diffuses inside the adsorbent (intra-particle diffusion). Models to describe these types of processes are commonly referred to as adsorption diffusion models. Normally, film diffusion is the limiting stage in systems that have poor mixing and/or dilute concentrations of adsorbate (Mohan, 2001) and, thus, the diffusion controlling step in most systems is the intra-particle one. Its most common expression is in the form proposed by Weber-Morris (Alkan, 2007):

$$q_t = k_{int}t^{0.5} + c \quad (2.7)$$

Since this model does not have an upper limit, its validity is normally limited to the first part of the adsorption process and it fails to describe the behavior for longer times.

2.6.2 Adsorption isotherms

- Langmuir model

The Langmuir model is one of the most used for the fit of experimental data. The model is based on the following assumptions (Dąbrowski, 2001):

- The surface of the adsorbent is uniform (i.e. homogeneous) and ideal (i.e. adsorption energy is constant over all sites);
- Adsorbed molecules do not interact with adjacent molecules (i.e. adsorption is localized) and all adsorption occurs through the same mechanism;
- Each adsorption site can hold one adsorbate molecule. In this way at maximum adsorption capacity only a monolayer is formed.

The expression for the Langmuir model is reported in Equation 2.8 and is normally used in its linearized form (Equation 2.9):

$$q_e = \frac{Q^0 b c_e}{1 + b c_e} \quad (2.8)$$

$$\frac{c_e}{q_e} = \frac{1}{b Q^0} + \frac{c_e}{Q^0} \quad (2.9)$$

Once the parameter b is obtained, the separation factor R_L can be calculated as

$$R_L = \frac{1}{1 + b c_0} \quad (2.10)$$

Depending on the value of R_L , one can determine whether the adsorption process is favorable or not. For:

- $R_L > 1$ the process is unfavorable
- $R_L = 1$ linear
- $0 < R_L < 1$ favorable
- $R_L = 0$ irreversible

- Freundlich model

Although the model proposed by Langmuir has successfully been applied in many cases, it has a major limitation in over-simplifying the properties of real adsorbents. In particular, one of the fundamental assumptions of his theory, which refers to the homogeneity of the adsorbent surface, is not justified in many cases (Dąbrowski, 2001).

Thus, other types of isotherms, such as the one suggested by Freundlich, which was initially proposed as an empirical model (Freundlich, 1906), find their application in describing the heterogeneity of the surface. The assumptions that have been used for the derivation of the model are that the surface is heterogeneous and patchwise, so sites having the same adsorption energy are grouped together in one patch. Patches are independent, with no interactions between patches. The expression of Freundlich's isotherm is reported in Equation 2.11 and its linearized form is shown in Equation 2.12:

$$q_e = k_f c_e^{\frac{1}{n}} \quad (2.11)$$

$$\log q_e = \log k_f + \frac{1}{n} \log c_e \quad (2.12)$$

While the Langmuir isotherm has a theoretical justification, the Freundlich isotherm represents an empirical model that can account for multi-layer adsorption, but has the main drawback of not having an upper limit (Q_{\max}) and is thus usually valid only within a restricted range of concentrations. More sophisticated models have been developed to try and give an upper limit to the Freundlich adsorption isotherm, such as the one derived by Sips in 1948 and commonly referred to as the Freundlich-Langmuir adsorption isotherm (Sips, 1948). However, their use is outside of the scope of this work.

2.7 Procedure for Adsorption Studies

0.1 g of dried activated carbon was placed in 10 ml vials and the adsorption experiments were performed using a thermo-incubator shaker: Bionexus BNIS-100. The temperature was controlled at 25 °C and the shaking at 400 rpm.

After completion of the experiment, the samples were filtered using 45 μm filters from WhatmanTM.

The adsorption capacity was calculated as:

$$q_t \left(\frac{\text{mg}}{\text{g}} \right) = \frac{(c_0 - c_t)V}{m} \quad (2.13)$$

where q_t is the adsorption capacity at time t , c_0 is the initial concentration of the component to be adsorbed, c_t is its concentration at time t , V is the liquid volume (10 ml) and m is the mass of adsorbent (0.1 g).

The value of q_t and c_t once equilibrium is reached are referred to as q_e and c_e .

2.8 Preparation of Solutions for Adsorption and Analytical Determination

2.8.1 Preparation of ammonia solutions and determination of ammonia concentration

Ammonia stock solutions with a concentration of 260 mg/L were prepared by adding 1 ml of 29% weight NH_4OH to a volumetric flask and diluting to 1 L with water.

The determination of the initial and final ammonia concentration was carried out using a UV-vis Colorimeter (MC-500) produced by Orbeco Hellige (FL, USA) using the ammonia high range reagent kit. The reagent kit, produced by Cleartech, is composed of reaction vials, containing a solution of lithium hydroxide and sodium salicylate, and two powder bags, ammonia salicylate and ammonia cyanurate. Blanks were produced by adding 0.1 ml of deionized water to the vials and then 5 ml of ammonia salicylate followed by 5 ml of ammonia cyanurate. For the samples, 0.1 ml of the solution was added to the vials followed by the same sample preparation. After 20 minutes, the samples were analyzed in the colorimeter. As can be observed in Figure 2.10, changes in the ammonia concentration produce a colorimetric reaction that makes the reagent kit switch from the yellow color of the blank (right side of Figure 2.10) to a green with intensity depending on the concentration (as moving to the left of Figure 2.10).

The samples were analyzed in triplicates and the results showed good agreement ($\pm 2\%$).

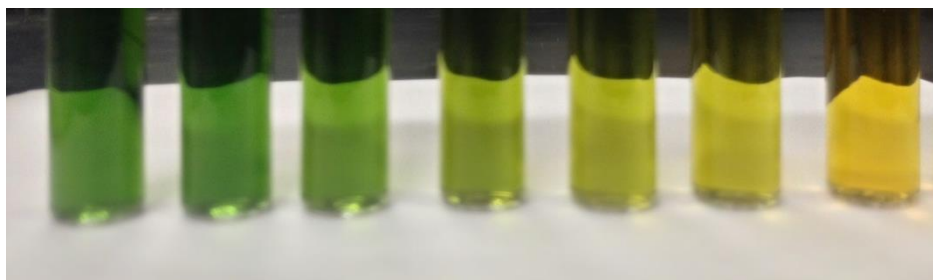


Figure 2.10- Colorimetric reaction for the determination of ammonia concentration

2.8.2 Preparation of naphthenic acids solutions and determination of naphthenic acids concentration

Real samples of oil sands process affected water (OSPW) were obtained from a tailing pond in Western Canada and analyzed by GC-MS to determine the concentration of naphthenic acids, which were in the order of 100 mg/L, with a solution pH of 8.5.

Synthetic naphthenic acids solutions were prepared by dissolving 25 mg each of 4-Pentylbicyclo[2.2.2]octane-1-carboxylic acid, 12-Hydroxydodecanoic acid, Dicyclohexylacetic acid and 1-Methyl-1-cyclohexanecarboxylic acid (all purchased from Sigma Aldrich) in 1 L of a 0.1% NH_4OH solution to allow their dissolution by bringing the original pH in the same range as the real OSPW, due to the low solubility of these compounds at lower pH.

The quantitative analysis of naphthenic acids is challenging, expensive and time consuming. Mohamed (2008) presents the UV-vis analysis at 263 nm as one of the most reliable methods to screen the total concentration of naphthenic acids in water. This method has the advantage of being fast and inexpensive, while still providing quantitative information. Thus, all the samples were analyzed in a Thermo Scientific 220 UV visible spectrophotometer at 263 nm. Figures 2.8 and 2.9 report the UV-vis spectra and the calibration curve for both the real and synthetic OSPW. Another advantage of this method is that no dilution was required, thus the samples were analyzed as received and the reproducibility of replicates was extremely accurate (no significant differences were observed).

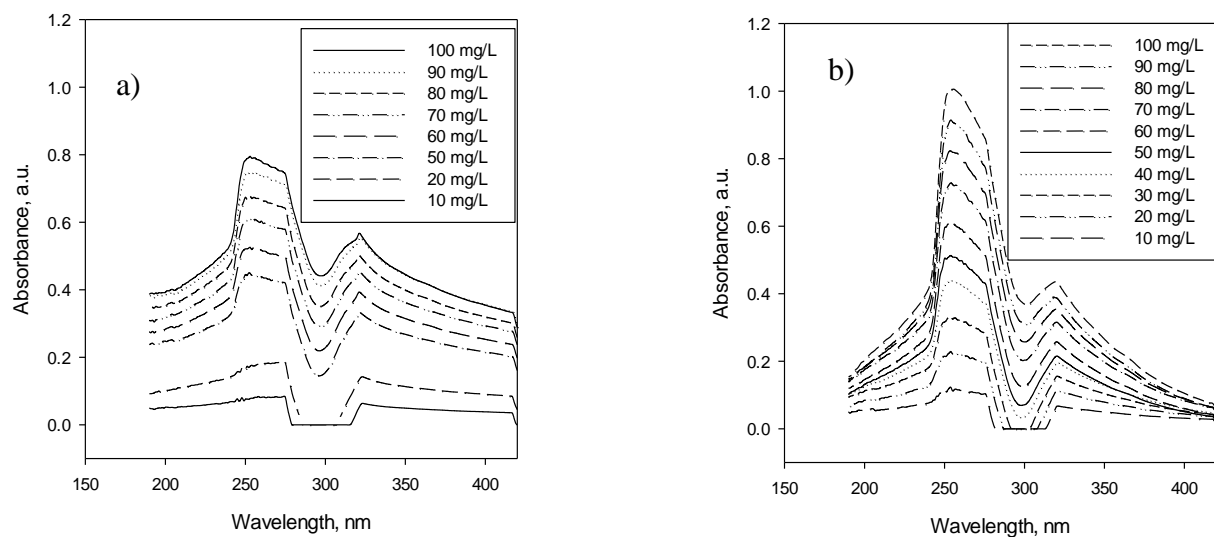


Figure 2.11- UV-vis spectra of a) model compounds solution b) real Oil Sands Process Water (OSPW)

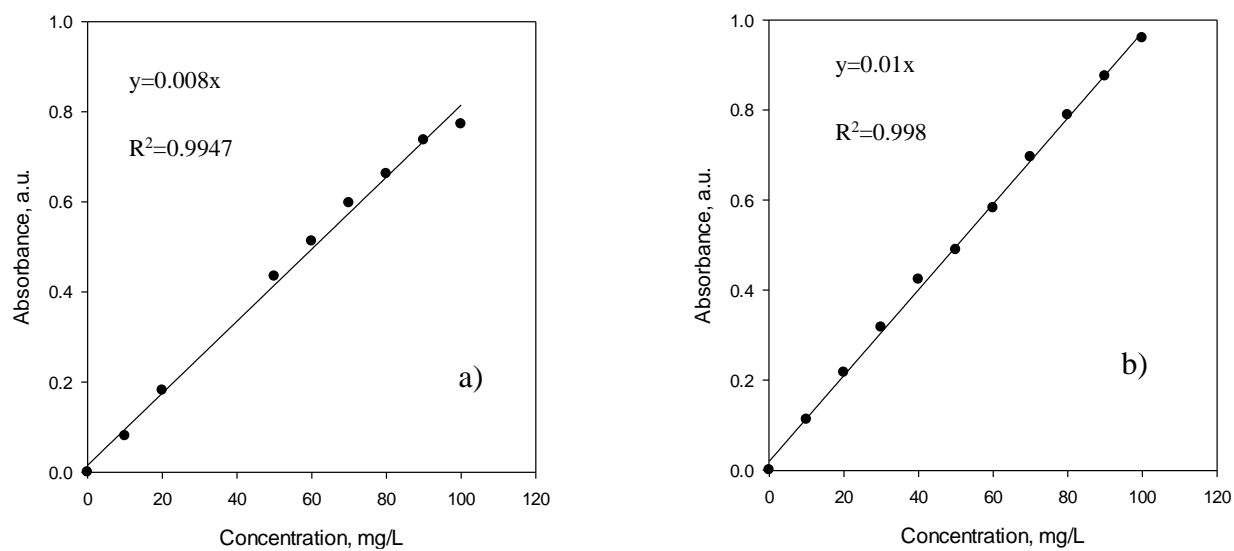


Figure 2.12- Calibration curve at 263 nm for a) model compounds solution b) real Oil Sands Process Water (OSPW)

2.8.3 Preparation of mercury solutions and determination of mercury concentration

Mercury (II) stock solution with a concentration of 1000 mg/L was prepared by dissolving 1.354 g of HgCl_2 in about 700 ml of distilled water and 1.5 ml of concentrated HNO_3 . The solution was then brought to the final volume of 1 L with distilled water.

The method used for the determination of mercury is by colorimetric reaction with Rhodamine 6G (Ramakrishna, 1975), which is based on the formation of a pink-coloured product (Figure 2.13) when Rhodamine 6G is treated with tetraiodomercurate, whose intensity varies with the concentration of mercury. Thus, the samples were analyzed by transferring a suitable aliquot (up to 10 ml) of the sample solution containing not more than 25 μg of mercury to a 25 ml volumetric flask. 5 ml of a buffered potassium iodide (Caledon) and 5 ml of the Rhodamine 6G (Sigma Aldrich) solutions were added while mixing to allow the colorimetric reaction to occur. The solution was then diluted to the mark with distilled water, and the absorbance was measured in UV adsorption at 663 nm in a Thermo Scientific 220 UV visible spectrophotometer at 575 nm against a reagent blank.

The calibration curve obtained with known concentrations of mercury is shown in Figure 2.14.



Figure 2.13- Colorimetric reaction of Rhodamine 6G with tetraiodomercurate

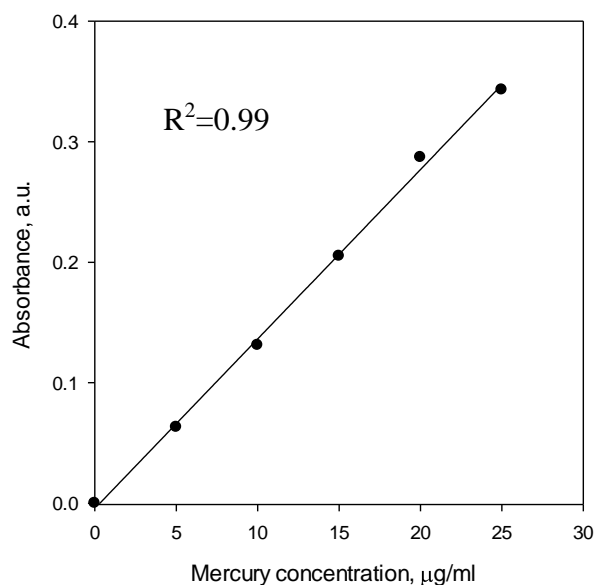


Figure 2.14- Calibration curve with Rhodamine 6G

The concentrations of mercury used in the study were varied between 1000 and 50 mg/L. It was thus necessary to dilute the samples with known concentrations of distilled water to bring them into the range of analysis and then recalculate the original concentration of the solution.

Experiments were performed in duplicates and analyzed in triplicates and the reproducibility was shown to be excellent, with errors <3%.

Chapter 3

3. Application of the Jiggled Bed Reactor to the development of Effective Pyrolysis and Activation Processes for the Production of Activated Carbons from Biomass

3.1 Introduction

About 3 million tonnes of olive oil are produced per year, worldwide, and this production has increased by over 40 % over the last decade (Dermeche, 2013). The large amounts of olive residues associated with the extraction of olive oil represent a major environmental problem, with detrimental impacts on soil microbial populations, aquatic systems, and air pollution through phenol emissions. The transformation of olive residues into a high value product would be both economically and environmentally attractive.

A promising application of olive residues is the production of char through pyrolysis (Zabaniotou, 2000; Gerçel, 2007; Biagini, 2009; Damartzis, 2009; Ounas, 2011; Manyàa, 2013). The resulting char has been successfully used to produce green polymer composites (Papanicolaon, 2011). Its most attractive use, however, seems to be for further conversion to activated carbons through treatment at moderate temperature with air (Wahby, 2009) or, more commonly, at high temperature with either carbon dioxide (Wahby, 2009, Al-Khalid, 1998) or steam (Bacaoui, 2001, Gonzales, 2009). Past studies have shown that the properties of the activated char depend on the conditions of the pyrolysis step and, mostly, the activation step (Jung, 2014; Lua, 2000; Valente Nabais, 2011; Yang, 2003; Yang, 2010). Important parameters that have been identified are the heating rate, the maximum activation temperature, and the composition of the activation gas (Yang, 2010). It is expected that the optimum activation parameters depend on the nature of the original biomass and its processing conditions.

It would, therefore, be advantageous to be able to quickly screen for the optimal pyrolysis and activation conditions with a test reactor that could:

- Simulate the pyrolysis and activation conditions that would be encountered in typical commercial units such as fluidized beds or rotating kilns;
- Perform pyrolysis and activation consecutively, simulating future commercial operations, which will have to reduce energy costs and contamination;
- Operate with a wide range of heating rates;
- Be able to reach the high temperatures required for activation (i.e. up to 900 °C);
- Handle material with characteristics that would prevent fluidization in traditional fluidized beds;
- Produce enough activated char for not only BET analyses but, also, for the measurement of its adsorption performance for various pollutants.

The Institute for Chemicals and Fuels from Alternative Resources (ICFAR) has developed a new Jiggled Bed Reactor (JBR) that meets these criteria.

The objectives of the current study are to adapt the JBR (Latifi, 2012) to the consecutive pyrolysis and activation of biomass, and demonstrate its application to the development of effective processes for the production of activated carbons from olive residues. The results obtained with various biomasses (Kraft lignin, willow, miscanthus, switchgrass) are compared and the most attractive feedstocks identified.

3.2 Materials and Methods

The pyrolysis and activation reactions, and the material characterization were carried out as described in Chapter 2. For this chapter, the pyrolysis was carried out in a batch mode (as described in paragraph 2.3.1), maintaining the pyrolysis step conditions (heating rate of 95 °C/min and a pyrolysis temperature of 500 °C) constant for all the experiments.

3.3 Results and Discussion

3.3.1 Pyrolysis char yield

The yield of the char produced from olive residue at 500 °C, using slow pyrolysis and before activation, is 29 wt%. Its surface area, as determined by BET, is only 6.56 m²/g. In order to validate the use of the JBR for slow pyrolysis reactions, the results obtained are compared with

thermogravimetric analysis (TGA), which is one of the most commonly used techniques to study the thermal decomposition of solids. The heating rate, peak temperature and holding time are reproducing exactly the conditions encountered in the JBR. The TGA profile and weight loss derivative are reported in Figure 3.1 a) and b). The yield obtained with the TGA is 30.2 % vs. 29 % obtained with the JBR, which validates the use of the JBR as an accurate tool for the slow pyrolysis step. The weight loss derivative shows how the peak in the weight loss happens at a temperature of around 375 °C, thus validating the selection of 500 °C with a short holding time for the pyrolysis reaction.

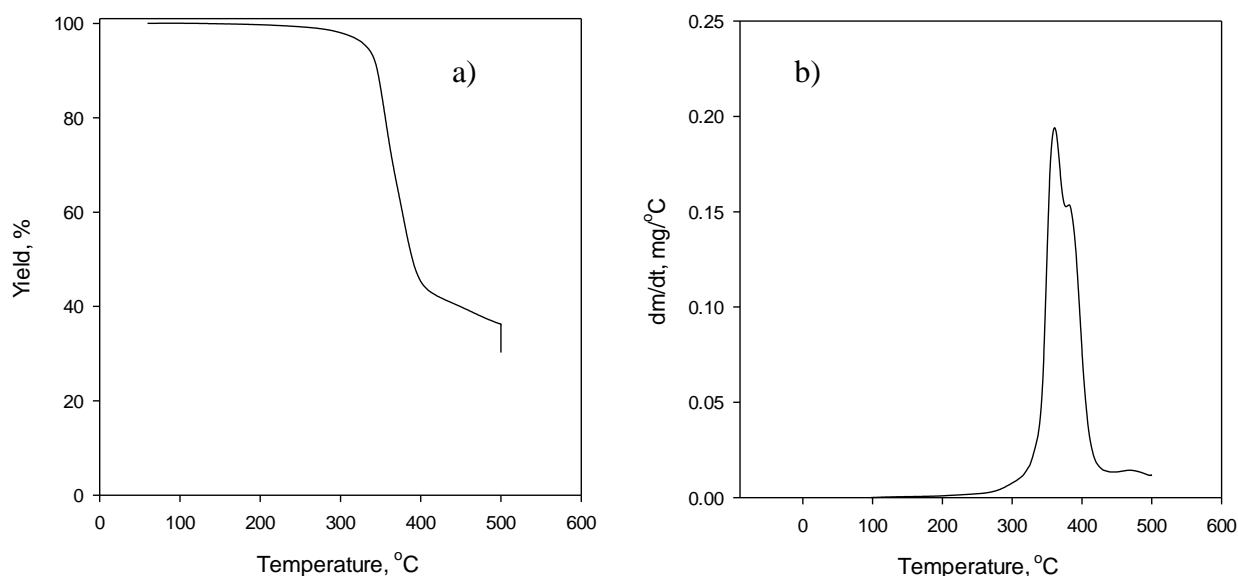


Figure 3.1- a) Thermogravimetric profile and b) weight loss derivative of olive residue obtained with TGA obtained in the same conditions used for slow pyrolysis in the JBR

3.3.2 Impact of activation conditions

In order to investigate the impact of the CO₂ activation conditions on the yield and surface area of the sample, the activation temperature, time and CO₂ flowrate are varied.

The mechanism of CO₂ activation is based on the endothermic Boudouard reaction ($\text{CO}_2 + \text{C} \leftrightarrow 2\text{CO}$). Thermodynamically, an endothermic reaction promotes the forward reaction at elevated temperatures, and in this case, the equilibrium does not favour CO production until temperatures higher than 700 °C (Zhang, 2004), which is the reason why a starting temperature of 800 °C is selected for this study.

The normal CO₂ flowrate range, based on the literature, has been identified as 1.67 to 33.33 cm³/(min*g_{char}). For the experiments of this study, this range has been expanded from 2.27 to 90 cm³/(min*g_{char}), or 10 to 400 ml/min for a typical pyrolytic char mass of 4.41 g.

It has been previously reported in the literature (Jung, 2014; Yang, 2003; Yang, 2010) that the surface area of the sample increases with the activation time up to a certain value, after which it starts to decrease as a consequence of pore walls collapse. In our case, the phenomenon was observed after an activation time of 120 minutes. Thus, the activation time is selected between 10 minutes and 2 hours, in order to prevent the collapse in surface area.

Table 3.1 lists the conditions of the experimental trials.

Table 3.1- Summary of experiments and results

Temperature (°C)	Activation time (min)	Flowrate (ml/min)	Yield (from dry biomass)	Surface area (m ² /g)	Run n°
800	30	20	25.0%	152	1
800	30	100	24.0%	340	2
800	30	200	23.7%	357	3
800	60	100	22.6%	535	4
800	60	200	20.6%	646	5
850	10	100	24.9%	140	6
850	20	200	23.3%	274	7
850	30	100	22.2%	305	8
850	30	200	22.5%	404	9
850	60	100	20.0%	618	10
850	60	200	19.9%	735	11
850	120	200	9.4%	1262	12
900	30	100	21.3%	468	13
900	30	200	20.0%	538	14
900	30	400	21.1%	582	15
900	60	100	15.9%	884	16
900	60	200	16.0%	906	17
900	60	400	13.5%	882	18

Figure 3.2 a) shows that the effect of the activation gas flowrate on the yield of activated char is moderate: a minor decrease in yield is observed with increasing gas flowrate. Figure 3.2 b) shows,

on the other hand, that there is a strong effect of the activation gas flowrate on the BET surface area of the activated char for lower flowrate values, which then reaches a plateau.

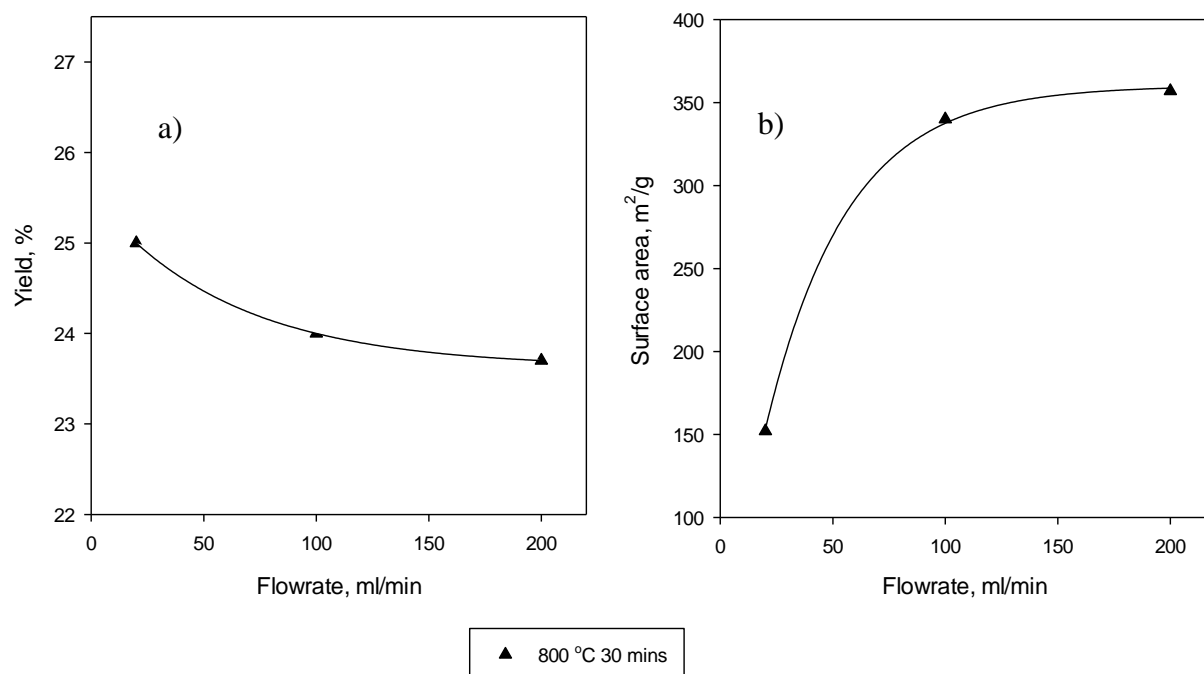


Figure 3.2: Effect of activation gas flowrate on a) the activated char yield and b) the activated char surface area

Because of the excellent mixing achieved with the JBR, the effect of the gas flowrate is not the result of external mass transfer limitations but it is likely caused by changes in partial pressure of the carbon dioxide within the reactor bed. It has been observed by micro-GC analyses that the ratio of CO to CO₂ in the reactor exhaust gases for a flowrate of 200 ml/min is 1/9 (molar). This means that under those conditions, there is a large excess of CO₂, which makes its partial pressure very high. For the rest of the study, a flowrate of 200 ml/min is, therefore, used to obtain results that are nearly independent of the flowrate.

Figure 3.3 shows that the activation temperature has a strong effect on both the yield of activated char a) and its BET surface area b). Increasing the activation temperature speeds up the oxidation reactions of the carbon dioxide with the carbon, allowing more carbon to react within a specified time, resulting in both a lower activated carbons yield and a larger BET surface area.

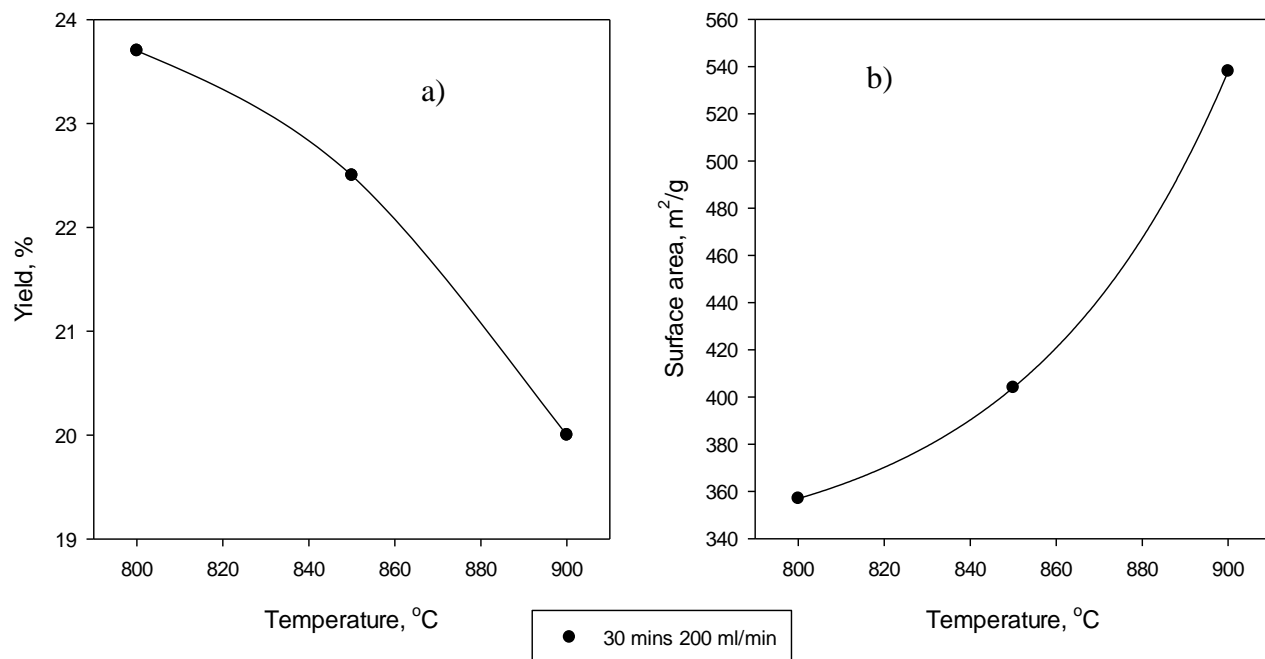


Figure 3.3: Effect of activation temperature on a) the activated char yield and b) the activated char surface area

Figure 3.4 shows that increasing the activation time reduces the yield of activated char and greatly increases its BET surface area. This confirms that the activation is kinetically controlled, which is consistent with the impacts of the activation temperature (Figure 3.3) and of the carbon dioxide partial pressure, which is affected by the carbon dioxide flowrate (Figure 3.2).

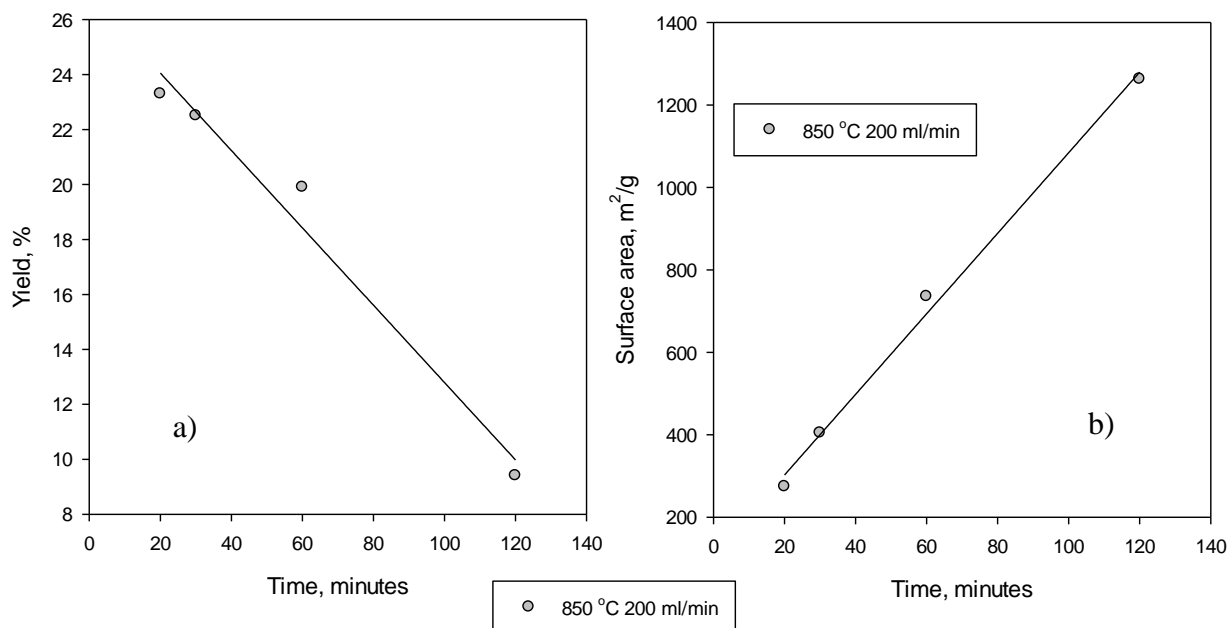


Figure 3.4: Effect of activation time on a) the activated char yield and b) the activated char surface area

Figure 3.5 indicates that there is a linear relationship between increases in surface area and reductions in the yield of activated carbons. This general trade-off does not appear to be significantly affected by changes in gas flowrate or activation temperature, although the flowrate and temperature were shown to affect the kinetics of the activation process. Similar trends have previously been observed by Azargohar (2008) and Zabaniotou (2008), and indicate that the creation of a well-developed surface area depends on the amount of carbon removed during the activation, which creates porosity in the material.

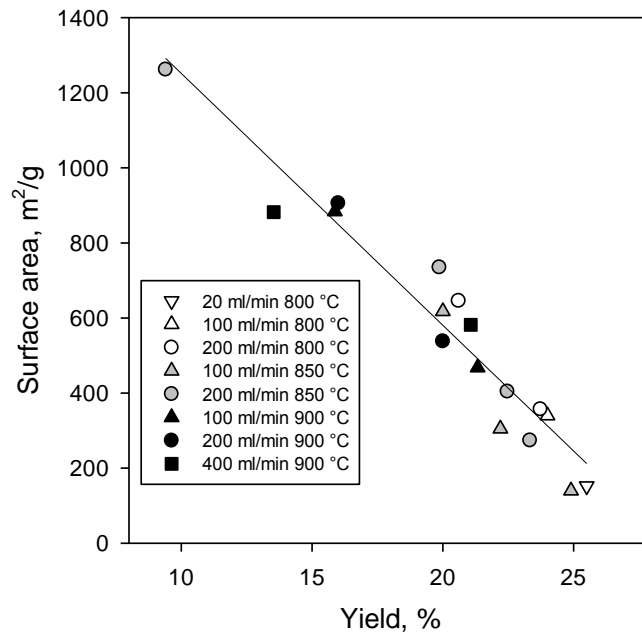


Figure 3.5: Relation between yield and surface area during olive residue activation (points with the same symbol were obtained at the same temperature and flowrate but different times)

3.3.3 Activation kinetics

Figure 3.4 shows that both yield and surface area vary linearly with time. Thus, within the range of the operating conditions tested, the reaction behaves as a zero order, in which the kinetics is apparently independent of the carbon concentration. Zero-order kinetics is always an artifact of the conditions under which the reaction is carried out. Clearly, a zero-order process cannot continue after a reactant has been exhausted. The rate of reaction is proportional to the product of the concentration of carbon dioxide at the reacting surface by the exposed carbon surface per unit volume of the reactor. Assuming that the reaction is purely controlled by kinetics, thus neglecting the impact of transport phenomena such as external or internal mass transfer limitation, we can explain the kinetics results by considering that:

- The concentration of carbon dioxide at the reacting surface would be equal to the concentration of carbon dioxide in the bulk of the gas. Due to the large excess of carbon dioxide in our study, its concentration is not affected by the extent of the reaction, which is in agreement with the behavior observed by Senneca (2007) at elevated CO₂ partial pressures for the gasification reaction of olive residue;

- For the exposed carbon surface per unit volume of the reactor, it is not possible to talk about concentration, due to the fact that the reaction is in the solid phase. The rate of reaction is proportional to the specific area of available carbon, in agreement with the results interpretation provided by Valente Nabais (2011).

However, in the absence of mass transfer limitations, the rate of reaction should speed up as more surface becomes available (i.e. the surface area increases). This is in disagreement with the experimental results; two explanations are possible for this behavior:

- Pore diffusion limitation: the reaction front moves deeper into the particle as the reaction proceeds which causes the reaction to slow down as the pores become deeper, balancing the positive effect of increased surface area of the particle;
or
- By considering that the area of reactive carbon is the one at the bottom of the pores, which assuming cylindrical pore shape does not change significantly with time, rather than the BET surface area. In this case, both the specific area of reactive carbon and the carbon dioxide concentration are approximately constant with time, which explains the approximately zero order the reaction. This also implies that kinetic constants are not intrinsic kinetic constants, but apparent kinetic constants, proportional to the concentration of carbon dioxide and the specific area of reactive carbon, which are constant, in the range of operating conditions studied.

Therefore, we can describe the kinetic as:

$$Y = Y_0 - k_y t \quad (3.1)$$

where Y_0 is the yield of non-activated char (equal to 29%).

As a result, the kinetic constants can be determined as the slope of the yield vs. time plot (as in Figure 3.4) for each temperature. The results are reported in Table 3.2.

Table 3.2- Determination of k_y for different temperatures

T, °C	800	850	900
$k_y, 10^{-3} \cdot \text{min}^{-1}$	1.3	1.6	2.3

where k_y is defined with the Arrhenius equation:

$$k_y = k_{y0} e^{\left(\frac{-E_{ay}}{RT}\right)} \quad (3.2)$$

Figure 3.6 shows that the Arrhenius equation gives a good fit of the experimental data. Table 3.3 provides the values of k_{y0} and E_{ay} obtained from the data.

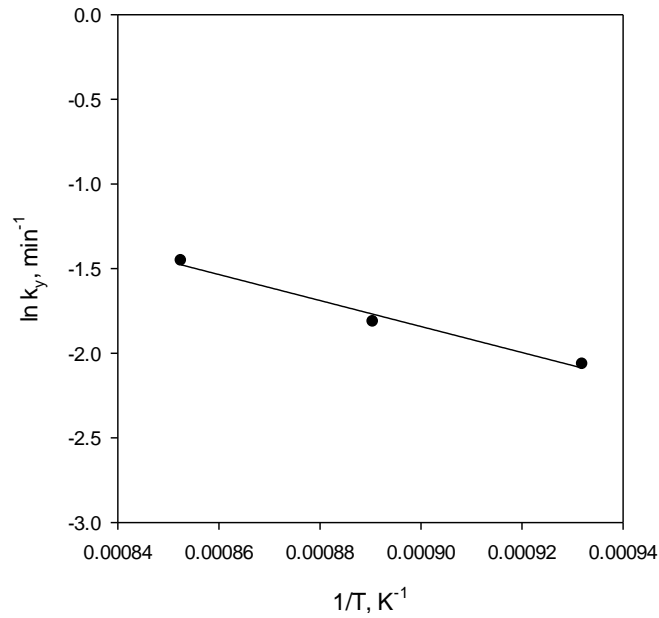


Figure 3.6- Linearized Arrhenius plot for yield

Table 3.3- Determination of k_{y0} and E_{ay}

k_{y0}, min^{-1}	$E_{ay}, \text{J/mol}$
121	61207

Figure 3.7 shows the comparison between the values of yield obtained using the values of k_{y0} and E_{ay} of Table 3.3 and the experimental values. It can be observed that the two are in good agreement.

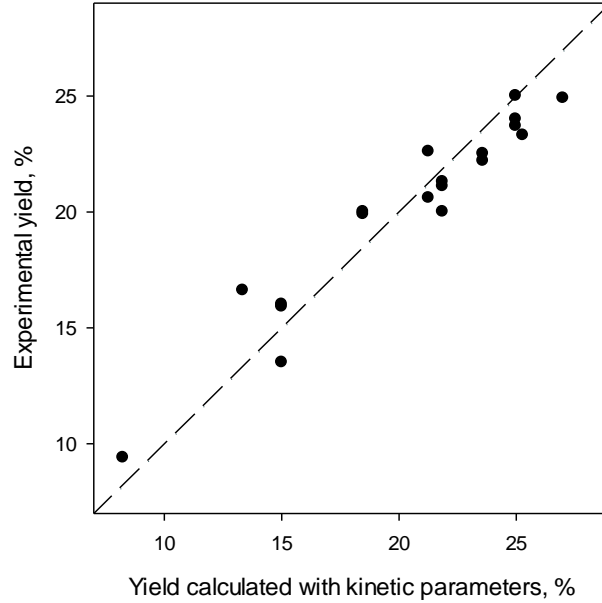


Figure 3.7- Comparison between the yield calculated with the kinetic parameters and the yield obtained experimentally

An apparent kinetic constant can also be defined to describe the surface area evolution, in order to explain the relationship between the weight loss and the pore evolution and can be expressed as:

$$a = a_0 + k_s t \quad (3.3)$$

The values of k_s for different temperatures are shown in Table 3.4.

Table 3.4- Determination of k_s for different temperatures

T, °C	800	850	900
$k_s, \text{m}^2/(\text{g} \cdot \text{min})$	9.6	11.4	15.3

Figure 3.8 shows that the Arrhenius equation gives a good fit of the experimental data and Table 3.5 provides the values of k_{s0} and E_{as} obtained from the data.

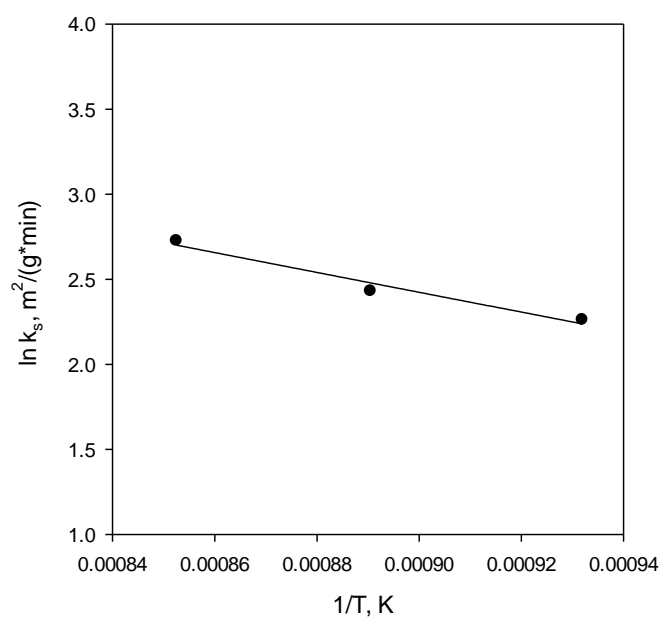


Figure 3.8- Linearized Arrhenius plot for surface area

Table 3.5- Determination of k_{s0} and E_{as}

k_{s0} , m ² /g*min ⁻¹	E_{as} , J/mol
2001	48166

Figure 3.9 shows the comparison between the values of surface area obtained using the values of k_{s0} and E_{as} previously calculated and the experimental values. It can be observed how the two are in good agreement.

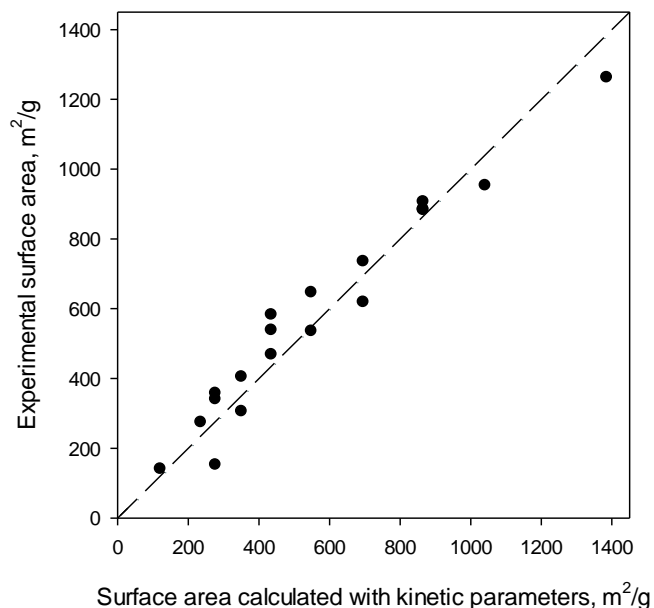


Figure 3.9- Comparison between the surface area calculated with the kinetic parameters and the one obtained experimentally

Figure 3.10 shows the relationship between the surface area and yield calculated using the kinetic parameters compared with the experimental one.

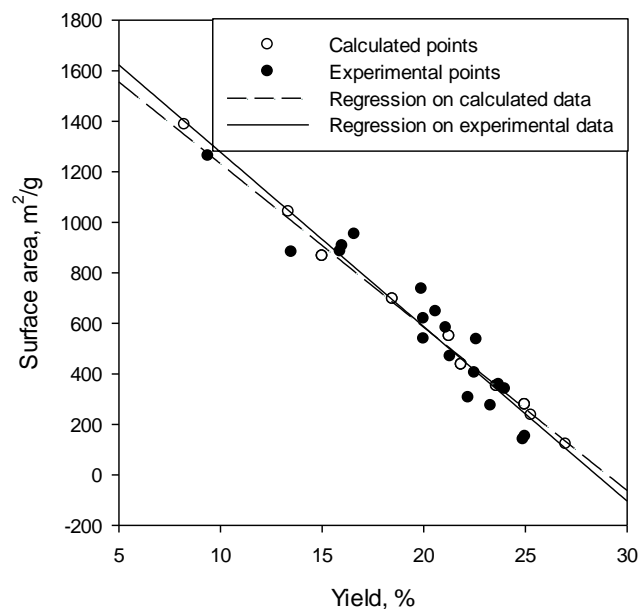


Figure 3.10- Comparison between the surface area vs. yield plot obtained experimentally (closed symbols) or calculated (open symbols) using the kinetic parameters

The linear relationships with time of both the yield and the surface area result in a linear relationship between yield and surface area. Combining Equations 3.1 and 3.3 gives:

$$Y = \left(Y_0 + \frac{k_y}{k_s} a_0 \right) - \frac{k_y}{k_s} a \quad (3.4)$$

3.3.4 Characterization of the porous structure

Using the t-plot method (previously described in Paragraph 2.5.3) to examine the adsorption isotherms for all the samples, it is possible to observe a trend in the formation of micropores as the reaction proceeds, as shown in Figure 3.11.

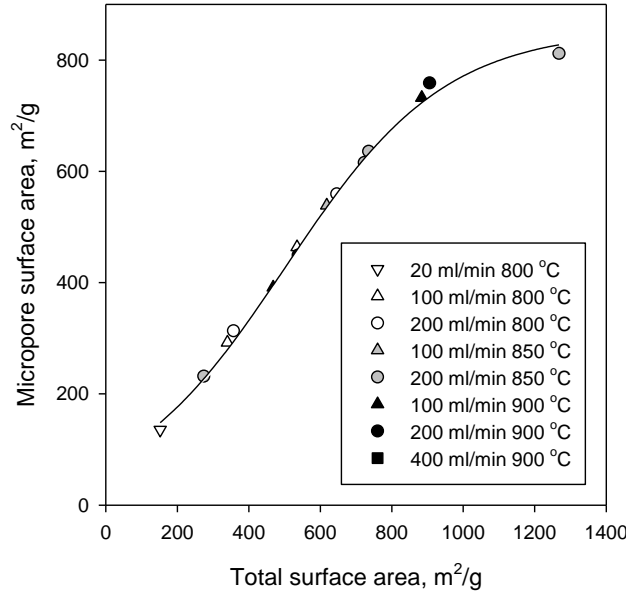


Figure 3.11: Relationship between micropore surface area and total surface area for different activated olive residue samples

These results suggest that the initial char is a scarcely porous material, characterized by a low surface area and the presence of meso and macropores on the surface, as can also be observed by SEM pictures shown in Figure 3.12. Through activation, micropores that were original plugged by tars open up to give an increase in the surface area as well as in the micropore surface area, as shown in Figure 3.11. A SEM image of the activated particle, showing the well-developed porous structure of the sample, is shown in Figure 3.13. As the activation process proceeds, there is another phenomenon happening, which is the enlargement of pre-existing pores. This becomes

significant for longer activation times (aggressive activation conditions, as previously reported in Figure 2.9) leading to an increase in the mesopore surface area. Further activation of these samples generates a collapse in the porous structure of the char and, thus, a decrease in the total surface area. This also supports the previous interpretation of the kinetic results, implying that the area at the bottom of the pores does not change significantly, and that no new pores are formed during the process. If the reaction were allowed to proceed further, there would be first an enlargement of the pores, followed by a collapse in the surface area that would lead to a decrease in the number of pores, altering the equilibrium between carbon dioxide concentration and reactive surface of carbon exposed. This can explain why other studies found that, at higher values of carbon conversion, a different kinetic regime is observed (Umeki, 2012).

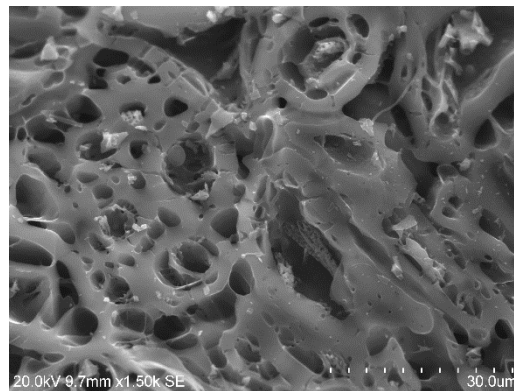


Figure 3.12- SEM image of non activated char sample from olive residue

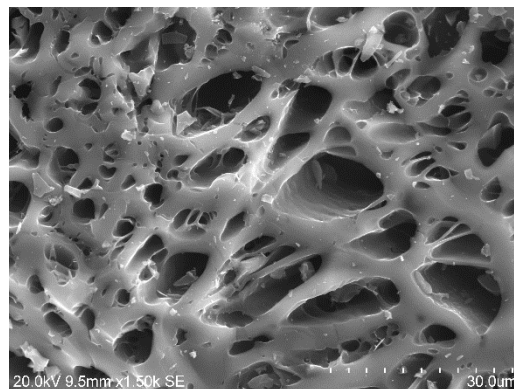


Figure 3.13- SEM image of activated char sample from olive residue

3.3.5 Possible integration of activation with the pyrolysis process

As described in the introduction, in order to make this process economically feasible, it is necessary to integrate the bio-char activation with the pyrolysis process, to maximize the recovery of valuable products. Therefore, a conceptual integrated process is shown in Figure 3.14, consisting in the use of the combustion gases for the activation, after burning the non-condensable gases produced by the pyrolysis reaction. Industrially, this process is very attractive because it uses wet gases that are largely available in many plants.

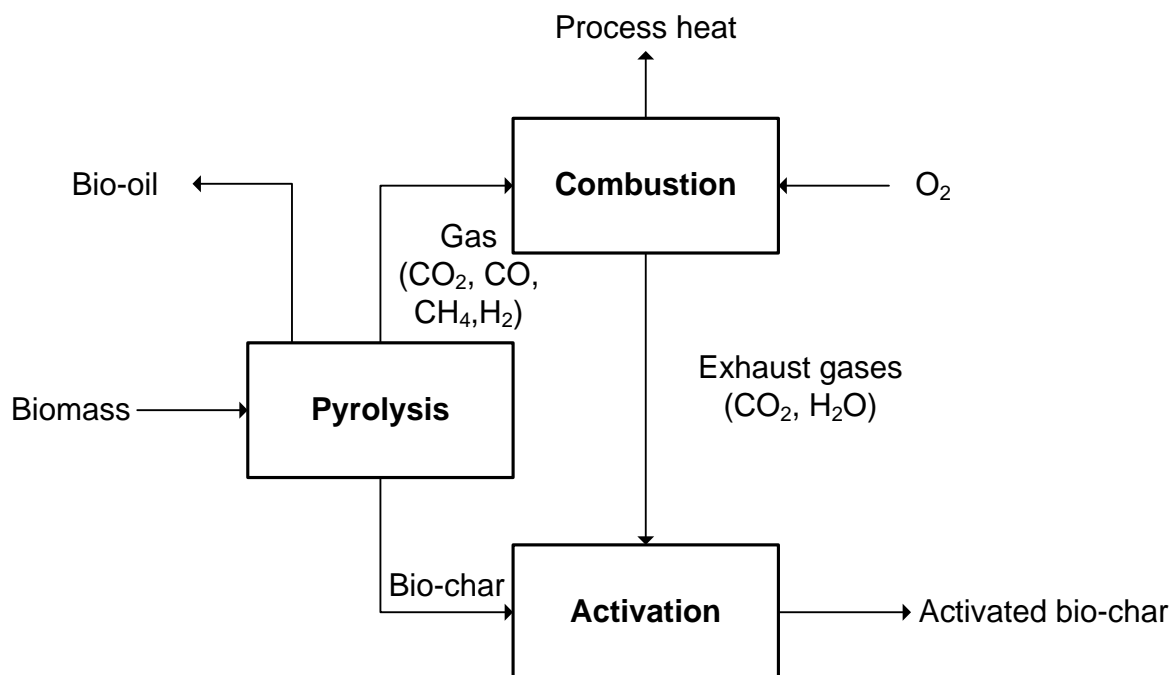


Figure 3.14- Integration of activation with the pyrolysis process

The composition of the gases resulting from the biomass pyrolysis, and analyzed with a micro-GC, is reported in the Appendix A to Chapter 3. The combustion of 1 mole of gas would give 1.45 moles CO₂ and 0.44 moles of H₂O, generating a stream with about 75% CO₂ and 25% H₂O, on a molar basis. A stream with this composition has been generated using the set up described in Paragraph 2.3.3 and experimentally utilized to simulate the proposed conceptual process.

Figure 3.15 shows the results obtained with the simulated exhaust gas composition for experiments carried out for 1 h with a total gas flowrate of 200 ml/min with 75% CO₂ and 25% H₂O in comparison with 100% CO₂.

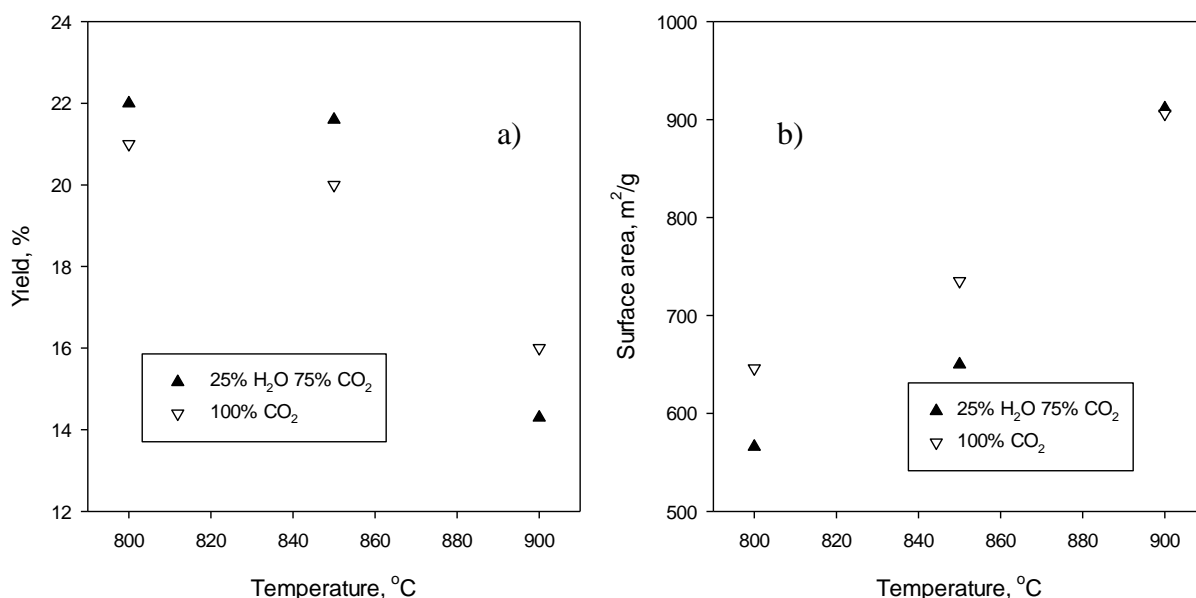


Figure 3.15- a) Yield b) Surface area variation with activation temperature using simulated combustion gases (open symbols) or pure CO₂ (closed symbols) as activating agent

The results obtained with the wet gas mixture simulating combustion gases are comparable to the results obtained with the pure CO₂. This is in agreement with the results obtained by Minkova (2000), who carried out experiments in presence of pure steam and a mixture of steam and CO₂. This can be explained once more using partial pressure: despite the fact that the partial pressure of CO₂ is decreased, the overall partial pressure of activating agents remains the same, since steam is also an activating agent.

The trade-off between yield and surface area, including the experiments with wet gases, is shown in Figure 3.16. It can be observed that the results agree with the linear trend obtained with pure dry carbon dioxide, meaning that the results obtained with dry gases are still relevant when the wet gas mixture is used. This is further corroborated by the fact that no significant difference is observed also in the porous structure, as shown in Figure 3.17. Since the experiments with dry gases are simpler to carry out, only dry gases will be utilized to carry out the rest of the experimental work reported in this thesis.

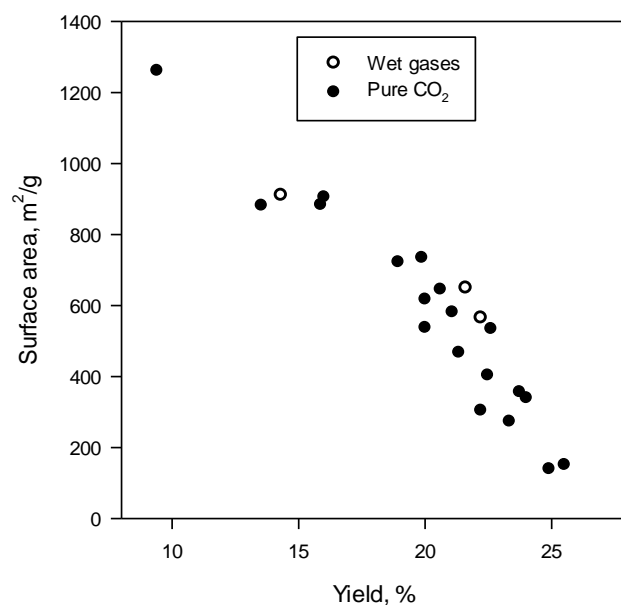


Figure 3.16- Trade-off between surface area and yield for char samples activated with pure CO_2 (closed symbols) and CO_2 /steam mixture (open symbols)

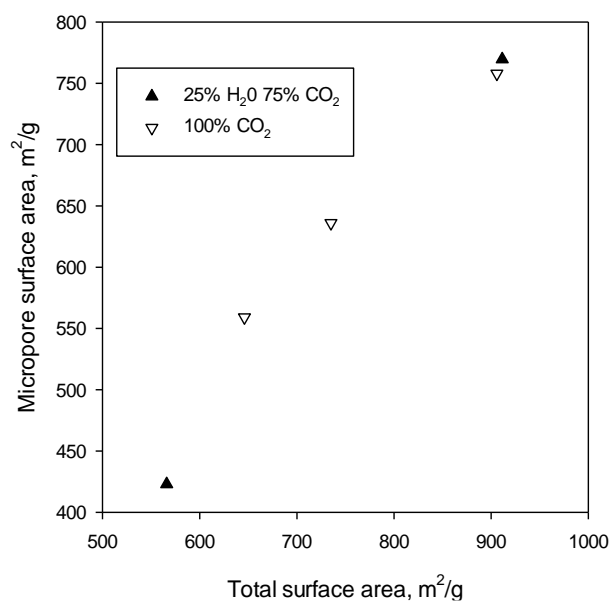


Figure 3.17- Relationship between micropore surface area and total surface area for char samples activated with pure CO_2 (closed symbols) and CO_2 /steam mixture (open symbols)

3.3.6 Impact of feedstock characteristics

In order to determine the impact of the feedstock characteristics on the linear trade-off parameters, the curves relating the surface area and the yield were obtained for different feedstocks. The feedstocks examined were selected from those reported in Table 2.2. Previous studies reported that the fixed carbon and ash content are two parameters that might influence the production of activated carbon from a certain feedstock, thus the selection criteria was:

Table 3.6- Selection criteria for the comparison of different biomasses

	Ash content	Fixed carbon content
Kraft lignin	Low	High
Olive residue	High	High
Willow	Low	Low
Switchgrass	High	Low
Miscanthus	High	Low

Miscanthus also has a much higher cellulose content than switchgrass (45 vs. 32%), which represents the major difference between the two feedstocks.

For each feedstock, at least three experimental conditions were investigated in order to obtain the slope and the intercept of the trade-off relationship between surface area and yield, as shown in Figure 3.18. Individual curves for each feedstock are reported in Appendix B to the Chapter.

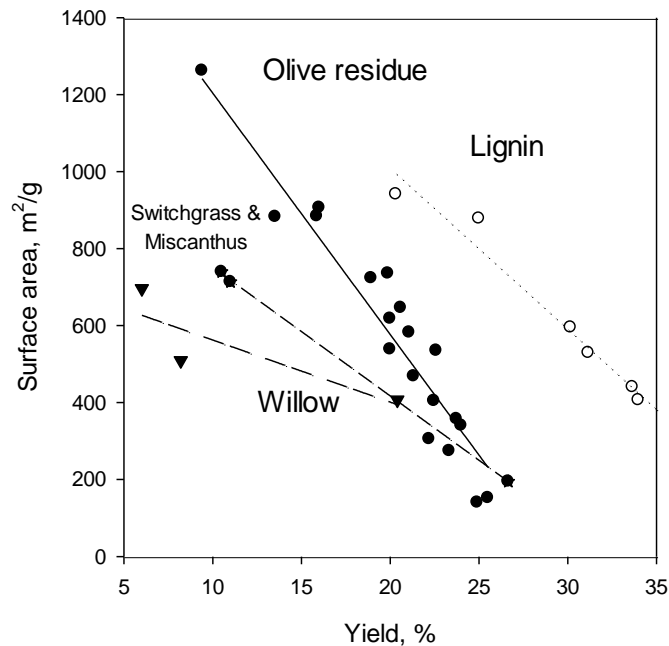


Figure 3.18- Surface area vs. yield trade-off for different feedstocks

What is of interest is to study how the trade-off between the yield and the surface area changes for different feedstocks. Ideally, we would identify a feedstock as attractive if it is located in the upper-right portion of the surface area vs. yield plot. Thus, the relevant parameters are the intercept (ideally the highest surface area that can be achieved before the porous structure starts to collapse) and the slope of the curve. This can be described with equation 3.5:

$$\text{Surface area} = \text{Intercept} - \text{Slope} * \text{Yield} \quad (3.5)$$

The experimental values of intercept and slope are reported in Table 3.9 for the different feedstocks. It can be noted how the value of the intercept increases when going from grass-type feedstocks, like switchgrass and miscanthus, to materials with higher lignin and fixed carbon content, such as olive residue and Kraft lignin.

Table 3.7- Surface area vs. yield parameters for different feedstocks

	Fixed carbon content, weight %	Ash content, weight%	Intercept	Slope
Olive residue	22	2.7	1831	62
Willow	16	1.2	1206	85
Switchgrass	15	2.9	1302	58
Miscanthus	14	2.7	1450	55
Kraft lignin	31	0.3	1982	40

The intercept and the slope can be correlated with the values of fixed carbon and ash content for the samples analyzed, based on the empirical correlations reported in Equations 3.6 and 3.7:

$$Intercept = 617.17 + 44.89 * (\% Fixed carbon content + \% ash content) \quad (3.6)$$

$$\frac{Intercept}{Slope} = -2.27 + 1.62 * \% Fixed carbon content - \% ash content \quad (3.7)$$

Figure 3.19 compares the values of intercept and slope obtained experimentally with the ones calculated from the correlations.

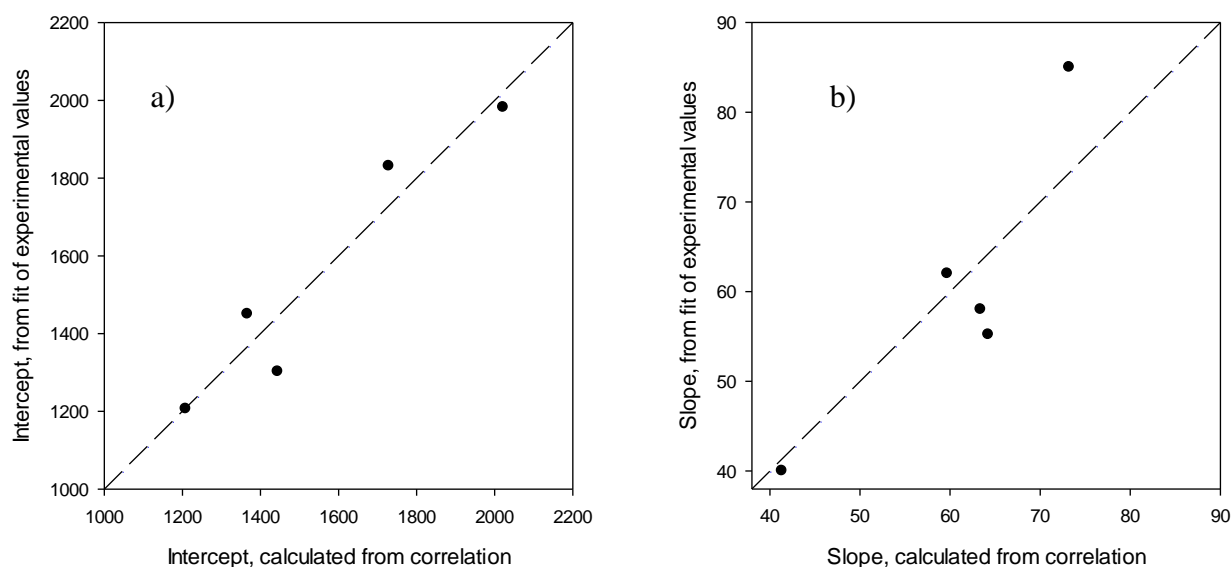


Figure 3.19- Comparison between calculated and experimental values for a) intercept b) slope of the surface area vs. yield trade-off for different feedstocks

The fit for the intercept gives a regression coefficient $R^2=0.92$ with a p-value of 0.01, thus proving the statistical significance of the correlation found. The correlation for the slope has a slightly lower value of $R^2=0.8$, but the p-test also confirms the significance ($p=0.04$).

Based on the previously reported results, it is clear how it is more profitable to focus on feedstocks with a high fixed carbon and low ash content. For this reason, two feedstocks are selected for the subsequent study: olive residue and lignin, for which the surface area/yield trade-off is shown in Figure 3.20. In agreement with the results previously found, lignin seems to be the most attractive feedstock, having high fixed carbon and very low ash content. However, olive residue is also attractive and easier to handle, making it a suitable feedstock for the screening stages.

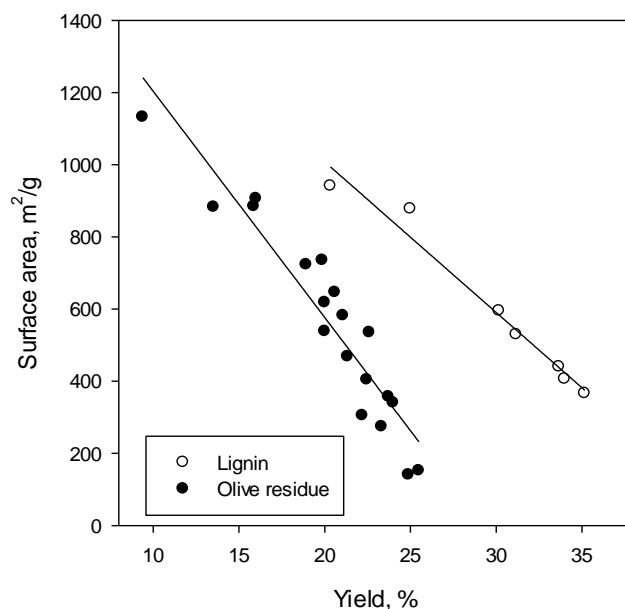


Figure 3.20- Surface area vs. yield trade-off comparison for olive residue and lignin

When looking at the characterization of the porous structure, it can be observed how, for the same total surface area, lignin has a higher fraction of mesopores, as shown in Figure 3.21. Also, the average pore diameter is 19 Å for olive and 22 Å for lignin, one corresponding to a microporous material and the other to a mesoporous. SEM pictures of lignin (Figure 3.22) also reveal the presence of macropores located on the external surface, which give a sponge-like structure to the particle. This texture is beneficial for an adsorbent material since larger pores serve as feeder to smaller ones (meso- and micropores). Infact, the presence of larger pores onto the surface can favor the penetration of larger molecules reducing the surface diffusion limitation, corroborating the hypothesis that lignin based-activated carbons are potentially very attractive for the adsorption of larger molecules.

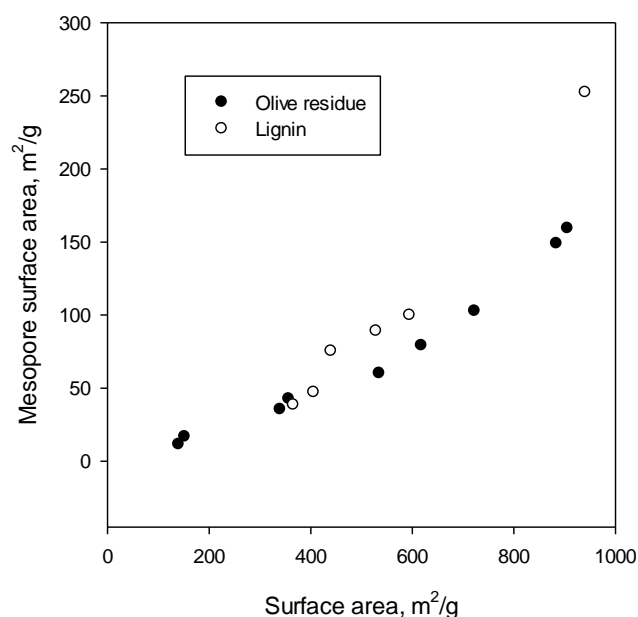


Figure 3.21- Comparison between mesopore surface areas for olive and lignin activated carbons

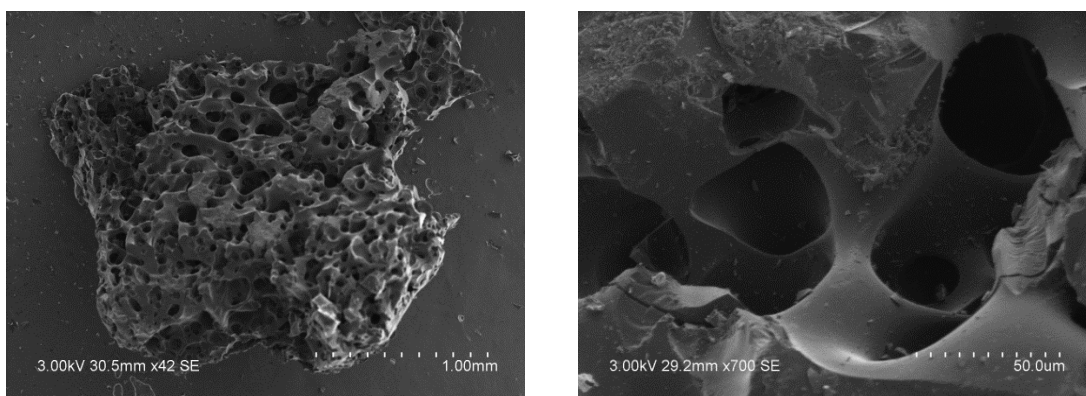


Figure 3.22- SEM images of lignin activated carbon samples

In particular, materials with a microporous structure are mostly used for gases and air treatment, while mesoporous materials are more suitable for applications such as wastewater treatment. A standard test that is often performed for adsorbent materials is methylene blue adsorption. Methylene blue is a large molecule and, thus, its adsorption capacity is used as an index of mesoporosity of a material.

From the results presented in Figure 3.23, it is clear that the correlation between the mesopore surface area and methylene blue adsorption capacity is very strong for both feedstocks and how lignin based activated carbons, having larger mesopore volume, have higher adsorption capacities, up to 100 mg/g.

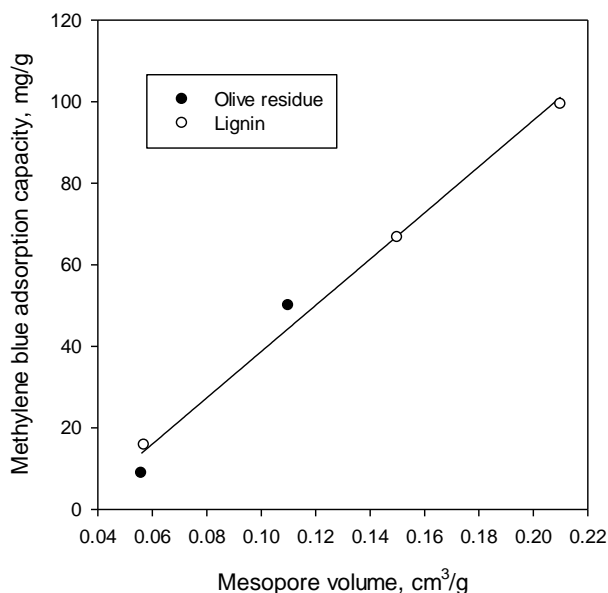


Figure 3.23- Methylene blue adsorption capacity as a function of mesopore volume for selected samples of olive residue and lignin activated carbons

3.4 Conclusions

In this chapter, the use of the JBR for slow pyrolysis and activation was successfully validated and optimal parameters for the activation of olive residue were identified. The study of the kinetics of the process and product characterization was carried out. A possible scheme to integrate the activation and pyrolysis processes was also presented.

The results obtained with olive residue were compared with other biomasses and screening criteria for the selection of the starting feedstock for the production of activated carbons were proposed. Based on the results obtained, feedstocks with high fixed carbon content (olive residue and lignin) were selected as the most attractive precursor and their porous structure was compared to reveal that one (olive) produces a mostly microporous material, while the other (lignin) has a larger fraction of mesopores.

Appendix to Chapter 3

A.

The composition of the pyrolysis gases for the pyrolysis of olive residue at a temperature of 500 °C and heating rate of 95 °C/min, as measured by micro-GC, is reported in Table 3.6.

Table 3.8- Composition of pyrolysis gases

CO	CO ₂	CH ₄	H ₂
58%	16%	13%	9%

Thus, the combustion of this stream would generate (neglecting incomplete combustion and and C+) a stream with the composition reported in Table 3.9.

Table 3.9- Combustion reactions for the non-condensable gases stream

Amount (moles)	Reaction
58%	$2\text{CO} + \text{O}_2 \rightarrow 2\text{CO}_2$
13%	$\text{CH}_4 + 2\text{O}_2 \rightarrow \text{CO}_2 + 2\text{H}_2\text{O}$
16%	CO_2
9%	$2\text{H}_2 + \text{O}_2 \rightarrow 2\text{H}_2\text{O}$

B.

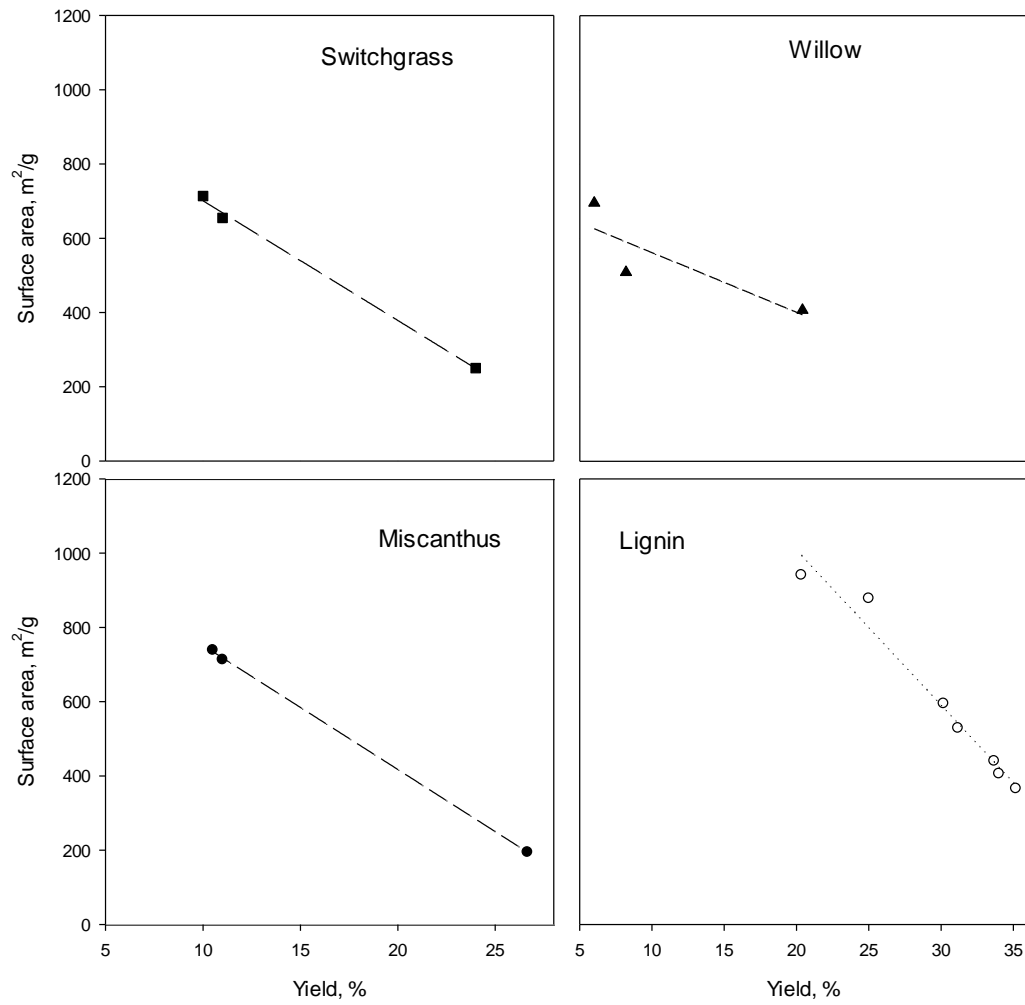


Figure 3.24- Surface area vs yield trade-off for individual feedstocks

Chapter 4

4 Development of a Model for the Prediction of the Yield and Surface Area during Activated Carbons Production in the Jiggled Bed Reactor

4.1 Introduction

The modelling of a process is fundamental for better understanding the characteristics of the process itself and for optimization of its operating conditions.

A great amount of work in the literature is dedicated to the kinetic modelling of gasification reactions (Umeki, 2012; Senneca, 2007; Ollero, 2002; Cetin, 2005), while a limited number of authors have given attention to the contribution of physical parameters, which are very important in the case in which the reaction is applied to the production of activated carbons.

In general, the kinetic parameter of the process can be described as:

$$k = k_0 e^{-\frac{E_a}{RT}} p_{CO_2}^n \quad (4.1)$$

and the variation of the conversion of material is described by:

$$\frac{dx}{dt} = k(T, p) f(x) \quad (4.2)$$

x is the carbon burn-off normally described as:

$$x = \frac{m_0 - m}{m_0} \quad (4.3)$$

where m is the final mass of char and m_0 its initial mass.

The determination of the function $f(x)$ enables to distinguish between different types of models in the literature:

- Volume reaction model (VRM) (Molina, 1998) is a homogeneous model that assimilates the heterogeneous reaction of gasification to a homogeneous reaction: the reaction takes place at the totality of available sites and the structure of the particle is assumed not to change. For this type of models, the function $f(x)$ is usually described as:

$$f(x) = (1 - x) \quad (4.4)$$

- Shrinking core model (SCM) is a model in which the reaction is considered to occur initially at the external surface of the particle and gradually move inside of it. As a result, the particle size is reduced during the process (Yagi and Kunii, 1995; Morris, 2012) and the reaction rate decreases monotonically. The function $f(x)$ is commonly written as:

$$f(x) = (1 - x)^{\frac{2}{3}} \quad (4.5)$$

- Random pore model (RPM), originally presented by Bathia and Permuter (1981). The model considers that gasification occurs only on the inside surface of the micropores, which occupy most of the surface area of the particle. As a function of the reaction progress, the surface area first increases and then decreases as a consequence of coalescence of pores.

In order to account for this phenomenon, the function $f(x)$ is written as:

$$f(x) = (1 - x)\sqrt{1 - \psi \ln(1 - x)} \quad (4.6)$$

ψ is a surface function parameter related to the pore structure of the non-reacted sample ($x = 0$), which can be calculated using Equation 4.7.

$$\psi = \frac{4\pi L_0(1 - \varepsilon_0)}{S_0^2} \quad (4.7)$$

where S_0 is the pore surface area per unit volume, L_0 is the pore length and ε_0 the solid porosity. Despite the fact that this model is known to be one of the most accurate, and the literature also reports more complex models based on these principles (Faramarzi, 2015; Feng, 2003) developed for specific applications, ψ cannot be measured directly. This is because the structural parameters such as L_0 and S_0 are not provided by BET measurements that are commonly carried out to characterize activated carbons. While ranges of values for some porous materials or simplified

forms for their estimation are available, a rigorous calculation, in order to successfully apply the model, would require solving partial differential equations involving high computational time and, thus, would not be of immediate application. Very detailed models are hard to develop, as well as to apply: therefore, simplifications based on visual observations are encouraged, depending on the final objective of the model. In the case of this study, for example, a simpler equation could indeed be used, since the desired operating range is before the collapse of the surface area.

None of the above three models can accurately fit the experimental data of this study, as shown in part C of the Appendix associated to this chapter. None of the above three models can predict the surface area, which is a crucial parameter for activated carbon.

Therefore, the objective of this chapter is to develop a simple model in which the reaction kinetics can be related to the physical properties of the carbon. The model should allow for the prediction of the surface area as well as the yield.

4.2 Model Assumptions

Physically, as illustrated schematically in Figure 4.1, the reactions that are taking place during activation can be described as:

- 1) Oxidation of the whole surface;
- 2) Faster oxidation of some parts of the char (inside the pores)
 - a. In the vertical direction (increases pore depth)
 - b. In the horizontal direction (increases pore diameter).

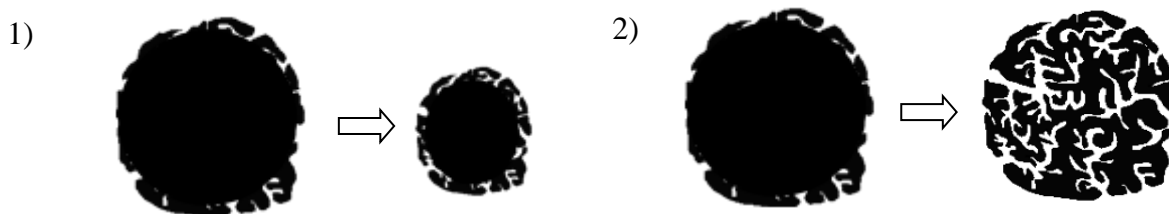


Figure 4.1- Reactions occurring within a char particle during activation

The proposed model is based on the following assumptions:

- No external mass transfer limitation: this is a reasonable assumption based on the results shown in Figure 3.2 where the impact of the flowrate is minimal, thus proving there is no external mass transfer limitation;
- Straight pores (cylindrical shape). This is a very common approximation validated in the literature by Bathia and Permuter (1981) and Feng (2003);
- Shrinking rate negligible with respect to the pore opening rate. In order for the activation to work, the external area of the particles must decrease much more slowly than the volume of the pores increases. Figure 4.2 shows how the particle size distribution evolves during activation: the volume-averaged particle diameter does not change significantly after activation, because most of the particle size reduction happens during pyrolysis. The particle shrinking rate is, thus, negligible and the average particle radius R_{p0} (see Appendix A to Chapter 4 for the selection of the appropriate diameter) is 297.5 μm ;
- Moreover, since in the case of activated carbons the results are usually reported in terms of yield rather than conversion, the model will have the yield as a parameter.

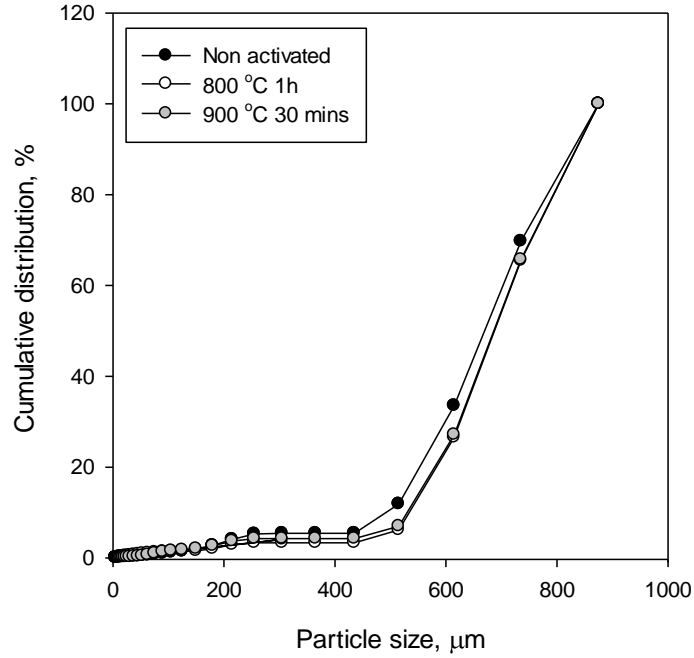


Figure 4.2- Particle size distribution for activated and non-activated samples of olive residue

4.3 Materials and Methods

The model was tested for activation experiments starting from the same pyrolysis conditions (500 °C, 95 °C/min heating rate), using the experimental results reported in Chapter 3 for olive residue activated carbons.

4.4 Model Development and Validation

Based on the assumption described earlier, the model development is based on the following considerations:

- The particle radius R_{p0} is constant with time (no particle shrinking) and equal to 297.5 μm;
- The pore diameter d increases with time (pore enlargement);
- The pore depth y increases with time (pore deepening).

Thus, the reactions can be described as:

- Pore enlargement:

$$\frac{d(d)}{dt} = k_1 p_a$$

(4.8)

However, in order for the surface area to increase, d_0 must increase much more slowly than y increases; otherwise, the enlargement of the pores would result in a collapse of pore walls and a decrease in the number of pores which would, in turn, cause a decrease in the surface area.

A proof of this can be provided by the results illustrated in Figure 4.3, previously shown in Chapter 3: the increase in the microporosity is almost constant with the increase in total surface area, until the activation conditions become more severe. Thus, the creation of new surface area can be attributed to the opening of new pores in the microporous range that were previously plugged, and not by the enlargement of pre-existing pores. Valente Nabais (2011) also observed a similar behavior in the production of activated carbons from almond shells, namely an increase in the mesopore/micropore ratio at higher conversion, leading to a subsequent collapse in the surface area.

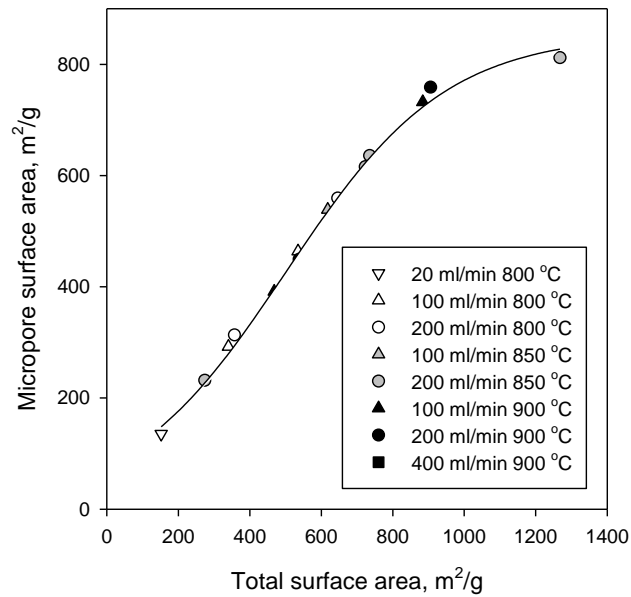


Figure 4.3- Evolution of micropore and total surface area during activation of olive residue activated carbon

This can also be proved by the evolution of the average pore diameter with time observed with the activation of olive residue char, performed in this study (Figure 4.4), obtained with the t-plot method as described in Paragraph 2.5.3. This result is supported by the findings of the study of Feng (2003) on the variation of the pore structure during coal chars gasification. Their observation is that all the pores participate in the gasification reaction equally except for very small micropores ($<10 \text{ \AA}$) and, thus, the increase in surface area and pore volume is distributed amongst all pore diameters until the final stages of the reaction (not considered in this study).

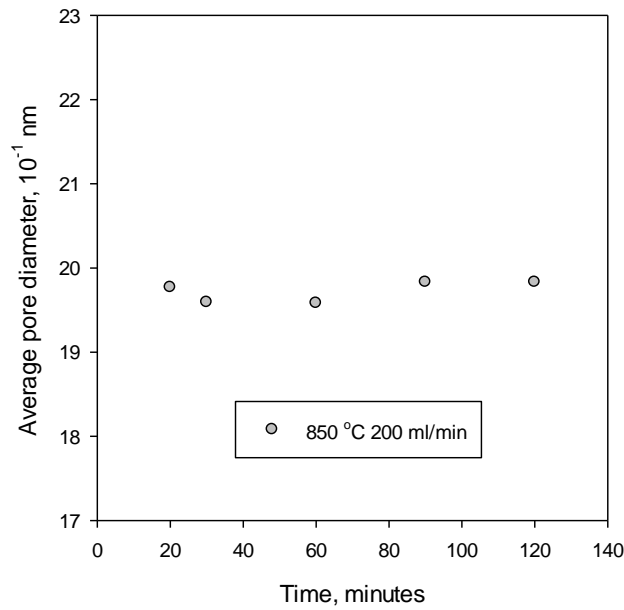


Figure 4.4- Evolution of average pore diameter with activation time for an activation temperature of 850 °C and 200 ml/min CO₂ flowrate

Thus, pore enlargement can be neglected and $k_I=0$.

- Pore deepening:

$$\frac{dy}{dt} = k_2 p_a$$

(4.9)

Thus, considering that the initial pores have negligible depth,

$$y = k_2 p_a t$$

(4.10)

Physically, the area of the pores in one particle of activated char can be described as:

$$A = \pi \int_{i=1}^{i=n_p} d_i y_i \quad (4.11)$$

If we assume that all the pores have the same diameter, equivalent to the average pore diameter, and the same depth, then Equation 4.11 becomes:

$$A = n_p \pi d_0 y \quad (4.12)$$

Combining Equations 4.10 and 4.12, the expression for A becomes:

$$A = \pi d_0 n_p k_2 p_a t \quad (4.13)$$

Also, it has been proven by micro-GC analyses that the molar concentration of CO_2 during activation is approximately constant, as previously discussed in Chapter 3, since the reaction is carried out with excess of CO_2 . Thus, the term $(k_2 p_a)$ can be replaced by the constant term k . Therefore, the equation that describes the formation of internal area can be rewritten as:

$$A = \pi n_p d_0 k t \quad (4.14)$$

The creation of the pore volume can be written with an expression equivalent to the one previously used for the area:

$$V_{pores} = \frac{\pi}{4} \int_{i=0}^{i=n} d_i^2 y_i \quad (4.15)$$

Using the same assumption that all the pores have the same diameter, equivalent to the average pore diameter and the fact that the average pore diameter does not change significantly with time, we can rewrite Equation 4.15 as:

$$V_{pores} = n_p \frac{\pi}{4} d_0^2 y = n_p \frac{\pi}{4} d_0^2 k t \quad (4.16)$$

Now, if one assumes:

- Negligible change in density between the different parts of char (the one that fills up the pores and thus reacts during activation and the one that is located on the outer surface of the particle);
- Negligible pore volume for the initial char;
- Negligible area at bottom of pore compared with side wall;

the only part of material that disappears is the result of the pore clearing, thus replacing material that was originally “filling up” the whole particle with voids and can be expressed in terms of volume:

$$V_c = V_{c0} - V_{pores} = V_{c0} - n_p \frac{\pi}{4} d_0^2 y = V_{c0} - n_p \frac{\pi}{4} d_0^2 kt \quad (4.17)$$

where V_c is the volume of one particle of activated char and V_{c0} is the volume of one particle of initial char.

However, the yield is described as:

$$\begin{aligned} Y &= \frac{\text{mass activated char}}{\text{mass of biomass}} = \frac{\text{mass activated char}}{\text{mass non activated char}} * \frac{\text{mass non activated char}}{\text{mass of biomass}} \\ &= \frac{m_c}{m_{c0}} Y_0 = \frac{V_c \rho_c}{V_{c0} \rho_{c0}} Y_0 \end{aligned} \quad (4.18)$$

where m_c is the mass of activated carbon and m_{c0} is the mass of original char.

Using the assumption of negligible change in density between the different parts of the char:

$$\frac{m_c}{m_{c0}} = \frac{V_c}{V_{c0}} = \frac{V_{c0} - \frac{\pi}{4} n_p d_0^2 kt}{V_{c0}} \quad (4.19)$$

and, thus, changes in the yield can be expressed as:

$$Y = Y_0 \left(\frac{V_{c0} - V_{pores}}{V_{c0}} \right) = \left(\frac{\frac{4}{3} \pi R_{p0}^3 - n_p \frac{\pi}{4} d_0^2 k t}{\frac{4}{3} \pi R_{p0}^3} \right) Y_0 \quad (4.20)$$

The full derivation of the expression is reported in Appendix B to the chapter.
Equation 4.20 can also be re-written as:

$$Y = Y_0 - Y_0 \left(\frac{3n_p}{16R_{p0}^3} d_0^2 k \right) t = Y_0 - k_y t \quad (4.21)$$

This relationship is analogous in its form to Equation 3.1, which was derived empirically from the experimental data. Thus, the model has already been validated and a new expression for k_y can be written:

$$k_y = \left(\frac{3d_0^2 Y_0}{16R_{p0}^3} \right) n_p k \quad (4.22)$$

Given that the value of k_y is known as a function of temperature from Chapter 3, the value of $n_p k$ can be obtained, where n_p is constant with activation conditions, while k changes with the activation temperature.

$Y_0 = \text{constant} = 29\%$ (from experimental values obtained in Chapter 3)

$d_0 = \text{constant (average)} = 1.9 \text{ nm}$ (see Figure 4.4)

R_{p0} (volume mean radius) = constant = 297.5 μm (See Figure 4.2)

The value of $n_p k$ is then calculated from Equations 4.22 and the results for the different temperatures are listed in Table 4.1.

Table 4.1- Calculated value of $n_p k$

T, °C	800	850	900
$k_y, 10^{-3} \text{ min}^{-1}$	1.3	1.6	2.3
$n_p k, 10^5 \text{ m/min}$	1.8	2.1	3.2

Using the Arrhenius equation we obtain:

$$n_p k = n_p k_0 e^{\left(\frac{-E_a}{RT}\right)} \quad (4.23)$$

And can then calculate the value of $n_p k_0$ and E_a (as reported in Table 4.2) from Equation 4.24

$$\ln(n_p k) = \ln(n_p k_0) - \frac{E_a}{RT} \quad (4.24)$$

Table 4.2- Determination of $n_p k_0$ and E_a

$k_{y0}, \text{ min}^{-1}$	$n_p k_0, \text{ m}$	$E_a, \text{ J/mol}$
121	$1.6 \cdot 10^8$	61207

It can now be observed that A , the surface area in one particle, can be related to a , the surface area per gram of activated carbon. In fact,

$$a = A \frac{\text{number of particles}}{\mathcal{G}_{\text{activated carbon}}} = A \frac{\text{number of particles}}{\mathcal{G}_{\text{non-activated carbon}}} \frac{\mathcal{G}_{\text{non-activated carbon}}}{\mathcal{G}_{\text{activated carbon}}} \quad (4.25)$$

Given the fact that the model considers that the particle size does not change with time, it excludes particle fragmentation and, thus, the number of particles per gram of non-activated carbon is constant. Using the value of $n_p k$ previously obtained to calculate A for all the experimental conditions and comparing it with the real values of a , one can observe that the surface area can be successfully predicted by the model, as reported in Figure 4.5 a), and that the number of particles per gram of non-activated carbon is equal to $1.2 \cdot 10^4$. However, given that the reaction is stopped at a value of conversion such that the surface area does not collapse, one could assume that even the value of (grams of non-activated carbons/g activated carbons) is nearly constant in the range of operating conditions considered in this study. This would imply that

$$a \approx A * \text{constant} \approx A * C \quad (4.26)$$

and the expression for the surface area a can be written as:

$$a = C\pi n_p d_0 k t$$

(4.27)

Figure 4.5 b) shows the comparison between the experimental values of surface area and the values calculated using Equation 4.27 and $C=8.2 \cdot 10^3$. Although it is a rough approximation to assume that the ratio (grams of non-activated carbons/g activated carbons) is constant, this effect becomes significant only for the more severe experimental conditions presented in this study. Thus, for the rest of this study, the surface area has been evaluated using Equation 4.27.

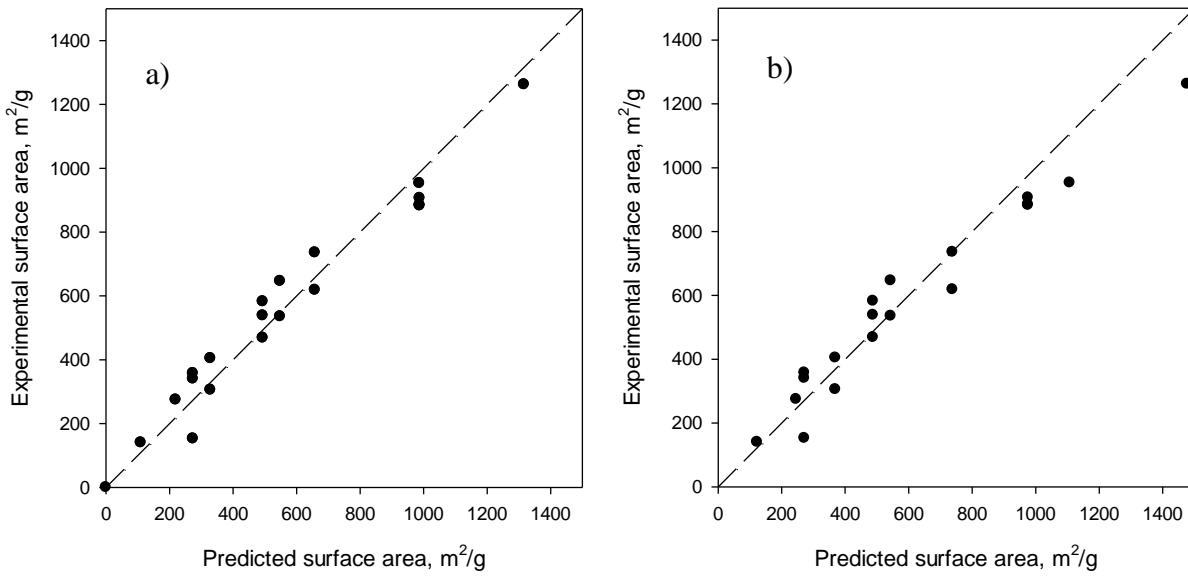


Figure 4.5- Comparison between experimental values of surface area and a) a calculated with Equation 4.25 b) a calculated with Equation 4.27

To obtain the relationship between yield and surface area, neglecting the value of A_0 , Equation 4.20 can be rewritten by combining Equations 4.14 and Equations 4.16 as:

$$Y = Y_0 \left(\frac{\frac{4}{3} R_{p0}^3 - A \cdot \frac{d_0}{4}}{\frac{4}{3} R_{p0}^3} \right)$$

(4.28)

or

$$A = \frac{16}{3d_0} R_{p0}^3 \left(1 - \frac{Y}{Y_0} \right)$$

(4.29)

Therefore, the reason for the linear relationship between the yield and the surface area, for a given set of pyrolysis conditions, is that the oxidation occurs only inside the pores and only in the vertical direction (no pore enlargement). This means that for each unit volume of material lost, a unit volume of pore length (y), and thus of surface area, is created.

4.5 Using the Model for the Optimization of the Activation Process

In order to determine which activation condition is the most attractive, it should be noted how maximizing the result of $Y*a$ means, in fact, maximizing the surface area produced with respect to the initial amount of processed biomass. This way, one can make sure that the process is being optimized without excessively compromising on the yield in order to obtain a high surface area. Thus, using Equation 4.27 and 4.21, neglecting as a first approximation the value of the initial surface area,

$$Y = Y_0 - Y_0 \frac{3n_p}{16R_{p0}^3} d_0^2 kt \quad (4.21)$$

$$a = C\pi n_p d_0 t \quad (4.27)$$

and given that the values of d_0 and R_0 are known not to be dependent on the activation conditions, one can state that:

$$Ya = f(t, T) \quad (4.30)$$

The function maximum can be found as:

$$0 = \frac{d(Ya)}{dt} = \frac{df(t, T)}{dt} \quad (4.31)$$

$$Ya = Y_0 \left(1 - \frac{3n_p k}{16R_{p0}^3} d_0^2 t \right) * C\pi d_0 (n_p k) t = C\pi Y_0 d_0 (n_p k) t - C \frac{3}{16} \frac{\pi Y_0 d_0^3}{R_{p0}^3} (n_p k)^2 t^2 \quad (4.32)$$

Using equation 4.23, one obtains:

$$\frac{d(Ya)}{dt} = \pi Y_0 d_0 \left(n_p k_0 e^{\left(\frac{-E_a}{RT} \right)} \right) - \frac{3 \pi Y_0 d_0^3}{8 R_{p0}^3} \left(n_p k_0 e^{\left(\frac{-E_a}{RT} \right)} \right)^2 t = 0 \quad (4.33)$$

This equation shows that there is an optimum activation time for each temperature. Solving the equation and plotting the optimum activation time t as a function of the activation temperature, the graph plotted in Figure 4.6 can be obtained.

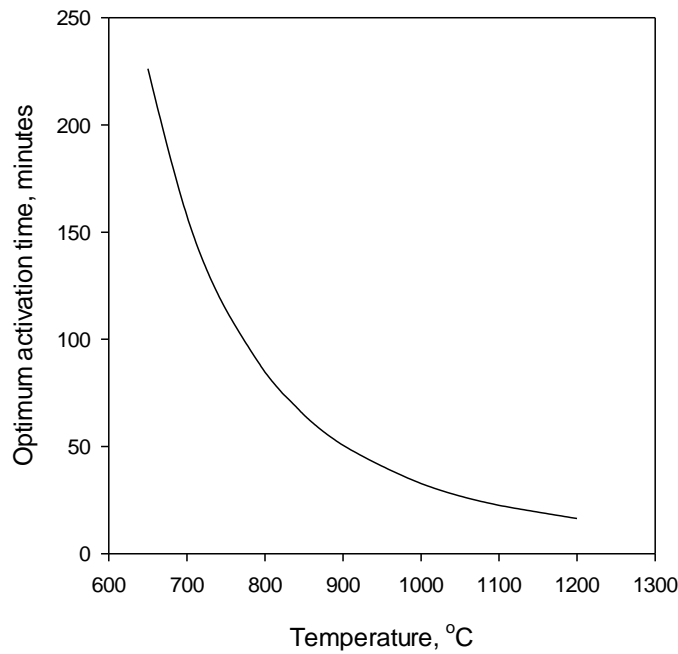


Figure 4.6- Variation of the optimum activation time with the activation temperature

Some of the experimental conditions used in Chapter 3 are extremely close to real solutions of Equation 4.33, such as 850 °C and 1h activation time, or 900 °C and 1h activation time. In fact, by plotting the Yield*Surface area graph as a function of the yield, as reported in Figure 4.7, the maximum in the value of Yield*Surface area is located between the two mentioned operating conditions. As a result, for the following chapter, where the optimum conditions for activation are fixed, the selected operating conditions are 850 °C, 1h activation time and 200 ml/min flow of CO₂ (to ensure that the partial pressure of CO₂ is high enough for the model to apply).

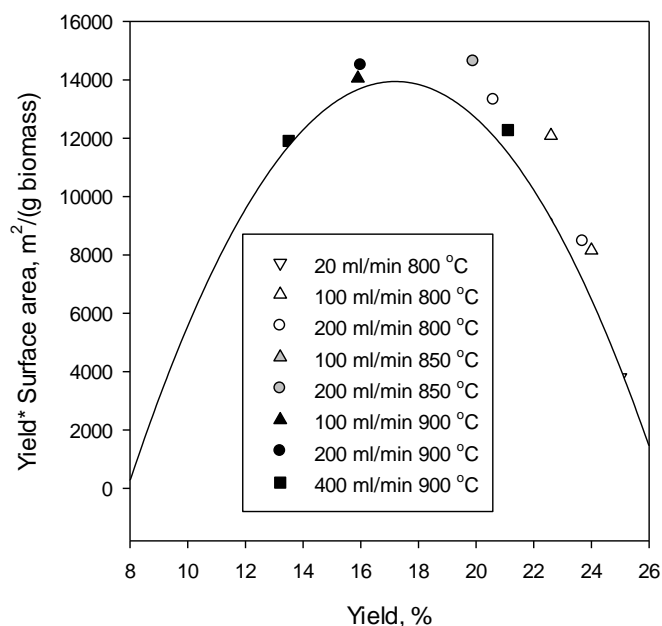


Figure 4.7- Selection of experimental conditions to maximize Yield*Surface area

4.6 Conclusions

A simple model was developed to predict the evolution with time of the yield and the surface area during the production of activated carbons in a jigged bed reactor. The model could explain the experimental findings described in Chapter 3 and predict the surface area, the yield and the trade-off between the two. The model is limited to the range of conditions that are of interest for practical uses of the carbons, since it is limited to conditions for which there is no collapse of the surface area. The model was successfully applied to the optimization of the operating conditions for activation.

Appendix to Chapter 4

A. Which expression of the particle size we use?

$$Y = \frac{1}{N} \sum_{i=0}^N x_i Y_i \quad (4.34)$$

$$A = \frac{1}{N} \sum_{i=0}^N x_i A_i \quad (4.35)$$

$$A = \left(1 - \frac{Y}{Y_0}\right) \frac{16R_{p0}^3}{3d_0} = \frac{1}{N} \sum_{i=0}^N x_i A_i = \frac{1}{N} \left(1 - \frac{Y}{Y_0}\right) \frac{16}{3d_0} \sum_{i=0}^N x_i R_{p0i}^3 \quad (4.36)$$

Which is the expression of the volume mean diameter

B.

By assuming:

- No changes in density between the different parts of char
- No particle size reduction (same as before, proved)
- Negligible pore volume for the initial char (proved)
- Negligible area at bottom of pore compared with side wall

given the fact that the particle size does not change, and neither does average the pore diameter, all the changes in the mass of the particle are attributable to changes in the volume of the pores and, in particular, to its depth.

Using Equation 4.18, we can write, analogously to the case of surface area formation, the expression for pore volume creation as:

$$r_v = \frac{dV}{dt} = n_p \frac{\pi}{4} d_0^2 \frac{dy}{dt} = n_p \frac{\pi}{4} d_0^2 k \quad (4.37)$$

and, thus,

$$V_c = V_{c0} - n_p \frac{\pi}{4} d_0^2 y = V_{c0} - n_p \frac{\pi}{4} d_0^2 kt \quad (4.38)$$

where V_c is the volume of the char particle at time t and V_{c0} is the volume of the non-activated char particle.

Now, using the fact that there is no difference in the density of different parts of char, we can express the yield as volume %:

$$\begin{aligned} Yield &= \frac{\text{mass activated char}}{\text{mass of biomass}} = \frac{\text{mass activated char}}{\text{mass non activated char}} * \frac{\text{mass non activated char}}{\text{mass of biomass}} \\ &= \frac{m_c}{m_{c0}} Y_o = \frac{V_c \rho_c}{V_{c0} \rho_{c0}} Y_o \end{aligned} \quad (4.39)$$

V_{c0} is the char volume of the “full” char particle (due to the fact that the initial pore volume is negligible), when the pores are plugged, and can be expressed, by considering the particle as a sphere (See Figure 3. 12) as:

$$V_{c0} = \frac{4}{3} R_{p0}^3 \quad (4.40)$$

Thus,

$$Yield = Y_o \left(\frac{V_{c0} - V_{pores}}{V_{c0}} \right) \quad (4.41)$$

C. Comparison with other models

In order to prove the goodness of the fit obtained with the proposed model, the results are compared with those obtained with the three models previously cited: the volume reaction model (VRM), shrinking core model (SCM) and random pore volume (RPM).

In order to provide an estimate for ψ , the simplified formula proposed by Feroso (2008) is used:

$$\psi = \frac{2}{2 \ln(1 - x_{max}) + 1} = 1.5 \quad (4.42)$$

Which is in the range of values commonly encountered for char (~0.5-50, Feroso (2008, 2011)). The models parameters are estimated by linearization of the Equations shown in the introduction after separation of variables and integration:

$$-\ln(1 - x) = k_{VRM}t \quad (4.43)$$

$$3 \left(1 - (1 - x)^{\frac{1}{3}} \right) = k_{SCM}t \quad (4.44)$$

$$\left(\frac{2}{\psi} \right) \left(\sqrt{(1 - \psi \ln(10x))} - 1 \right) = k_{RPM}t \quad (4.45)$$

Assuming that the concentration of the gasifying agent remains constant through the reaction (and thus the partial pressure), k becomes a function of temperature only and can be expressed by the Arrhenius equation (Feroso, 2008).

$$k = k_0 e^{\left(-\frac{E_a}{RT} \right)} \quad (4.46)$$

Thus, the model parameters reported in Table 4.3 are calculated.

Table 4.3- Models parameters

	k_0, min^{-1}	$E_a, \text{J/mol}$
VRM	46.5	84412
SCM	0.25	39749
RPM	221.4	99502

After the determination of the conversion profile, the results are converted into yield in order to be compared with the results obtained with the model proposed in this chapter:

$$x = 1 - \frac{m}{m_0} = 1 - \frac{m}{m_{biomass}} \frac{m_{biomass}}{m_0} = 1 - \frac{Y}{Y_0} \quad (4.47)$$

The comparison between values predicted with the different models and the experimental values is shown in Figure 4.8, while Table 4.4 shows the values of the SSE (sum of squared errors) and the MPE (mean percent error) for the different models.

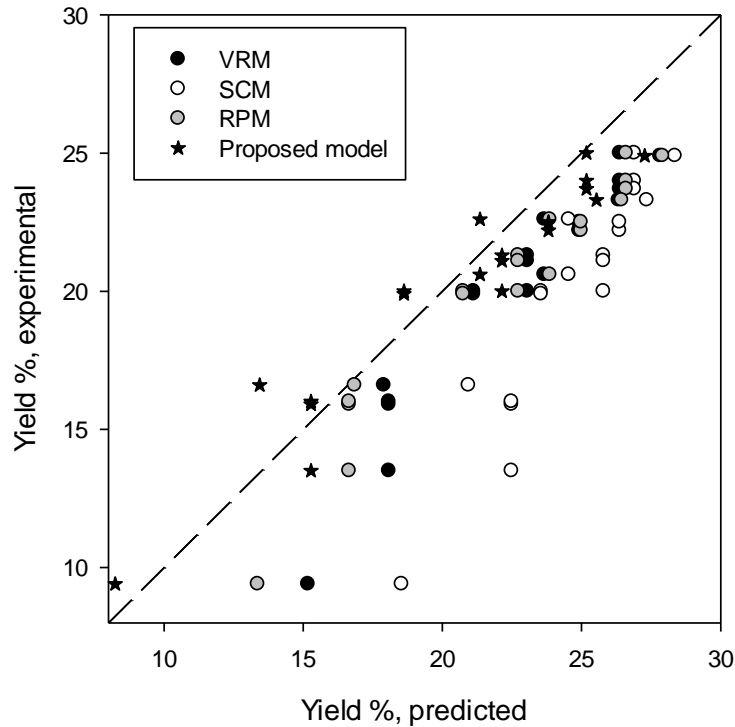


Figure 4.8- Comparison of the predicted vs. experimental yields for the different models

Table 4.4- Values of SSE and MPE for the different models

	VRM	SCM	RPM	Proposed model
SSE	134	394	103	59
MPE	14%	27%	11%	7%

The model presented in this chapter shows the best fit with the experimental results, followed by the RPM and the VRM. The SCM has the worse fit with the experimental results, as expected: in fact, this model predicts a monotonically decrease in the reaction rate as the reaction proceeds, in contradiction with what observed in the results of this study.

Chapter 5

5. Influence of Pyrolysis Conditions on the Production of Activated Carbons in a Jiggled Bed Reactor

5.1 Introduction

With the jiggled bed reactor, it is possible to study both fast and slow pyrolysis conditions in the same reactor. Consequently, a wider range of heating rates can be studied to determine their impact on the production of activated carbons from biomass.

The biorefinery concept suggests that the focus should not be on a single product, such as activated carbons. Therefore, the biomass conversion is conducted in two steps. The first conversion stage is pyrolysis, conducted at temperatures and heating rates that provide a high yield of valuable liquid bio-oil, which can be subsequently used for chemicals or liquid fuels (Bridgwater, 2012). In the second step, the pyrolytic char co-product is activated to produce valuable activated carbons. In addition, the permanent gases produced by the pyrolysis process are combusted to generate energy as well as provide an activation agent. Although a great number of studies have shown the impact of the activation parameters on the production of activated carbons from biomass (Jung, 2014; Lua, 2000; Valente Nabais, 2011; Yang, 2003; Yang, 2010), the influence of the pyrolysis conditions on the final activated carbons properties have rarely been investigated, as previously mentioned in Chapter 2.

The objectives of the work described in this chapter include:

- Determination of the impact of pyrolysis heating rate and temperature on the final properties of pyrolysis char and, consequently, on the produced activated carbons;
- Determination of whether the surface area vs. yield trade-off still exists;
- Determination of the impact of the heating rate and temperature during pyrolysis on the activation kinetics;
- Verification of whether the model previously developed could be adapted to predict the results obtained under different pyrolysis conditions.

5.2 Materials and Methods

The material used in this study was olive residue. The operating conditions for pyrolysis were the ones described in Paragraph 2.3.1 and 2.3.2. The activation conditions were the most attractive as determined during the work described in Chapter 4: 850 °C, 1h, 200 ml/min of CO₂ flow.

5.3 Results and Discussion

5.3.1 Impact of heating rate and pyrolysis temperature on char yield prior to activation

The production of activated carbons is carried out into two steps: carbonization and activation. While most studies focus on the impact of the activation step, it is important to consider the effect of the pyrolysis process (first step) on the final properties of the activated carbons, which will most likely depend on its influence on the pyrolysis char. The effects of pyrolysis temperature and heating rate on the yield of pyrolytic char are shown in Figure 5.1.

The yield of char decreases with increasing the pyrolysis temperature for a fixed heating rate. For a fixed temperature, the yield increases with decreasing heating rate. The heating rate appears to have a stronger effect on the yield than the pyrolysis temperature, as for a heating rate of 95 °C/min, an increase in temperature from 475 to 550 °C only causes a decrease in yield from 32.8% to 28.7%, while for a fixed temperature of 500 °C, the increase in yield between fast pyrolysis and 47.5 °C/min heating rate is from 26.6% to 32.5%.

The curves were fitted using the best global fit for all the families of points, thus showing the limited impact of the pyrolysis temperature (represented for example in Figure 5.1 a by the slope of the curves) when compared to the heating rate (represented by the intercept of the linear fit in the same curve).

A higher heating rate during pyrolysis causes a higher reaction rate and results in more volatile matter which is released from the biomass during pyrolysis, resulting in a lower char yield. In the case of slow pyrolysis, secondary char formation is increased by the longer residence time of vapors and solid in the reactor, thus increasing char yield (Crombie, 2015). Increasing the pyrolysis temperature leads to an increased conversion of volatile matter into vapors and gaseous products. The release of volatile matter is most pronounced between 350 and 400 °C, in agreement with the

thermo-gravimetric profile of the feedstock reported in Chapter 3 (Figure 3.1 b)), thus explaining the limited impact of the pyrolysis temperature as opposed to the heating rate for the higher pyrolysis temperatures of this study, which are selected to give a high yield of bio-oil co-product.

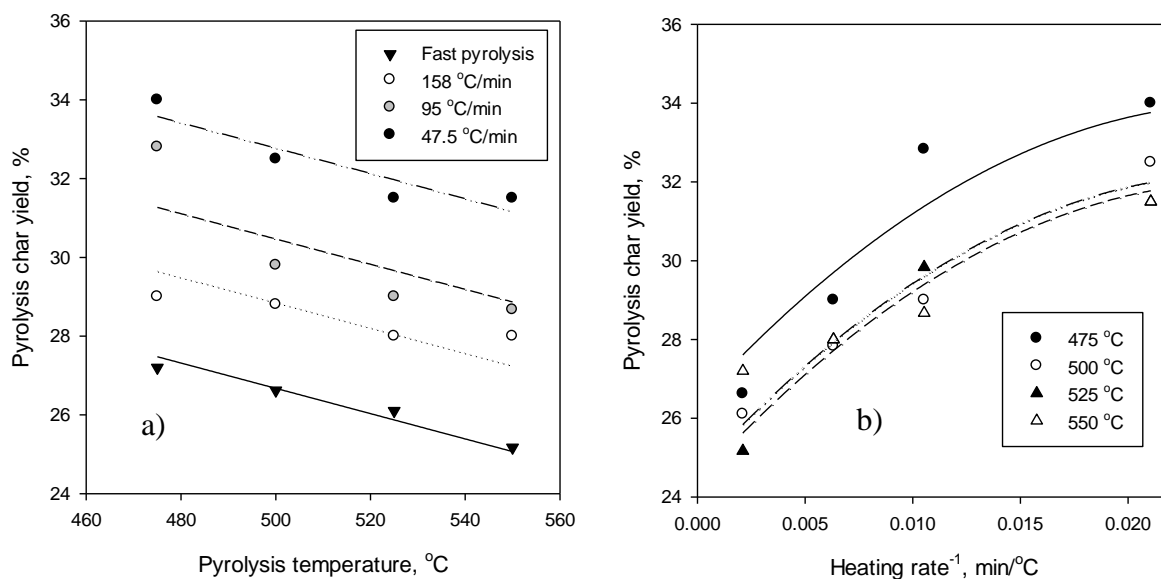


Figure 5.1- Effect of pyrolysis temperature and heating time on the char yield (no activation) in the JBR

5.3.2 Impact of heating rate and pyrolysis temperature on activated carbons properties

The effects of the pyrolysis temperature on the activated char yield and surface area are shown in Figure 5.2 for different heating rates. The impact of the temperature on the activated char yield is similar to the one previously observed for the char yield prior to activation, since the yield at 95 °C/min heating rate decreases from 20.7% to 17.5% with a pyrolysis temperature increase from 475 to 550 °C. The surface area increases from 547 to 711 m²/g under the same conditions. The increase in the surface area can be explained by the fact that a higher pyrolysis temperature will allow a larger amount of volatiles to escape the particle, thus removing more of the heavier compounds and favoring the formation of more internal pores within the char structure. These results are also supported by the findings of Widayatno (2014) and Paethanom (2012).

The curves were fitted using the best global fit for all the families of points, thus showing the limited impact of the pyrolysis temperature (represented by the slope of the curves) when compared to the heating rate (represented by the intercept of the linear fit).

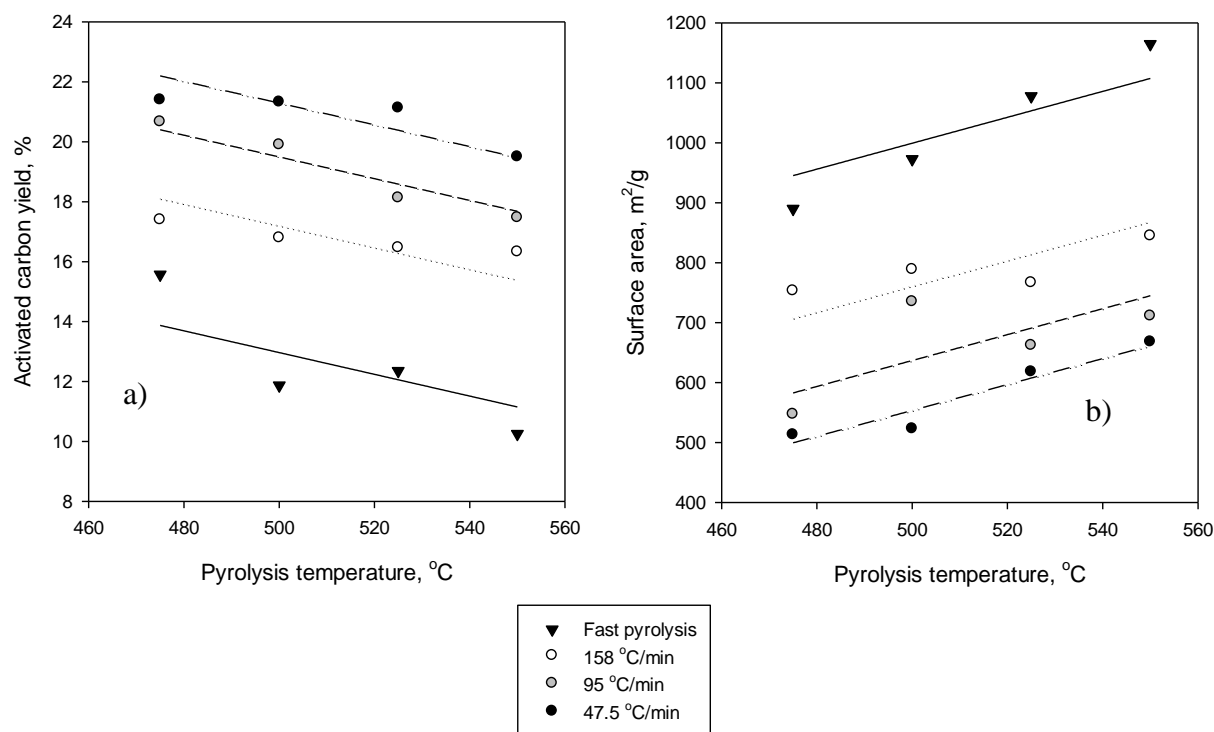


Figure 5.2- Effect of pyrolysis temperature on a) the activated char yield and b) surface area

As previously observed for the char yield, the parameter that seems to affect more significantly both the yield and surface area of the activated carbons is the heating rate (Figure 5.3). During fast pyrolysis, the temperature inside the sample increases to the final temperature at an extremely high speed. This leads to an extremely fast devolatilization, which results in a more developed internal porosity available to further development during activation. On the other hand, during slow pyrolysis, the devolatilization is slower and does not destroy the particle structure as much. Lua (2004), who studied the impact of the heating rate on the production of activated carbons from pistachio-nut shells, observed the same behavior as the heating rate during pyrolysis was increased, although all the experimental conditions were varied only within the slow pyrolysis range.

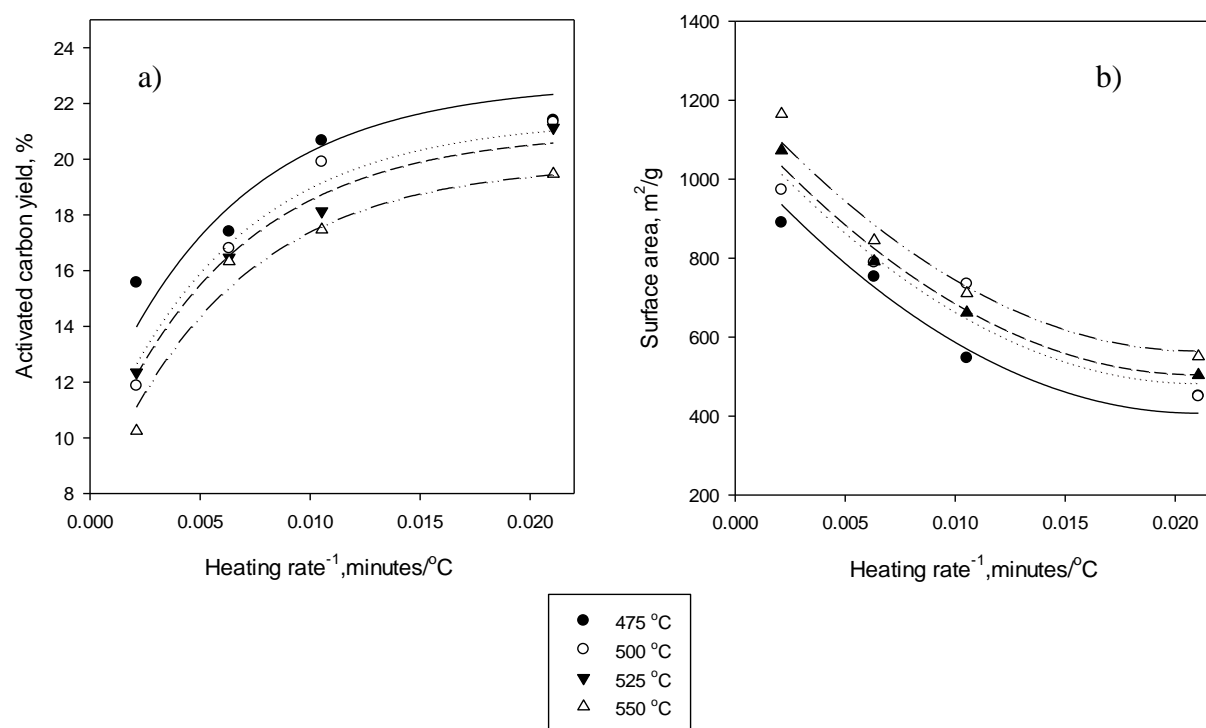


Figure 5.3- Effect of heating rate on a) the activated char yield and b) surface area

In Chapter 3, it was observed that a linear trade-off exists between the yield and the surface area for samples produced under the same pyrolysis conditions, by varying the activation parameters such as temperature, flowrate and activation time. Figure 5.4 shows that this same relationship exists for samples produced with the same activation parameters, starting from char produced under different pyrolysis conditions.

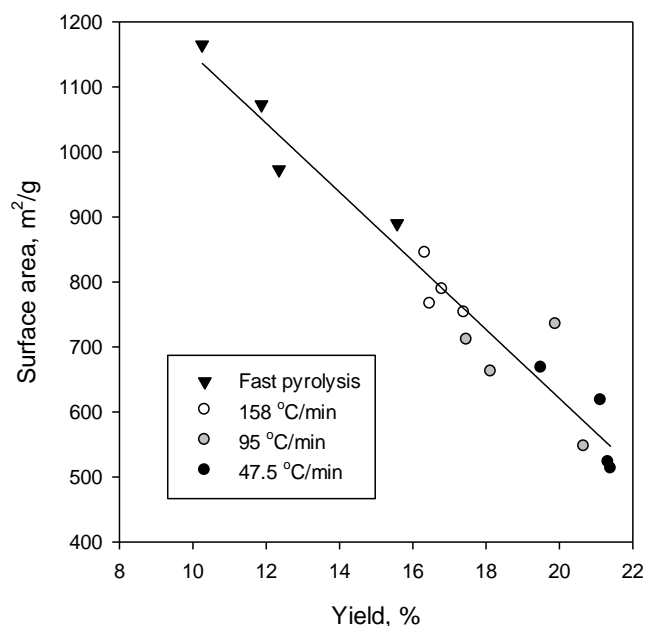


Figure 5.4- Yield vs. surface area trade-off for activated carbon produced from char obtained with different heating rates during the pyrolysis step

Figure 5.5 a) further corroborates these findings by showing how all the results obtained in Chapter 3, by varying the activation parameters, and those obtained in this chapter, by changing the pyrolysis step conditions, overlap to give the same trade-off. Figure 5.5 b) shows instead samples obtained with the same heating rate (95 °C/minute) but different pyrolysis temperatures (open symbols) and different activation conditions (black symbols), showing how the pyrolysis temperature has a marginal role when compared to the one of the heating rate that is clearly visible in Figures 5.3 and 5.4.

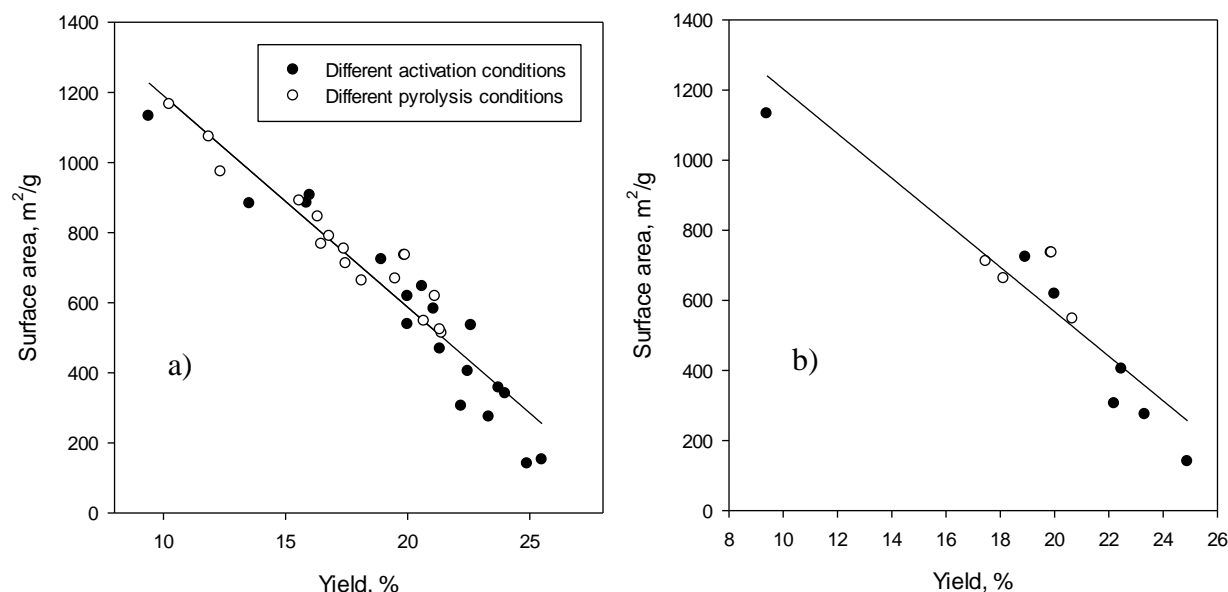


Figure 5.5- Surface area vs. yield for different activation (black symbols) and pyrolysis conditions (open symbols) for a) all the experimental conditions from Chapter 3 and 5 b) for samples produced with a heating rate of 95 °C/min

Previous studies on the reactivity of char during gasification reported a higher apparent reactivity of carbons produced from fast pyrolysis as opposed to slow pyrolysis (Cetin, 2005). However, little or no attention was paid in those studies to the formation of the surface area, since their purpose was to examine the fuel properties of the chars. What is suggested by our results is that not only the reactivity in terms of mass loss is higher, but that the final product has equivalent properties also in terms of surface area, and, more importantly, in the porous structure, shown in Figure 5.6 and 5.7.

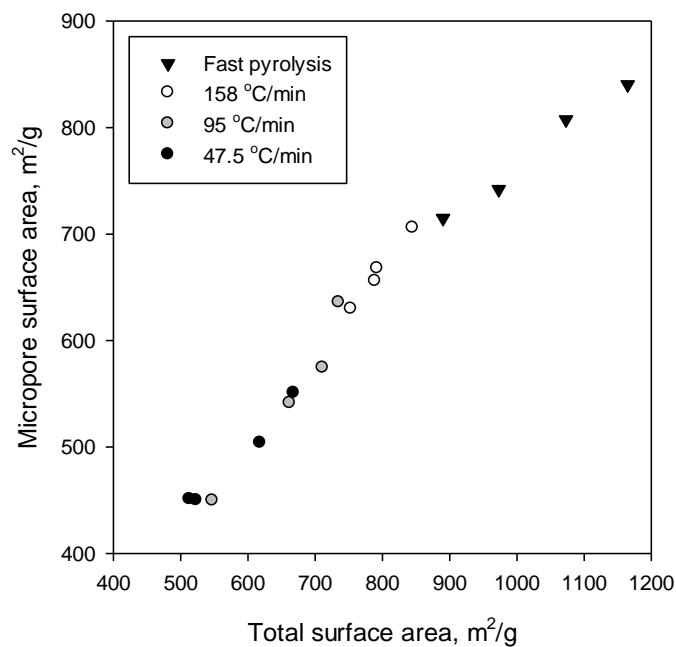


Figure 5.6- Micropore surface area as a function of total surface area

Figure 5.7 shows how indeed the development of the microporous structure follows the same trend independently on whether the carbon is produced starting from different activation or pyrolysis conditions.

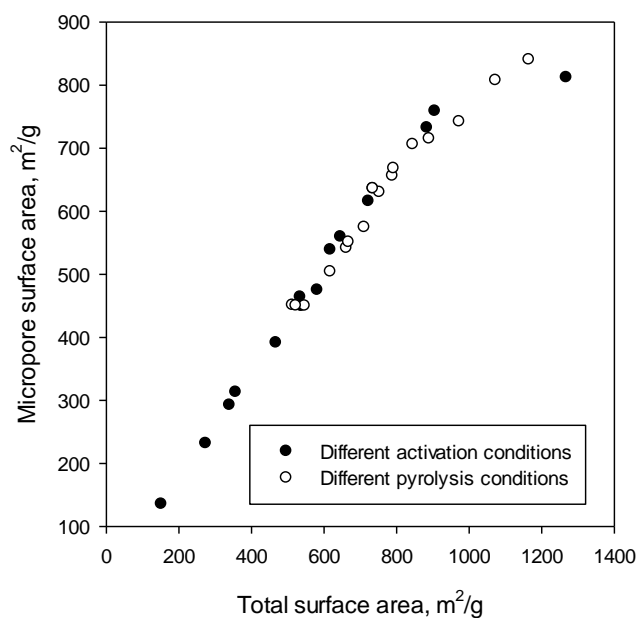


Figure 5.7- Variation of the relationship between micropore surface area and total surface area for different activation conditions and different pyrolysis conditions

Therefore, it is interesting to apply the physical model developed in Chapter 4 to these results to better understand the causes of this phenomenon.

5.3.3 Impact of heating rate and pyrolysis temperature on the activation kinetics: application of the kinetic and physical models

From Chapter 3, we remember that the activation can be described as a zero order reaction, where the yield and surface area kinetics are:

$$Y = Y_0 - k_y t \quad (3.1)$$

$$a = a_0 + k_s t \quad (3.3)$$

or from Chapter 4

$$Y = Y_0 - Y_0 \frac{3n_p}{16R_{p0}^3} d_0^2 k t \quad (4.21)$$

and

$$a = a_0 + C\pi n_p d_0 k t \quad (4.27)$$

The model is potentially still valid in the same form for the results presented in this chapter. However, in order to extend the model to explain the results obtained under different pyrolysis conditions, the impact of the heating rate and temperature during pyrolysis on the model inputs has to be investigated, since it was originally developed for materials produced under the same pyrolysis conditions (thus, a_0 , R_{p0} , n_{p0} , d_0 and Y_0 were the same for all activation conditions).

- Y_0 , the yield of pyrolytic char, varies with the heating rate and pyrolysis temperature, as previously shown in Figure 5.1;
- a_0 , the initial surface area of the samples is shown to not be significantly affected by the pyrolysis temperature, but rather by the heating rate: as shown in Table 5.1, chars produced from fast pyrolysis have a value of surface area almost one order of magnitude larger than the ones produced from slow pyrolysis. This is a result that is well supported from similar findings

in the literature (Zhang, 2013) and, as previously mentioned, is due to the extremely high heating rate that the particles undergo during pyrolysis, causing the vapors to escape from different channels than the preferential ones attributable to the biomass structure in the case of slow pyrolysis and, as a consequence, cause more damage to the structure.

Table 5.1- Initial surface area for different activation conditions

	$a_0, \text{m}^2/\text{g}$
Fast pyrolysis	91 ± 2.3
158 °C/min	10.9 ± 3.0
95 °C/min	6.2 ± 0.6
47.5 °C/min	5.4 ± 0.7

In particular, the initial surface area of the sample shows an exponential increase with increasing heating rates, as shown in Figure 5.8.

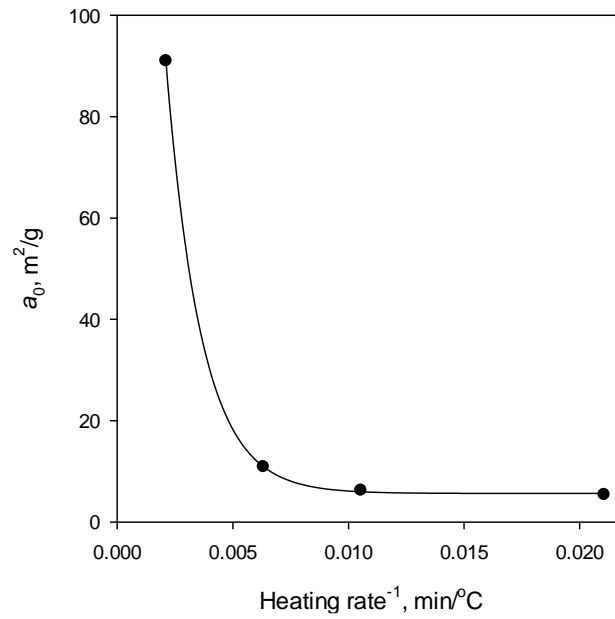


Figure 5.8- Variation of the initial surface area a_0 with the reciprocal of the heating rate during pyrolysis

The results can be described as:

$$a_0 = 91.9 * e^{\left(-\frac{5.3}{\text{Heating rate}}\right)}$$

(5.1)

- d_0 : Figure 5.9 shows the variation of the pore diameter d_0 with the pyrolysis conditions. No specific trend is observed, and the value can be considered nearly constant for all the conditions.

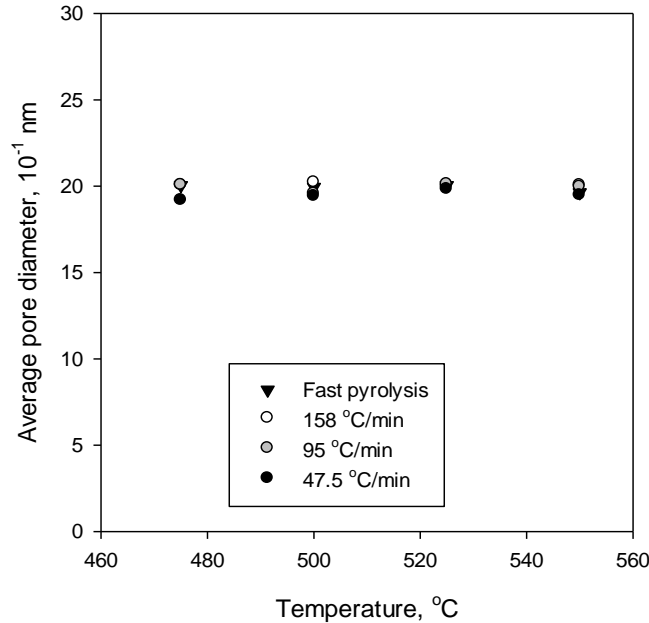


Figure 5.9- Average pore diameter as a function of pyrolysis temperature and heating rate

- R_{p0} : the particle radius does not change significantly during the activation process, as shown in Chapter 4. The non-activated carbon particles produced from fast pyrolysis have a smaller particle size than the ones produced with a heating rate of 95 °C/min, while no significant difference was observed between 95 and 158 °C/min. Unexpectedly, the particles produced with a heating rate of 47.5 °C/min have intermediate values of particle size. This is possibly attributable to the fact that the samples corresponding to lowest heating rate are the ones with the longest residence time in the reactor and, thus, suffer the most from attrition phenomena that might lead to the formation of fines. Nevertheless, the differences between the real values are almost insignificant, as can be seen in Table 5.2, but the real values need to be used in the model.

Table 5.2 Particle radius for different pyrolysis conditions

	Radius, μm
Fast pyrolysis	282.5 ± 3
158-95 $^{\circ}\text{C}/\text{min}$	299 ± 5
47.5 $^{\circ}\text{C}/\text{min}$	292.5 ± 2

The values of k_y and k_s can thus be calculated and are shown in Figure 5.10 a) and b).

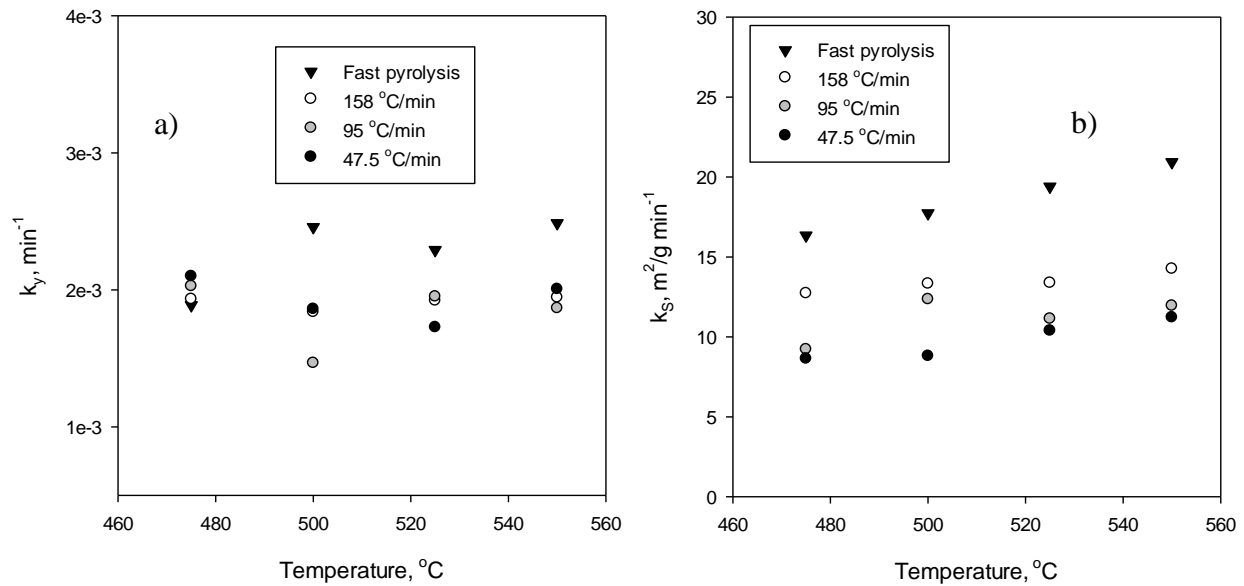


Figure 5.10- a) k_s and b) k_y as functions of temperature for different heating rates

Both k_y and k_s , the apparent kinetic parameters, increase with the pyrolysis heating rate. The only condition for which the pyrolysis temperature seems to have a significant impact is in the case of fast pyrolysis. It has been observed that, for higher heating rates, the peak temperature in biomass decomposition is shifted towards higher temperatures (Garcia-Perez, 2008). This has also been observed by Zhang (2013) in his comparative study between bio-chars produced under slow heating in a TGA and high heating rates in a wire mesh reactor. This can explain the slight influence of temperature in the case of fast pyrolysis, while it is almost irrelevant for the other conditions.

The fact that the rate of reaction is higher for samples produced with higher heating rates matches the results of the previously mentioned studies by Cetin (2004, 2005) as well as the one of Pottmaier (2013), which compared the reactivity during combustion of chars produced from slow pyrolysis and fast pyrolysis. Slow pyrolysis chars have more homogeneous characteristics than those from fast pyrolysis, which in this study is attributed to the fact that the latter evidently imposes significant changes in the physicochemical properties of the nascent chars, thus enhancing their reactivity.

Using the physical model previously developed, this result can be explained by calculating the value of n_pk , which is shown as a function of the reciprocal of the heating rate in Figure 5.11.

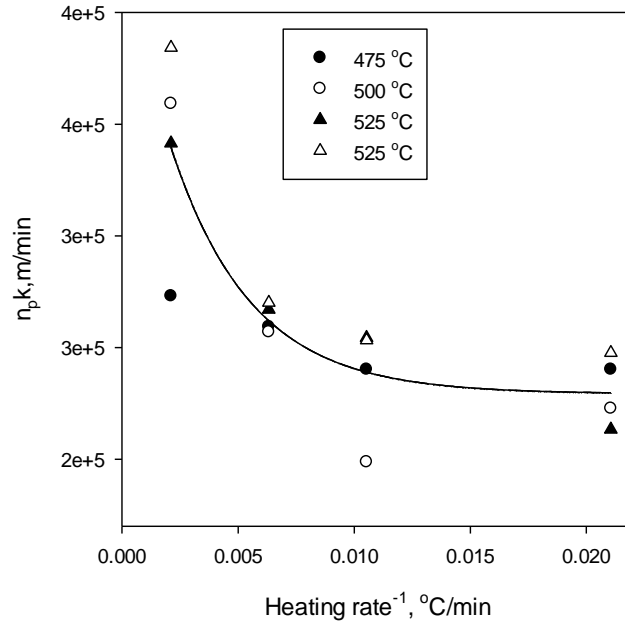


Figure 5.11- Values of n_pk as a function of the pyrolysis heating rate

Thus, the value of n_pk increases with the pyrolysis heating rate, neglecting the influence of pyrolysis temperature, according to:

$$n_pk = 2.2 * 10^5 + 2.0 * 10^5 * e^{\left(-\frac{288}{\text{Heating rate}}\right)} \quad (5.2)$$

Assuming that k is the intrinsic kinetic parameter and thus only dependent on the activation temperature (which is constant for all the samples in this study), the higher reactivity of the char

produced from fast pyrolysis is likely due to the higher number of pores formed during the pyrolysis reaction. This can also be observed from SEM pictures reported in Figure 5.14 in the Appendix. The release of volatiles from the biomass particle during fast pyrolysis has in fact been defined as a “bursting bubble” by Kruger (2011), which means that the vapors do not escape from the natural channels that are found in the original biomass, but more pores are created, which become available for further development during activation.

In order to investigate how well the model can predict the surface area vs. yield trade-off under these conditions, Equation 4.28 is re-arranged to become:

$$Y = Y_0 \left(\frac{\frac{4}{3} R_{p0}^3 + A_0 \frac{d_0}{4} - A \frac{d_0}{4}}{\frac{4}{3} R_{p0}^3} \right) \quad (5.3)$$

which translates into

$$A = \left(1 - \frac{Y}{Y_0} \right) \frac{\frac{4}{3} R_{p0}^3}{\frac{d_0}{4}} + A_0 \quad (5.4)$$

Figure 5.12 shows that the model still works very well at predicting both the yield (Figure 5.12 a) and the surface area (Figure 5.12 b), when the corrections to account for the initial conditions of the char after pyrolysis are applied.

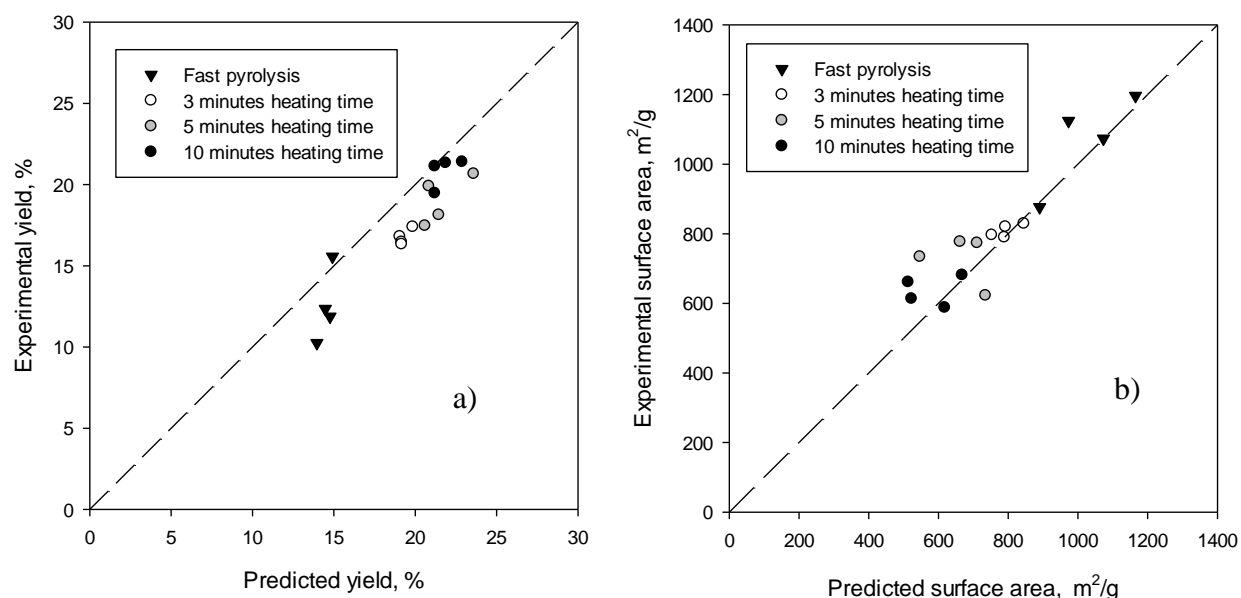


Figure 5.12- Predicted vs. experimental a) yield b) surface area for activated carbon produced from char obtained with different heating rates during the pyrolysis step

Considering a more general case, it could be of interest also to see how the model would behave in the case the characterization of the initial material for the different pyrolysis conditions is not available, and thus, the previously mentioned corrections cannot be made. The model would slightly overestimate some values, but, overall, still hold valid. In particular, the model would be worse at describing the results obtained with fast pyrolysis and lower heating rates. This can be due to the fact that these are the conditions that show the largest difference from the ones used to develop the model (for example in terms of negligible initial pore volume of the char in the case of fast pyrolysis conditions); moreover, in the case of fast pyrolysis, a more significant impact of the temperature was observed, which is not accounted for in the model. Nevertheless, this could be of significant importance in the case in which the number of experimental trials needs to be minimized to obtain preliminary information.

In Chapter 4, the activation conditions were optimized by looking at the values of yield*surface area. Plotting the result of yield*surface area obtained in this chapter as a function of the pyrolysis temperature and heating rate (Figure 5.13) shows that there is no significant difference in using slow or fast pyrolysis when both parameters are considered: we can produce less of a higher surface area sample or more of a lower surface area sample, which is in agreement with the previously discussed results. Moreover, it also indicates that the optimum activation conditions previously

identified in Chapter 4 are not too much dependent on the initial pyrolysis conditions, thus validating the results of this study even though the study of the optimization of activation parameters is carried out only for one set of pyrolysis conditions.

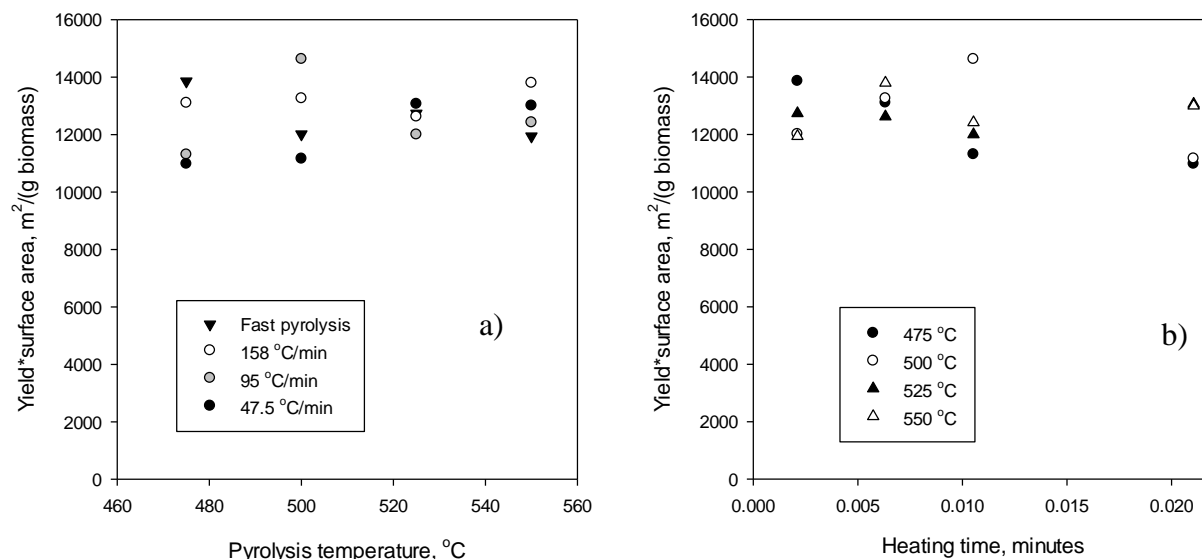


Figure 5.13- Yield*surface area as a function of a) heating time and b) pyrolysis temperature

5.4 Conclusions

The experimental results showed that the type of pyrolysis process has the most significant impact on the final product properties of the activated carbons produced under constant activation conditions, in terms of yield, BET surface area, micropore surface area and total pore volume. The kinetic and physical models derived in Chapter 3 and 4 were successfully applied to the results obtained under the new operating conditions and provided better insight onto the phenomena occurring during the process. A higher heating rate during pyrolysis makes the carbon precursor more reactive during activation due to the formation of a larger number of pores, which is a consequence of the extremely rapid evolution of volatiles from the particle during fast pyrolysis.

Appendix to Chapter 5

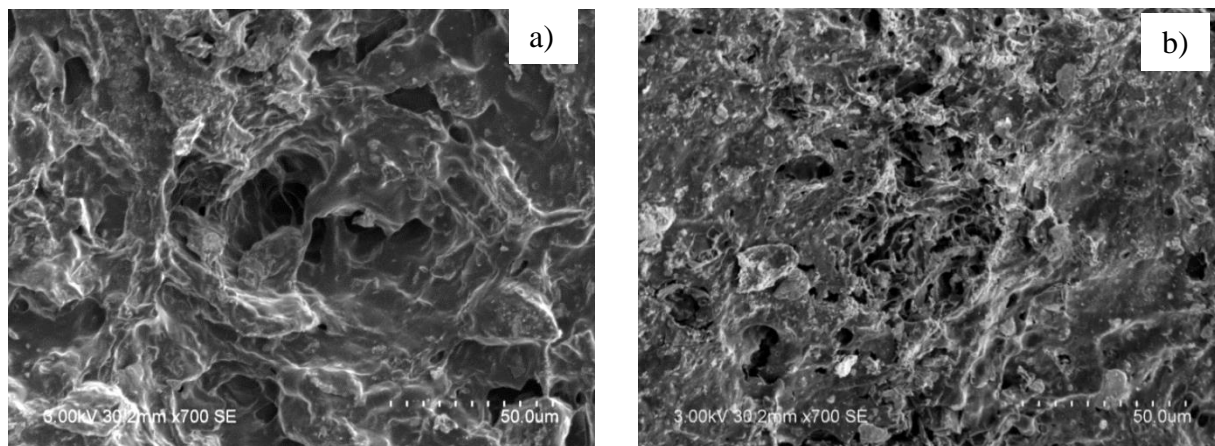


Figure 5.14- Detail of the surface of the char produced by a) slow pyrolysis and b) fast pyrolysis

SEM images confirm the larger number of pores for fast pyrolysis samples when compared to slow pyrolysis, due to the more rapid vapor evolution during the pyrolysis step that causes the initial char produced from fast pyrolysis to have a higher reactivity as compared to the slow pyrolysis one.

Chapter 6

6. Comparison of the Results Obtained in the JBR with a Pilot Scale Bubbling Bed Reactor and Impact of the Use of a Binder during the Production of Activated Carbons

6.1 Introduction

Previous chapters assumed that the JBR can be used to easily and conveniently study, at a laboratory scale, reactions that are normally carried out in fluidized bed reactors at a larger scale. The objective of this chapter is to validate this assumption by comparing results obtained with the JBR and a pilot scale bubbling bed reactor, such as the char yield and properties, as well as the yield and surface area of the produced activated carbons. The JBR is then used to determine whether granulation could solve the feeding difficulties encountered in fluidized bed pyrolyzers with cohesive materials such as Kraft lignin.

6.2 Materials and Methods

In this chapter, three feedstocks were used:

- Birch bark
- Kraft lignin
- Olive residue.

More information on these feedstocks can be found in section 2.1 of Chapter 2.

Samples of lignin and olive residue powders were granulated in a high shear granulator with the addition of 6% molasses as organic binder, to obtain particles in the 1-2 mm size range.

The pyrolysis was carried out using two reactors:

- The bubbling bed reactor described in section 2.4, operated at temperatures between 500 and 550 °C;

- The JBR, under batch conditions (with 95 °C/min heating rate, as described in section 2.3.1) and under fast pyrolysis conditions (as described in section 2.3.2), in the same temperature range as the bubbling bed.

All the activation experiments were carried out in the JBR, as described in section 2.3.1

6.3 Results and Discussion

6.3.1 Validation of JBR through comparison to bubbling bed with birch bark

Table 6.1 reports the char yields obtained in the JBR and in the bubbling bed for the pyrolysis of birch bark at 500 and 550 °C. Both units give yields that are very similar: the differences are less than reproducibility errors previously reported in Chapter 2.

Table 6.1- Comparison between char and activated char yield and surface area in the JBR and in the bubbling bed during birch bark fast pyrolysis

	Bubbling bed	JBR
Pyrolytic char yield, 500 °C	16%	17%
Pyrolytic char yield, 550 °C	7.5%	8%

Table 6.2 shows the elemental analysis of the carbons produced at 550 °C in the JBR and in the bubbling bed: the differences are within the reproducibility errors reported in Chapter 2.

Table 6.2- Elemental analysis of char produced from birch bark at 550 °C

	C	H	N	O
Bubbling bed	79%	2%	0.7%	15%
JBR	79%	3%	0.6%	16%

Table 6.3 shows the results of activation carried out on the char sample produced at 550 °C at 850 °C for 30 minutes.

Table 6.3- Results of activation carried out in the JBR starting from char pyrolyzed in the bubbling bed or in the JBR

	Bubbling bed	JBR
Activated carbon yield, from char	18%	18%
Activated carbon surface area, m ² /g	504	550

While the yield of activated char is the same, there is a small difference in the surface area. This can be explained by small differences in the heating rate of the two reactors that would impact the activation kinetics. According to Equation 5.2, the variation of the heating rate, provided it is high enough to fit in the fast pyrolysis conditions, would have a marginal impact on the results, since it is described by an exponential decrease. A difference in the heating rate between, for example, 1000 °C/min and 500 °C/min would only generate a difference in the value of $n_p k$ between $3.99 \cdot 10^5$ and $3.65 \cdot 10^5$, which would result in a surface area of 581 and 532 m²/g respectively, and a yield of 18.6 and 17%, thus making the results relevant according to the findings presented in Figure 5.11. Another cause for small differences could be attributed to a little loss of reactivity due to cooling and re-heating in the case of the bubbling bed. Nevertheless, the results are comparable and provide a good match.

Thus, the JBR is a good tool to simulate the results obtained with fast pyrolysis in a bubbling bed reactor, in terms of:

- Char yield
- Char elemental composition
- Activated carbons yield and surface area.

6.3.2 Application to Kraft lignin and impact of the use of granules

Kraft lignin presents exceptional challenges (Lago, 2015):

- It becomes sticky when heated: it cannot be fed into a pyrolyzer with traditional feeders;
- It forms a sticky foam when processed in a regular fluidized bed pyrolyzer.

Thus, the bubbling bed pyrolyzer previously described has been modified to meet the needs of this particular feedstock (Tumbalam-Gooty, 2014) with:

- The use of a pulse feeder, which prevents disadvantages commonly encountered using screw feeders in the handling of cohesive feedstocks such as plugging and blockage;
- The use of additional mechanical agitation within the fluidized bed, which is able to break the agglomerates formed during fast pyrolysis of Kraft lignin.

Granulation could also be used with the bubbling bed instead of the pulse feeder. The JBR can then be used as a tool to investigate whether granulation would be preferable than using a pulse feeder, which requires the use of additional inert gas diluting the products gases and vapors and negatively impacting the condensation system, thus making the bio-oil recovery more challenging and energy-intensive. In addition, the study allows to investigate the consequences of granulation on the properties of the activated carbons produced.

The feeding of the granules in the JBR was successful. However, as Figure 6.1 shows, despite the fact that all the points (granulated and un-granulated) are still found in the same surface area vs. yield trade-off, the points obtained under the same operating conditions do not overlap, possibly showing a decrease in the effective reaction kinetics when the granules are used.

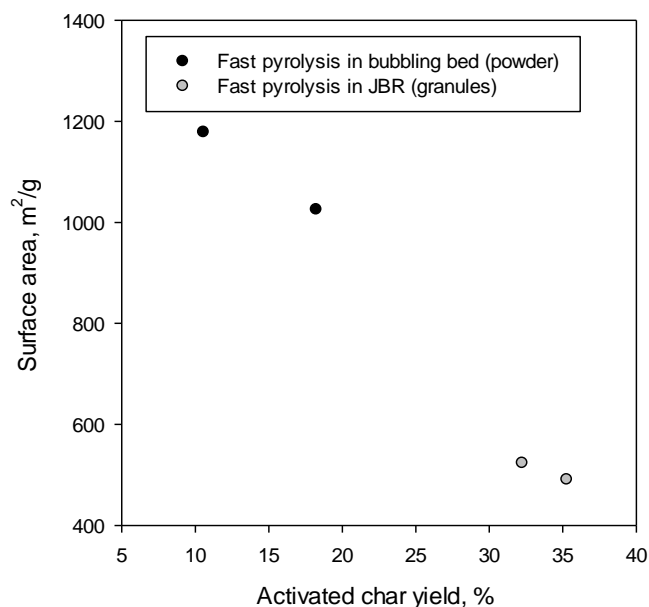


Figure 6.1- Comparison between results obtained with bubbling bed and JBR with lignin fast pyrolysis and activation conditions of 1h 900 °C and 1h 850 °C, 200 ml/min CO₂ flowrate

In order to determine whether the negative impact is due to the agglomeration observed during fast pyrolysis, slow pyrolysis experiments are carried out in the JBR, with both lignin powder and with granules.

Figure 6.2 shows the results obtained at constant standard activation conditions (850 °C, 1h, 200 ml/min CO₂ flow) for slow and fast pyrolysis with granulated and un-granulated samples. The same effect previously observed for fast pyrolysis can be seen in the case of slow pyrolysis: the points all fall on the same line, but granulation slows down the opening of the pores, resulting in a higher yield and a smaller surface area.

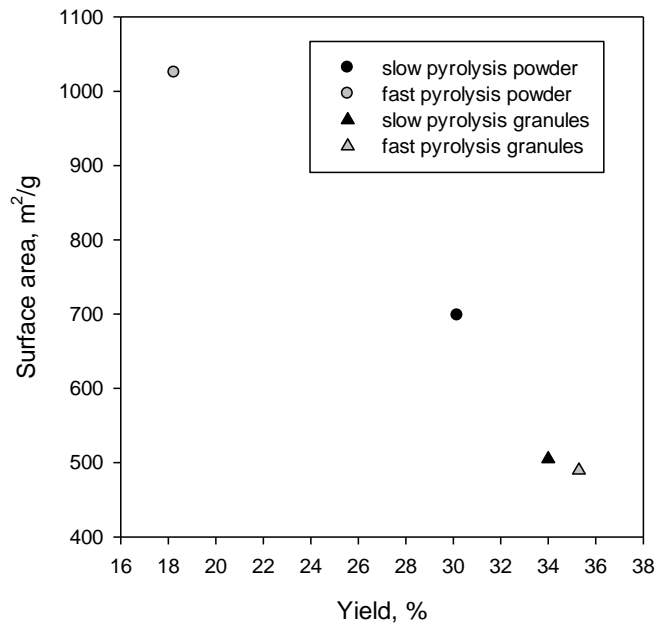


Figure 6.2- Comparison between results obtained with granulated and ungranulated lignin for slow and fast pyrolysis (activation conditions: 850 °C, 1h, 200 ml/min CO₂ flow)

In order to better understand the results obtained, the values of $n_p k$ are calculated for all the samples. n_p is the number of pores per unit mass of the original char and k is the kinetic rate constant for the gasification reaction with carbon dioxide of the material clogging the char pores (see Chapter 4). A lower value of $n_p k$ means that, for a given activation time, less material is gasified, resulting in a smaller surface area, according to Equation 4.15, and a larger yield, according to Equation 4.22. Table 6.4 shows the values of $n_p k$ calculated for slow and fast pyrolysis conditions for granulated and un-granulated lignin.

Table 6.4- Comparison of $n_p k$ values for slow and fast pyrolysis with granulated and un-granulated lignin

	$n_p k, 10^5 \text{ m/min}$
Slow pyrolysis, powder	1.7
Fast pyrolysis, powder	2.5
Slow pyrolysis, granules	1.4
Fast pyrolysis, granules	1.3

The same limitation due to the use of granules is observed even in the case of slow pyrolysis, which is known to be less affected by phenomena like agglomeration. In particular, the value of n_{pk} is significantly reduced (almost halved) in the case of fast pyrolysis when granules are used. In the case of slow pyrolysis, the reduction is less relevant but still present. It is interesting to observe that, when granules are used, the value of n_{pk} seems not to be affected by the pyrolysis conditions. This is opposed to the increased reactivity observed for samples produced under fast pyrolysis conditions described in Chapter 5 in the case of un-granulated olive residue, and in this chapter in the case of un-granulated lignin. It is also of interest to notice that, when the binder is used, the average pore diameter is reduced from 22 Å, in the case of un-granulated lignin, to 19.9 Å, as a further indication that the development of the pores is inhibited by the presence of the binder.

This could be attributable to heat and mass transfer limitations within the granules. It appears that granulating lignin has a detrimental impact on the reactivity and the creation of surface area. However it is not clear in which of the two steps (pyrolysis or activation) this phenomenon takes place.

To determine whether the step that is impacted is the pyrolysis or the activation, the char yields (without activation) are compared for both slow and fast pyrolysis.

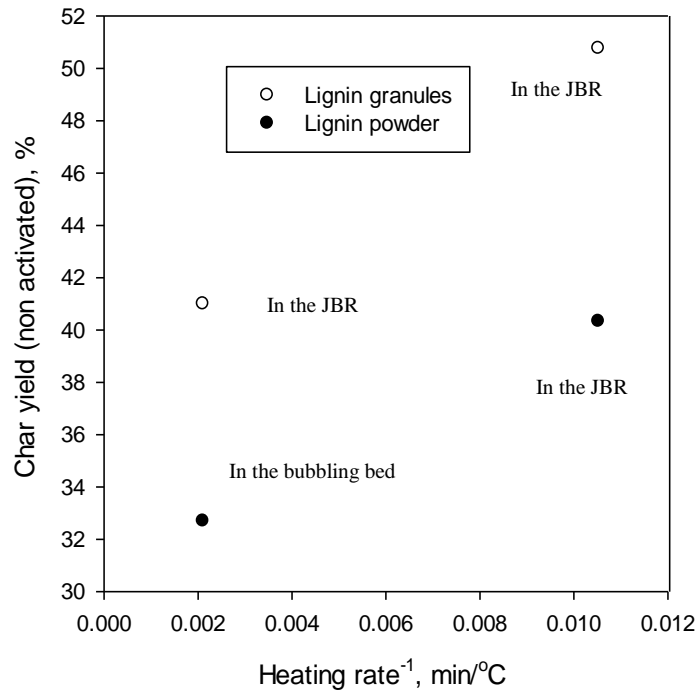


Figure 6.3- Influence of the use of granules on lignin pyrolysis on the char yield as a function of the reciprocal of the heating rate.

Figure 6.3 shows that a strong impact of the use of granules is found in the pyrolysis step, for both slow and fast pyrolysis conditions. The yield increases by nearly 10% points when granules are used. Thus, granulation impacts the pyrolysis step and, consequently, the activation step since, as discussed in Chapter 5, the precursor has a significant impact on the activation process.

Effective (internal) heating rate is even lowered in the case when granules are used, which is an obvious consequence of the larger particle size when compared to the powdered, raw Kraft lignin, but it is not sure whether it could be to any extent attributable to the presence of the binder. The difference in the previously obtained results can, thus, be attributed to two main differences in the lignin used:

- Use of granules, which contain a binder;
- Difference in the particle size (powder vs. granules).

While the particle size is known to have a major impact on the pyrolysis step, it is interesting to see whether also the use of the binder alone has an effect.

Granulation presents several advantages: besides significantly improving the processability of cohesive feedstocks like Kraft lignin, thus allowing them to be easily fed into the pyrolysis reactor, it might be of interest for the production of granular activated carbons (GAC). Granular activated carbons are produced through the use of a binder and in particular, molasses have received an increasing attention over other binders, being a residue (Pendyal, 1999).

In order to study the impact of the presence of the binder alone, the same experiments are performed with olive residue. Olive residue can be fed directly into the JBR in the form of original biomass (as reported in Chapter 5) as well as in granules of the same size, obtained after grinding the olive residue into a fine powder and then granulating it with the use of the binder, thus enabling the study of the effect of the presence of the binder alone, isolating it from the difference in particle size. The granules have the same size as the original residue (1-1.5 mm). This ensures that internal mass and heat transfer resistances would be similar in both experiments. Figure 6.4 shows the results for the yield of non-activated char.

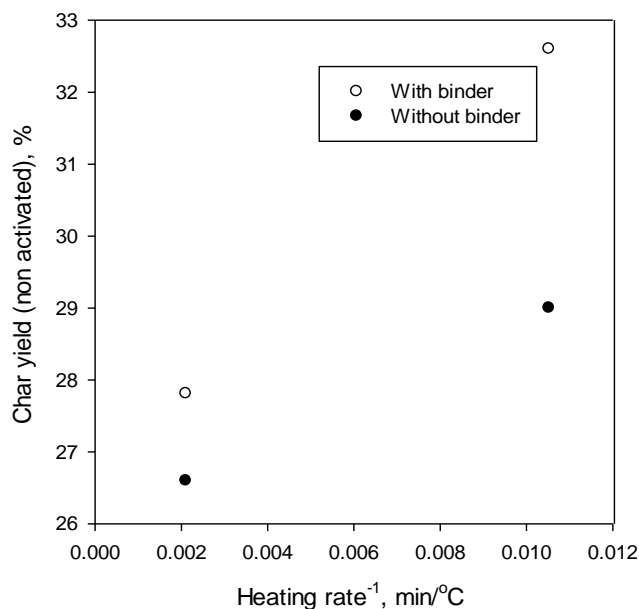


Figure 6.4- Influence of the use of granules on olive residue pyrolysis in the JBR

The results obtained with olive residue also show an increase in the yield in the case where granules are used, despite the fact that the effect is significantly smaller than in the case of lignin (an increase from 28 to 32% as compared to the one from 40 to 50% in the case of lignin). This can be explained

with the addition of the difference in particle size in the case of lignin (powder vs. granules), while, in the case of olive residue, it is attributable to the binder alone.

The trade-off between the yield and surface area for the activated samples under constant activation conditions is shown in Figure 6.5 for granulated and non-granulated olive residue, for both slow and fast pyrolysis. The trend is similar to the one obtained in Figure 6.2 and indicates how even the use of the binder alone has an impact on the kinetics of the activation process.

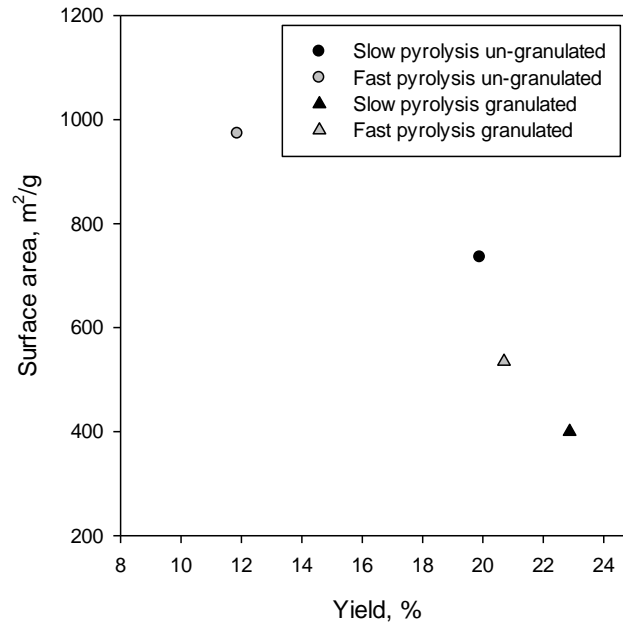


Figure 6.5- Comparison between results obtained with granulated and ungranulated olive residue for slow and fast pyrolysis (activation conditions: 850 °C, 1h, 200 ml/min CO₂ flow)

Table 6.5 shows the values on $n_p k$ for the different cases.

Table 6.5- Comparison of $n_p k$ values for slow and fast pyrolysis with granulated and un-granulated olive residue

	$n_p k, 10^5 \cdot \text{m/min}$
Slow pyrolysis, un-granulated	2.0
Fast pyrolysis, un-granulated	3.6
Slow pyrolysis, granulated	1.4
Fast pyrolysis, granulated	1.9

Similarly to what previously observed in the case of lignin, the values of $n_p k$ are smaller when granules are used; moreover, the impact of the pyrolysis conditions (fast vs. slow) is less significant in presence of the binder. Even under fast pyrolysis conditions, the granulated sample has a reactivity which is lower than the one of the non-granulated sample produced under slow pyrolysis conditions.

Based on the considerations previously made for the model, and assuming once again that k is a purely kinetic parameter, it can be stated that the use of a binder has a negative impact on the parameter n_p , which was found to be the parameter that affected the reactivity the most in Chapter 5. This is most likely due to clogging of the pores that are formed during pyrolysis. The unsuitability of molasses as a binder can be attributed to its high ash content (6%) which results in the presence of inorganics plugging the pores, thus reducing the surface area and creating internal heat and mass transfer limitations which can explain the increase in the yield of char.

Thus, in presence of the binder, the samples reactivity is decreased and the advantage of using high heating rates is lost. However, this does not imply that, given longer times, the points obtained with the granules would not “move up” towards higher surface areas and lower yields: it is in fact expected that they would. However, this would require longer activation times and may thus reduce the attractiveness of the process.

Previous studies reported in the literature had identified a strong effect of the use of binders for the production of GAC (Marshall, 2000). Already in 1946, Morgan and Fink found out that the binder impacted the characteristics of the carbons. The presence of the binder alters the natural structure of the biomass, which affects the devolatilization behavior. In particular, Ahmedna (2000) found that different binders affected the formation of surface areas in different ways: thus, it is possible that, by the selection of an appropriate binder, the detrimental impact can be lowered, thus allowing for improved handling of solids without having detrimental impacts on the product properties.

6.4 Conclusions

The study proved that the JBR is a good tool to simulate results obtained with fast pyrolysis in a bubbling bed reactor, given that the same char yield, the same char properties and same activated carbon yield and surface area were obtained for birch wood.

The increased reactivity obtained from the fast pyrolysis of olive residue was observed also in the case of lignin. However, in order for that to be true, there is the need for a reactor that can handle unprocessed, fine cohesive particles, like the bubbling bed.

Granulation was shown to have a detrimental impact on the formation of pores in the char precursor, which reduces its reactivity during activation, thus making the use of the physical and kinetic models previously developed unsuitable to the case where a binder is used.

Chapter 7

7. Applications

This chapter covers the application of the activated carbons produced with the methodology previously described for adsorption of selected contaminants.

7.1 Structure of the Chapter

The chapter includes the investigation of three specific applications: adsorption of ammonia from wastewater (Section 7.2), of naphthenic acids from Oil Sands Process-affected Water (OSPW) (Section 7.3) and of mercury from wastewater (Section 7.4).

Ammonia is a colorless gas with a very sharp odor which easily dissolves in water. Ammonia is very important to plant, animal, and human life. It is found in water, soil, and air, and is a potential source of nitrogen for plants and animals. Most of the ammonia in the environment comes from livestock manure and the natural breakdown of dead plants and animals (Agency for Toxic Substances & Disease Registry, 2004).

In water, most of the ammonia changes to the ionic form of ammonia, known as ammonium ions, which are represented by the formula NH_4^+ . Ammonium ions are not gaseous and have no odor. Ammonium is the most common form found in wells, rivers, lakes, and wet soils. In high concentration, ammonia is toxic to human health, flora and fauna, and contributes to oxygen depletion in the environment and eutrophication of surface water.

Eighty percent of all manufactured ammonia is used as fertilizer. 30% of the total is applied directly to soil in the form of pure ammonia. The rest is used to make other fertilizers containing ammonium compounds, usually salts. Ammonia is also used to manufacture plastics, explosives and synthetic fibers, while many cleaning products also contain it in the form of ammonium ions (Rodrigues, 2007)

The new EPA regulations dated August 2013 set maximum ammonia concentration in wastewater to be between 0.99 and 4.4 mg/L at 20°C and neutral pH. However, when the ammonia concentration in drinking water is higher than 0.2 mg/L, it causes taste and odor problem (Health Canada, 2013). EPA guidelines for industrial use have not set a limit for ammonia concentration

in recycled water, however high concentrations can cause problems such as fouling and corrosion. For these reasons, the maximum concentration used is 8.6 mg/L or 2 mg/L if the material is made of a copper alloy.

Based on previous studies (Rambabu, 2013), important parameters for ammonia adsorption are:

- Microporosity
- Quantity of acidic surface functional group.

Thus, the following materials have been selected:

- Olive char non-activated (to study how the activation improves the adsorption capacity), prepared according to the procedure reported in Paragraph 2.3.2 without activation, designated as Raw Olive Char (ROC);
- Olive char activated with CO₂ (because of its high microporosity), prepared according to the procedure reported in Paragraph 2.3.2, designated as CO₂ Activated Carbon (CAC);
- Olive char activated with CO₂ treated with HNO₃ (to increase the number of acidic surface functional groups), prepared according to the procedure reported in Paragraph 2.3.4, designated as Acid-treated Activated Carbon (AAC).

The study provides the comparison of adsorption performance and shows the adsorption isotherms to provide further insight into the adsorption mechanism that governs adsorption of ammonium. Application of kinetic models is beyond the scope of this work and identified as minor due to the relatively fast attainment of equilibrium for all the samples (within three hours).

Oil Sands Produced Water (OSPW) is a complex alkaline mixture of organic and inorganic compounds that is generated after the Clark hot water extraction of bitumen from oil sands operations. OSPW is mainly retained on site, and a part of it is recycled back into the process to reduce fresh water consumption. As a result, it becomes corrosive and highly toxic due to the high concentration of organic salts and organic compounds such as naphthenic acids. Naphthenic acids (NAs) are a mixture of alkyl-substituted acyclic and cycloaliphatic carboxylic acids, which are natural components of bitumen. Their concentration in OSPW is up to 120 mg/L (Iramanesh, 2014). Naphthenic acids are the main reason for OSPW toxicity (He, 2012), and have been proved

to be toxic to a number of aquatic species (Melvin, 2013). For this reason, a policy of no release is in place, and OSPW is being retained on site in tailing ponds, which are occupying over 170 km² in the Athabasca region (Gunawan, 2014). Storage of tailings water represents a temporary solution but is a substantial cost to the industry, and the risk of large spills of NAs leaching into surrounding aquatic environments is high. A significant amount of effort is devoted to finding appropriate solutions for the remediation of these sites.

Being widely available in the oil sands processing facilities, the use of coke for the adsorption of NAs is the most obvious choice when it comes to the selection of a material. However, studies by Zubot (2011) have shown that coke has a major drawback in the quantity of Vanadium that is contained in the ashes, which is released during the adsorption process. Kraft lignin is also an abundant material in Canada, which has attracted special interest due to the decline in the pulp and paper industry. Thus, finding high value applications for lignin has become one of the mandates of many research institutions in Canada. Recently, a joint partnership between the Federal Government, FPIInnovations and West Fraser Timber Co. Ltd. has announced the implementation of Canada's first commercial-scale lignin recovery plant in Hinton, AB under the Investments in Forest Industry Transformation (IFIT) Program (Canadian Biomass, 2014). This plant has the objective of promoting the use of lignin for high value applications, and it would increase the availability of lignin close to the oil sands operation sites.

The study described in this chapter aims at comparing the performance at equilibrium of lignin-based activated carbons with commercial activated carbons and coke for the adsorption of naphthenic acids from real OSPW as well as from a synthetic solution of NAs, since most of the experimental studies found in the literature deal with model compounds.

The adsorption capacity of the different adsorbents is correlated with their physico-chemical characteristics and the adsorption isotherms of the best performing materials are shown. Zubot (2011) suggested that, despite the fact that a short-term equilibrium time can be identified for the adsorption of OSPW, when prolonged contact (up to 230 days) was allowed, a slow but significant decrease of concentration was observed. For this reason, the author carried out two types of studies: short term adsorption studies (up to 40h) and long term (up to 230 days). Since OSPW is currently stored in tailing ponds, long contact times could be applied by introducing the adsorbent directly into the pond. For this study, only short term experiments were conducted. Application of kinetic models is, thus, beyond the scope of this work.

Mercury is toxic when ingested by living organisms. A special characteristic of mercury that makes it particularly dangerous is its strong attraction to biological tissues and its slow elimination from living organisms. In particular, mercury accumulates in aquatic environments and works up the food chain through fish, causing various neurological diseases and disorders. The major sources of mercury pollution are anthropogenic, amounting to ~8 million tons of mercury per year in Canada (De, 2013). Examples of sources of mercury contamination are the effluents from chloralkali, pulp & paper, oil refining, electrical, rubber processing and fertilizer industries (Baeyens et al., 1996), as well as batteries production. Another major source of mercury emissions into the atmosphere are flue gases from coal combustors used in electricity generation, contributing to 34% of the total emissions (De, 2013). Changing in regulations regarding mercury pollution will be the main reason for the growth of the activated carbons market in the following years, as explained in the introductory chapter, making it a very up-to date contaminant to study.

In this chapter, the performance of olive and lignin-based activated carbons is compared with the one of commercial activated carbons. The adsorption capacity is correlated with the carbon characteristics and both the application of kinetic models and adsorption isotherms are presented.

7.2 Adsorption of Ammonia: Results and Discussion

Table 7.1 shows the yield and surface area characteristics of the adsorbent samples used for the study (Raw Olive Char (ROC), CO₂ Activated Char (CAC) and Acid-treated Activated Char (AAC)).

Table 7.1- Yield and surface area of the different samples

	Yield %	Surface area m ² /g	Micropore surface area m ² /g	Mesopore surface area m ² /g
ROC	29	7	3	4
CAC	21	735	636	99
AAC	N.A.	354	298	56

Table 7.2 shows the elemental analysis of the three different types of adsorbent carbon used in this study. It can be observed that, while the ROC and CAC samples have similar elemental composition, the HNO₃ washing has a significant impact on three parameters: the nitrogen content, the oxygen content, and the removal of ashes.

Table 7.2- Elemental analysis of the different activated carbon samples

	N	C	H	O	Ash
ROC	0.7	76.8	3.2	9.4	9.8
CAC	0.6	79.1	1.6	6.6	11.8
AAC	1.2	70.8	1.6	23.2	3.1

Table 7.3 shows the content of acidic surface groups as determined from ammonia Temperature-Programmed Desorption (TPD), as described in Chapter 2.

It can be observed that during activation, the thermal treatment removes some of the acidic surface groups that were originally present in the non-activated char sample, while the HNO₃ treatment seems to significantly increase the content of acidic groups.

Table 7.3- Acidic surface groups obtained from TPD, $\mu\text{mol/g}$

ROC	CAC	AAC
214	160	1627

While the CO₂ activation significantly increases the surface area, the HNO₃ treatment decreases it, due to the decrease in the micropore volume because of pore blockage by surface oxide groups (Rambabu, 2013).

The equilibrium time for ROC, CAC and AAC samples is not too much dependent on the activation method and surface modification of the sample. The equilibrium time, obtained for an initial ammonia concentration of 40 mg/L is determined to be 1, 1.5 and 1.5 h respectively for HNO₃, NA and CO₂ samples, as shown in Figure 7.1. For the following part of the study, experiments are all carried out with 24h contact time.

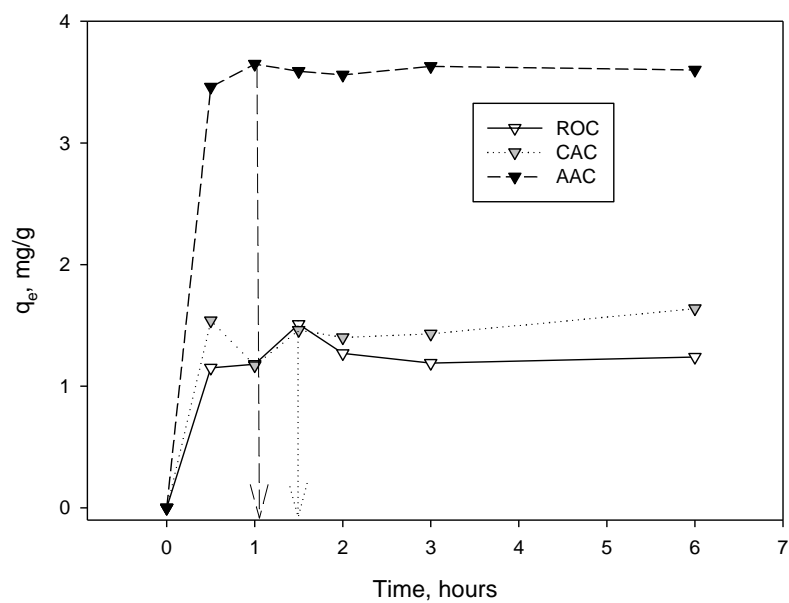


Figure 7.1- Determination of equilibrium time

The total surface area of the sample appears to have no impact on the adsorption performance, and neither does the micropore surface area, as shown in Figure 7.2. The AAC sample, which has intermediate values of both, shows the best performance.

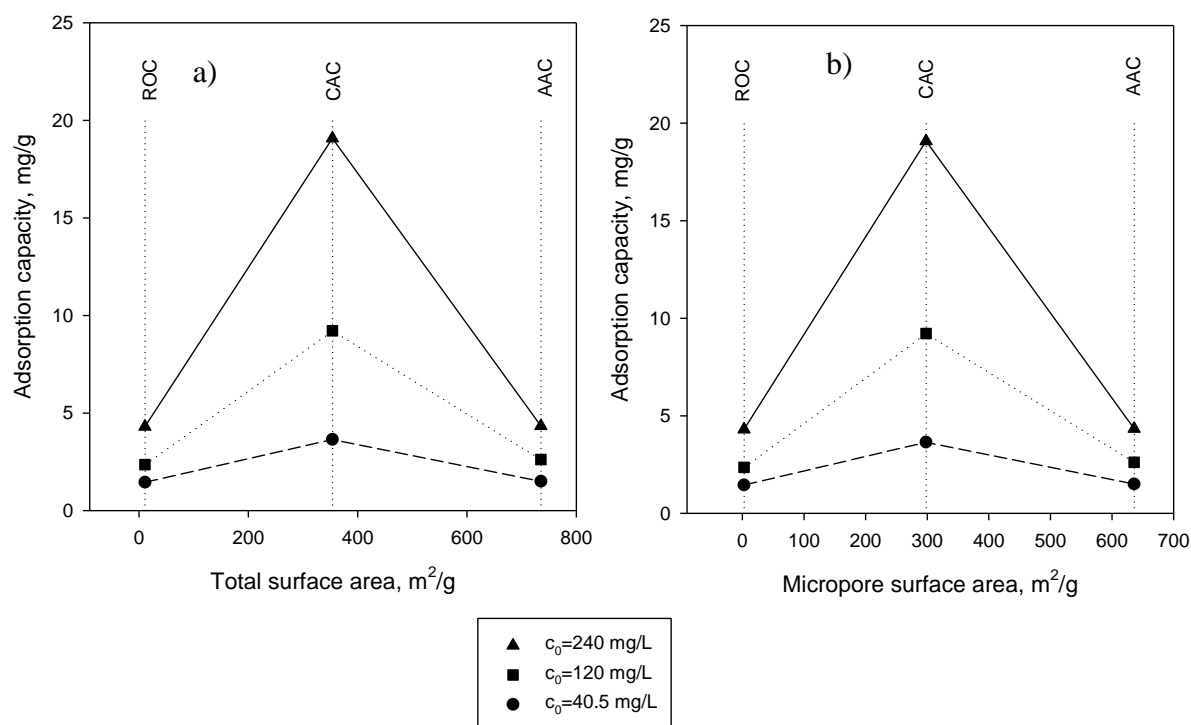


Figure 7.2- Effect of surface area on adsorption capacity for the different char samples.

It is however important to notice that the AAC sample shows a wider average pore size distribution than the CAC sample: it is thus possible that the presence of a larger quantity of macropores on the outer surface facilitates the adsorption process into the smaller pores. The presence of larger cracks on the surface of the particle in the case of AAC samples is clearly shown in the SEM pictures reported in Figures 7.3 a), b) and c). This is attributable to the oxidation reaction that occurs during HNO₃ treatment, while the destruction of the ordered internal porous structure with the HNO₃ treatment is shown in Figures 7.4 a) and b) where it is compared to that of CAC.

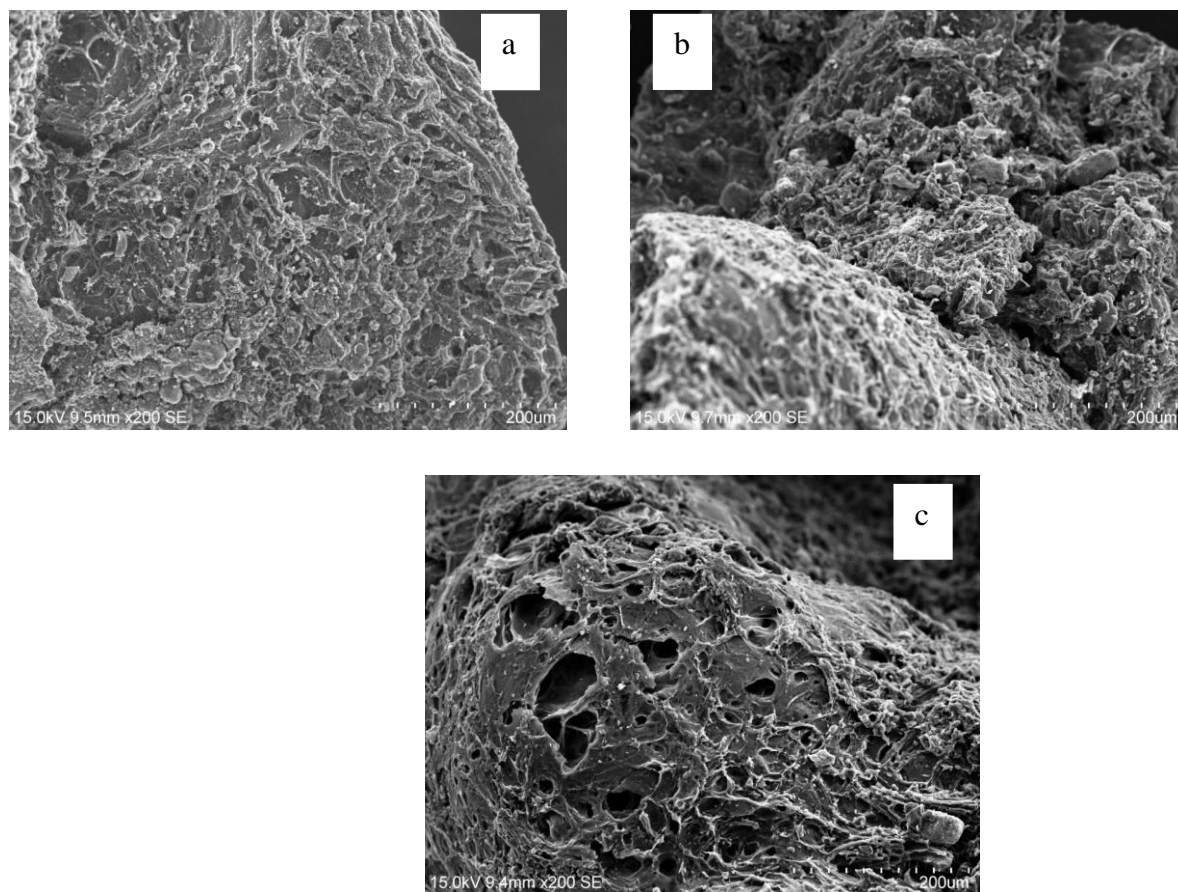


Figure 7.3- Outer surface of a) Raw Olive Char (ROC), b) CO₂ Activated Char (CAC), c) Acid-treated Activated Char (AAC).

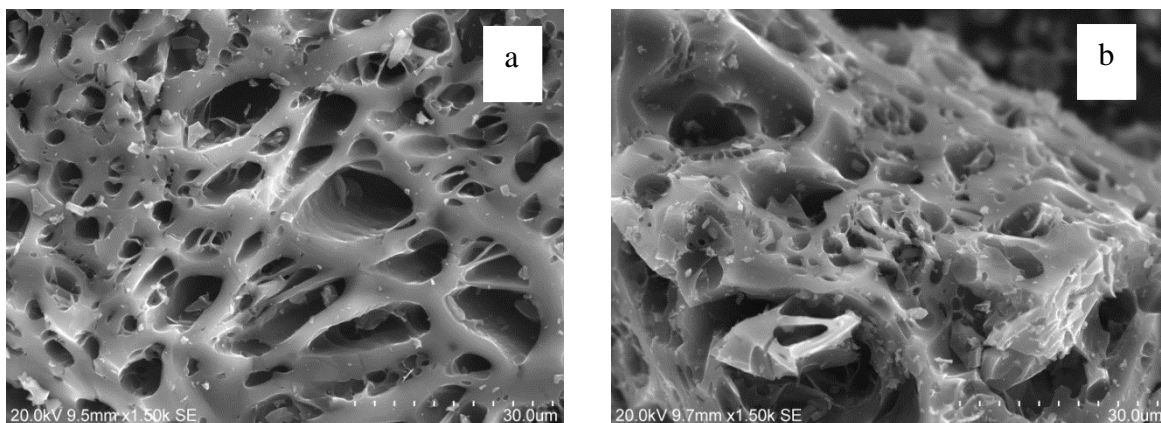


Figure 7.4- Internal surface of CO₂ activated (CAC) and HNO₃ treated char samples (AAC)

On the other hand, the adsorption capacity correlates very well with the quantity of acid surface groups, as shown in Figure 7.5 and as supported by previous studies (Huang, 2008).

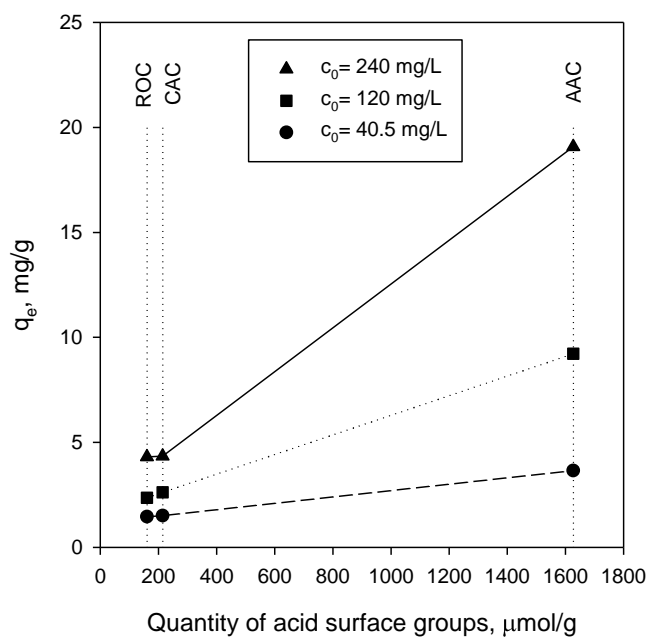


Figure 7.5- Equilibrium adsorption capacity as a function of acid surface groups content.

Thus, by modifying the surface functional groups of the CAC, it is possible to achieve removal efficiencies of up to 90%, as opposed to a maximum of 37% for the activated and non-activated samples, as reported in Table 7.4.

Table 7.4- Comparison of the removal efficiencies of the different char samples

c_0 , mg/L	ROC	CAC	AAC
240	18%	18%	82%
120	20%	22%	76%
40.5	36%	37%	90%

In order to provide better understanding of the adsorption process, the experimental results are fitted with the Langmuir and Freundlich adsorption isotherms.

Table 7.5 shows the adsorption isotherm parameters, the regression coefficient (R^2) and the goodness of the model in predicting the experimental results SSE (using the calculated parameters from the fit), as shown in Figure 7.6. The fit of the linearized forms of the Langmuir and Freundlich adsorption isotherms is omitted from the chapter and reported in the Appendix to Chapter 7.

Table 7.5- Langmuir and Freundlich isotherm parameters

		Langmuir		Freundlich
ROC	Q^0	6.7	k_f	0.26
	b	0.008	n	1.96
	R ²	0.8	R ²	0.94
	SSE	0.26	SSE	0.24
CAC	Q^0	6.2	k_f	0.29
	b	0.01	n	2
	R ²	0.92	R ²	0.98
	SSE	1.55	SSE	0.31
AAC	Q^0	28.6	k_f	1.44
	b	0.027	n	1.59
	R ²	0.48	R ²	0.92
	SSE	998	SSE	20

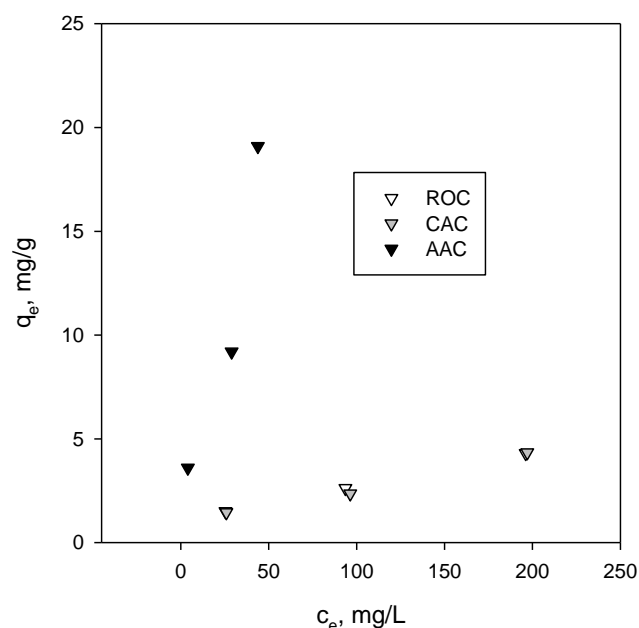


Figure 7.6- Adsorption isotherms

The Freundlich model provides a better fit of the results obtained. The Freundlich adsorption coefficient n is larger than 1, which indicates the heterogeneity of the surface and, possibly, the involvement of chemisorption during the adsorption process (Haghseresht, 1998).

Figure 7.7 shows the separation factor for the three samples. Despite the fact that the value is always in the favorable range (0 to 1) for all samples, the values obtained for AAC sample are significantly lower. Due to the decrease in the driving force as the concentration becomes smaller, it is expected that this value will increase and eventually, for very small concentrations, the adsorption process would become unfavorable. Thus, the lower values obtained for AAC sample indicate that the adsorption process would still be favorable for concentrations lower than the ones achievable with the other two samples.

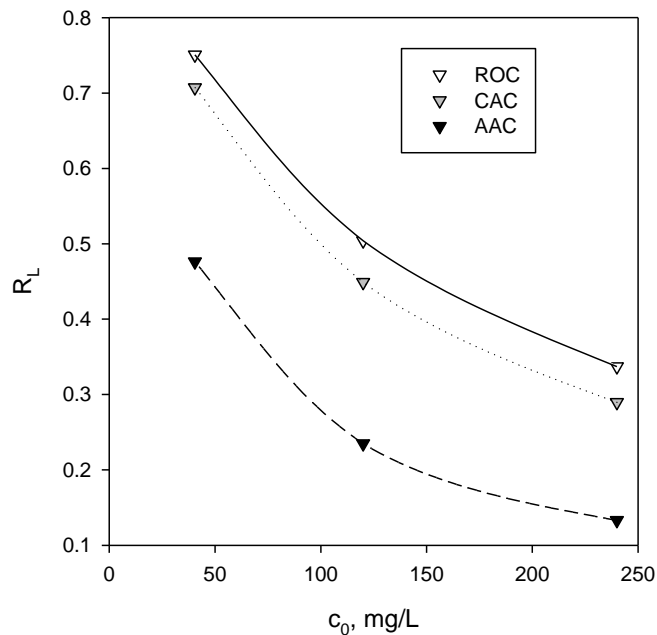


Figure 7.7- Separation factor for different types of activated carbons

Based on the previous results, AAC is selected for the optimization of operating parameters. In order to investigate the effect of carbon loading on the equilibrium concentration, maximum adsorption capacity and efficiency of removal, experiments are performed by increasing the quantity of carbon from 10 g/L (corresponding to 0.1 g of carbon in 10 ml of solution, used in the rest of the study) to 20 g/L while leaving the liquid quantity constant.

The decrease in the total adsorption capacity at equilibrium q_e with the increase in the quantity of adsorbent shown in Figure 7.8 can be explained by overlapping of adsorption sites as a result of overcrowding of adsorbent particles in the case of the lower ammonia concentration (40 mg/L). In the case of the higher concentration (240 mg/L), they can be attributed to an increase in the total surface area and the availability of more adsorption sites. This would allow for a decrease in the amount of ammonia adsorbed per gram of carbon (Garg, 2003), despite an increase in the overall removal efficiency from 82% to 91% when the adsorbent dose was increased from 10 to 20 g/L. However, the increase in the removal efficiency does not seem enough to justify doubling the dose of adsorbent.

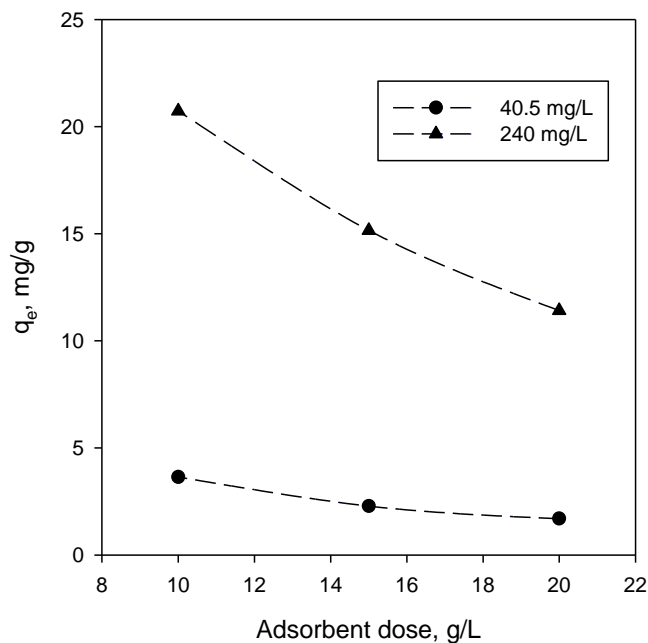


Figure 7.8 - Effect of adsorbent dose on equilibrium adsorption capacity for AAC

In order to study the effect of temperature on the adsorption process, three different temperatures are examined: 25, 35 and 45 °C, with an initial concentration c_0 of 40.5 mg/L. The equilibrium concentration c_e increases with the increase in temperature, and consequently the equilibrium adsorption capacity q_e decreases (as reported in Figure 7.9), proving the negative impact of temperature on the adsorption process. This also indicates that the adsorption process is an exothermic process.

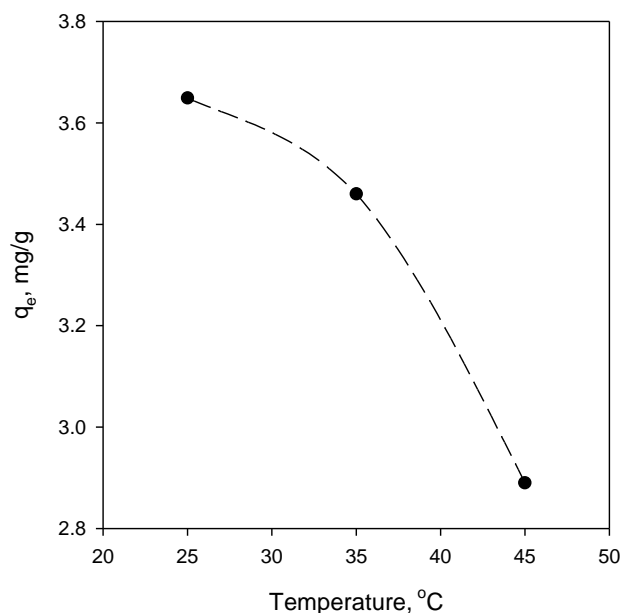


Figure 7.9- Effect of temperature on the equilibrium adsorption capacity for AAC

CONCLUSIONS:

The CO₂ activated and non-activated char samples showed adsorption capacities of the same order of magnitude, despite their significant differences in surface area and the high microporosity observed in the CO₂ activated sample. The adsorption capacity significantly improved after HNO₃ treatment. Despite having a lower micropore surface area than the CO₂ activated one, HNO₃ treated olive activated char was able to remove 90% of the ammonia in the solution. After calculating the adsorption isotherms, it was found that the adsorption of ammonia follows the Freundlich model, with adsorption coefficients $n > 1$, which means that the surface is highly heterogeneous and there might be chemisorption effects, which was further corroborated by the fact that the concentration of acidic surface groups was governing the adsorption of ammonia.

7.3 Adsorption of Naphthenic Acids: Results and Discussion

The characteristics of the samples used in the study are reported in Table 7.6.

Table 7.6- Properties of the carbons used (SP=slow pyrolysis, FP= fast pyrolysis)

	Yield %	Surface area m ² /g	Micropore surface area m ² /g	Mesopore surface area m ² /g	Total basic groups mmol/g
Lignin SP char, non-activated	40.3	0.9	0.3	0.6	0.05
Lignin SP activated char	19.5	919	672	247	0.32
Lignin FP char, non-activated	32.7	27	18	9	0.54
Lignin FP activated char	18	1025	676	349	0.76
Petroleum coke, non-activated	N.A.	8	6	2	0.05
Petroleum coke, activated	N.A.	12	3	9	0.05
Commercial coconut activated carbon	N.A.	1378	1115	263	0.60

The selected model compounds are shown in Table 7.6. They have been selected since are representative of acyclic linear, acyclic non-linear, mono and dicyclo naphthenic acids.

Table 7.7- Model compounds selected for the study

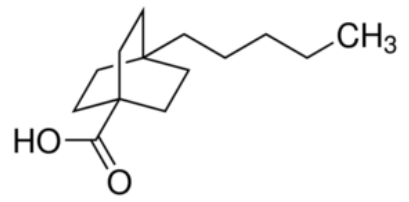
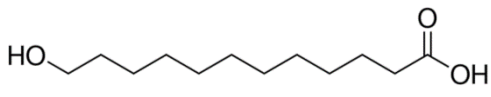
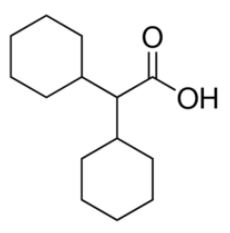
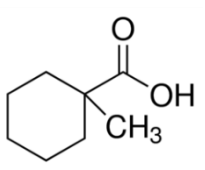
4-Pentylbicyclo[2.2.2]octane-1-carboxylic acid	12-Hydroxydodecanoic acid
$C_{14}H_{24}O_2$ $n=12$ $z=-4$ 	$C_{12}H_{24}O_3$ $n=12$ $z=0$ 
Dicyclohexylacetic acid	1-Methyl-1-cyclohexanecarboxylic acid
$C_{14}H_{24}O_2$ $n=12$ $z=-4$ 	$C_8H_{14}O_2$ $n=12$ $z=-2$ 

Figure 7.10 shows an example of the determination of equilibrium time. The equilibrium for both OSPW and model compounds is reached between 5 and 6 h. Small differences can be explained by the fact that the OSPW has a large number of other components, such as sodium and bicarbonates that result in competitive adsorption (Zubat, 2011), which are absent in the synthetic one. Thus, all adsorption tests are conducted for 24 h to allow for equilibrium to be reached in order to study the adsorption capacity at equilibrium.

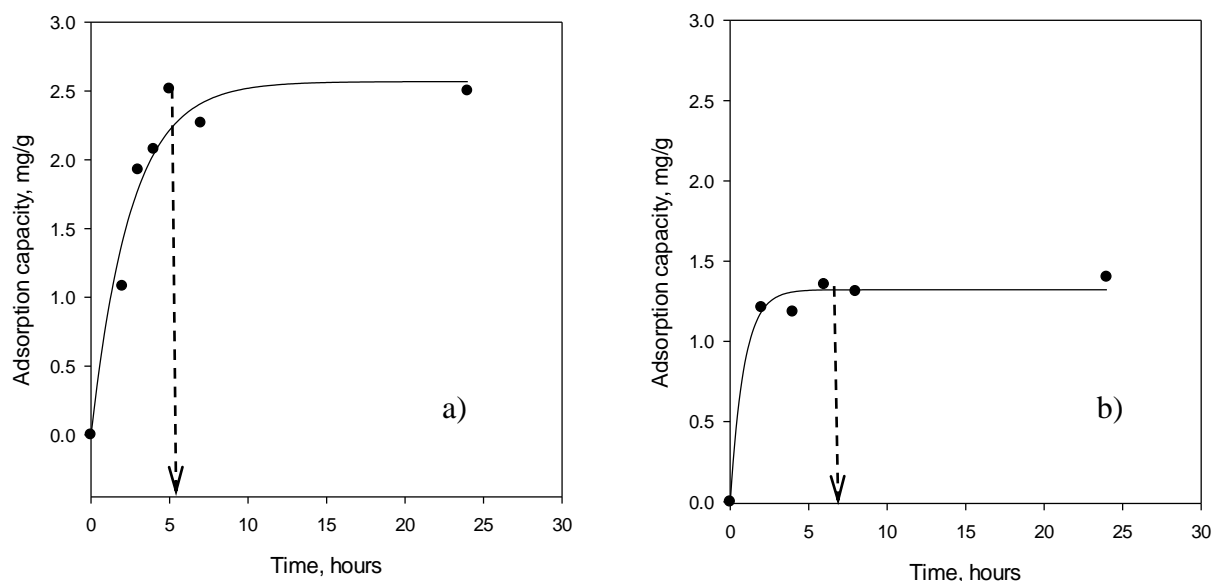


Figure 7.10- Example of equilibrium time determination (for lignin fast pyrolysis non activated) a) with NAs solution b) with OSPW

Table 7.7 shows the equilibrium adsorption capacity for the different samples.

Table 7.7- Equilibrium concentration of different types of activated carbons for model compounds solution and OSPW

	q_e (mg/g) (model compounds)	q_e (mg/g) (OSPW)	Symbol
Petroleum coke, non-activated	1.2	0.9	■
Lignin SP char, non-activated	1.2	0.9	●
Lignin FP char, non-activated	2.5	1.4	▲
Commercial coconut activated carbon	7.1	5.4	◆
Petroleum coke, activated	3.7	1.4	□
Lignin SP activated char	8.1	3.7	○
Lignin FP activated char	8.9	6.3	△

Once again, the relatively small difference between the solution of NAs and the OSPW results can be explained by competitive adsorption with other contaminants that are present in the OSPW (sodium, bicarbonates, calcium, and magnesium). Samples produced from lignin show performances that are better than commercial activated carbons and coke, which might also be due

to the fact that the CO₂ activation of coke proved to be unsuccessful in increasing the surface area of the raw coke samples, as previously reported in the literature also by Rambabu (2013).

For the adsorption of model compounds, the adsorption capacity is somehow related to the total surface area, as shown in Figure 7.11 ($R^2=0.81$). The fit is significantly improved ($R^2=0.92$) when the adsorption capacity is considered as a function of the mesopore surface area. This is due to the large size of the compounds, and, thus, samples with a significant microporous contribution may not be effective for this application.

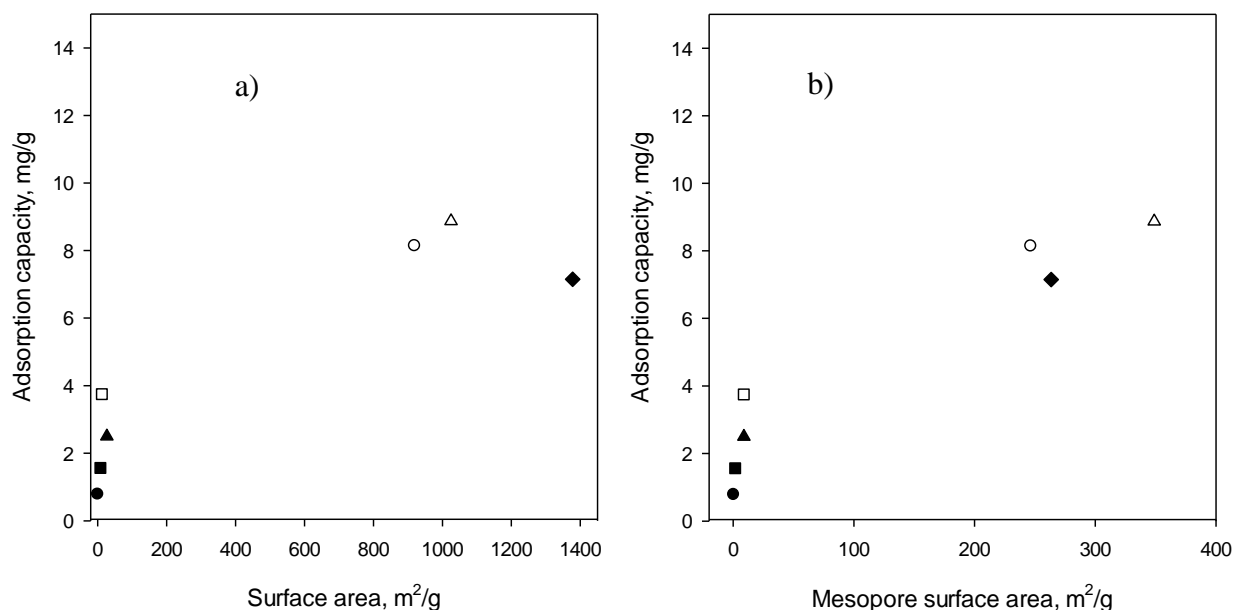


Figure 7.11- Relationship between a) surface area b) mesopore surface area and adsorption capacity for the adsorption of model compounds onto different types of activated carbons. Symbols legend: ■ Non activated petroleum coke ● Non activated slow pyrolysis lignin char ▲ Non activated fast pyrolysis lignin char ◆ Commercial coconut activated carbon □ Activated petroleum coke ○ Activated lignin slow pyrolysis char △ Activated lignin fast pyrolysis char

The same type of relationship can be obtained for real OSPW, as reported in Figure 7.12 ($R^2=0.60$ for total surface area, $R^2=0.95$ for mesopore surface area).

The conclusion is that, in both cases, the mesopore surface area plays a crucial role in the adsorption performance for naphthenic acids, due to the large size of the molecules (Bithun, 2013), thus explaining the fact that Kraft lignin based activated carbons are able to outperform all other carbons, including the commercial grade ones.

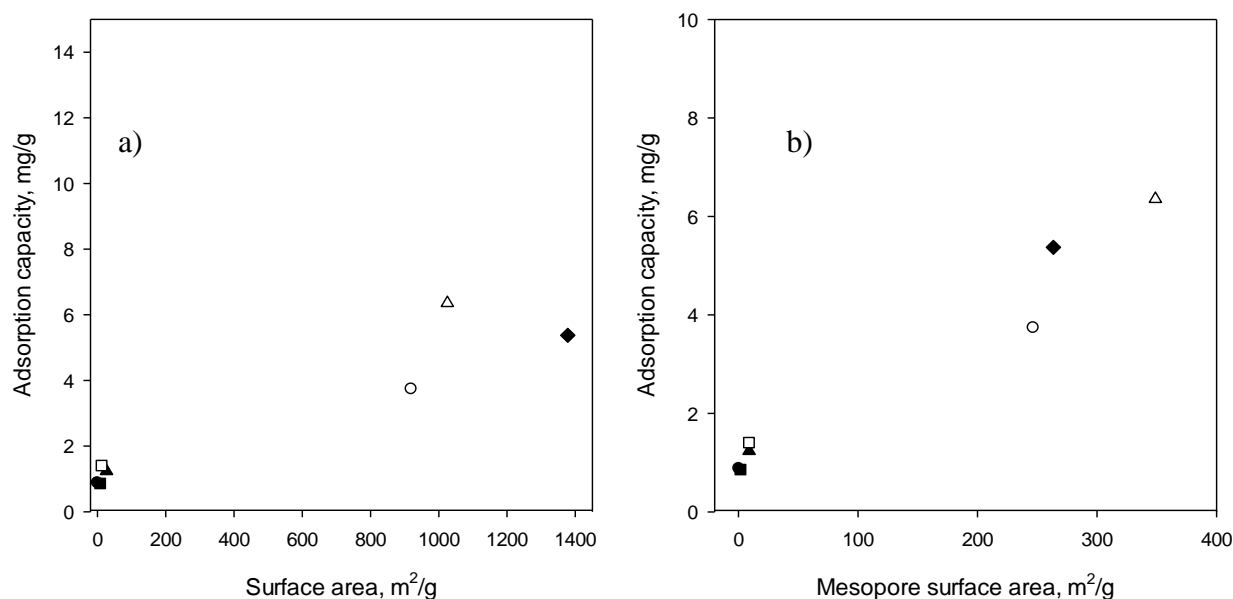


Figure 7.12- Relationship between a) surface area b) mesopore surface area and adsorption capacity for the adsorption of NAs from OSPW onto different types of activated carbons. Symbols legend: ■ Non activated petroleum coke ● Non activated slow pyrolysis lignin char ▲ Non activated fast pyrolysis lignin char ♦ Commercial coconut activated carbon □ Activated petroleum coke ○ Activated lignin slow pyrolysis char △ Activated lignin fast pyrolysis char

It is suggested in the literature that the adsorption of NAs onto activated carbons might be related to the content of basic surface groups (Bithun, 2013). However the linear fits of the results reported in Figure 7.13 are weaker than the ones previously discussed for the mesopore surface area ($R^2=0.5$ for model compounds and 0.68 for OSPW).

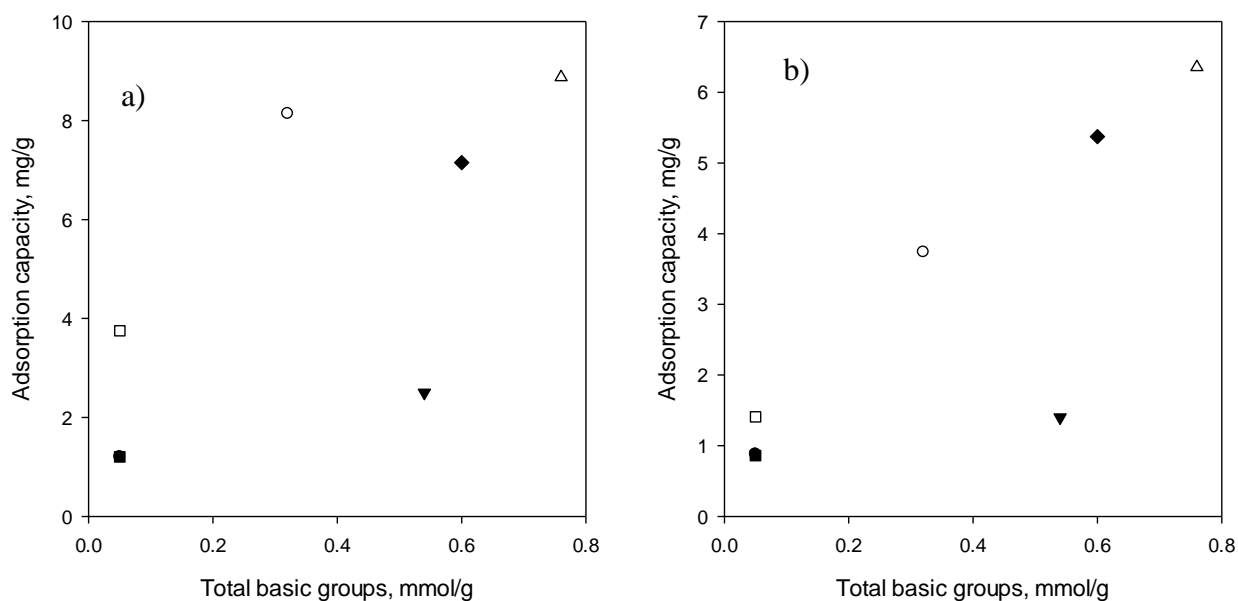


Figure 7.13- Relationship between total basic group concentration and adsorption capacity for the adsorption of a NAs from a) model compounds solution b) OSPW onto different types of activated carbons. Symbols legend: ■ Non activated petroleum coke ● Non activated slow pyrolysis lignin char ▲ Non activated fast pyrolysis lignin char ◆ Commercial coconut activated carbon □ Activated petroleum coke ○ Activated lignin slow pyrolysis char △ Activated lignin fast pyrolysis char

The previous results show that lignin is the best performing feedstock for the adsorption of NAs and the model compounds solution reasonably approximates the results obtained with real OSPW. In order to better understand the adsorption mechanism, adsorption isotherms are obtained for two lignin samples: the one produced from slow pyrolysis, and the one from fast pyrolysis, using the real OSPW. Table 7.8 reports the adsorption isotherms parameters; the linearized graphs for the determination of the parameters are omitted from the chapter and reported in the Appendix. Figure 7.14 shows the fit of the Langmuir and Freundlich models with the experimental results.

Table 7.8- Freundlich and Langmuir parameters for lignin samples

		Langmuir		Freundlich	
		Q^0		k_f	
Lignin SP activated char	Q^0	4.2		k_f	0.005
	b	0.07		n	0.73
	R^2	0.7		R^2	0.99
	SSE	10.87		SSE	0.39
Lignin FP activated char	Q^0	8.3		k_f	0.014
	b	0.34		n	0.74
	R^2	0.85		R^2	0.97
	SSE	81		SSE	0.42

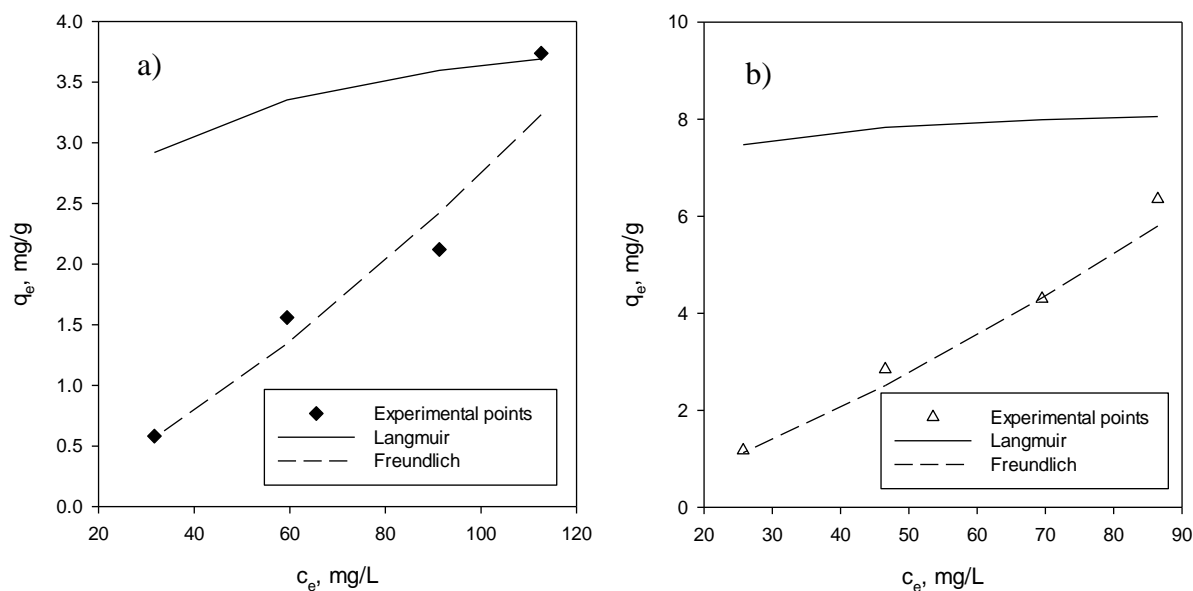


Figure 7.14- Adsorption isotherm results for a) slow pyrolysis lignin b) fast pyrolysis lignin and OSPW

No fit is observed for the Langmuir adsorption isotherm, while a very good fit is found with the Freundlich model. This result is in agreement with the findings from Bithun (2013) for the adsorption of naphthenic acids onto coke particles and can be attributed to the non-homogeneous surface of the lignin-based activated carbons.

CONCLUSIONS:

The performance of different activated chars for the removal of NAs from synthetic and real OSPW was compared. Good agreement was found in the results obtained with the synthetic and the real solution. Lignin based activated carbon outperformed other materials, including commercial grade activated carbon, for the removal of NAs, which was showed to be attributed to its higher mesoporosity. Adsorption isotherms revealed that the adsorption process is best described by the Freundlich isotherm, possibly because of the highly heterogeneous structure of lignin-based activated char.

7.4 Adsorption of Mercury: Results and Discussion

Table 7.9 and 7.10 show the characteristics of the different types of carbons used for the mercury adsorption experiments.

Table 7.9- Yield and surface area characteristics of the different types of carbons used

	Yield %	Surface area m ² /g	Micropore surface area m ² /g	Mesopore surface area m ² /g
Commercial (coconut) activated carbon	N.A.	1339	1083	256
Lignin activated char	31	529	440	89
Olive residue activated char	21	735	636	99

Table 7.10- Elemental analysis of the samples

	N	C	H	O	S	Ash
Commercial activated carbon	0.1	58.2	0.5	38.9	0	2.2
Lignin activated char	0.5	77.5	0.4	18.2	1.1	2.3
Olive residue activated char	0.6	79.1	1.6	6.6	0	11.7

The determination of the equilibrium time is shown in Figure 7.15: equilibrium is reached at significantly different times depending on the type of activated carbon, as reported in Table 7.12

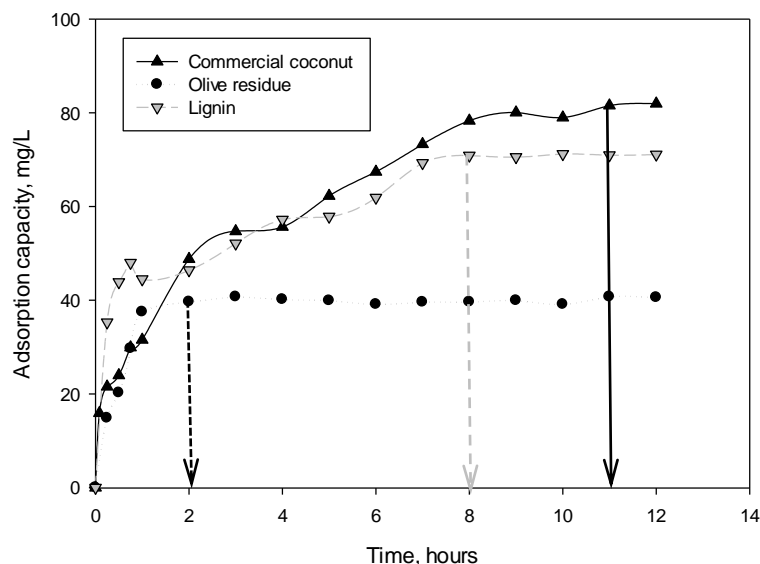


Figure 7.15- Determination of equilibrium time

Table 7.11- Equilibrium time

	Equilibrium time
Olive residue activated carbon	3h
Lignin activated char	8h
Commercial activated char	11h

In order to provide better insight into the kinetics of the adsorption process, the results are fitted with the first order, pseudo second order and particle diffusion models. For the fit of models presented in this chapter, the model parameters were evaluated by linear regression of the linearized forms of the equations, as reported in Chapter 2. For the prediction of the actual results using the parameters obtained by linear regression, the goodness of the fit is evaluated through the sum of squared errors (SSE), due to the difficulties in trusting the value of R^2 for non-linear trends. The calculated parameters are shown in Table 7.12. The linearized graphs for the determination of the parameters are omitted from the chapter and reported in the Appendix.

Table 7.12- Parameters calculated from fitting of linearized form of kinetic models (graphs omitted)

		First order	Pseudo second order	Particle diffusion
Commercial activated carbon	k	0.4	0.007	22.6
	Calculated q_e	83.6	89.2	81.6
	R^2	0.92	0.97	0.98
Lignin activated char	k	0.2	0.05	13.9
	Calculated q_e	83.6	89.3	81.6
	R^2	0.92	0.99	0.87
Olive residue activated char	k	3.1	0.03	33.0
	Calculated q_e	56.6	56.2	39.1
	R^2	0.94	0.96	0.91

The comparison of the prediction of the three kinetic models and the experimental results, using the parameters listed in Table 7.12, is shown in Figures 7.16, 7.17 and 7.18 for the three adsorbents, respectively. It appears that, in all cases, the best fit is achieved with the second order kinetic model, suggesting the possible formation of complexes. However, the second order kinetic model fails to predict the real values, especially in the initial part of the curve for the lignin sample, which are instead described best by the particle diffusion model. It is known that, despite the initial derivation of the model not considering liquid film diffusion, the Morris-Weber model can tell whether the intraparticle diffusion is in reality the only controlling phenomenon by looking at the extrapolating straight line. If the extrapolation of the straight line passes through the origin (i.e., y-intercept = 0), then the adsorption process is said to be solely intraparticle (internal) diffusion-controlled. This can easily be verified looking at the value of the constant term c . In the case of lignin, the value of c is 30. This indicates that there is a liquid layer diffusion which, however, cannot be explained by poor mixing or dilution of the solution. By combining this information with that obtained for the kinetic reaction models, one could hypothesize that the controlling phenomenon in the initial stages of the adsorption process is due to the formation of complexes, which needs to be further studied.

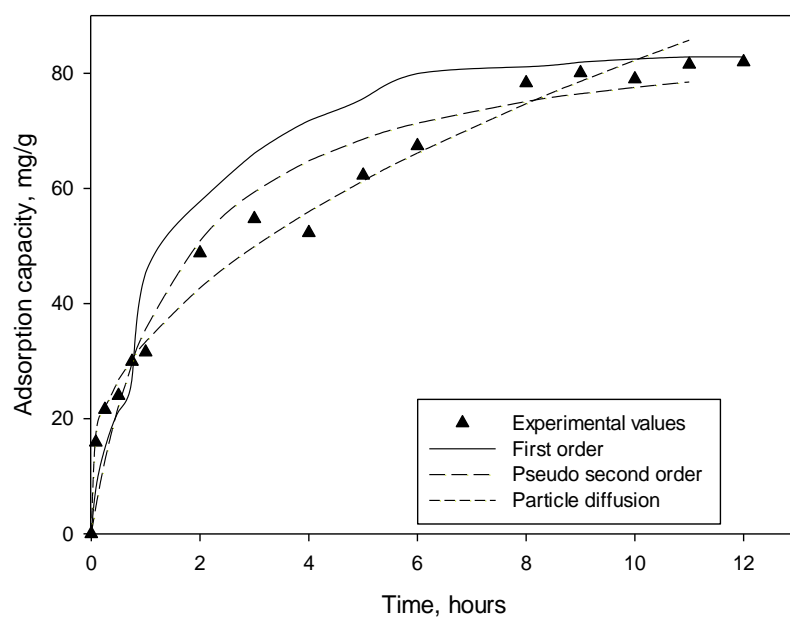


Figure 7.16- Comparison between experimental kinetic profile and predicted using kinetic parameters for commercial activated carbon

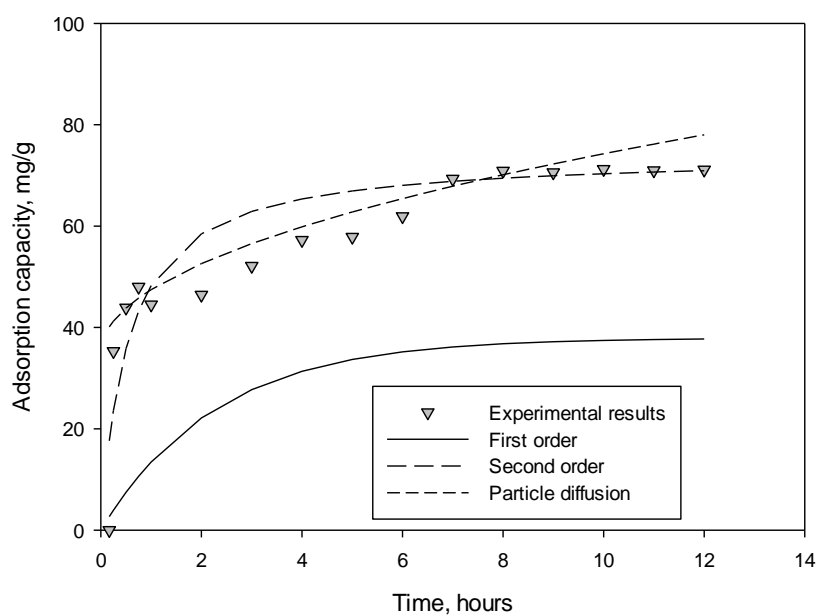


Figure 7.17- Comparison between experimental kinetic profile and predicted using kinetic parameters for lignin activated char

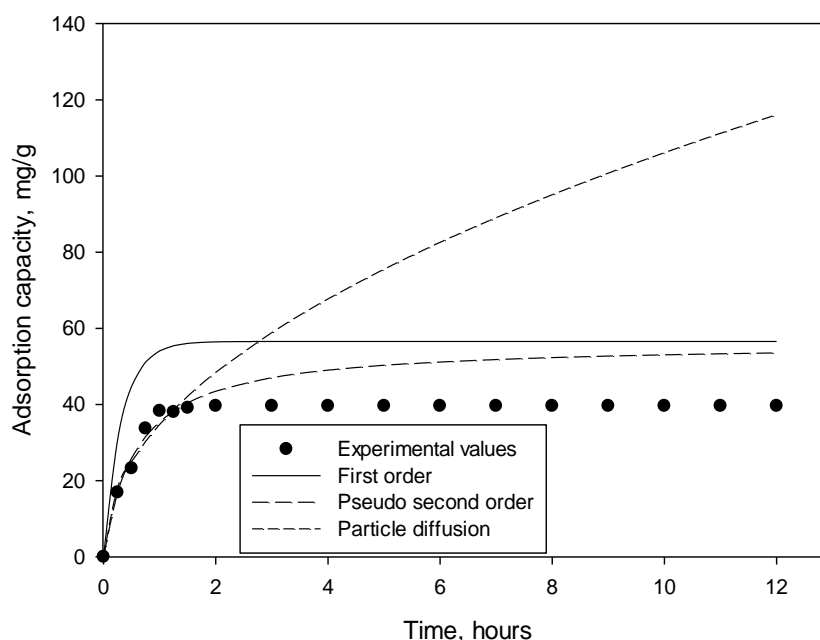


Figure 7.18- Comparison between experimental kinetic profile and predicted using kinetic parameters for olive residue activated char

Table 7.13 reports the goodness of fit test for the different models, evaluated through the sum of squared errors (SSE), due to the difficulties in trusting the value of R^2 for nonlinear trends.

Table 7.13- Goodness of fit (SSE) for the different models

		First order	Pseudo second order	Particle diffusion
Commercial activated carbon	SSE	1266	132	498
Lignin activated char	SSE	17838	166	1036
Olive residue activated char	SSE	4964	1478	29118

In order to understand the different performance for the materials, we attempted to correlate the maximum adsorption capacity observed experimentally with the characteristics of the carbons. It appears from the graph in Figure 7.19 that there is a correlation between the mesopore surface area and the adsorption capacity, which appears to be accompanied by a detrimental impact of the ash content, since the olive samples have an ash content of approximately 12%, while the lignin and commercial activated carbon of only about 2%. In order to have one extra point for samples with high ash content, another sample of olive residue activated carbon with higher surface area (1078 m^2/g , with a mesopore surface area of 264 m^2/g) is included in the study.

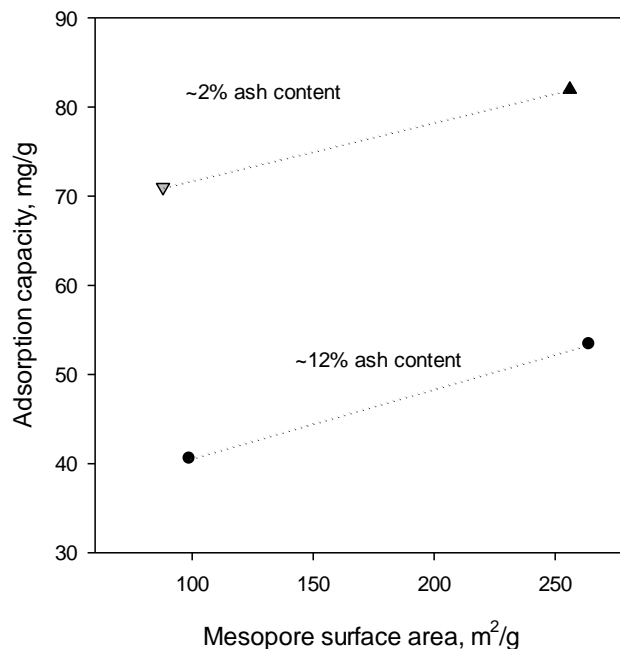


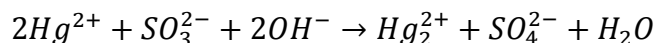
Figure 7.19- Relationship between adsorption capacity and mesopore surface area for activated carbons with different ash contents. Symbols legend: ● Olive residue activated chars ▲ Commercial coconut activated char ▼ Lignin activated char

The results are successfully expressed by means of the correlation shown in Equation 7.1

$$\text{Adsorption capacity} = 65.249 + 0.07 * \text{Mesopore surface area} - 2.4 * \% \text{Ash content} + \% \text{Sulfur content}$$

(7.1)

Which indicates that the ash content has a significant detrimental impact on the adsorption, while in the case of lignin, the fit can be improved by keeping into account the sulfur content. Krishnan and Anirudhan (2002) reported enhanced adsorption of Hg(II) on activated carbon containing sulfur even at low concentrations (around 1%, thus comparable to our study) due to the formation of $\text{Hg}(\text{HS})_2$ and $\text{Hg}_2(\text{HS})_2$ species and their retention in the pores of the carbon particles by the following possible redox reaction reported in Equation 7.2.



(7.2)

The plot in Figure 7.20 shows how the values of adsorption capacity calculated by mean of the correlation are in agreement with the experimental results.

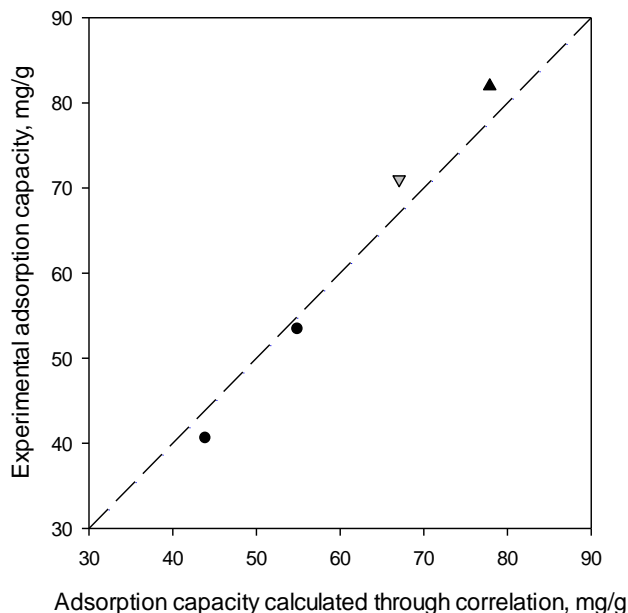


Figure 7.20- Adsorption capacity calculated through the correlation in Equation 7.1 vs. experimental adsorption capacity. Symbols legend: ● Olive residue activated chars ▲ Commercial coconut activated char ▼ Lignin activated char

The correlation proposed, which explains the adsorption capacity by mean of both physical and chemical properties of the carbons, can help understanding the results of the kinetic study, including the possibility of the formation of surface complexes. This is of extreme importance in showing the suitability of a feedstock like lignin for the adsorption of mercury. Because sulfur plays a beneficial role in the removal of mercury, a number of researchers have tried to modify the surface properties of the carbon in order to add sulfur-containing groups (Bylina, 2009, Skodras, 2007, Yang, 2007). In the case of Kraft lignin, this is not necessary because the sulfur is already present in the material.

The adsorption isotherms of the samples are shown in Table 7.16. For the commercial activated carbon, no fit was found: the values of Q^0 and k_f obtained with the two models were negative, thus implying that none of the two is suitable to describe the phenomenon.

Table 7.16- Determination of Freundlich and Langmuir parameters (Graph omitted)

		Langmuir	Freundlich	
Lignin activated char	Q^0	82.6	k_f	2.9
	b	0.017	n	1.7
	R^2	0.92	R^2	0.98
	SSE	55	SSE	491
Olive residue activated char	Q^0	64.5	k_f	0.9
	b	0.0026	n	1.7
	R^2	0.95	R^2	0.99
	SSE	22.7	SSE	7.6

The fit of the experimental data with the above determined parameters is shown in Figure 7.21 and 7.22.

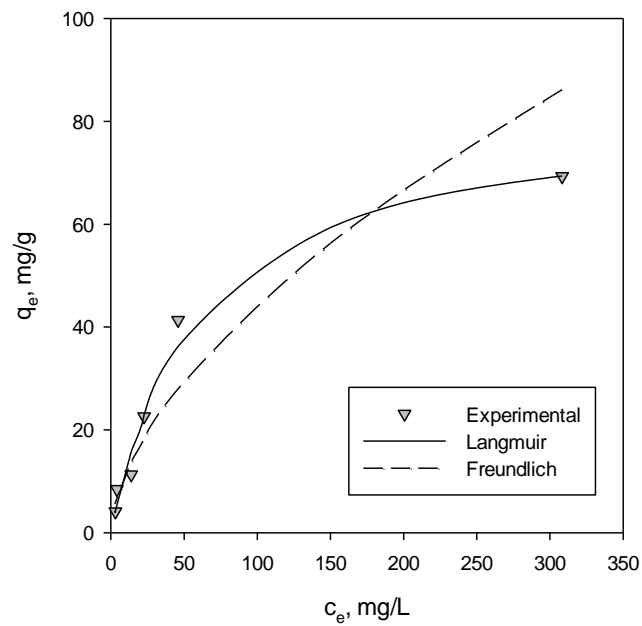


Figure 7.21- Langmuir and Freundlich adsorption isotherms for lignin

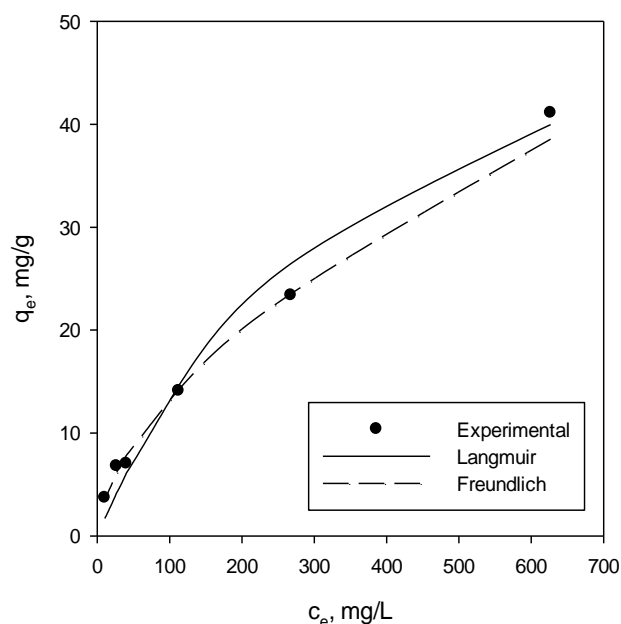


Figure 7.22- Langmuir and Freundlich adsorption isotherms for olive residue

In these cases, the Freundlich model is better to predict the olive residue data, whereas the Langmuir model is better at predicting the results in the case of lignin. This can also be attributed to the fact that the range of concentrations investigated is large and, as previously mentioned, the Freundlich model is normally valid for limited ranges of concentrations and it does not have an upper limit, while it is evident from Figure 7.21 that a plateau has already been reached. It is also important to note that the values of n are >1 , indicating the contribution of chemical interactions to the adsorption process, in agreement with the correlation found.

Now, using the parameters for the adsorption isotherms, we can calculate the separation factor as illustrated in Figure 7.23

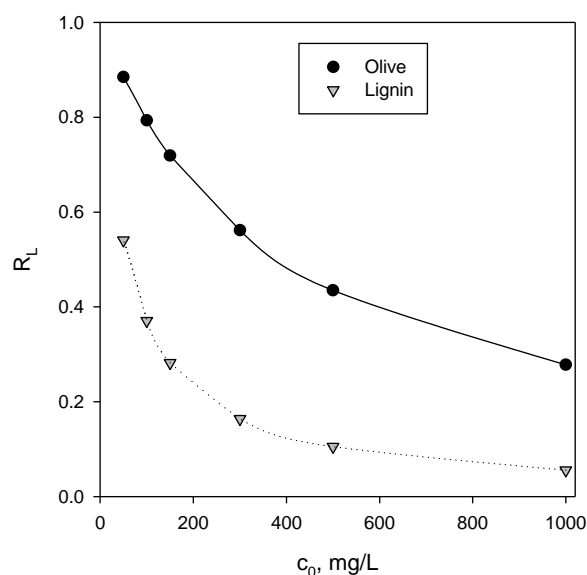


Figure 7.23- Separation factor for olive and lignin activated chars

For both feedstocks, the separation factor is always between 0 and 1, indicating favorable adsorption. However, in the case of olive residue, the process becomes close to unfavorable conditions ($R_L=1$) when lower concentrations are considered, meaning that adsorption is favorable only for polluted water containing a high content of mercury. On the other hand, lignin activated carbon still shows favorable adsorption even at lower concentrations.

CONCLUSIONS

In conclusion, olive residue and lignin activated chars were successfully applied to the removal of mercury from wastewater. In particular, lignin activated char showed to have a performance comparable to the one of commercial activated carbon, which, based on the correlation found, is due to the low ash content and the fact that it contains sulfur. The adsorption experiments with olive residue and lignin were successfully fit with kinetic models and adsorption isotherms to provide further insight into the adsorption process.

7.5 Conclusions

In this chapter, three different applications were studied for the activated carbons produced.

For the adsorption of ammonia, it was shown that the olive residue could be modified by a surface treatment with HNO_3 to increase its content of acidic surface functional groups, which was shown to be the governing parameter for the adsorption.

In the case of naphthenic acids, comparable results were obtained between real oil sands process affected wastewater and the model compounds solution. Lignin based activated carbons were shown to outperform other types of materials, including commercial grade activated carbon. This was successfully correlated with the higher contribution of mesopores to the total surface area in the case of lignin.

For the adsorption of mercury, lignin was shown to be a very attractive feedstock, once again due to the mesoporosity, but also extremely low ash content and the natural presence of sulfur.

As a global conclusion, it appears that lignin is a more attractive adsorbent for liquid applications, which is well in agreement with our previous hypothesis from Chapter 3. Olive residue, due to its high microporosity, could successfully be used for gas phase adsorption, or, because of the relatively high ash content, as a catalyst.

Appendix to Chapter 7

Determination of adsorption isotherms parameters

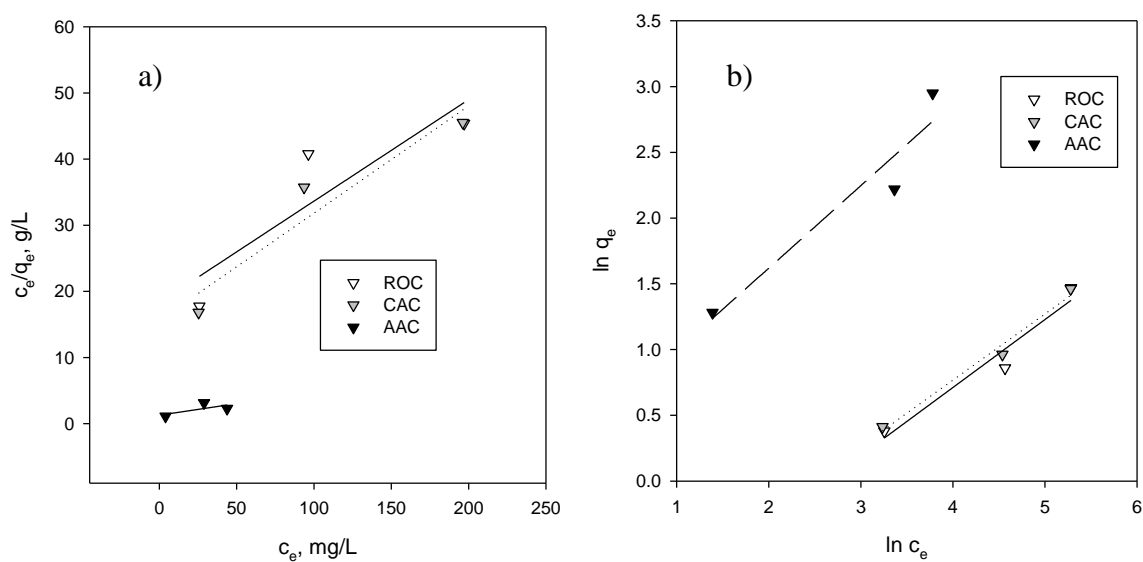


Figure 7.24- Determination of a) Langmuir b) Freundlich adsorption parameters (Section 7.2)

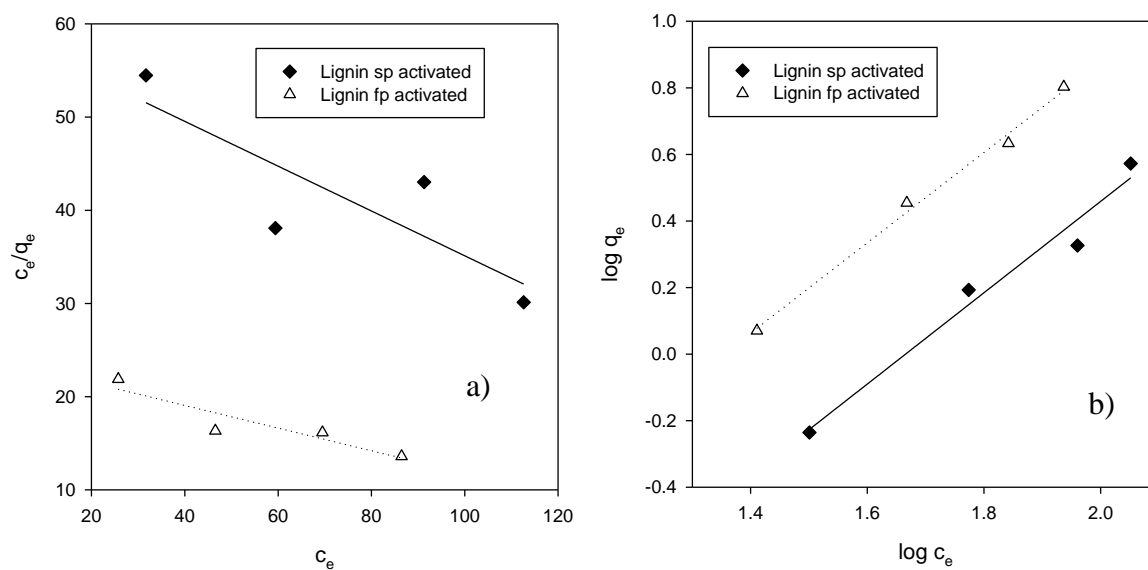


Figure 7.25- Determination of a) Langmuir b) Freundlich adsorption parameters (Section 7.3)

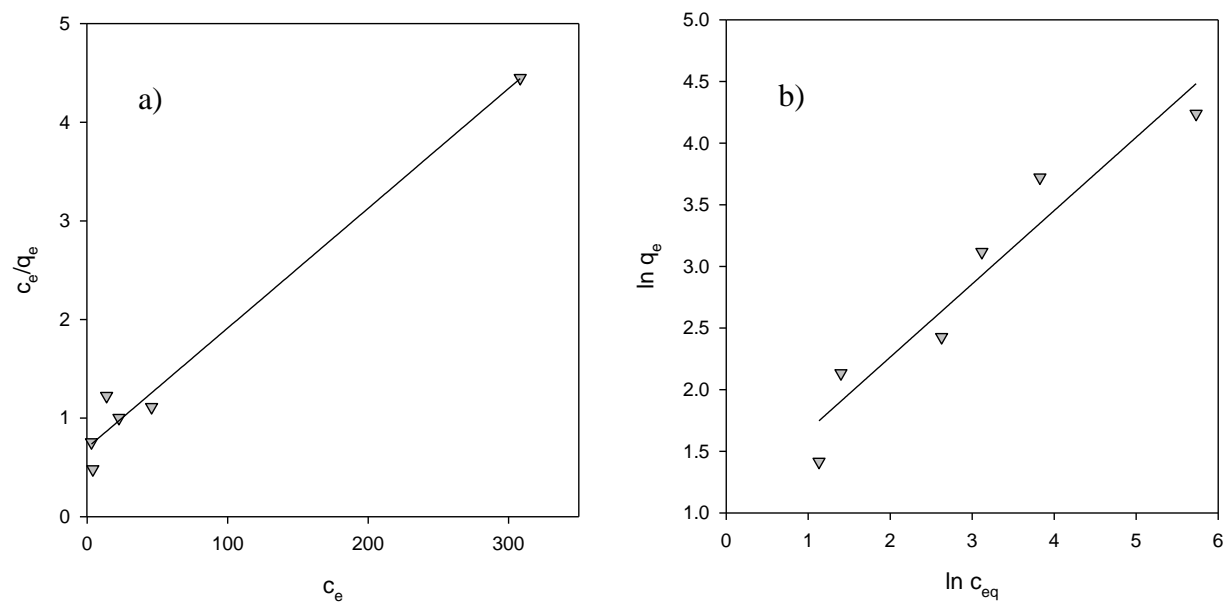


Figure 7.26- Determination of a) Langmuir b) Freundlich adsorption parameters for lignin activated carbon (Section 7.4)

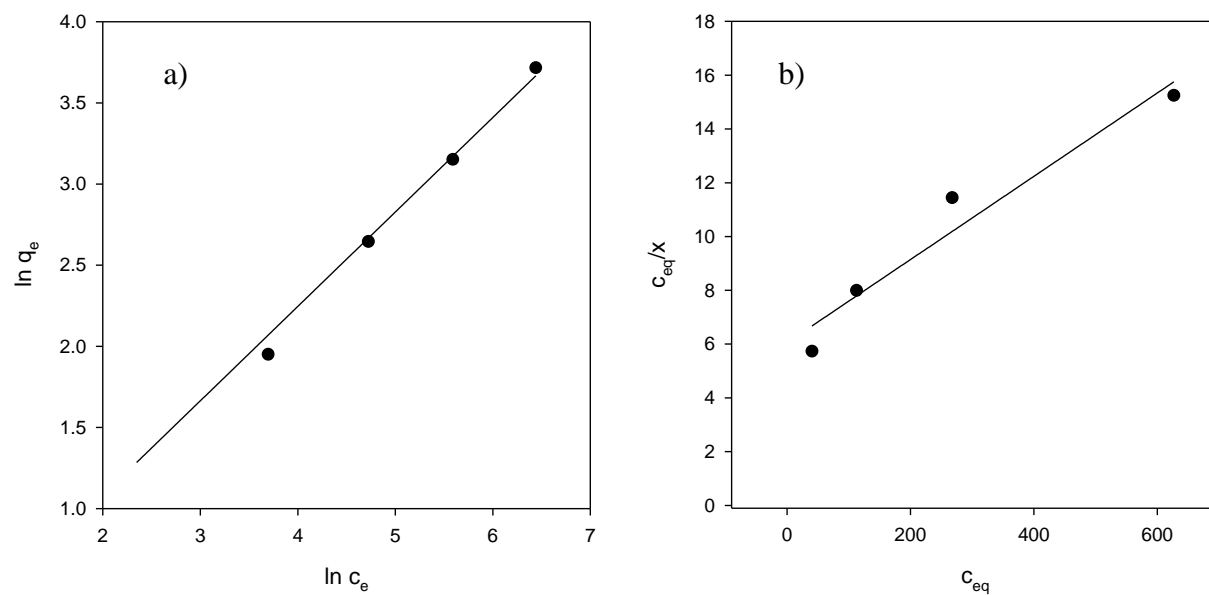


Figure 7.27 -Determination of a) Langmuir b) Freundlich adsorption parameters for olive residue activated carbon (Section 7.4)

Determination of kinetic parameters

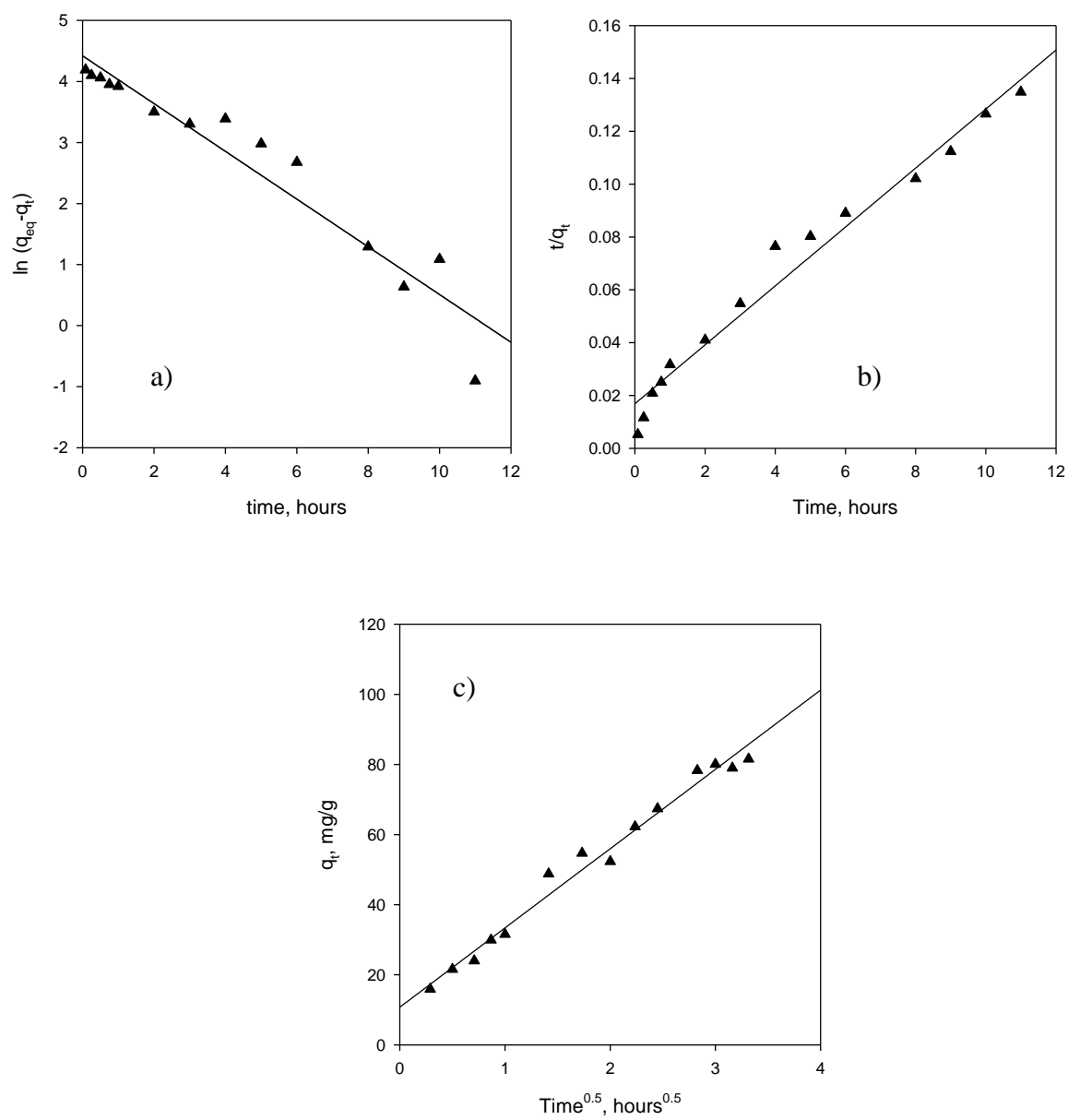


Figure 7.28- Determination of kinetic parameters for commercial coconut activated carbon a) First order b) Pseudo second order c) Particle diffusion (Section 7.4)

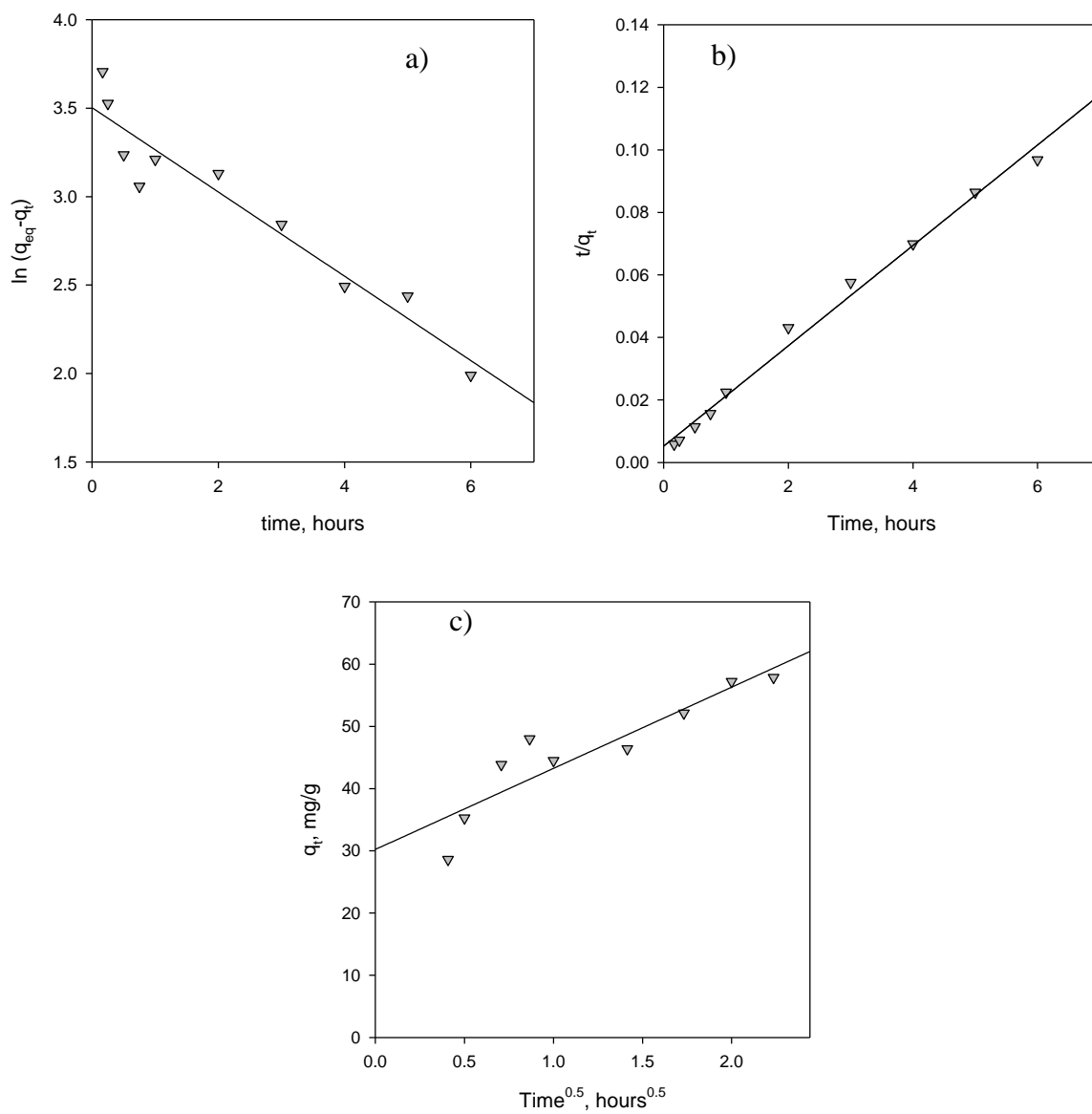


Figure 7.29- Determination of kinetic parameters for lignin activated carbon a) First order b) Pseudo second order c) Particle diffusion (Section 7.4)

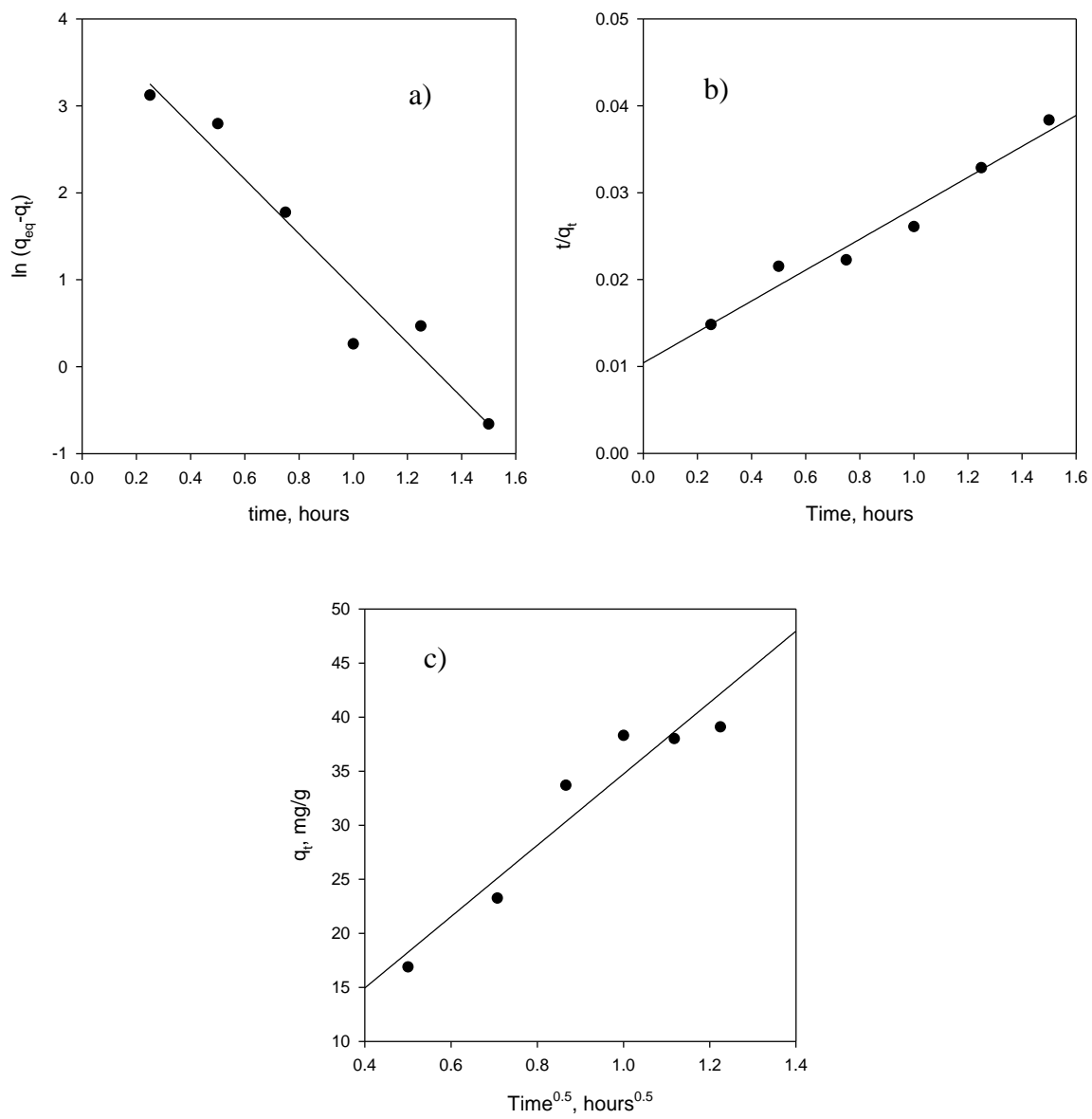


Figure 7.30- Determination of kinetic parameters for olive residue activated carbon a) First order b) Pseudo second order c) Particle diffusion (Section 7.4)

Chapter 8

8. Conclusions and Recommendations

This chapter summarizes the conclusions from the previous chapters and provides recommendations for future work.

8.1 Conclusions

In this thesis, the use of the JBR as a tool for fast and reliable optimization of the pyrolysis and activation of biomass was validated.

The results obtained in the JBR showed good comparison with larger scale reactors, thus allowing the screening of new pyrolysis and activation conditions as well as different feedstocks in a fast and reliable way. Based on the results obtained, feedstocks with high fixed carbon content (olive residue and Kraft lignin) were selected as the most attractive precursors for the production of activated carbons.

Kinetic and physical models were successfully identified and applied to the study of the impact of activation and pyrolysis conditions on the final properties of activated carbons. The model allowed to identify optimum operating conditions for the activation process and to explain the impact of the pyrolysis conditions and granulation on the final product properties and on the reaction kinetics. The results obtained with fast pyrolysis are promising for the integration of activated carbons and bio-oil production.

The activated carbons produced in the JBR were successfully used as adsorbents for different environmental applications and showed good performances. In particular, activated carbon produced from Kraft lignin showed to outperform commercial activated carbon for wastewater treatment applications.

8.2. Recommendations

Since this study showed that the JBR is a very good tool to study the properties of the solid product from reactions that require good heat and mass transfer, it would be of interest to optimize the condensation system, thus enabling the collection of the liquid product.

It is recommended that the developed model is tested with different feedstocks and it could be extended to study the impact of pressure, initial particle size and shape.

It could be of interest to get better understanding on the impact of granulation and test different types of binders to identify the best one.

It is also recommended that different activation gases are tested, and in particular their impact on the physico-chemical properties of the activated carbon and on its performance during adsorption.

For better valorization of olive residue, gas phase adsorption tests should be carried out, as well as studies to identify whether it could be a suitable type of carbon for catalysts production.

References

- Abdul Khalil, H.P.S., Firoozian, P., Bakare, I.O., Akil, H. Md., Noor, A. Md., "Biomass based carbon black as filler in epoxy composites: Flexural and therššl properties", *šterials and Design* (2010), 31, 3419–3425
- Abiven, S., Schmidt, M. W. I. and J. Lehmann, "Biochar by design", *Nature Geoscience* (2014), 7, 326-327
- Agency for Toxic Substances & Disease Registry, "Toxicological profile for ammonia", CAS#: 7664-41-7 (2004)
- Ahmedna, M., Marshall, W.E., Rao, R.M., "Production of granular activated carbons from selected agricultural byproducts and evaluation of their physical, chemical and adsorption properties", *Bioresource Technology* (2000), 71, 113-123
- Alkan, M., Demirbař, Ö., Dođan, M., "Adsorption kinetics and thermodynamics of an anionic dye onto sepiolite", *Microporous and Mesoporous Materials* (2007), 101(3)
- Al-Khalid, T.T., Haimour, N.M., Sayed, S.A., Akash, B.A., "Activation of olive-seed waste residue using CO₂ in a fluidized-bed reactor", *Fuel Processing Technology* (1998), 57, 55–64
- Antal, M.J. Jr, Croiset, E., Dai, X., Dealmeida, C., Mok, W.S.-L., Norberg, N., "High yield biomass charcoal", *Energy&Fuels* (1996), 10, 652-658
- Antal, M.J. Jr, "The art, science and technology of charcoal production", *Ind.Eng.Chem.Res.* (2003), 42, 1619-1640
- Azadi, P., Inderwildi, O. R., Farnood, R., & King, D. A, "Liquid fuels, hydrogen and chemicals from lignin: A critical review", *Renewable and Sustainable Energy Reviews* (2013), 21,506
- Azargohar, R. and Dalai, A., "Steam and KOH activation of biochar: Experimental and modeling studies", *Microporous and Mesoporous Materials* (2008), 110(2), 413-421

- Bacaoui, A. Yaacoubi, A. Dahbi, C. Bennouna, R. Phan Tan Luu, F.J. Maldonado-Hodar, J. Rivera-Utrilla, C. Moreno-Castilla, "Optimization of conditions for the preparation of activated carbons from olive-waste cakes." *Carbon* (2001), 39, 425–432
- Baeyens, R., Ebinghous, R., Vasilev, O., "Global and Regional Mercury Cycles: Sources, Fluxes and Mass Balances", Kluwer Academic Publishers, the Netherlands, 1996
- Bambang, W., Guan, G., Rizkiana, J., Hao, X., Wang, Z., Samart, C., Abudula, A., "Steam reforming of tar derived from *Fallopia Japonica* stem over its own chars prepared at different conditions", *Fuel* 132 (2014), 204-210
- Basu, P., "Biomass Gasification, Pyrolysis and Torrefaction Practical Design and Theory", Elsevier Inc., London, UK, 2013
- Berruti, F., "Development and applications of a novel intermittent solids feeder for pyrolysis reactors" (2013). University of Western Ontario - Electronic Thesis and Dissertation Repository. Paper 1617
- Bhatia, S.K., Perlmutter, D.D., "A random pore model for fluid-solid reactions", *AIChE J* 1980, 26 (3), 379–85
- Biagini, E., Simone, M., Tognotti, L., "Characterization of high heating rate chars of biomass fuels", *Proceedings of the Combustion Institute* (2009), 32, 2043–2050
- Bylina, I.V., Tong, S., Jia, Q.C., "Thermal analysis of sulphur impregnated activated carbons with mercury adsorbed from the vapour phase", *Journal of Thermal Analysis and Calorimetry* (2009), 96 (1), 91–98
- Boateng, A.A., Mullen, C.A., Goldberg, N., Hicks, K.B., Jung, H.-J.B. and Lamb, J.F.S., "Production of bio-oil from Alfalfa stems by fluidized bed fast pyrolysis", *Industrial and Engineering Chemistry Research* (2008), 47, 4115-4122
- Bonelli, P.R., Della Rocca, P.A., Cerrella, E.G., Cukierman, A.L., "Effect of pyrolysis temperature on composition, surface properties and thermal degradation rates of Brazil Nut shells", *Bioresource Technology* (2001), 76, 15-22

Brewer, C.E., Schmidt-Rohr, K., Satrio, J.A., Brown, R.C., “Characterization of biochar from fast pyrolysis and gasification systems”, *Environmental Progress & Sustainable Energy* (2009), 28, 386-396

Brewer, C.E., Hu, Y-Y., Schmidt-Rohr, K., Lohanachan, T.E., Laird, D.A., Brown, R.C., “Extent of pyrolysis impacts on fast pyrolysis biochar properties”, *Journal of Environmental Quality* (2011), 41 (4), 1115-1122

Brewer, C.E., "Biochar characterization and engineering" (2012). Graduate Theses and Dissertations. Paper 12284, <http://lib.dr.iastate.edu/etd>

Bridgwater, A.V., Meier, D., Radlein, D., “An overview of fast pyrolysis of biomass”, *Organic Geochemistry* (1999), 30, 1479-1493

Bridgwater, A.V., Peacocke, G.V.C, “Fast pyrolysis processes for biomass”, *Renewable and Sustainable Energy Reviews* (2000), 4, 1–73

Bridgwater, A.V., “Review of fast pyrolysis of biomass and product upgrading”, *Biomass and Bioenergy* (2012), *Biomass and Bioenergy* (2012), 38, 68-94

Briens, C., Piskorz, J., Berruti, F., “Biomass valorization for fuel and chemicals production – A review”, *International Journal of Chemical Reactor Engineering* (2008), Volume 6

Brown, R., “Biochar production technology”, in Lehmann and Joseph, “Biochar for Environmental Management: Science and Technology”, Earthscan, London, UK, 2009

Burton, A., Wu, H., “Mechanistic investigation into bed agglomeration during biomass fast pyrolysis in a fluidized-bed reactor”, *Energy & Fuels* (2012), 26 (11), 6979–6987

Cameron Carbon Incorporated, “Activated carbon manufacture, structure & properties”, (2006), www.cameroncarbon.com, last accessed June 13th 2015

Canadian Biomass, “NRCan invests in West Fraser lignin recovery process”, (June 2014), <http://www.canadianbiomassmagazine.ca/news/nrcan-invests-in-west-fraser-lignin-recovery-process-4610>, Last accessed May 6th 2015.

Capareda, S., “Introduction to Biomass Energy Conversion”, CRC Press, 2013

Chandra, T.C., Mirna, M.M., Sunarso, J., Sudaryanto, Y., Ismadji, S., “Activated carbon from durian shell: Preparation and characterization”, *Journal of the Taiwan Institute of Chemical Engineers* (2009), 40, 457–462

Crombie, K., Mašek, O., Sohi, S.P., Brownsort, P., Cross, A., “The effect of pyrolysis conditions on biochar stability as determined by three methods”, *GCB Bioenergy* (2013), 5 (2), 122-131

Crombie, K., Mašek, O., “Pyrolysis biochar systems, balance between bioenergy and carbon sequestration”, *GCB Bioenergy* (2015), 7, 349–361

Cruz, D.C., "Production of bio-coal and activated carbon from biomass" (2012). University of Western Ontario - Electronic Thesis and Dissertation Repository. Paper 1044

Damartzis, T., Kostoglou, M., Zabaniotou, A., “Simulation of the agro-biomass (olive kernel) fast pyrolysis in a wire mesh reactor considering intra-particle radial and temporal distribution of products”, *International Journal of Chemical Reactor Engineering* (2009), 7:A1

De, M., Azargohar, R., Dalai, A.K., Shewchuk, S.R., “Mercury removal by bio-char based modified activated carbons”, *Fuel* (2013), 103, 570–578

de Ruiter, G., Helle, S., Rutherford, M., “Industrial and Market Development of Biochar in British Columbia”, *Pacific Institute for Climate Solutions Report* (2014)

Dermeche, S., Nadoura, M., Larroche, C., Moulti-Matia, F., Michaud, P., ”Olive mill wastes: Biochemical characterizations and valorization strategies”, *Process Biochemistry* (2013), 48, 1532–1552

Dufour, A., Celzard, A., Fierro, V., Martin, E., Broust, F., Zoulalian, A., “Catalytic decomposition of methane over a wood char concurrently activated by a pyrolysis gas”, *Applied Catalysis A: General* (2008), 346, 164–173

Duman, G., Onal, Y., Okutucu, C., Onenc, S., Yanik, J., ”Production of activated carbon from pine cone and evaluation of its physical, chemical, and adsorption properties”, *Energy and Fuels* (2009), 23, 2197–2204

EPA National Air Pollution Emissions Trends Update, 1970-1997 (1998)

Fan, M., Marshall, W., Daugaard, D., Brown, R.C., “Steam activation of chars produced from oat hulls and corn stover”, *Bioresource Technology* (2004), 93, 103–107

Faramarzi, A.H., Kaghazchi, T., Ebrahim, H.A., Ebrahimi, A.A., “A mathematical model for the prediction of pore size distribution development during activated carbon preparation”, *Chemical Engineering Communications* (2015), 202, 131-143

Fellows, C. M., Brown, T. C. and Doherty, W. O.S. “Lignocellulosics as a Renewable Feedstock for Chemical Industry: Chemicals from Lignin” (2011), in *Green Chemistry for Environmental Remediation* (eds R. Sanghi and V. Singh), John Wiley & Sons, Inc., Hoboken, NJ, USA

Feng, B., Bhatia, S.K., “Variation of the pore structure of coal chars during gasification”, *Carbon* (2003), 41, 507-523

Fermos, J., Arias, B., Pevida, C., Plaza, M., Rubiera, F., Pis, J.J., “Kinetic models comparison for the steam gasification of different nature fuel chars”, *Journal of Thermal Analysis and Calorimetry* (2008), 91 (3), 779-786

Freundlich, H., “Über die Adsorption in Lösungen”. *Z Phys Chem.* (1906), 57(A), 385–470

Garcia-Perez, M., Wang, X.S., Shen, J., Rhodes, M.J., Tian, F., Lee, W-J., Wu, H., Li C-Z, “Fast pyrolysis of oil mallee woody biomass: effect of temperature on the yield and quality of pyrolysis products”, (2008) *Ind. Eng. Chem. Res.* , 47, 1846-1854

Garg, V.K., Gupta, R., Yadav, A.B, Kumar, R., “Dye removal from aqueous solution by adsorption on treated sawdust”, *Bioresource Technology* (2003), 89, 121–124

Gonzalez, J.F., Roma, S., Encinar, J.M., Martinez, G., “Pyrolysis of various biomass residues and char utilization for the production of activated carbons”, *Journal of Analytical and Applied Pyrolysis* (2009), 85, 134–141

Gunawan, Y., Nemati, M., Dalai, A.K., “Biodegradation of surrogate naphthenic acids under denitrifying conditions”, *Water Research* (2014), 51, 11-24

Guo, S., Peng, J., Li, W., Yang, K., Zhang, L., Zhang, S., Xia, H., “Effects of CO₂ activation on porous structures of coconut shell-based activated carbons” *Applied Surface Science* (2009), 255, 8443–8449

Gupta, V.K., Ali, I., Saleh, T.A., Siddiqui, M. N., Agarwal, S., “Chromium removal from water by activated carbon developed from waste rubber tires”, *Environ Sci Pollut Res* (2012)

Haghseresht, F., Lu, G. Q., “Adsorption characteristics of phenolic compounds onto coal-reject-derived adsorbents”, *Energy & Fuels* (1998), 12, 1100-1107

Hameed, B.H., Tan, A.I.A.W., Ahmad, L., “Preparation of oil palm empty fruit bunch-based activated carbon for removal of 2,4,6-trichlorophenol: optimization using response surface methodology”, *Journal of Hazardous Materials* (2009), 164 , 1316–1324

Health Canada, www.hc-sc.gc.ca, Last accessed September 20th 2014

He, Y., Patterson, S., Wang, N., Hecker, M., Martin, J.W., El-Din, M.G., Giesy, J.P., Wiseman SB. “Toxicity of untreated and ozone-treated oil sands process-affected water (OSPW) to early life stages of the fathead minnow (*Pimephales promelas*)”, *Water Res* (2012), 46 (19), 6359-6368

Huang, C-C., Li, H-S., Chen, C-H., “Effect of surface acidic oxides of activated carbon on adsorption of ammonia”, *Journal of Hazardous Materials* (2008), 159, 523–527

Huang, X., “Fabrication and properties of carbon fibers”, *Materials* (2009), 2, 2369-2403

Ioannidou, O., Zabaniotou, “Agricultural residues as precursors for activated carbon production-A review”, *Renewable and Sustainable Energy Reviews* (2007), 11, 1966-2005

Infiniti Research Limited, “Global Activated Carbon Market 2015-2019”, (2014), www.infinitiresearch.com, last accessed March 17th 2015

Iramanesh, S., Harding, T., Abedi, J., Seyedeyn-Azad, F., “Adsorption of naphthenic acids on high surface area activated carbons”, *Journal of Environmental Science and Health, Part A* (2014), 49, 913-922

IRENA, “Global bioenergy: supply and demand projections for the year 2030”, A Working Paper for REmap 2030 (2014)

Kastner, J.R., Miller, J., Geller, D.P., Locklin, J., Keith, L.H., Johnson, T., “Catalytic esterification of fatty acids using solid acid catalysts generated from biochar and activated carbon”, *Catalysis Today* (2012), 190, (1), 122–132

Kastner, J.R., Mani, S., Juneja, A., “Catalytic decomposition of tar using iron supported biochar”, *Fuel Processing Technology* (2015), 130, 31-37

Klasson, K. T., Uchimiya, M., Lima, I. M., Boihem, L. L. Jr., “Feasibility of removing furfurals from sugar solutions using activated biochars made from agricultural residues”, *BioResources* (2011), 6(3), 3242-3251

Kong, H., He, J., Gao, Y., Han, J., Zhu, X., “Removal of polycyclic aromatic hydrocarbons from aqueous solution on soybean stalk-based carbon” *J. Environ. Qual.* (2011), 40, 1737–1744

Krishnan, K.A., Anirudhan, T.S., “Removal of mercury (II) from aqueous solutions and chlor-alkali industry effluent by steam activated and sulphurized activated carbons prepared from bagasse pith: Kinetics and equilibrium studies”, *Journal of Hazardous Materials* (2002), 92 (2), 161–183.

Kruger, J.S., “Autothermal processing of renewable liquids”, PhD Thesis, University of Minnesota (2011)

Kwapinski, W., Byrne, C.M.P., Kryachko, E., Wolfram, P., Adley, C., Leahy, J.J., Novotny, E.H., Hayes, M.H.B., “Biochar from biomass and waste”, *Waste Biomass Valor* (2010), 1, 177-189

Jung, S.H., Kim, J.-S., “Production of biochars by intermediate pyrolysis and activated carbons from oak by three activation methods using CO₂”, *Journal of Analytical and Applied Pyrolysis* 107 (2014) 116–122

Lago, V., "Application of mechanically fluidized reactors to lignin pyrolysis" (2015). University of Western Ontario - Electronic Thesis and Dissertation Repository. Paper 2779

Latifi, M., "Gasification of bio-oils to syngas in fluidized bed reactors" (2012). University of Western Ontario - Electronic Thesis and Dissertation Repository. Paper 490

Lehmann, J., Kern, D.C., Glaser, B. and Woods, W.I., "Amazonian Dark Earths: Origin, Properties, Management", Kluwer Academic Publishers, the Netherlands, 2003

Lehmann, J. and Joseph, S., "Biochar for Environmental Management: Science and Technology", Earthscan, London, UK, 2009

Lehmann, J., Rillig, M.C., Thies, J., Masiello, C.A., Hockaday, W.C., Crowley, D., "Biochar effects on soil biota - A review", *Soil Biology & Biochemistry* (2011), 43, 1812-1836

Li, D. Berruti, F., Briens, C., "Improved lignin pyrolysis for phenolics production in a bubbling bed reactor – Effect of bed materials", *Bioresource Technology* (2015), 189, 7–14

Lin, L., Li, Y., Ko, F.K., "Fabrication and properties of lignin based carbon nanofiber", *Journal of Fiber Bioengineering and Informatics* (2013), 6 (4), 335-347

Lippens, B.C., de Boer, J.H., "Studies on pore systems in catalysts: V. The t Method", *Journal of Catalysis* 4, 319-323 (1965)

Lowell, S., Shields, J.E., "Adsorption isotherms", *Powder Surface Area and Porosity*, Springer Netherlands, 1984

Lou, C.W., Lin, C.W., Lei, C.H., Su, K.H., Hsu, C.H., Liu, Z.H., Lin, J.H., "PET/PP blend with bamboo charcoal to produce functional composites", *Journal of Materials Processing Technology* (2007), 192–193, 428–433

Lua, A. C., Guo, J., "Activated carbon prepared from oil palm stone by one-step CO₂ activation for gaseous pollutant removal", *Carbon* 38 (2000) 1089–1097

Lua, A.C., Yang, T., Guo, J., "Effects of pyrolysis conditions on the properties of activated carbons prepared from pistachio-nut shells", *J. Anal. Appl. Pyrolysis* 72 (2004) 279–287

Manyàa, J.J., Roca, F.X., Perales, J.F., “TGA study examining the effect of pressure and peak temperature on biochar yield during pyrolysis of two-phase olive mill waste”, *Journal of Analytical and Applied Pyrolysis* (2013), 103, 86–95

Markets and Markets, “Global Activated Carbon Market: Products & Applications (2011–2016)” (2012), Report Code: AD1577, marketsandmarkets.com, last accessed March 17th 2015

Marshall, W. E, Ahmedna, M., Rao, R. M., Johns, M. M., “Granular activated carbons from sugarcane bagasse: production and uses”, *International Sugar Journal* (2000), 102 (1215), 147–151

Mašek, O., Brownsort, P., Cross, A., Sohi, S., “Influence of production conditions on the yield and environmental stability of biochar”, *Fuel* (2013), 103, 151–155

Melvin, S.D. , Lanctôt, C.M., Craig, P.M. , Moon, T.W., Peru, K.M., Headley, J.V., Trudeau, V.L., “Effects of naphthenic acid exposure on development and liver metabolic processes in anuran tadpoles”, *Environmental Pollution* (2013), 177, 22–27

Minkova, V., Marinov, S.P., Zanzi, R., Björnbom, E., Budinova, T., Stefanova, M., Lakov, L., “Thermochemical treatment of biomass in a flow of steam or in a mixture of steam and carbon dioxide”, *Fuel Processing Technology* 62 (2000) 45–52

Mohamed, H. M., Wilson, L.D., Headley, J.V., Peru K.M., “Screening of oil sands naphthenic acids by UV-Vis absorption and fluorescence emission spectrophotometry.”, *J Environ Sci Health A Tox Hazard Subst Environ Eng* (2008), 43(14), 1700–1705

Moilanen, A., “Thermogravimetric characterizations of biomass and waste for gasification processes”, *VTT Publications* (2006) 607

Molina, A., Mondragon, F., “Reactivity of coal gasification with steam and CO₂”, *Fuel* (1998), 77 (15), 1831–1839

Morris, E., Choi, R., Ouyang, T., Jia, C.Q., “Constant thickness porous layer model for reaction between gas and dense carbonaceous materials”, *Industrial & Engineering Chemistry Research* (2012), 51(44), 14376–14383

Mullen, C.A., Boateng, A.A., Goldberg, N.M., Lima, I.M., Laird, D.A., Hicks, K.B., “Bio-oil and bio-char production from corn cobs and stover by fast pyrolysis”, *Biomass and Bioenergy* (2010), 34, 67-74

Muradov, N., Fidalgo, B., Gujar, A.C., Garceau, N., T-Raissi, A., “Production and characterization of *Lemna minor* bio-char and its catalytic application for biogas reforming”, *Biomass and Bioenergy* (2012), 42, 1212-131

Nodwell, M., “On the interactions between naphthenic acids and inorganic minerals”, Thesis, Department of Chemical and Biological Engineering, The University Of British Columbia (2011)

Ollero, P., Serrera, A., Arjona, R., Alcantarilla, S., “Diffusional effects in TGA gasification experiments for kinetic determination”, *Fuel* (2002), 81, 1989-2000

Onay, O., “Influence of pyrolysis temperature and heating rate on the production of bio-oil and char from safflower seed by pyrolysis, using a well-swept fixed-bed reactor”, *Fuel Processing Technology* 88 (2007) 523–531

Ormsby, R., Kastner, J.R., Miller, J., “Hemicellulose hydrolysis using solid acid catalysts generated from biochar”, *Catalysis Today* (2012), 190, (1), 89–97

Otani, S., Fukuoka, Y., Igarashi, B., Sasaki, K., ”Method for producing carbonized lignin fiber”, US Patent n. 3461082, 1969

Ounas, A., Aboulkas, A., El Harfi, K., Bacaoui, A., Yaacoubi, A., “Pyrolysis of olive residue and sugar cane bagasse: Non-isothermal thermogravimetric kinetic analysis”, *Bioresource Technology* (2011), 102, 11234–11238

Ozbay, N., Putun, E., “Characterization of chars from steam pyrolysis of apricot pulp”, *Energy sources, Part A* (2011), 33, 1504-1513

Papanicolaou, G.C., Xepapadaki, A.G., Angelakopoulos, G.C., Zabaniotou, A., Ioannidou, O., “Use of solid residue from olive kernel pyrolysis for polymer matrix composite manufacturing: physical and mechanical characterization”, *Journal of Applied Polymer Science* (2011), 119, 2167–2173

Pendyal, B., Johns, M.M., Marshall, W.E., Ahmedna, M., Rao, R.M., “The effect of binders and agricultural by-products on physical and chemical properties of granular activated carbons”, *Bioresource Technology*. (1999), 68, 247-254

Peterson, S.C., “Evaluating corn starch and corn stover biochar as renewable filler in carboxylated styrene -butadiene rubber composites”, *Journal of Elastomers and Plastics* (2011), 0(00), 1-12

Pottmaier, D., Costa, M., Farrow, T., A. M. Oliveira, A.A.M., Alarcon, O., Snape, C., “Comparison of rice husk and wheat straw: from slow and fast pyrolysis to char combustion”, *Energy Fuels*, (2013), 27 (11), 7115–7125

Ramakrishna, T.V., Aravamudan, G., Vijayakumar, M., “Spectrophotometric determination of mercury (II) as the ternary complex with Rhodamine 6G and iodide”, *Analytica Chimica Acta* (1976), 84, 369-375

Rambabu, N., Azargohar, R., Dalai, A.K., Adjaye, J., “Evaluation and comparison of enrichment efficiency of physical/chemical activations and functionalized activated carbons derived from fluid petroleum coke for environmental applications”, *Fuel Processing Technology* (2013), 106, 501-510

Rambabu, N., Badoga, S., Soni, K.K., Dalai, A.K., Adjaye, J., “Hydrotreating of light gas oil using a NiMo catalyst supported on activated carbon produced from fluid petroleum coke”, *Frontiers of Chemical Science and Engineering* (2014), 8 (2), 161-170

Rao, M.M., Reddy, D.H.K. K., Venkateswarlu, P., Sessaiah, K., “Removal of mercury from aqueous solutions using activated carbon prepared from agricultural by-product/waste”, *Journal of Environmental Management* (2009), 90, 634-643

Rodrigues, C.C., de Moraes, D. Jr., da Nobrega, S.W., Barboza, M.G., “Ammonia adsorption in a fixed bed of activated carbon”, *Bioresource Technology* (2007), 98, 886–891

Rodriguez-Mirasol, J., Cordero, T. and Rodriguez, J.J., “Preparation and characterization of activated carbons from eucalyptus kraft lignin”, *Carbon* (1993), 31, 87-95

Samih, S. and Chaouki, J., “Development of a fluidized bed thermogravimetric analyzer”, *AIChE Journal*, (2015), 61 (1), 84–89

Sarkar, B., “Adsorption of single-ring model naphthenic acid from oil sands tailings pond water using petroleum coke-derived activated carbon”, Thesis, Department of Chemical Engineering and Applied Chemistry University of Toronto (2013)

Skodras, G., Diamantopoulou, Ir., Sakellaropoulos, G.P., “Role of activated carbon structural properties and surface chemistry in mercury adsorption”, *Desalination* (2007), 210, 281–286

Senneca, O., “Kinetics of pyrolysis, combustion and gasification of three biomass fuels”, *Fuel Processing Technology* 88 (2007) 87-97

Şensöz, S., Angin, D., “Pyrolysis of safflower (*Charthamus tinctorius* L.) seed press cake: Part 1. The effects of pyrolysis parameters on the product yields”, *Bioresource Technology* 99 (2008) 5492–5497

Sips, R., “On the structure of a catalyst surface”, *J. Chem. Phys.* (1948), 16, 490-495.

Sixta, H., “Handbook of pulp”, (2006), Weinheim, Germany: Wiley-VCH Verlag GmbH

Sutcu, H. & Demiral, H. “Production of granular activated carbons from loquat stones by chemical activation”, *Journal of Analytical and Applied Pyrolysis* (2009), 84 (1), 47-52

The Freedonia Group, “World Activated Carbon, Industry Study with Forecasts for 2018 & 2023”, (2014) Study #3172, 432 pages, www.freedoniagroup.com, last accessed March 17th 2015

Transparency Market Research, “Activated Carbon Market - Global Industry Analysis, Size, Share, Growth, Trends and Forecast”, (2013), <http://www.transparencymarketresearch.com/activated-carbon-market.html>, last accessed March 17th 2015

Tumbalam,-Gooty, A., Li, D., Briens, C., & Berruti, F., “Kraft-lignin pyrolysis and fractional condensation of its bio-oil”, *Journal of Analytical and Applied Pyrolysis*, (2014), 106, 33-40

Tumuluru, J.S., Sokhansanj, S., Hess, J.R., Wright, C.T., Boardman, R.D., “A review on biomass torrefaction process and product properties for energy applications”, *Industrial Biotechnology* (2011), 7 (5), 384-401

Uchimiya, M., Wartelle, L.H., Klasson, K.T., Fortier, C.A., Lima, I.M., “Influence of pyrolysis temperature on biochar property and function as a heavy metal sorbent in soil”, *Journal of Agricultural Food and Chemistry*, (2011), 59, 2501-2510

Umeki, K., Moilanen, A., Gómez-Barea, A., Kontinen, J., “A model of biomass char gasification describing the change in catalytic activity of ash”, *Chemical Engineering Journal* (2012), 207, 616–624

Valente Nabais, J. M., Laginhas, C.E.C, Carrott, P.J.M., Ribeiro Carrott, M.M.L., “Production of activated carbons from almond shell” *Fuel Processing Technology* 92 (2011) 234–240

Van der Stelt, M.J.C, Gerhauser, H., Kiel, J.H.A., Ptaninski, K.J., “Biomass upgrading by torrefaction for the production of biofuels: A review”, *Biomass and Bioenergy* (2011), 35 (9), 3748–3762

Wahby, Z. Abdelouahab-Reddam, R. El Mail, M. Stitou, J. Silvestre-Albero, A. Sepúlveda-Escribano, F. Rodríguez-Reinoso, “Mercury removal from aqueous solution by adsorption on activated carbons prepared from olive stones”, *Adsorption* (2011) 17, 603–609

Wang, S., Wang, H., Yin, Q., Zhu, L., Yin, S., “Methanation of bio-syngas over a bio-char supported catalyst”, *New J. Chem.* (2014), 38, 4471-4477

Weyerhaeuser, http://www.weyerhaeuser.com/Sustainability/Customers/Innovation_ last accessed May 25th 2015

World Health Organization,

http://www.who.int/water_sanitation_health/dwq/wsh0304_01/en/index4.html, last access May 15th 2015

Yagi S, Kunii D. “Studies on combustion of carbon particles in flames and fluidized beds” In: *Symposium (International) on Combustion* 1955, 5(1); 231–244

Yang, T., Lua, A.C., “Characteristics of activated carbons prepared from pistachio-nut shells by physical activation”, *Journal of Colloid and Interface Science* (2003), 267, 408-417

Yang, H., Xua, Z., Fan, M., Bland, A.E., Judkins, R.R., “Adsorbents for capturing mercury in coal-fired boiler flue gas”, *Journal of Hazardous Materials* 146 (2007) 1–11

Yang, K., Peng, J., Xia, H., Zhang, L., Srinivasakannan, C., Guo, S., “Textural characteristics of activated carbon by single step CO₂ activation from coconut shells”, *Journal of the Taiwan Institute of Chemical Engineers* (2010), 41, 367–372

Yang, Y., Brammer, J.G., Mahmood, A.S.N., Hornung, A. “Intermediate pyrolysis of biomass energy pellets for producing sustainable liquid, gaseous and solid fuels”, *Bioresource Technology* 169 (2014) 794–799

Zabaniotou, A., Stavropoulos, G., Skoulou, V., “Activated carbon from olive kernels in a two-stage process: industrial improvement”, *Bioresource Technology* (2008), 99, 320–326

Zhang, T., Walawender, W.P., Fan, L.T., Fan, M., Dugaard, D., Brown, R.C., “Preparation of activated carbon from forest and agricultural residues through CO₂ activation”, *Chem. Eng. J.* (2004), 9, 105-153

Zhang, Z., Yani, S., Zhu, M., Li, J., Zhang, D., “.Effect of temperature and heating rate in pyrolysis on the yield, structure and oxidation reactivity of pine sawdust biochar”, *Proceedings of Chemeca 2013: Challenging Tomorrow. Vol. 2013 Barton ACT : Engineers Australia, 2013. p. 7*

Zhu, L., Yin, S., Yin, Q., Wang, H., Wang, S., “Biochar: a new promising catalyst support using methanation as a probe reaction”, *Energy Science & Engineering* (2015), 3(2), 126-134

Zubot, W., MacKinnon, M.D., Chelme-Ayala, P., Smith, D.W., El-Din, M.G., “Petroleum coke adsorption as a water management option for oil sand process-affected water”, *Science of the Total Environment* (2012), 427-428, 364-372

Appendix I

I. Production of Bio-Coal from Biomass in a Mechanically Fluidized Reactor (MFR)

I.1 Introduction

Bio-coal is the term that is commonly used to refer to carbonaceous materials derived from biomass and their use as fuel.

The direct use of biomass as fuel finds major limitations in (Tumuluru, 2011):

- The tendency of biomass to absorb moisture (hydrophilic behavior), which makes it subject to biological degradation and perishing during storage;
- High energy required for grinding, due to its fibrous nature. This limits the application of biomass in pulverized boilers;
- Low energy density, which is the main cause for high transportation cost.

When the main use for the carbon product is for fuel, the process selection is generally oriented towards torrefaction. Torrefaction is a milder pyrolysis process, due to the relatively low temperatures used in the process (200-300 °C). Typically, during torrefaction, 70% of the biomass is retained as a solid product, containing 90% of the initial biomass content.

During the torrefaction process, the tenacious fibrous structure of the original biomass material is destroyed through the breakdown of hemicellulose and, to a lesser degree due to the mild temperatures, of cellulose molecules, so that the material becomes brittle and easier to grind (Ciolkosz et al, 2011). The removal of hydroxyl groups results in a change in nature from hydrophilic to hydrophobic, thus overcoming some of the limitations previously described. Also, through the removal of some light volatiles, O and H are removed, leading to an increase in the heating value of the solid.

In the following chapter, different biomasses are torrefied at temperatures of 260 to 300 °C in a mechanically fluidized reactor (MFR). This chapter is adapted from a published presentation (Colomba, 2013).

I.II Materials and Methods

Torrefaction

The torrefaction experiments were conducted in a batch Inconel mechanically fluidized reactor (MFR) having an inside diameter 90 mm, a height of 130 mm and a net volume capacity of 815 ml.

The agitator speed was set at 40% of the maximum power of the motor, corresponding to 65 rpm. The temperature that controls the heaters was measured at the top of the reactor (in the freeboard) and related to the one of the bed via drawback measurements (due to the impossibility to measure the actual bed temperature when the stirrer is on). Drawback measurements reported that the actual bed temperature was 95% of the one measured at the top of the reactor. Another thermocouple was placed at the bottom of the reactor to verify the measurements.

The sample (50 grams) was loaded in the reactor, the reactor was sealed and purged with nitrogen to remove the oxygen and then heated up to reach the maximum temperature at a rate of 15 °C/min. Once reached, the maximum temperature was maintained for 15 minutes. After 15 minutes, the heaters were turned off and the reactor was cooled down in a water bath to a temperature lower than 100°C within 2 minutes.

Heating value (HHV)

The heating value was measured in a bomb calorimeter (IKA C200 Calorimeter)

Moisture uptake

The moisture uptake was measured by placing 5 grams of biomass or bio-coal onto aluminum dishes which were stored at 15 °C in a saturated water environment. At selected times, samples were collected and analyzed in a halogen moisture balance HB43-S (Mettler Toledo).

Grindability

For the grindability determination the samples were ground in an IKA Werke model MF10 basic microfine grinder running at 4500 RPM. A known mass of sample has to pass a 1 mm screen before exiting the grinder. The grinding energy data was recorded using a Watt's Up PRO power meter. The grinder plugs into the meter which then plugs into the wall. The instantaneous power consumption was recorded via USB into a computer. After the grinding was complete, the data acquisition was stopped. Grinding was deemed complete when the instantaneous power consumption returned to the steady state value for the grinder. To obtain the actual grinding energy from the data, the total power was integrated and the power consumption of the empty grinder was subtracted.

I.III Results and Discussion

Figure I.1 reports the yield of different biomasses. While the yield at 260 °C is between 80 and 90%, the one at 300 °C is significantly lower, ranging from 55 to 70%.

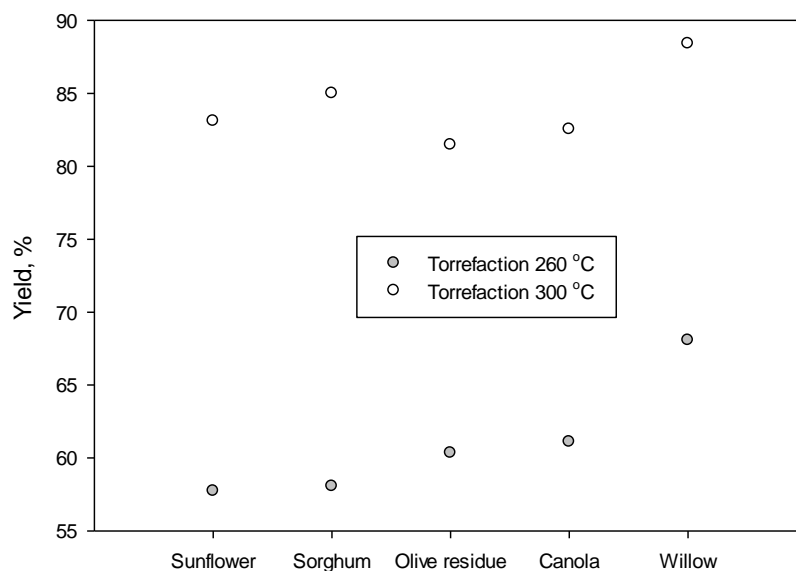


Figure I.1- Torrefaction yield of different biomasses at 260 and 300 °C

Despite the fact that no significant correlation was found between the feedstock composition and the yield after torrefaction, it appears that the latter is strongly affected by the type of feedstock.

This is in agreement with the results of Sadaka and Negi (2009), which, in their comparison between wheat straw, rice straw and cotton gin waste noticed a smaller weight loss for cotton gin, which was attributed to its smaller lignin content. The maximum weight loss obtained was 23.86% for wheat straw, 30.86% for rice straw and 9.67% for cotton gin waste, showing how the feedstock composition influences to a great extent the product yield.

The calorific value of the biomasses, shown in Figure I.2 is significantly increased by torrefaction and varies greatly depending on the feedstock. Feedstocks with the higher calorific value after torrefaction are sunflower husk, sorghum and olive residue, attributable to their high lignin content in the case of olive residue and to the oils found in the extractives for the other two. A temperature of 300 °C results in a higher HHV as compared to 260 °C.

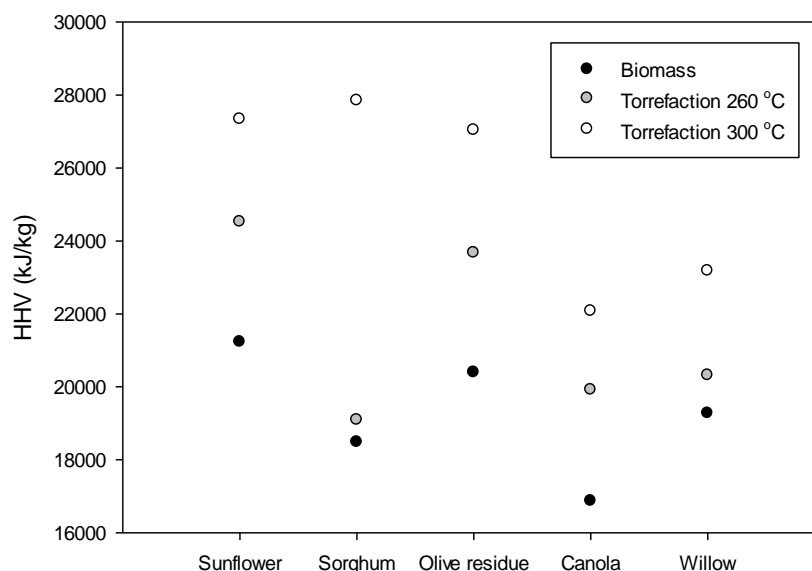


Figure I.2- HHV for different torrefied biomasses

However, the energy recovery shows that operating at 260 °C is more profitable than going to higher temperature. This is because of the significant mass loss at 300 °C, which is also the boundary temperature for torrefaction, which is attributable to the beginning of devolatilization but is not counterbalanced by an equivalent increase in the HHV, resulting in an overall lower energy recovery. As previously mentioned, the main advantage of torrefaction is that around 70% of the initial mass is preserved as a solid product, that contains 90% of the biomass energy content (can reach up to 98%, according to Pimchai et al, 2010), which is in agreement with our results.

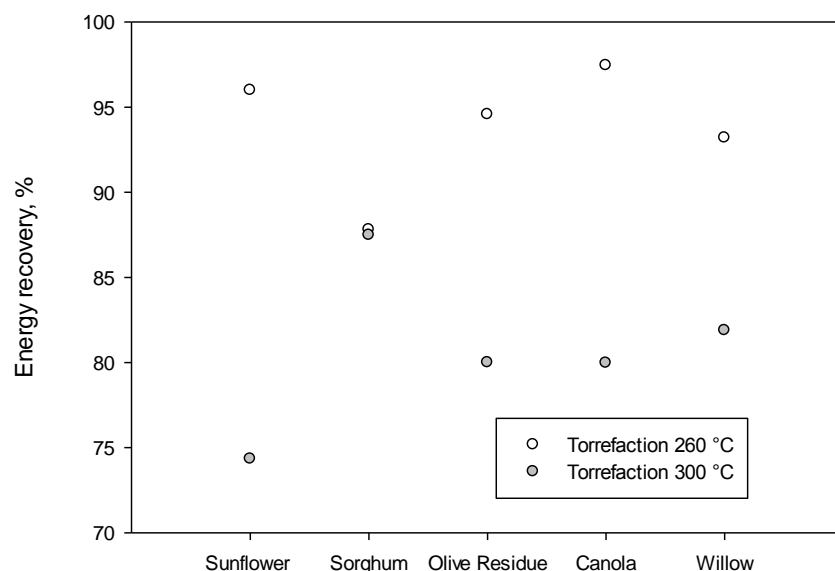


Figure I.3- Energy recovery as a function of torrefaction temperature for different feedstocks

Some processability challenges are encountered with sorghum. At 300 °C, the particles “pop”, and the formation of a large agglomerate around the stirrer is observed, as shown in Figure I.4. This could be attributable to the large content of extractives from sorghum. Despite its high calorific value, for this feedstock other types of processing might be more suitable, or at least the extraction of the residual oils prior to torrefaction should be carried out.





Figure I.4- Morphology of sorghum particles a. untreated b. torrefied at 260 °C c. popping of the seeds at 300 °C, d. stirrer after torrefaction at 300 °C

The Van Krevelen plot for the biomasses is reported in Figure I.5 and compared to the one of bituminous coal (from Tumuluru, 2011). It can be observed how, with the increase of temperature, the points shift towards values typical of coal, meaning that these biomasses would be suitable for use as fuels. This is also supported by results of Cruz (2012) and Phanphanich (2011), who showed that the elemental composition of torrefied pine chips and logging residues are very close to those of bituminous coal, making torrefied biomass potentially suitable for co-firing.

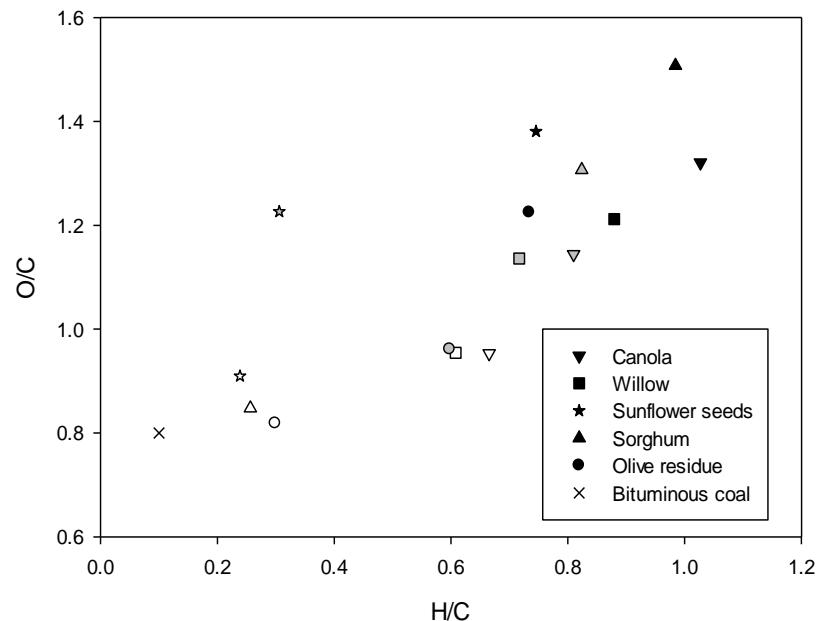


Figure I.5- Van Krevel diagram for the different biomasses. Black symbols: untreated biomass, grey symbols: torrefaction at 260 °C, white symbols: torrefaction at 300 °C

The hygroscopic behavior of the samples needs to be considered, since bio-coal may need to be stored for long time outside, and the increase in its water content may modify its properties as a fuel.

It has been proved by Foley (1986) that the volatile matter of bio-coal influences its moisture uptake. Typical moisture absorption for bio-char is between 3-8% in weight, but when the volatile matter is high, the moisture uptake can reach a value of 15%. The work of Pimchuai (2010) clearly shows that torrefaction is probably the most effective way to change the hydrophilic nature of biomass. Measuring the moisture content of a sample which had been immersed in water for 2h, they obtained an increase of 2.16% for torrefied sawdust, compared to 150.33% for the untreated biomass, while for water hyacinth the values were respectively 17.71% and 197.54%. These results, though encouraging, show that the reduction in the water absorption are different for different biomasses.

Ferro (2004), after producing bio-coal from pine, birch, lucen, sugarcane bagasse and straw and wood pellets torrefaction, stored it in air to study the humidity regain of the torrefied products. After 15 days, the moisture content was 2% for bagasse, 1.2 for lucen and 1% for pine and the two different types of pellets, while the original biomass had a moisture content of approximately 6%.

Results confirming these were also obtained by Acharjee (2011), who exposed the torrefied biomass to different relative humidity ambient to study their equilibrium moisture content. It was also noticed that the capacity of torrefied biomass to adsorb water decreases with an increase in the process temperature.

A possible explanation for the hydrophobic nature of the biomass after torrefaction is that after the loss of OH groups the biomass loses its capability of hydrogen bonding, thus becoming hydrophobic. Figure I.6 shows the trend of moisture content for a period of 21 days for willow: the reduction in moisture uptake is significant for both the samples torrefied at 260 and 300 °C.

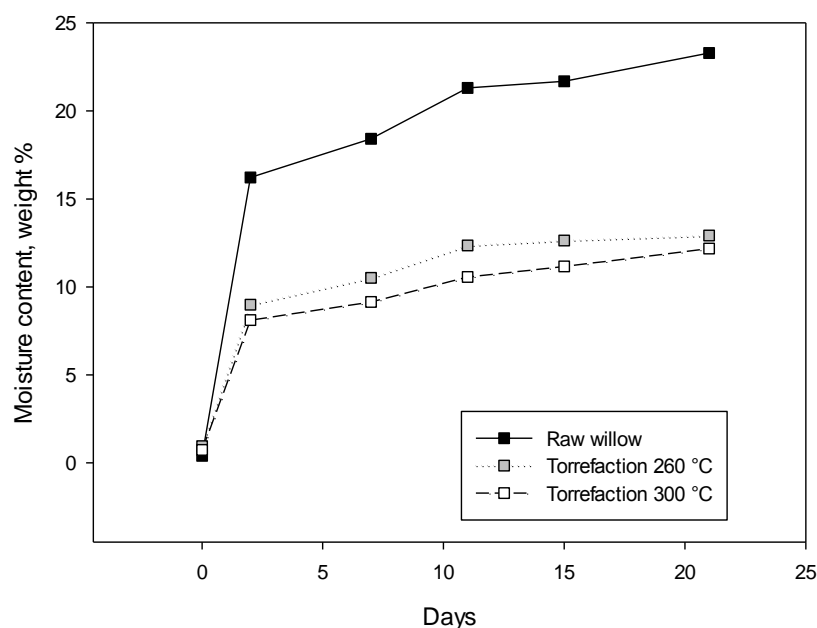


Figure I.6- Variation of the moisture content in willow over a period of 21 days in saturated water atmosphere

This is valid for all the samples, with a maximum reduction up to 50%, as shown in Figure I.6. The results of the sorghum are not reported, as they showed a different trend. This could be attributable to the fact that the particles “popped”, as previously shown, resulting in the creation of a sponge-like structure that adsorbed more water.

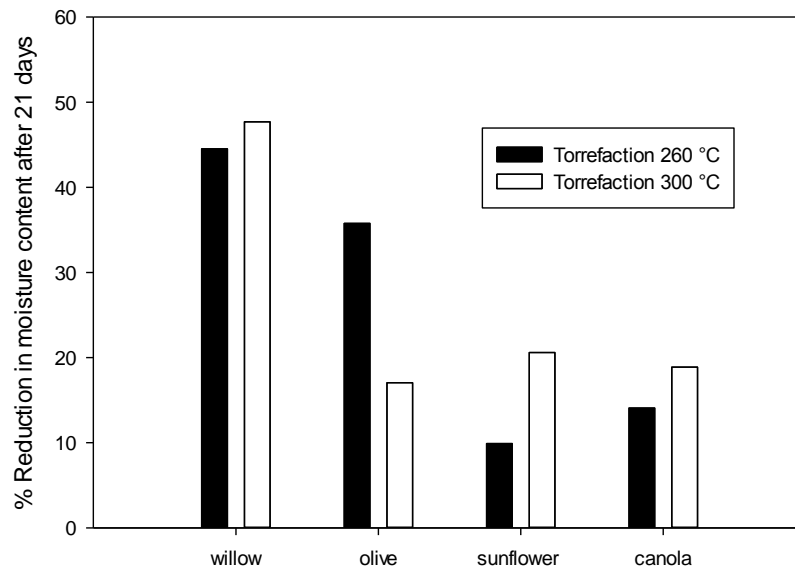


Figure I.7- Reduction in moisture content after 21 days as compared to virgin biomass

In particular, it is interesting to see that, in the case of sunflower husk and sorghum, after 21 days there are sign of biological activity, as shown in Figure I.7. This is not observed on any of the torrefied samples, which are thus successfully stabilized against biological activity. Similar behavior was also observed by Cruz (2012)



Figure I.8- Example of biological activity on the virgin biomass samples of sunflower husk and sorghum after 21 days

Grindability is an important parameter for coal quality evaluation: since it is likely that coal has to be milled to obtain a specified particle size, the amount of energy required for the operation has to be considered, as it can affect the process efficiency. Biomass grindability is very poor, while it has been proved by Abdullah (2009; 2010), that the one of bio-coal is much improved. Phanphanic

(2011) showed that the specific energy required for grinding wood chips was reduced from 237 kWh/ton to 23-78 kWh/ton after torrefaction at 275-300°C, obtaining a value more similar to coal (7-36 kWh/ton). In particular, energy consumption was six times less than the original biomass for logging residues and ten times for wood chips. These results are also supported by Arias (2008), who reported an improvement in the grindability of torrefied woody biomass with respect to the original one, in the temperature range 240-280°C. Similar results for the grindability characteristics were obtained by Chen (2011), who also confirmed through SEM observation that the shape of the particles was modified to a more spherical one by torrefaction.

The grindability results of selected samples are presented in Figure I.9. As a term of comparison, the results are presented as percentage with the respect to the consumption of the original biomass. In the case of sorghum, this comparison is not possible due to the difficulties in recovering the solid product from the stirrer, as previously explained. In the case of olive residue and sunflower husk, the comparison would be irrelevant. As shown in Figure I.10, the combination of heat and attrition with the stirrer results in the grinding of the particles inside the reactor itself. The comparison of the grinding energy is still possible for canola and willow samples, as reported in Figure I.9, which shows a significant reduction in the grinding energy requirement, of around 80%, in agreement with the results previously cited from the literature.

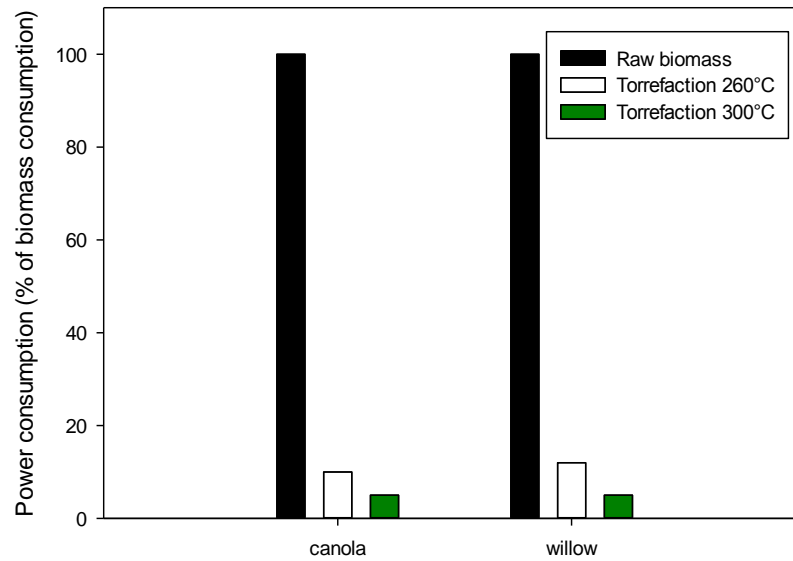


Figure I.9- Reduction in the energy required for grinding for torrefied samples



Figure I.10- Example of particle size reduction in the MFR as the torrefaction temperature is increased to 300 °C

I.IV Conclusions

This study investigated the torrefaction of different biomasses in a mechanically fluidized reactor (MFR). Although an increase in temperature from 260 to 300 °C showed an improvement in all the parameters considered (HHV, hydrophobicity, grindability), it was also accompanied by a higher mass loss and, consequently, low energy yield. The properties of biomass after torrefaction were suitable for co-firing.

I.V References

Abdullah, H., Mediaswanti, K.A., Wu, H., “Biochar as a fuel:2. Significant differences in fuel quality and ash properties of biochars from various biomass components of mallee trees”, *Energy&Fuels* (2010), 24, 1972-1979

Abdullah, H., Mourant, D., Li, C.Z., Wu, H., “Bioslurry as a fuel:3. Fuel and rheological properties of bioslurry prepared from the bio-oil and biochar of mallee biomass fast pyrolysis”, *Energy&Fuels* (2010), 24, 5669-5676

Acharjee, T.C., Coronella, C.J., Vasquez, V.R., “Effect of thermal pretreatment on equilibrium moisture content of lignocellulosic biomass”, *Bioresource Technology* (2011), 102, 4849–4854

Arias, B., Pevida, C., Feroso, J., Plaza, M.G., Rubiera, F., Pis, J.J., “Influence of torrefaction on the grindability and reactivity of woody biomass”, *Fuel Processing Technology* (2008), 89, 169-175

Ciolkosz, D., Wallace, R., “A review of torrefaction for bioenergy feedstock production”, *Biofuels, Bioproducts and Biorefining* (2011), 5 (3), 317–329

Colomba, A., Berruti, F. and Briens, C., "Production of bio-coal from biomass in a Mechanically Fluidized Reactor (MFR)" in "BioEnergy IV: Innovations in Biomass Conversion for Heat, Power, Fuels and Chemicals", Manuel Garcia-Perez, Washington State University, USA Dietrich Meier, Thünen Institute of Wood Research, Germany Raffaella Ocone, Heriot-Watt University, United Kingdom Paul de Wild, Biomass & Energy Efficiency, ECN, The Netherlands Eds, ECI Symposium Series, Volume (2013). http://dc.engconfintl.org/bioenergy_iv/14

Cruz, D.C., "Production of bio-coal and activated carbon from biomass" (2012). University of Western Ontario - Electronic Thesis and Dissertation Repository. Paper 1044

Ferro, T.D., Vigoroux, V., Grimm, A., Zanzi, R., “Torrefaction of agricultural and forest residues”, II-0185-FA, conference publication (2004)

Foley, G. Earthscan Technical Report No. 5; International Institute for Environment and Development; Russell Press: Nottingham, U.K., 1986.

Phanphanich, M., Mani, S., “Impact of torrefaction on the grindability and fuel characteristics of forest biomass”, *Bioresource Technology* (2011), 102, 1246-1253

Pimchuai, A., Dutta, A., Basu, P., “Torrefaction of agriculture residue to enhance the combustible properties”, *Energy&Fuels* (2010), 4638-4645

Sadaka, S., Negi, S., “Improvement of biomass physical and thermochemical characteristics via torrefaction process”, *Environmental Progress&Sustainable Energy*, (2009), 28, 427-434

Tumuluru, J.S., Sokhansanj, S., Hess, J.R., Wright, C.T., Boardman, R.D., “A review on biomass torrefaction process and product properties for energy applications”, *Industrial Biotechnology* (2011), 7 (5), 384-40

Appendix II

II. Arsenic Removal from Natural Water by Means of Bio-Char: the Case of Bangladesh

Tommaso Marengo, Anastasia Colomba, Silvia Fiore, Giuseppe Genon, Franco Berruti, Cedric Briens

Ready for submission to Bioresource Technology

II.I Abstract

The aim of this work was to find a suitable solution to remove arsenic contamination from groundwater in Bangladesh, using local resources and instrumentations. The proposed method was adsorption by means of biochar. A commercial activated carbon obtained from coconut husk and two self-produced biochars from miscanthus and coconut shell were tested: their main physical characteristics and adsorption capacities for arsenite and arsenate were evaluated. Adsorption isotherm and kinetic parameters for the adsorption of arsenite were identified for coconut husk and miscanthus. A sensitive interference of the presence of dissolved sodium in adsorption of inorganic arsenic was identified.

Adsorption analyses showed that miscanthus biochar has removal efficiencies comparable to the one of commercial carbon. However, adsorption does not seem the most suitable strategy for the purification of water from inorganic arsenic in the conditions found in Bangladesh, due to the low removal efficiency at low concentrations such as those found in typical natural waters in Bangladesh (500 µg/L.). Adsorption with biochar could be considered in a pre-treatment process, in the case where higher arsenic concentrations are found

Appendix III

III. Granulation of Bio-Char for Soil Amendment

Breanna Bowden-Green, Anastasia Colomba, Franco Berruti, Cedric Briens, Lauren Briens

Presented at 64th Canadian Chemical Engineering Conference

Abstracts

00218

FPT6

17:30 Monday PM

Exhibit Hall A

Granulation of Biochar for Soil Amendment B Bowden-Green <bbowdeng@uwo.ca>, **A Colomba** <acolomba@uwo.ca>, **F Berruti** <fberruti@uwo.ca>, **C Briens** <cbriens@uwo.ca> and **L Briens** <lbriens@uwo.ca>, Western University.

Pyrolysis burns biomass under zero oxygen conditions and produces gases, a liquid bio-oil and a solid biochar. A promising application of biochar is soil amendment as it can reduce nutrient leaching, increase water retention and increase microbial activity. However, biochar is a very fine powder which can be difficult to handle and could easily be blown away if applied directly to soils. Granulation of biochar into granules would produce larger particles that would be easier to handle and apply effectively to the soil. The goal of this study was therefore to investigate the potential for drum granulation of biochar. Biochar from birch bark, corn stalk and miscanthus was granulated varying the concentration of hydropropylmethyl cellulose in the binder solution, the added volume of binder solution and the rotation speed of the granulator drum. Strong and spherical granules in the 1 to 4 mm size range were obtained for all three types of biochar, but the optimal process parameters varied with the biochar. The corn stalk and miscanthus biochar required similar parameters while the birch bark biochar behaved differently reflecting the influence of the biochar properties on the granulation process.

Curriculum Vitae

Name: Anastasia Colomba

**Post-secondary
Education and
Degrees:** Politecnico di Torino
Torino, Italy
2006-2009 B.E.Sc.

Politecnico di Torino
Torino, Italy
2009-2011 M.E.Sc.

The University of Western Ontario
London, Ontario, Canada
2012-2015 Ph.D.

**Honours and
Awards:** Second Prize Winner (Oral Presentation)
5th Annual Sarnia-Lambton Research Bridges Symposium
Sarnia, Ontario, 2014

Graduate Student Teaching Award
Society of Graduate Students, the University of Western Ontario
London, Ontario, Canada, 2014

**Related Work
Experience** Teaching Assistant
The University of Western Ontario
2012-2014

Publications:

Colomba, A., Berruti, F. and Briens, C., "Production of bio-coal from biomass in a Mechanically Fluidized Reactor (MFR)" in "BioEnergy IV: Innovations in Biomass Conversion for Heat, Power, Fuels and Chemicals", ECI Symposium Series, Volume (2013).
http://dc.engconfintl.org/bioenergy_iv/14

Colomba, A., Latifi, M., Li, D., Berruti, F., Briens, C., "Application of the jigged bed reactor (JBR) to the development of effective pyrolysis and activation processes for the production of

activated char from biomass” In: Proceedings of 4th Green Process Engineering Congress (2014), Sevilla, Spain.